Structure-Property Relationships of Oligo(Phenylene Ethynylene)s

Zur Erlangung des akademischen Grades einer

Doktorin der Naturwissenschaften
(Dr. rer. nat.)

von der KIT-Fakultät für Chemie und Biowissenschaften
des Karlsruher Instituts für Technologie (KIT)

genehmigte

Dissertation

von

Qianyu Cai
aus Nanjing

Tag der mündlichen Prüfung: 23.10.2025
Erster Gutachter: Prof. Dr. Michael A. R. Meier
Zweiter Gutachter: PD. Dr. Zbigniew L. Pianowski

献给我的父母。

Word cloud compiled from the literary quotations printed by Gaussian 16 at the end of successful quantum-chemical calculations.

Declaration of Authorship

Die vorliegende Arbeit wurde von September 2022 bis August 2025 unter Anleitung von Prof. Dr. Michael A. R. Meier am Institut für Organische Chemie (IOC) und am Institut für Biologische und Chemische Systeme – Funktionelle Molekulare Systeme (IBCS-FMS) des Karlsruher Instituts für Technologie (KIT) angefertigt.

Hiermit versichere ich, dass ich die Arbeit selbständig angefertigt, nur die angegebenen Quellen und Hilfsmittel benutzt und mich keiner unzulässigen Hilfe Dritter bedient habe. Insbesondere habe ich wörtlich oder sinngemäß aus anderen Werken übernommene Inhalte als solche kenntlich gemacht. Die Satzung des Karlsruher Instituts für Technologie (KIT) zur Sicherung wissenschaftlicher Praxis habe ich beachtet. Des Weiteren erkläre ich, dass ich mich derzeit in keinem laufenden Promotionsverfahren befinde und auch keine vorausgegangenen Promotionsversuche unternommen habe. Die elektronische Version der Arbeit stimmt mit der schriftlichen Version überein und die Primärdaten sind gemäß Abs. A (6) der Regeln zur Sicherung guter wissenschaftlicher Praxis des KIT beim Institut abgegeben und archiviert.

Karlsruhe, 17.09.2025

Qianyu Cai

Acknowledgement

I am deeply grateful to all those who supported me and accompanied me along the way.

Mein besonderer Dank gilt zuerst dir, Mike. Danke, dass du mir die Möglichkeit gegeben hast, in so einem tollen Arbeitskreis zu promovieren. Danke für dein Vertrauen und für deine stetige Unterstützung.

Ein ebenso großer Dank geht an meine tollen Arbeitskollegen (Pinar, Svenja, Clara, Leon, Pete, Luca H., Henni, Celeste, Luca N., Sandra, Simon, Nichollas, Timo, Luis, Bohni, Francesca, Andreas, Federico, Caitlyn, Anja, Jonas, Michi, und Roman), die diese Zeit so besonders gemacht haben. Danke, Bohni, dass du mich in diese Gruppe „geholt“ hast und nach deiner Promotion noch ein paar Jahr geblieben bist. Ohne dich hätte ich länger gebraucht in die Gruppe einzuleben. Danke, Clara, meine Tischnachbarin, dass du immer ein offenes Ohr für mich hattest und mir stets weise Ratschläge gegeben hast. Danke, Sandra, meine erste Abzugnachbarin – es war ein Genuss, mit dir zusammenzuarbeiten, ohne dich wäre mir der Einstieg in die Promotion deutlich schwerer gefallen, Leon, mein 兄弟 (xiōng dì), danke für das süße Freitagsgebäck und die vielen Brainstormings über Chemie und alles andere. Celeste, you motivated me with your positive energy and showed me the possibility of finding the perfect balance between a PhD and a healthy lifestyle.

Bezüglich Synthese der Stäbchenmoleküle, geht mein Dank an Till – du bist einfach ein Macher; an Dani – für deine Besuche an MZE zwischendurch und das Teilen deiner Erfahrungen; sowie an all die Studierenden, insbesondere Ulrich Haug, Florian Richter, und Lars Boller, für ihre engagierte Mitarbeit.

Ich danke meinen Kollaborationspartnern Prof. Dr. Andreas-Neil Unterreiner und PD Dr. Zbigniew L. Pianowski für ihre Offenheit und Hilfsbereitschaft. Thank you Petko for your hard work and dedication. Danke, Marianne, für deine Untersützung zu jeder Zeit.

特别感谢 IOC 的中国同事们 Xujun, Yuting 以及 Haopu 一直以来的照顾!

Ein großes Dankeschön geht an meinen Freund André und seine Familie Antje und Isabelle. Danke, dass ihr immer für mich da seid.

Abschließend möchte ich meinen Eltern von Herzen danken, die mich all die Jahre hindurch bedingungslos unterstützt haben. 感谢我的父母一直以来无条件的信任与支持!

Abstract

Establishing reliable structure-property relationships and thus understanding how precise molecular structure governs a materials function is crucial in materials science. In this thesis, oligo(phenylene ethynylene)s (OPEs) are employed as model motifs to study the structure-relationship properties of sequence-defined macromolecules. The work is structured into three projects, investigating molecular sequencing in OPEs from both (opto-)electronic and structural perspective.

In the first project, aided by *in silico* design, two series of symmetric donor-acceptor-donor (D-A-D) OPE emitters were developed to cover the standard red, green, and blue (sRGB) color range. Systematic variation of the acceptor strength allowed precise tuning of the emission color, while extension of the conjugated backbone enhanced the contribution of locally excited (LE) emission character, manifesting in narrow full width at half maximum and higher quantum yield of the respective photoluminescence measurement in toluene.

In the second project, the conjugation-length dependent excited-state characteristics were further investigated in a series of donor-OPE-acceptor (D-OPE-A) sequences. The OPE segments linking a di-*tert*-butylcarbazole donor and a triphenyltriazine acceptor were varied from 0 to 3 propoxylated phenylene ethynylene units. Both theoretical and photophysical investigations revealed the gradual shift from charge transfer (CT)-dominated towards LE-dominated excited states with increasing donor-acceptor distances.

In the third project, an *ortho*-tetrafluoroazobenzene photoswitch was incorporated into the OPE backbone to introduce a reversible bending position. These systems remained responsive to light up to 620 nm and reached photostationary states with ~90% *Z*-contents. Additionally, size-exclusion chromatography (SEC) was applied as a complementary method to quantify the *E*/*Z* ratios and assess the thermal stabilitiy by monitoring Z→E back-isomerization.

In summary, this thesis advances the study of OPE-based systems toward electronic sequence design and dynamic geometric modulation, thereby establishing OPEs as powerful model systems for elucidating structure-property relationships in conjugated organic materials.

Zusammenfassung

Die Etablierung verlässlicher Struktur-Eigenschafts-Beziehungen und damit das Verständnis, wie die präzise molekulare Struktur die Funktion eines Materials bestimmt, ist entscheidend für Materialwissenschaften. In dieser Arbeit werden Oligo(phenylenethinylene) (OPEs) als Modellmotiv eingesetzt, um die Struktur-Eigenschafts-Beziehungen sequenzdefinierter Makromoleküle zu untersuchen. Aufgebaut wird dabei auf in früheren Arbeiten entwickelte Synthesestrategien. Die Arbeit gliedert sich in drei Projekte, in denen molekulare Sequenzierung in OPEs sowohl aus (opto-)elektronischer als auch aus struktureller Perspektive betrachtet werden.

Im ersten Projekt wurden mit Hilfe von *in silico*-Methoden zwei Serien symmetrischer Donor-Akzeptor-Donor (D-A-D)-OPE-Emitter entwickelt, die den Standardfarbraum Rot, Grün, und Blau (sRGB) abdecken. Durch die systematische Variation der Akzeptorstärke ließ sich die Emissionfarbe präzise einstellen. Darüber hinaus verstärkte sich die Verlängerung des konjugeirten OPE-Stranges den Beitrag der *local excited* (LE) Zustände, was sich durch schmaleren Emissionsbanden und höheren Quantunausbeuten der Photolumineszenz in Toluol äußerte.

Die Konjugationslängenabhängigkeit der angeregten Zustände wurde anhand einer Reihe von Donor-OPE-Akzeptor (D-OPE-A)-Sequenzen systematisch untersucht. Dabei wurden die OPE-Segmente, die einen Di-*tert*-butylcarbazol-Donor mit einem Triphenyltriazin-Akzeptor verbinden, von null bis drei propoxylierten Phenylenethinylen-Einheiten variiert. Sowohl theoretische Berechnungen als photophysikalische Untersuchungen zeigten dabei einen sukzessiven Übergang von *charge transfer* (CT)-dominierten zu LE-dominierten Zuständen mit zunehmendem Donor-Akzeptor-Abstand.

Im dritten Projekt wurde ein *ortho*-Tetrafluorazobenzol-Photoschalter in das OPE-Rückgrat integriert, um eine reversible Knickstelle via *E/Z*-Isomerisierung einzuführen.

Die Photoschalter blieben durch Licht von bis zu 620 nm Wellenlänge anspechbar und erreichten photostationäre Zustände mit *Z*-Isomer-Anteilen von bis zu 90 %. Erstmals wurde die Größenausschlusschromatographie (GPC) als komplementäre Methode eingesetzt, um die *E*/*Z*-Verhältnisse zu quantifizieren und die thermische Stabilität der Schalter zu bestimmen.

Zusammenfassend erweitert diese Arbeit die Untersuchung OPE-basierter Systeme um elektronisches Sequenzdesign und dynamisch, geometrische Modulation und etabliert OPEs damit als leistungsfähige Modellsysteme zur Aufklärung von Struktur-Eigenschafts-Beziehungen in konjugierten organischen Materialien.

Table of Contents

1 Introduction....1
2 Theoretical Background....3
2.1 Conjugated Organic Systems....3
2.1.1 Historical Walkthrough of π-Conjugated Molecules....3
2.1.2 Common Conjugated Polymers....7
2.1.3 Oligo(Phenylene Ethynylene)s (OPEs)....13
2.2 Macromolecular Dyes and their Photophysical Behaviors....21
2.2.1 General photophysics....21
2.2.2 Applications....25
2.3 Sequence-Defined Macromolecules....29
2.3.1 Necessity of Sequence Definition....29
2.3.2 Synthetic Strategies for Sequence Definition....32
3 Aim....43
4 Tuning the Emission-Color of Sequence-Defined OPEs....45
4.1 Motivation....45
4.2 Results and Discussion....46
4.2.1 Molecular Design and Synthetic Access....46
4.2.2 Theoretical Investigations....49
4.2.3 Steady-State Optical Characterization....55
4.3 Summary and Outlook....58
5 Donor-OPE-Acceptor Architectures....60
5.1 Motivation....60
5.2 Results and Discussion....61
5.2.1 Synthesis of D-OPE-A Oligomers....61
5.2.2 Computational Investigation....64
5.2.3 Steady State Photophysics....66
5.2.4 Transient Absorption Spectroscopy....72
5.3 Summary and Outlook....75

6 OPE-based Photowitches 78
6.1 Motivation 78
6.2 Results and Discussion 80
6.2.1 Synthesis and Initial Characterization 80
6.2.2 Characterization of Photoisomerization Behavior 83
6.2.3 Development of Quantification Using SEC 87
6.3 Summary and Outlook 93
7 Conclusions 95
8 Experimental Section 97
8.1 Materials 97
8.2 Instrumentation 98
8.3 Synthetic procedures 101
8.3.1 Modification of OPE Building Blocks 102
8.3.2 Synthesis of D-A-D OPEs 114
8.3.3 Iterative Synthesis of D-OPE-A Systems 128
8.3.4 Synthesis of OPE Photoswitches 149
9 Appendix 156
9.1 Computational Details 156
9.2 Additional Photophyisical Results 156
9.3 Investigation of Photostationary State 161
10 References 164

1 Introduction

"The most fundamental and lasting objective of synthesis is not production of new compounds, but production of properties." This statement, made by Geroge S. Hammond, father of modern photochemistry, in his 1968 Norris Award Lecture,[1] not only underlines the core values of synthetic chemistry and materials science but also reflects the main motivation of this thesis. Guided by this principle, the reliable elucidation of structures-property relationships is key to developing new functional materials and may be facilitated via precision molecular engineering such as sequence definition and stereo control. For instance, recent works investigated uniform sequence-defined oligomers as photoresist materials to decrease statistical noise and therefore achieve higher resolution in extreme ultraviolet (EUV) photolithography,[2] suggesting molecular sequence-definition as means to advance modern computer chips and in accordance to Moore's Law.[3]

A key challenge for polymer chemistry lies in moving from structure-tendency to structure-certainty: the ability to assign precise molecular properties to defined structural features and sequences. This challenge has stimulated growing interest in sequence-defined macromolecules, which provide an unprecedented level of control over molecular architecture.[4] Such systems mimic the structural logic of biopolymers, where a linear sequence of monomers encodes function and folding.[5]

In recent years, our research group has made important contributions to apply sequence-control towards conjugated backbones.[6–9] In particular, a modular platform based on oligo(phenylene ethynylenes) (OPEs), which combines rigid π-conjugation with the possibility of monomer-level sequence control. Through iterative Sonogashira cross-coupling and related strategies, structurally defined OPE oligomers with varying substitution patterns and lengths have been synthesized.[7,9] These systems display predictable optical signatures, well-resolved chromatographic profiles, and sequence-dependent behavior in solution.[8,10,11] However, while such systems offer high control

over the primary structure, the interpretation of their photophysical properties remains largely empirical.

At present, a major missing piece in our research is the integration of quantum mechanical analysis to connect defined molecular sequences with their resulting (electronic) properties. Questions such as how sequence affects orbital delocalization, charge-transfer character, and excited-state dynamics are central to designing materials with programmable function.[8]

A further structural dimension can be added through photoresponsive units, such as molecular photoswitches.[12] These motifs undergo reversible *E*/*Z* isomerization, enabling controlled changes in molecular geometry and, by extension, the secondary structure of macromolecules. Incorporating azobenzenes into rigid OPE backbones opens the possibility of externally modulating conformation and exploring how geometry affects conjugation and function at a molecular level.

This thesis combines structural definition, photophysical properties, and quantum chemical interpretation. Through this integrative approach, the work explores how sequence and conformation govern function in conjugated molecular systems, and how precision synthesis can be harnessed not just for control, but for understanding.

2 Theoretical Background

2.1 Conjugated Organic Systems

2.1.1 Historical Walkthrough of π-Conjugated Molecules

The exploration of organic conjugated molecules can be traced back nearly two centuries, but it was not until the later half of the 20th century that this class of compounds became widely recognized for its potential as functional electronic materials.[13–18] Parallel developments in both experimental and theoretical aspects turned them from molecular curiosities into foundational components of organic electronics.[19–21] To provide an overview of this development, Figure 1 summarizes the major advances from both perspectives.

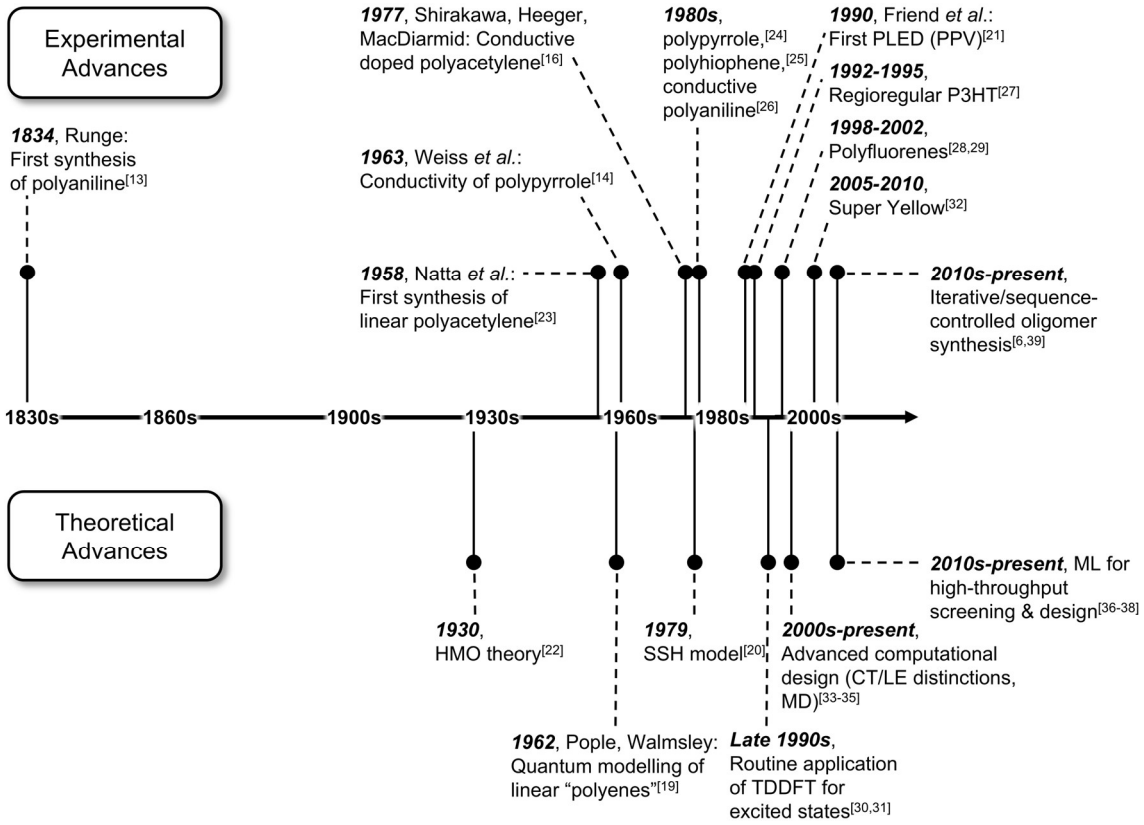

Figure 1. Major experimental and theoretical milestones in the development of π-conjugated macromolecular systems. Key advances in synthesis and applications are shown above the axis, while significant theoretical contributions are placed below.[6,13,22,23,19,14,15,20,24–26,21,27–39]

The earliest encounter with a synthetic conjugated polymer dates to 1834, when Runge reported the synthesis of "aniline black", a product of aniline oxidation that was primarily used as a textile dye.[13] Over the following century, various oxidation states of this material were gradually isolated, among which the fully reduced, colorless form (leucoemeraldine) corresponds to the structure of polyaniline (PANI) depicted in Figure 2.[13] The fact that these substances could exhibit electrical conductivity remained, however, undiscovered at that time.

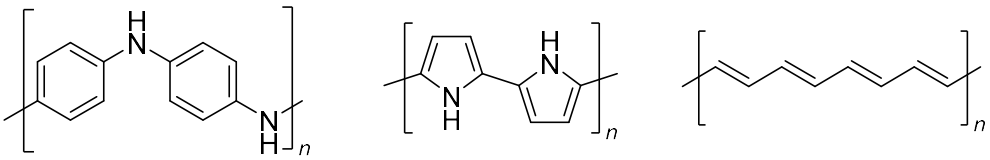

Figure 2. Representative parent structures of historically important π-conjugated polymers prior to the 1980s.[13,14,23]

In the early 1930s, the publication of Hückel's molecular orbital (HMO) theory enabled significant progress in the theoretical understanding of π-electron behavior, providing for the first time quantitative insights into delocalization and aromaticity.[22] Building upon this foundation, in 1962, Pople and Walmsley performed quantum modeling of linear polyenes, providing theoretical insights into bond alternation and the nature of defects using the more advanced Pariser-Parr-Pople (PPP) method.[19] This work was a significant precursor to later defect-based theories.

During this period, the community of preparative chemists also made a huge leap forward since Natta and co-workers successfully synthesized linear polyacetylene (PAc) using the catalyst discovered by Ziegler *et al.* for olefin polymerization (Figure 2).[23,40] In subsequent years, Weiss *et al*. polymerized pyrrole oxidatively using iron(III) chloride ($FeCl_3$) as the oxidizing agent.[14] They extensively investigated the conductivity of polypyrrole (PPy, Figure 2), but its potential as a conductive polymer remained unrecognized until the late 1970s.[13]

In 1977, the work led by Shirakawa, Heeger, and MacDiarmid demonstrated that doping polyacetylene with electron donors or acceptors could increase its conductivity

significantly.[15,41] For instance, one of their earliest studies on doping reported that the conductivity of *trans*-polyacetylene doped with ca. 20% iodine increased by seven orders of magnitude to 38 S cm^{-1} at room temperature.[15] This may be recognized as nearly "insulating" by today's standards when compared to the modern benchmark conjugated material poly(3,4-ethylenedioxythiophene):polystyrene sulfonate (PEDOT:PSS, see Section 2.1.2 for more details), whose latest entry exceeded 15000 S cm^{-1} after blade-coating and treating with concentrated trifluoromethanesulfonic acid.[42] Nevertheless, the research of Shirakawa *et al.* was groundbreaking at that time, opened up new avenues in the field of conductive materials, and induced an explosive growth in the design and synthesis of π-conjugated polymer systems. Thus, the synthesis of classically known conjugated polymer materials, such as the aforementioned polypyrrole and polythiophene (PT), the conductive form of polyaniline, and poly(*para*-phenylene) (PPP), etc., has been pursued and their conductive properties have been extensively investigated.[24–26,43] As a complement to Figure 2, the prototypical backbone structures of PT and PPP as well as PPV and PF are illustrated in Figure 3.

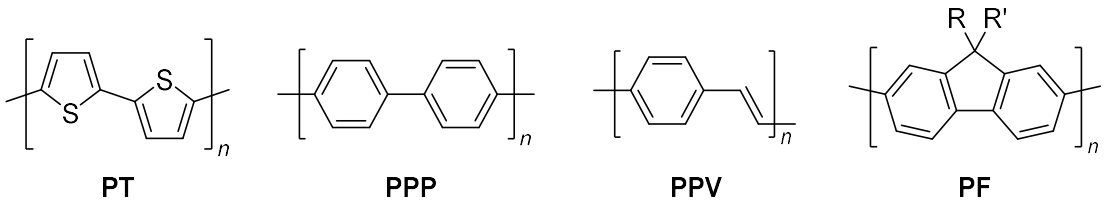

Figure 3. Representative parent structures of important π-conjugated polymers after the 1980s.[21,44,45]

Meanwhile, the theoretical efforts in this field have never stagnated. In 1979, Su, Schrieffer, and Heeger introduced a model, later known as the SSH-model, based on the formation of solitons, mobile defects of the conjugation chain, to describe the charge carrier in long-chain linear polyenes, thus gaining an initial understanding of the conducting behavior of the doped polyacetylene. They assessed this model from the perspectives of binding energy, length of conjugation, and activation energy, etc., and thus laid a foundational theoretical basis for understanding conductivity in conjugated polymers.[20]

In the decades that followed, a wide variety of π-conjugated polymers were developed, with a focus on tailored optoelectronic properties for specific utilities. Poly(*para*-phenylene vinylene) (PPV, Figure 3) and its derivatives were among the first to demonstrate practical application potential. Friend *et al.* reported in 1990 the first polymer light-emitting diode (PLED) using PPV, thus introducing polymers into OLED technology.[21] Around the same time, the development of regioregular alkylated PTs poly(3-alkylthiophene)s (PATs) provided enhanced charge carrier mobility and better solid-state organization, turning them into cornerstone materials in organic photovoltaics (OPVs) and organic field-effect transistors (OFETs).[27]

Conjugated polymers continued to evolve into the 21st century, with polyfluorenes (PFs, Figure 3) and their copolymers offering high photoluminescence quantum yields and tunable optical properties.[28,29] Commercial materials such as Super Yellow, a PPV derivative, emerged as reliable emissive materials in OLEDs, combining high efficiency with excellent processability.[32] The emphasis has since shifted towards fine-tuning molecular architecture, sequence control, and supramolecular organization to achieve better performance and functional diversity.[46–50]

In tandem with synthetic progress, the theoretical understanding of π-conjugation has also evolved significantly. In the late 1990s, time-dependent density functional theory (TDDFT) became a routine computational tool for predicting excited-state properties of conjugated molecules.[30,31] Since the early 21st century, a more precise distinction between charge-transfer (CT) and locally excited (LE) states has been established, enabling better interpretation of spectroscopic signatures and guiding material design. In addition, the integration of molecular dynamics (MD) simulations has allowed researchers to explore conformational disorder, thermal motion, and packing effects in soft π-systems.[33–35] More recently, the increasing availability of large-scale datasets has enabled the application of machine learning (ML) methods, accelerating property prediction and material screening in complex polymeric systems.[36–38]

In summary, the field of conjugated polymers has developed from fundamental curiosity about conductivity in organic solids to a major branch of materials science with

substantial technological impact. Polyaniline played a foundational role in early history, while materials like PPV, PATs, and PFs have shaped modern (opto-)electronic applications. The progression from simple linear backbones to sophisticated, sequence-defined architectures reflects the field's ongoing evolution towards precision and function at the molecular level.

In the following section, both conjugated polymer materials commonly used in industry and π-conjugated systems currently under intensive investigation by the scientific community will be presented.

2.1.2 Common Conjugated Polymers

While early conjugated polymers such as polyacetylene and polyaniline demonstrated the conceptual possibility of electrically conductive plastics, their limited stability and poor solubility, combined with processing challenges, hindered practical implementation.[51] In contrast, a number of π-conjugated polymers developed since the 1980s have achieved sufficient robustness, processability, and optoelectronic performance to find use in commercial and pre-commercial technologies. These materials are primarily employed in OLEDs,[32,52,53] OFETs,[54] OPVs,[55] and others. Figure 4 illustrates two representative stacked layer structures: (a) a light-emitting diode and (b) a solar cell. Conjugated structures play essential roles in several layers.

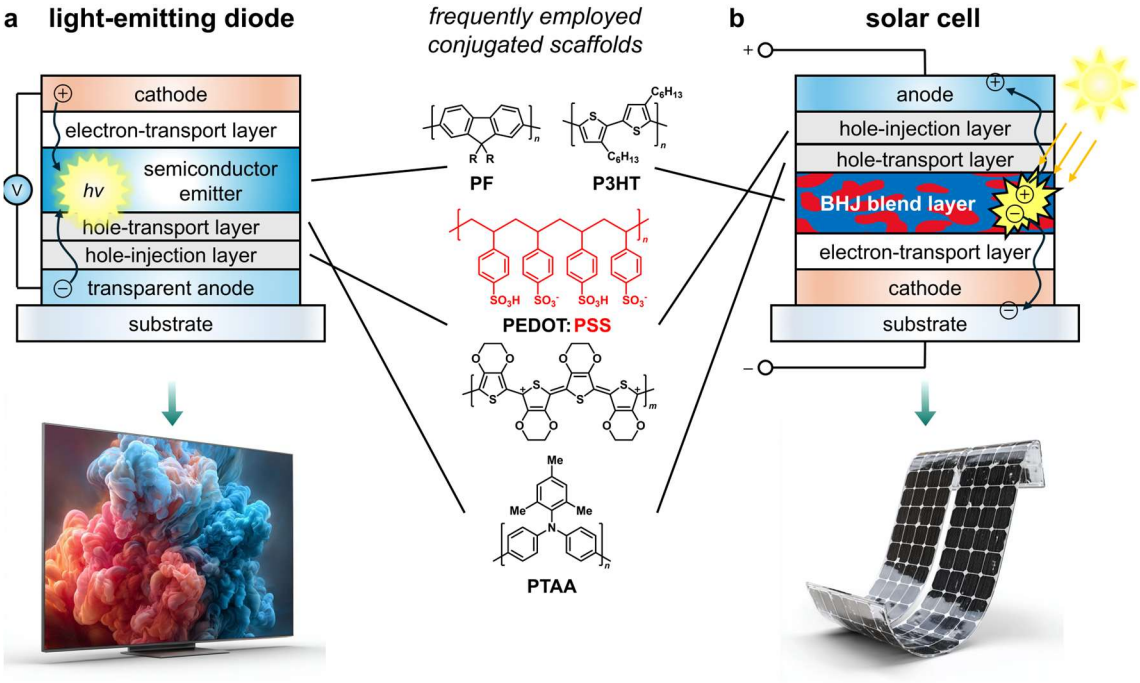

Figure 4. Schematic illustrations of a) an OLED stack with application in a display and b) an OPV stack with application in flexible solar cell panels, adapted from ref.[45]. The chemical structures of representative conjugated polymers are shown in the center and linked to their respective layers.[56] The application images were generated using MidJourney (www.midjourney.com).

One of the most commercially relevant materials is poly(3,4-ethylenedioxythiophene):polystyrene sulfonate (PEDOT:PSS). It combines a conducting polymer (PEDOT) with a water-soluble polyelectrolyte (PSS), resulting in a stable dispersion that can be processed from aqueous solution. PEDOT was first synthesized in the late 1980s by Bayer AG via oxidative polymerization of the EDOT monomer using iron(III) salts in aqueous media (Figure 5).[57] To overcome PEDOT's poor intrinsic solubility, it was blended with PSS, which acts as both a dispersant and charge-balancing counterion. PEDOT:PSS exhibits high transparency in the visible region, good mechanical flexibility, and excellent compatibility with solution-processing techniques, making it widely adopted as a hole-transport layer or transparent electrode in OLEDs, OPVs, and bioelectronics.[58,59]

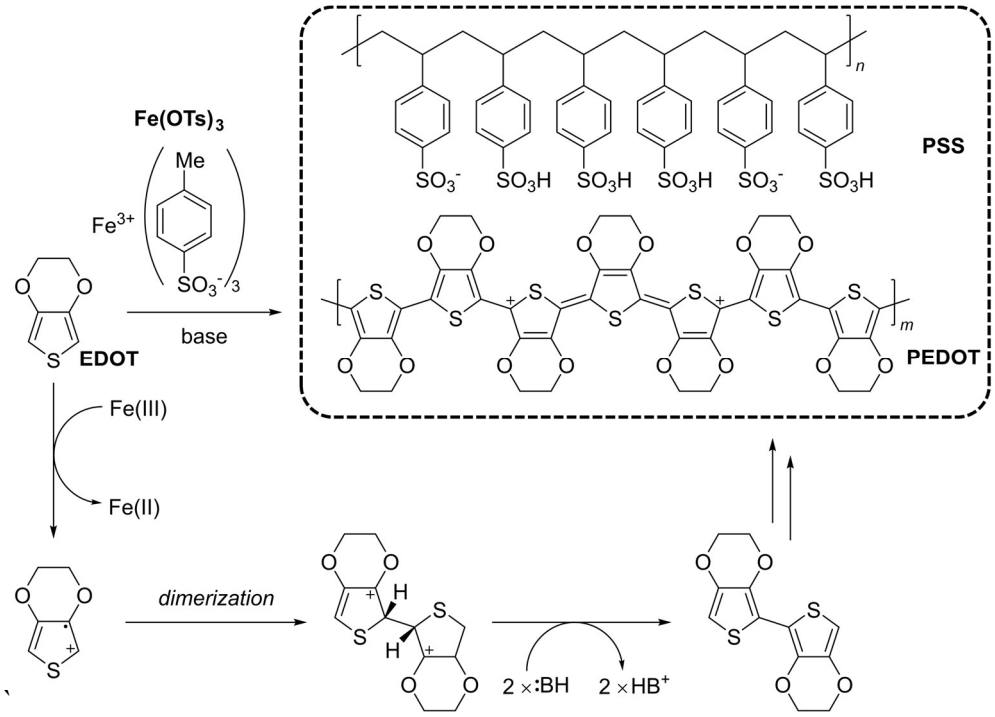

Figure 5. Synthesis of PEDOT:PSS following the Bayer AG method.[57]

Polyfluorenes (PFs) represent another class of conjugated polymers with industrial relevance, particularly in blue OLEDs and OFETs. These polymers are commonly synthesized via Suzuki-Miyaura cross-coupling or Yamamoto homo-coupling reactions (Figure 6).[46,60,61] The rigid and planar fluorene core contributes to high fluorescence efficiency and charge mobility, while side chains such as octyl groups enhance solubility and processability. Due to differences in molecular conformation, the aggregated state of PF chains in solid films exhibits an α-phase and β-phase. While the α-phase is the default state for many PFs, techniques such as solvent-swelling protocols or blending with other polymers can induce the formation of the β-phase, which has improved optoelectronic properties and is crucial for enhancing performance and device stabilities. Furthermore, structural modifications and stabilizing co-monomers have been introduced to improve photostability and device longevity. As such, polyfluorene derivatives continue to serve in emissive layers and host matrices in commercial OLED formulations.[54]

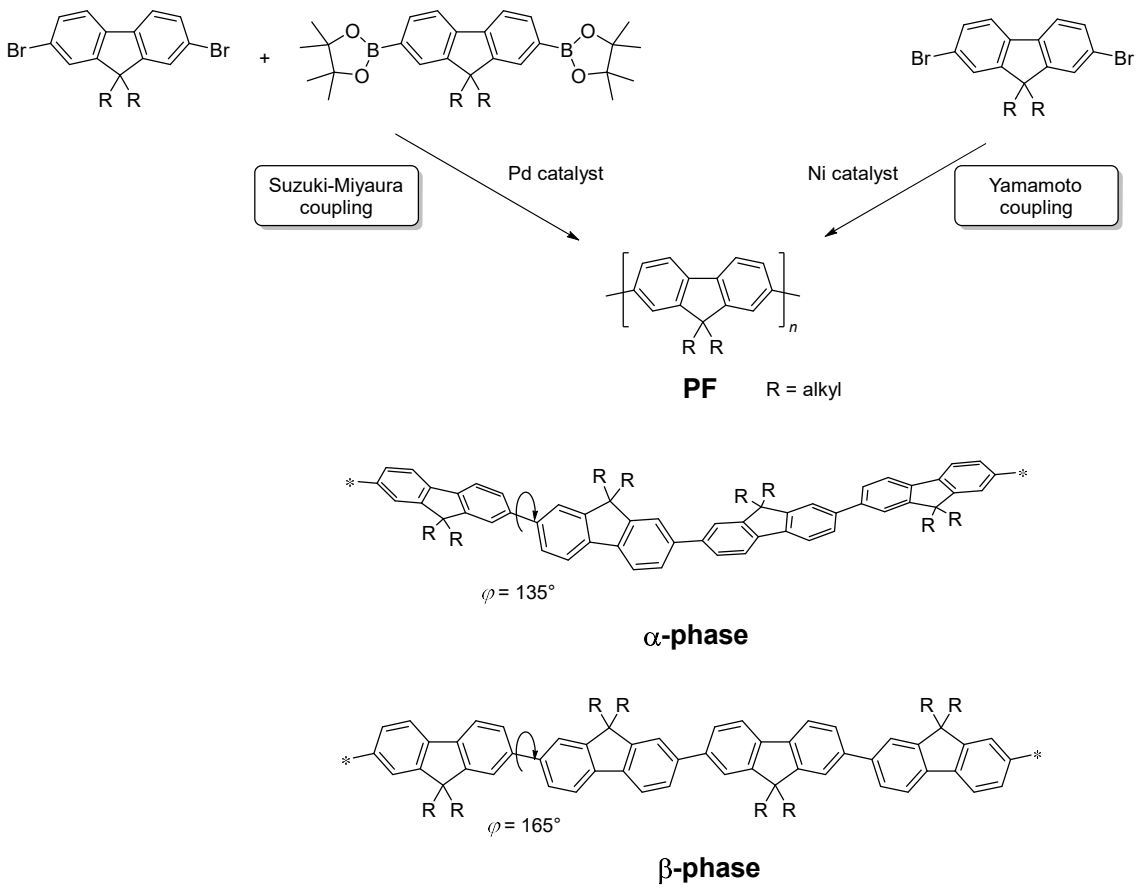

Figure 6. Top: representative synthetic routes to polyfluorenes.[60,61] Bottom: structures typical aggregated phases in polyfluorenes.[54]

Among the polymers discussed so far, PEDOT:PSS stands out for its industrial-scale production (2020: > 100 t/a) and broad commercial use.[56,62] Likewise, PF derivatives have gained significance in various device applications.[63–66] They are often used as copolymer blends that combine the favorable luminescent, electronic, and absorptive properties of PFs with comonomers like benzothiadiazoles or thiophenes to further tune the material properties.[64]

In addition, a wide variety of π-conjugated systems have attracted attention in academic research due to their tunable electronic properties, synthetic versatility, and potential for functional integration into emerging technologies.[46]

A prominent academic benchmark material is poly(3-hexylthiophene) (P3HT, Figure 4), a regioregular poly(3-alkylthiophene) whose synthesis was first reported by McCullough

and Lowe using a Grignard metathesis (GRIM) polymerization.[67] This classical method involves the nickel-catalyzed coupling of a Grignard reagent prepared from 2-bromo-3-hexylthiophene and magnesium, yielding high regioregularity (>98% head-to-tail) and moderate molecular weights (M_n ~ 11 kDa) on lab scale.[67,68] Regioregular P3HT exhibits a semicrystalline lamellar morphology, facilitating efficient charge transport and enabling its role as a model system for organic semiconductors.[69,70] Its key applications include OFETs, OPVs, and fundamental studies of charge transport, aggregation, and morphology evolution. Despite limited absorption coverage and moderate efficiencies in modern OPV architectures, P3HT is still widely used due to its synthetic accessibility, structural uniformity, and compatibility with solution processing.[71]

As mentioned in the last section, another common material is Super Yellow, a soluble armorphous PPV co-polymer that has become extensively used in OLED research (Figure 7a).[72] Commercially available as PDY-132 (Livilux®), Super Yellow can be synthesized via Gilch polymerization, a base-induced elimination method that produces high molecular weight polymers of M_n = 69 kDa at 62% yield (Figure 7b).[73,74] The introduction of long alkoxy side chains during polymer design improves solubility and film formation.[75] Super Yellow remains popular for OLEDs due to its stable yellow emission, high photoluminescence efficiency, and compatibility with standard solution-processing methods.[76] However, it is largely restricted to research and prototyping environments, with low production volumes and thus high costs (as of September 2025, Sigma-Aldrich lists Super Yellow at €1220 g^{-1}).[77]

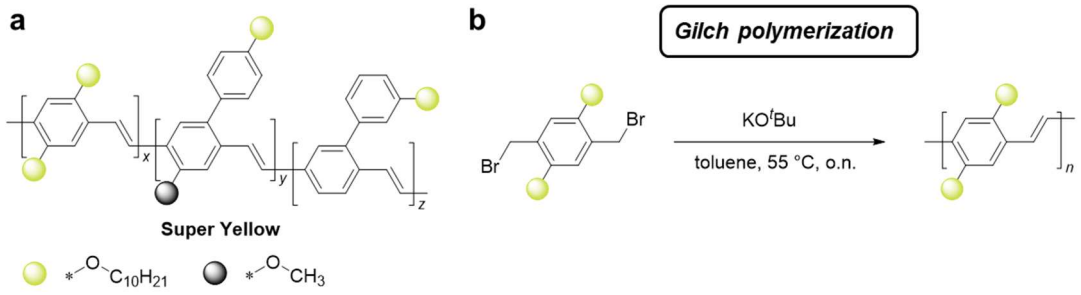

Figure 7. Super Yellow. a) Chemical structure. b) Simplified synthetic scheme of Super Yellow derivatives via Gilch polymerization.[73,74]

Structurally more complex than classical PPV (Figure 3), poly(arylene-1,2-diarylvinylene)s (PAV-DAs) represent an important subclass of conjugated polymers incorporating diarylvinylene units into the backbone. These systems have attracted increasing attention due to their high solid-state quantum yields and aggregation-induced emission (AIE) properties.[78] Traditionally, aryl substituted PPVs were accessed through reductive polyolefination protocols that employed hazardous reagents such as cobalt carbonyls (Figure 8a).[79] However, a recent study by Meier *et al.* introduced a novel elemental sulfur-mediated polyolefination strategy using bifunctional *N*-tosylhydrazones (Figure 8b), offering a safer and more practical route to PPV derivatives.[80] This polymerization method builds directly on their earlier work in developing sulfur-mediated olefination of *N*-tosylhydrazones, where tetraarylethylenes (TAEs) were synthesized through homocoupling and cross-coupling reactions under air-stable, scalable conditions.[81]

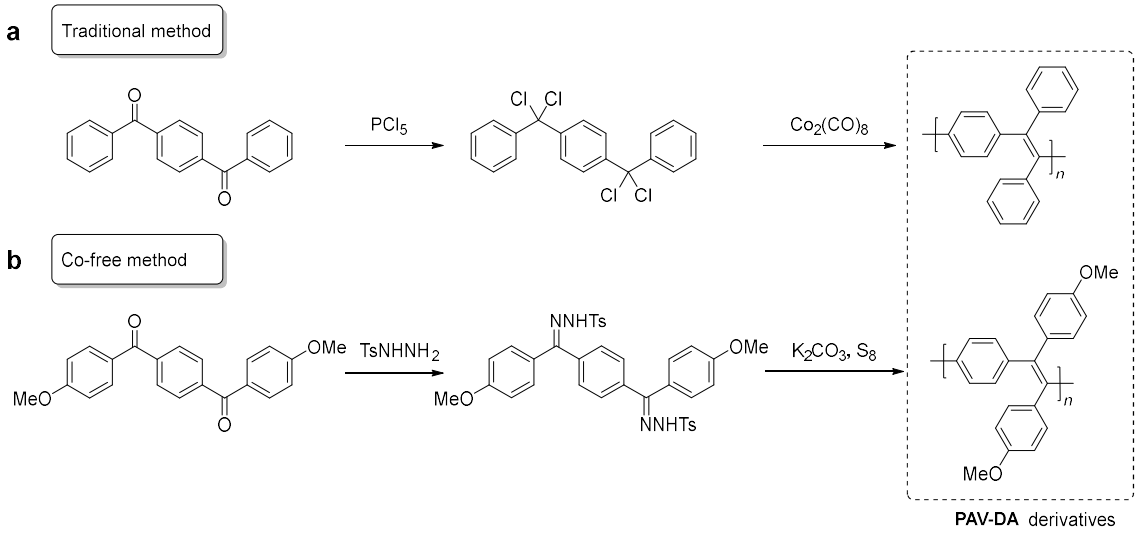

Figure 8. a) Reductive polyolefination of aryl-substituted PPVs using cobalt carbonyls.[79] b) Sulfur-mediated polyolefination of bifunctional N*-tosylhydrozones.[80]*

Poly(phenylene ethynylene) (PPEs) and related rigid polymers have been widely studied for their optical properties and electronic delocalization.[82–85] The *para*-connected derivatives have further been investigated as prototypical model system for one-dimensional conjugation. These rod-like polymers are typically synthesized via a Sonogashira cross-coupling reaction between a diiodoarene and a diethynylarene under

palladium/copper catalysis, typically carried out in amine solvents such as triethylamine or piperidine (Figure 9).[86] More recent advances have introduced microwave-assisted protocols and copper-free conditions, enhancing efficiency and reducing copper-related side reactions.[87,88]

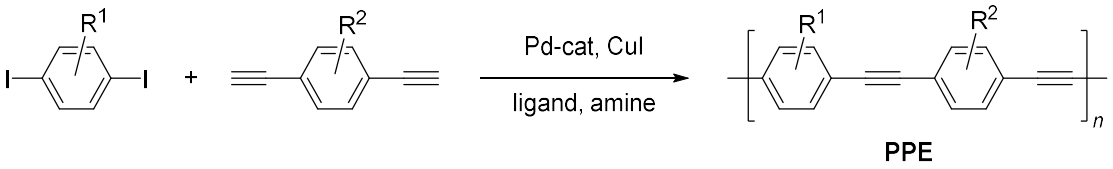

Figure 9. General synthetic route to PPEs via Sonogashira coupling polymerization.[86]

The polymeric materials discussed in this chapter are used as polydisperse mixtures in their respective fields of application. However, there is a growing academic interest in sequence-defined or precision conjugated polymers.[4,89,90] Their development is still largely confined to the academic domain due to synthetic challenges and limited scalability. A detailed discussion of the synthetic methods and specific examples of conjugated sequence-defined oligomers will be presented in Section 2.3.2.2.

2.1.3 Oligo(Phenylene Ethynylene)s (OPEs)

2.1.3.1 Recent Advances in PPE/OPE Research

Recent studies on poly- and oligo(phenylene ethynylene) (PPE/OPE) systems have highlighted their versatility as functional π-conjugated frameworks in diverse contexts, ranging from sensing to nanoelectronics.[82,86,91,92] The following sections examine their unique properties and explore how these characteristics translate into applications.

OPEs as Molecular Wires

One of the earliest and most enduring concepts associated with OPE systems is their role as molecular wires. The term “molecular wire” appeared already in the 1970s in the

context of molecular electronics. It refers to individual molecules that can mediate charge transport between two points, akin to metallic wires but on the molecular scale.[93] Requirements for molecular wires include a rigid, linear and conjugated backbone to support effective π-conjugation, minimal energetic barriers for charge delocalization, and chemical stability under operational conditions - criteria that OPE systems fulfill well due to their well-defined geometry, extended conjugation, and synthetic versatility.[92] As a result, OPEs and their derivatives became prototypical systems for investigating length-dependent charge transport, quantum tunneling, and the effects of conjugation and torsion on electron delocalization in one-dimensional architectures. As shown in Figure 10a, a molecular junction is the experimental configuration in which an OPE molecule functions as a molecular wire, connected to metal electrodes through anchoring groups, typically amine or thiol functionalities, that ensure robust electrical contact.[94] Recent studies have advanced this field by using OPEs to investigate unsymmetric effects,[95] substitution effects,[96] switching effects,[97] and to gain more understanding in quantum mechanics.[98–100]

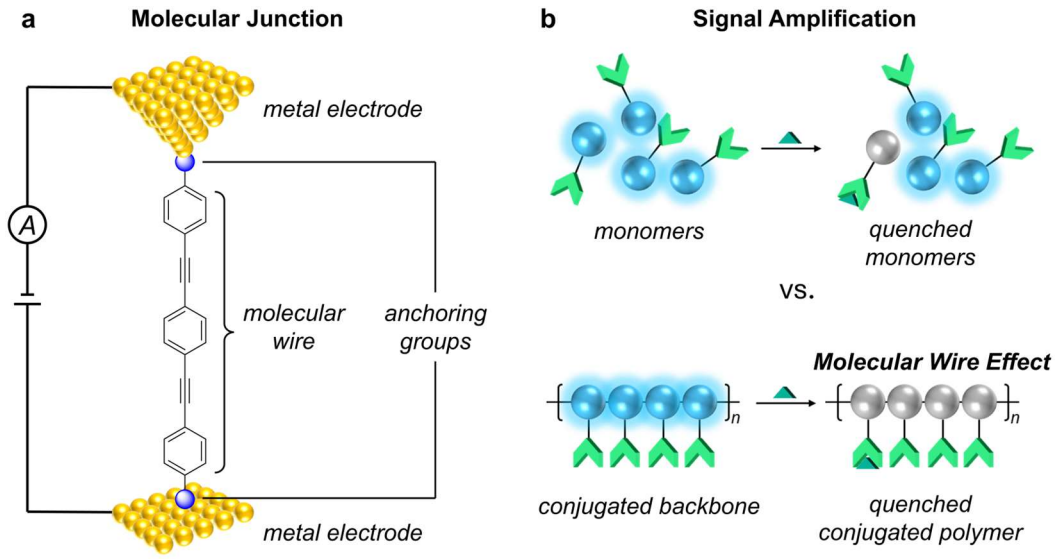

Figure 10. a) Schematic illustration of a set-up of molecular junction.[92] b) Signal amplification principle based on molecular wire effect.[101]

Signal Amplification and Sensing: The Molecular Wire Effect

Beyond their role in charge transport, OPE/PPE systems have also been employed in sensing applications that exploit the molecular wire effect, which refers to the transmission of a local perturbation, such as analyte binding, along the conjugated backbone, resulting in an amplified or an efficiently quenched optical or electronic signal (Figure 10b).[102] The π-conjugation that extends over the OPE backbone facilitates communication between remote binding sites and a central transducer unit. As a result, a single local binding event along the chain can cause a global change in conductivity or fluorescence. This signal amplification makes OPEs/PPEs good candidates as sensing materials.[103]

Primarily based on side-chain (receptor) design (Figure 11), the sensing abilities of OPEs/PPEs have been explored in the past two decades for analytes such as metal ions,[104,105] small molecules,[106,107] and biomolecules.[108,109]

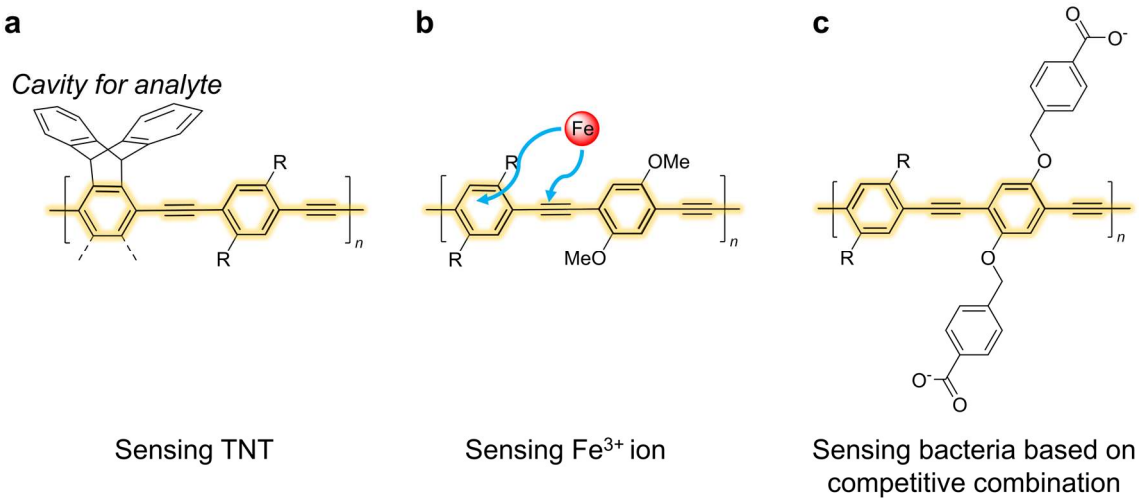

Figure 11. Design strategies of PPE-based sensors exploiting the molecular wire effect towards different analytes. a) TNT sensor incorporating a triptycene cavity.[110] b) Fe^{3+} sensor based on complexation with the conjugated backbone.[105] c) Negatively charged PPE sensor for bacteria detection based on competitive binding.[111] R: solubilizing groups.

OPEs in Self-assembly

Furthermore, OPEs have been extensively explored for their ability to self-assemble into ordered supramolecular architectures.[112] In solution, the self-assembly of OPEs is driven primarily by π-π stacking and solvophobic interactions, and can be modulated through side-chain engineering to induce hydrogen-bonding (H-bonding) or coordination sites for metal complexes.[11,113–116]

In 2021, Kartha, Fernández, and co-workers reported a series of linear OPE molecules only functionalized with three solubilizing dodecyl ether groups at both ends of the π-conjugated backbones (Figure 12).[11] In non-polar solvents such as methylcyclohexane, photoluminescence spectroscopy revealed that the aggregation tendency of these OPE systems increases with the length of the conjugated chain. Concentration- and temperature-dependent UV-Vis spectroscopy further supported these findings: for oligomers with $n = 4$ and $n = 5$ repeating units, a red-shifted shoulder emerged at higher concentrations and disappeared upon heating, consistent with aggregate formation. Given the molecular design, this aggregation behavior is most plausibly driven by π-π aromatic interactions between the conjugated backbones.

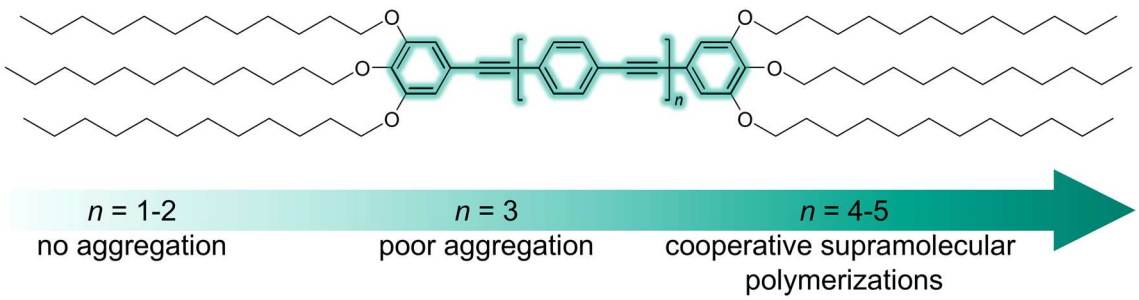

Figure 12. Chemical structure of the OPE compounds reported for the study of self-assembly through aromatic interactions (top) and their length-dependent aggregation ability in solution (bottom).[11]

In 2024, Wegelin and Meier reported a series of OPE mounted α-acyloxyamides. By employing the Passerini three-component reaction (P-3CR), they elegantly introduced a branching point to the carboxylic terminus of the rod-shaped OPE molecules, thus obtaining uniform first-generation dendrons (Figure 13).[113] The OPE moieties were obtained via an iterative strategy based on an in-house developed decarboxylative

Sonogashira type cross-coupling and subsequent saponification reaction (Figure 13 in Section 2.3.2.2), ensuring the monodispersity of each oligomer.[9] To facilitate processing, the repeating units of these OPEs were pre-functionalized with propoxyl groups, which provided moderate solubility during synthesis. Both photoluminescence spectroscopy and diffusion-ordered spectroscopy (DOSY) indicated that these branched macromolecules exhibit supramolecular self-assembly behavior in cyclohexane.[113]

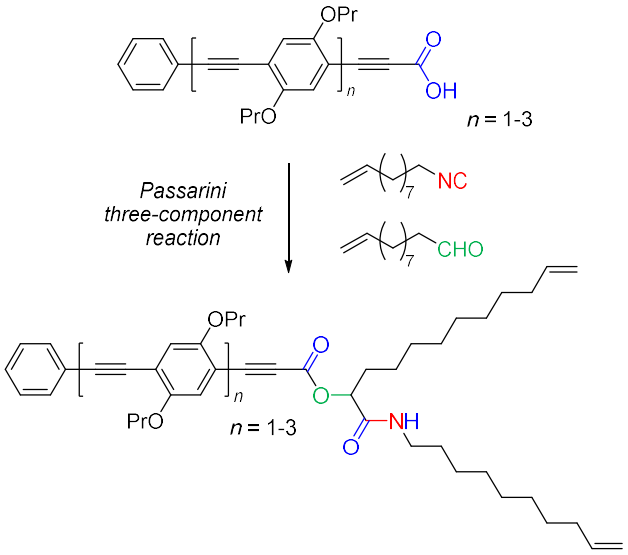

Figure 13. Synthesis of OPE dendrons via P-3CR.[113]

A practical application of OPE self-assembly is their use as luminescent liquid crystalline materials.[117–120] In a recent report, Soberats *et al.* exploited the use carboxylic acid groups, thus they focused explicitly on intermolecular H-bonding as means for supramolecular assembly (Figure 14a). The bis-dendronized OPE chromophore (TPE) forms an unconventional four-stranded orthogonal columnar liquid-crystalline phase via H-bonding between carboxylic acid groups (Figure 14b, left). In addition, its equimolar mixture with a pyridine modified oligo(phenylene vinylene) derivative co-assemble by π-π stacking and H-bonding between carboxylic acid and pyridinyl groups, forming an eight-stranded columnar liquid crystal (Figure 14b, right).[120]

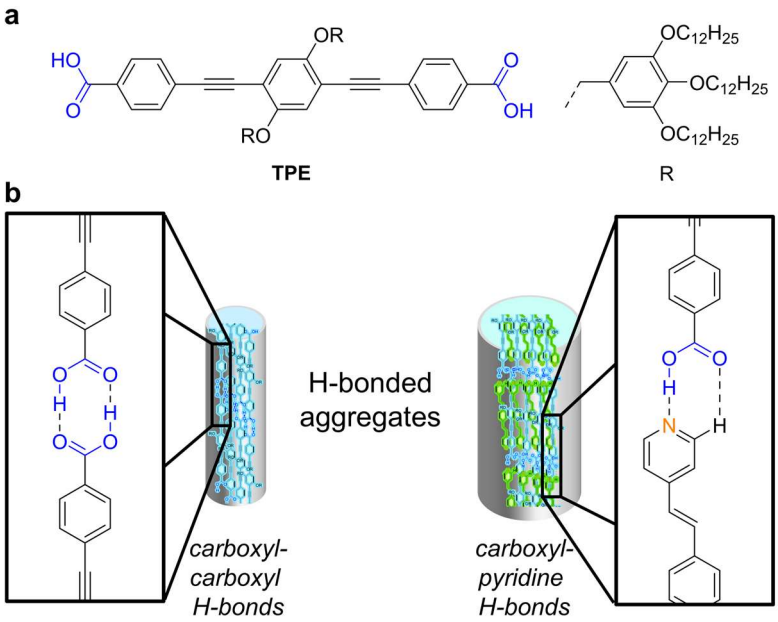

Figure 14. a) Chemical structure of TPE.[120] b) Schematic illustration of columnar liquid crystals, adopted from ref. [120].

Optoelctronics

PPE/OPE derivatives continue to play an important role in the development of organic optoelectronic devices.[118,121,122]

Two most recent examples were reported by Usta *et al.*, who designed OPE-based emitters with alternating donor and acceptor sequences (Figure 15).[122,123] The deep-blue emitter 2EHO-CNPE, incorporating an electron-donating alkoxyl-substituted unit and two cyano-substituted acceptor units, showed an emission maximum (λ_{max}) at 434 nm and a high photoluminescence quantum yield (PLQY) of 0.90 in chloroform. The choice of branched alkoxy side chains further enabled solution-processed OLEDs with a maximum external quantum efficiency (EQE_{max}) of 7.06%, representing the highest value reported so far for OPE/PPE-based emitters. This efficiency was attributed to a hot exciton mechanism (see Section 2.2.1).[123] Building on this design, Usta and co-workers developed 2EHO-TPA-CNPE by extending the structure with diphenylamino donor groups bridged by a phenylene unit, resulting in a green-emissive analogue that also exhibited good device performance with EQE_{max} of 5.5%.[122]

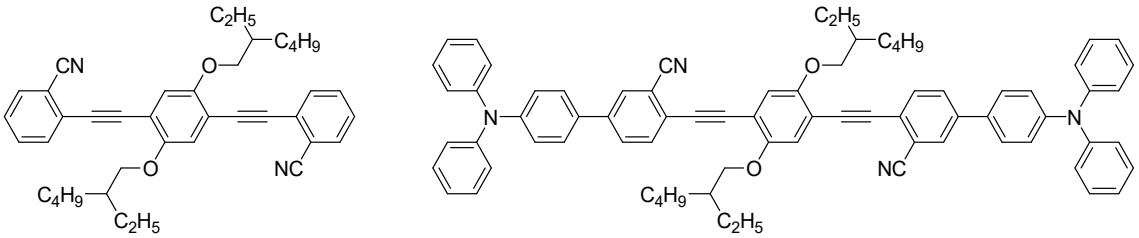

Figure 15. Chemical structure of 2EHO-CNPE and 2EHO-TPA-CNPE.[122,123]

Other works

The interplay between molecular geometry and electronic structure in OPE systems has been elucidated through theoretical studies. In 2020, Dreuw *et al.* investigated the excited singlet states of various conformers of an OPE dimer, *i.e.* 1,4-bis(phenylethylnyl)benzene, and its related derivatives using TDDFT. By introducing torsion to the aromatic rings (Figure 16a), they disrupted the π-conjugations.[124]

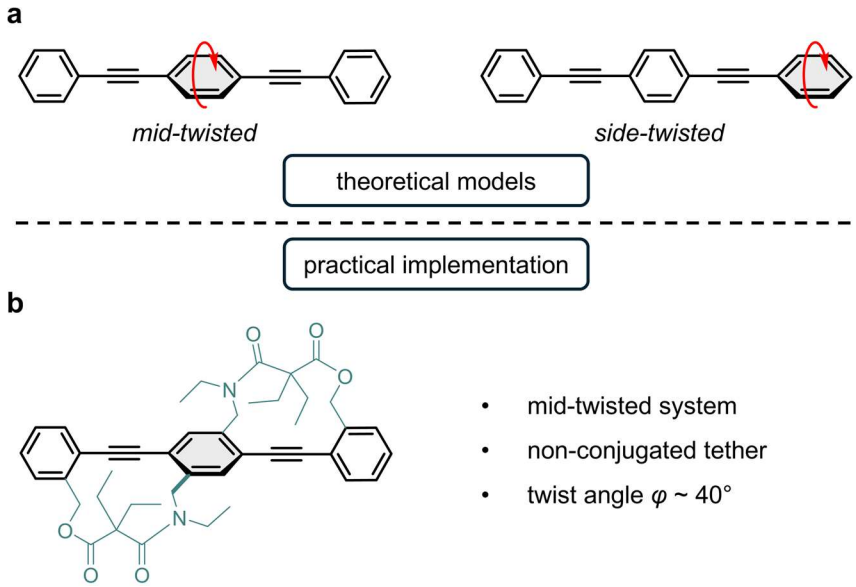

Figure 16. Schematic illustration of torsion control in OPE systems. a) Mid-twisted (left) and side-twisted (right) modes of 1,4-bis(phenylethynylene)benzene (BPEB) employed in theoretical studies.[124] *b) The practical implementation of a mid-twisted system using non-conjugated tether.*[125]

In a subsequent study, their co-investigators implemented the twist to the OPE backbone by installing a malonic acid monoamide moiety between adjacent aromatic rings (Figure

16b). This non-conjugated tether acts as a tight connector between the OPE units and forces the twist angle to reach 40° according to the single-crystal analysis and effectively constrained the intramolecular torsions.[125] However, a direct comparison of the photophysical properties between the twisted and non-twisted scaffolds remains due. Additionally, investigating the impact of such a twist in the context of the molecular wire effect could be of considerable interest.

2.1.3.2 Advantages of OPE Oligomers as Model Systems

OPEs are suitable model compounds for exploring sequence-property relationships due to their synthetic modularity, analytical simplicity, and straightforward computational simulation of their properties.

The well-established Sonogashira and related cross-coupling methods are tolerant of a wide range of electron-donating and electron-withdrawing functionalities, thereby enabling the electronic structure of each aromatic segment to be pre-modified by varying substituents or even by replacing with alternative arylene groups.[88,126,127]

Analytically, uniform OPEs offer distinct advantages stemming from their structurally defined nature. Techniques such as size-exclusion chromatography (SEC) yielded chromatograms with sharp, well-defined peaks, greatly simplifying data interpretation.[7,9] Subtle variations in molecular structure can therefore be reliably correlated with corresponding changes in optical and electronic properties, which is substantially more challenging with disperse macromolecules.

From a computational standpoint, conjugated oligomers require far fewer resources in comparison to saturated structures of comparable molecular weight.[35,128] The rigidity and planar nature of π-conjugated systems drastically reduce the number of conformers to be considered, enhancing both the efficiency and accuracy of computational methods such as density functional theory (DFT) and time-dependent DFT (TDDFT).

In summary, OPEs were specifically selected in this thesis as the central model compound family. Their precise sequence control and straightforward analytical characterization make them ideally suited for investigating the targeted fundamental structure-property relationships.

2.2 Macromolecular Dyes and their Photophysical Behaviors

As already introduced in earlier sections, π-conjugated systems exhibit rich photophysical behavior due to their delocalized electronic structures and tunable energy levels. In order to provide a foundation for understanding these systems, this section is structured into two parts:

- Section 2.2.1 briefly introduces the fundamental photophysical processes relevant to conjugated chromophores, including absorption, fluorescence, intersystem crossing, and exciton characters.
- Section 2.2.2 presents selected examples of macromolecular architectures that display dye-like behavior.

2.2.1 General photophysics

To comprehend the most fundamental photophysical processes in organic molecules, the Jabłoński energy diagram is typically utilized.[129,130] As shown in Figure 17, each electronic state is associated with a unique potential energy surface (PES), which is hereby simplified using an anharmonic oscillator model. The energy levels within the PES correspond to different vibrational states, each described by a distinct wave function. Based on the Franck-Condon principle, nuclear motion is negligible during electronic transitions for their short timescale. As a result, vertical transitions, *i.e.* those occurring without a change in nuclear geometry, are more probable when there is a higher degree of overlap between the vibrational wave functions of the initial and the final states.[131,132]

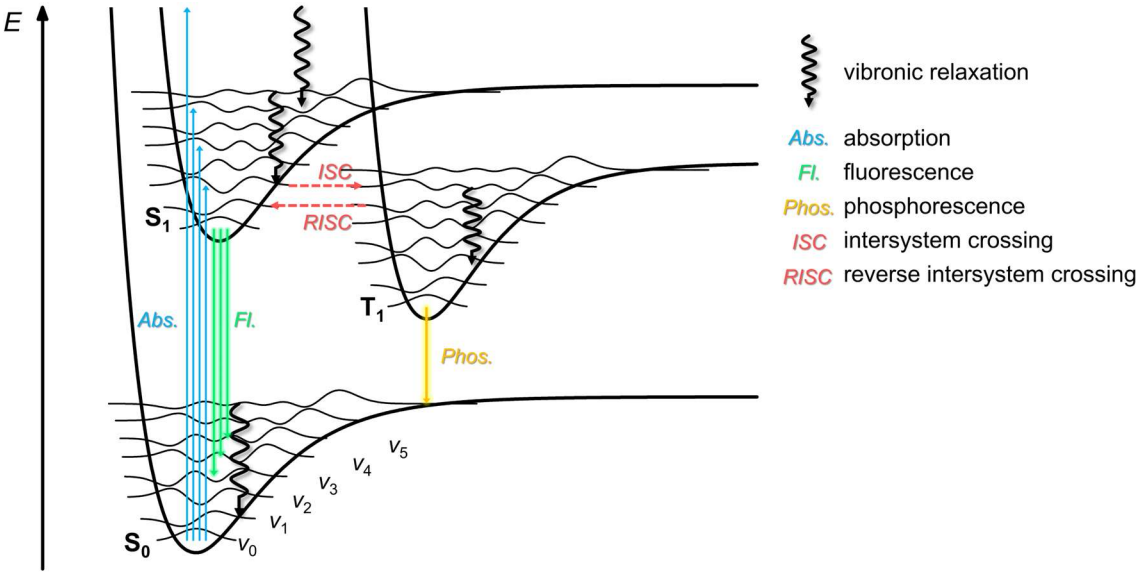

Figure 17. Illustration of a Jabłoński diagram.[129]

The process of a molecule being excited by a photon towards higher electronic states is called absorption. Depending on the wavelength of the photon, the excitation from the ground state (S_0) to any singlet excited states (S_n) is possible, as allowed by the spin selection rule. From a molecular orbital (MO) perspective, an electron is thus promoted from an occupied MO to an unoccupied one, leaving behind a positively charged hole. The resulting electron-hole pair formed by Coulomb attraction is referred to as an exciton.

As stated by Kasha's rule, radiative decay almost exclusively occurs from the lowest excited states of a given spin multiplicity.[133] Fluorescence arises from the first singlet excited state S_1, while phosphorescence originates from the lowest triplet state T_1. Additionally, several non-radiative decay processes may occur mainly driven by energy dissipation through geometry relaxation or heat release. In the predominant case of unchanged spin multiplicity, the excited molecule can relax either between two electronic states, such as $S_2 \rightarrow S_1$, or within an electronic state, from a higher to a lower vibrational level. The former is known as internal conversion (IC), and the latter vibrational relaxation (VR). As a result, the emitted photon is typically lower in energy than the absorbed one. This energy difference is called Stokes shift.[134,135]

Although formally forbidden by the spin selection rule, the relaxation process between electronics states of different spin multiplicity, *i.e.* from a singlet excited state to a triplet

state (intersystem crossing, ISC), can occur under circumstances of sufficiently small singlet-triplet energy gaps ($\Delta E_{S\text{-}T}$). With $\Delta E_{S\text{-}T} < 0.2$ eV, the endothermic process, reverse intersystem crossing (RISC), may also occur, driven by thermal activation from the surrounding environment. The resulting upconverted exciton from T_1 to S_1 can undergo radiative decay subsequently, which is referred to as thermally activated delayed fluorescence (TADF).[136]

As a promising strategy to harvest triplet excitons and thus improve spin statistics, TADF has been widely adopted in the design of OLED devices, first demonstrated by Adachi *et al*.[137–139] In this context, excitons are formed by electrical excitation, where injected electrons and holes recombine within the emitting layer to populate singlet and triplet excited states in 1:3 ratio (Section 2.1.2, Figure 4a).[140,141] In addition to TADF, many other strategies have been developed to harvest triplet excitons.[138] One such approach, pioneered by Ma *et al.*, involves RISC from higher-lying triplet (T_n, $n > 1$) states.[142–145] This mechanism, often referred to as hot exciton RISC (hRISC), typically requires a more sufficient triplet-singlet alignment.[146] In cases where T_n lies energetically above the receiving S_m ($m \geq 1$), the RISC process can proceed in absence of external heat input.[144]

These mechanistic differences stem from the distinct nature of the involved excited states. TADF typically proceeds through charge transfer (CT) states, where the electron and hole are spatially separated across donor and acceptor fragments. In contrast, hRISC often engages locally excited (LE) states or hybridized local and charge transfer (HLCT) states, which exhibit greater spatial overlap between the involved molecular orbitals (MO).[146] These differences in hole-electron displacement and MO overlap are conceptually visualized in Figure 18.[138]

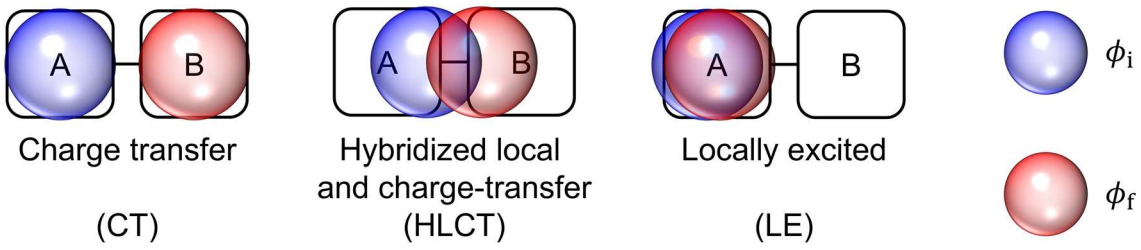

Figure 18. Schematic illustration of different exciton characters based on spatial distribution of molecular orbital associated with the hole (blue) and the electron (red) in a covalently connected two-fragment system (A-B), adopted from ref.[138].

In optical spectroscopy, these excited-state characteristics can be directly reflected. CT states exhibit broader fluorescence spectra due to strong coupling with solvent and vibrational modes, and the significant increase in dipole moment of the S_1 state relative to S_0 results in large Stokes shifts.[147] In contrast, LE states display narrower emission profiles and smaller Stokes shifts, which correlate with minimal electronic reorganization and only a small change in electrical dipole moment. The electronic properties of HLCT states depend on the surrounding medium: in polar solvents they are dominated by the CT contributions, whereas in less polar environments a larger degree of LE character is retained.[146]

Several models were proposed to describe the relationship between the Stokes shift and the environment. Among them, the Lippert-Mataga-equation describes the Stokes shift ($\bar{\nu}_A - \bar{\nu}_E$) as a function of orientation polarizability of the solvent Δf and the change in dipole moment of the molecule from ground state to the excited one:

$$\bar{\nu}_A - \bar{\nu}_E = \frac{2}{hc}\Delta f \frac{(\mu_G - \mu_E)^2}{a^3} + \text{const.} \quad (1)$$

with Δf expressed as

$$\Delta f = \frac{\varepsilon_r - 1}{2\varepsilon_r + 1} - \frac{n_D^2 - 1}{2n_D^2 + 1} \quad (2)$$

where ε_r is referred to as solvent dielectric constant and n_D represents the refractive index.[135,148,149]

Understanding and controlling the balance between LE and CT character is central to the design of efficient organic emitters, particularly in applications such as TADF, photodetectors, and nonlinear optical materials. These considerations become even more nuanced in macromolecular environments, where sequence, backbone rigidity, and intermolecular interactions all modulate excited-state behavior.

2.2.2 Applications

Achieving higher external quantum efficiency (EQE) is the general goal in OLED development. It is generally described as the product of internal quantum efficiency (η_{int}) and out-coupling efficiency (η_{out}):

$$\mathrm{EQE} = \eta_{\mathrm{in}}\eta_{\mathrm{out}} = \gamma\eta_r\Phi_{\mathrm{PL}}\eta_{\mathrm{out}} \quad (3)$$

where the value of η_{int} depends on the charge balance factor (γ), the exciton utilization efficiency (η_r) and the photoluminescence quantum yield (PLQY, Φ_{PL}).[150]

While small-molecule design advances towards higher η_r by means of efficient exciton harvesting from dark states, such as via TADF mechanisms,[138] the macromolecular counterpart focuses on improving processability, achieving a more controllable doping ratio, and optimizing the deposited molecule arrangement.[151,152] In the following section, several representative macromolecular dyes, specifically designed towards these features and employed in OLED applications, are presented.

The first selected example is a polynorbornene reported by Wang *et al.* in 2020 (Figure 19).[153] The norbornene monomer bearing donor and acceptor units at *cis*, *exo*-2,3-positions (D-A monomer) was synthesized via a tandem Suzuki coupling-norbornadiene insertion reaction.[154] Single-crystal analysis of the monomer revealed that one electron-donating acridan plane of the dendron-like teracridan structure is aligned parallel to the peripheral phenyl groups in the triphenyl-*s*-triazine acceptor, attributed to the non-

conjugated nature of sp^3-hybridized N-atoms. This orientation facilitated face-to-face stacking of donor and acceptor, thereby enabling through space charge transfer (TSCT).

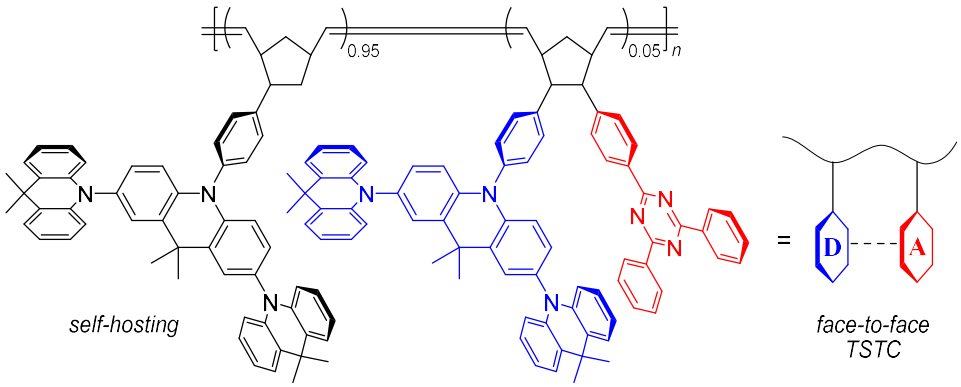

Figure 19. Chemical structure of the self-hosting through-space TADF polymer and a simplified illustration of the face-to-face TSCT mechanism.[155]

Subsequently, the D-A monomer was copolymerized at 5 mol% as a "dopant" with a monosubstituted norbornene monomer serving as the "host" by ring-opening metathesis polymerization (ROMP), resulting in a non-conjugated polymer backbone. The resulting sky-blue-emitting polymer (λ_{max} = 479 nm) retained the TADF characteristics from its disubstituted monomer. Notably, a non-doped OLED setup with this polymer achieved thus a maximal EQE of 18.8%.[155]

In 2015, Yamamoto *et al.* reported the use of carbazole-based dendrimers featuring a triphenyl-*s*-triazine core for solution-processed OLED application.[156] This self-hosting design minimized exciton diffusion and concentration quenching, enabling high-performance without the need for a separate host matrix. Among four dendrimer generations studied, the G3-based device exhibited EQE of 3.4%. Over the past decade, the dendritic design strategy has been further refined towards higher performance OLED materials.[152,157]

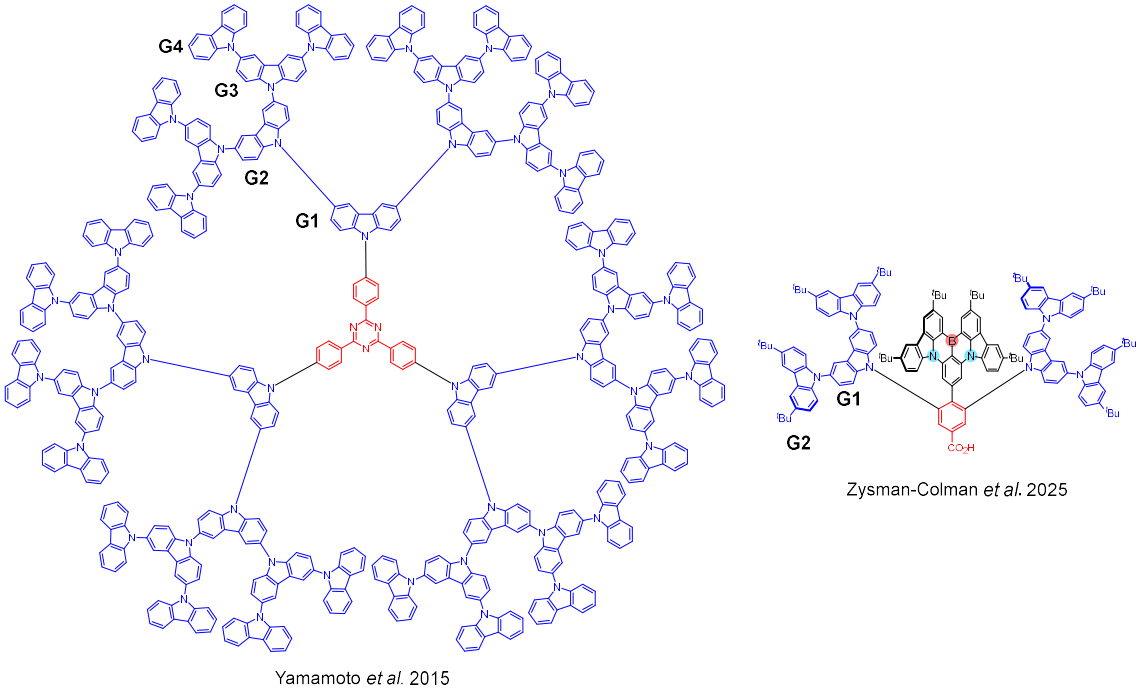

Figure 20. Dendritic examples of TADF dyes. Left: carbazole dendrimers attached to a 2,4,6-triphenyl-s-triazine core; Right: Two second-generation carbazole-based donor dendrons and a benzoate acceptor attached to a MR-TADF structure. Blue: donor; red: acceptor; black: MR-TADF moiety.[156,158]

Combining the concept of macromolecular self-hosting emitter with the modern multiresonance (MR) TADF architecture, Zysman-Colman *et al*. reported very recently carbazole dendrons covalently attached to a MR-TADF core (Figure 20, right).[158] For the OLED device fabricated using G2 dendron as non-doped emitter, an impressive EQE_{max} of 24% at 180 cd m^{-2} with a narrow green emission at 495 nm and full width at half maximum (FWHM) of only 27 nm was achieved. Notably, the device exhibited a small efficiency roll-off, maintaining an EQE above 20% at a brightness of 1000 cd m^{-2}, which meets the requirements for high-end display applications.[159,160]

While the exciton utilization and suppression of aggregation induced quenching are crucial, the orientation of the transition dipole moment (TDM) of the emitting molecules within the host matrix is another powerful tool tune device performance. A high degree of horizontal TDM increases the light outcoupling efficiency η_{out}, resulting in a higher EQE. A randomly orientated TDM (η_{out} = 20-25%) ensemble yields an orientation factor a of 0.33 (Figure 21a), whereas the fully horizontal orientation corresponds to a = 0

(Figure 21b).[161,162] The latter presents an ideal scenario for achieving outstanding outcoupling efficiency of 50% and has therefore attracted considerable attention in the field of optoelectronics.[163]

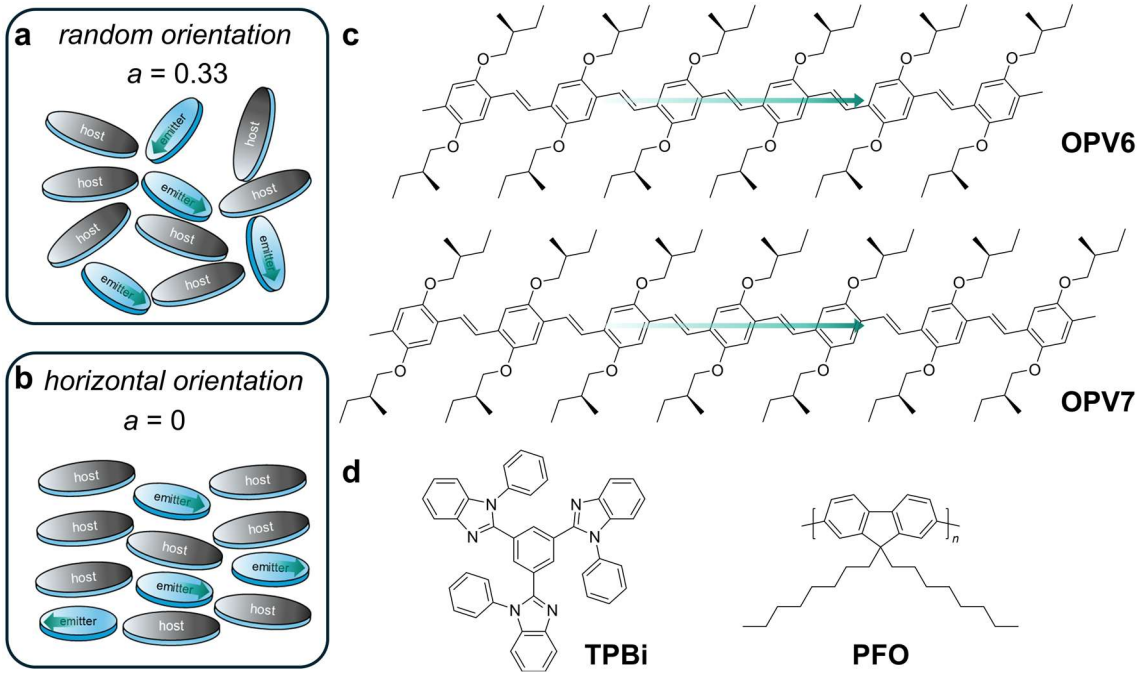

Figure 21. Conceptual illustration of transition dipole moment (TDM) orientation: a) randomly oriented TDM enssemble and b) horizontally aligned TDM ensemble.[139] c) Chemical structure of OPV6 and OPV7. d) Chemical structures of the small-molecule host TPBi and the rigid polymer PFO.[164,165]

Senes *et al.* investigated the relationship between TDM orientation and molecular length using a series of oligo(*p*-phenylene vinylene) molecules (OPV*n*, *n* = 2-7).[164] Despite the use of isotopic small molecular host 2,2',2''-benzene-1,3,5-triyltris(1-phenyl-1*H*-benzimidazole) (TPBi), angular dependent fluorescence revealed that increasing molecular length leads to lower *a* values, indicating a stronger preference for horizontal orientation in longer OPV*n* molecules. In particular, OPV6 and OPV7, when doped at 10 wt% in TPBi and deposited as 40 nm-thick films, exhibited preferential horizontal orientation, with *a* value of 0.27 and 0.20, respectively.[164]

In a follow-up study, a polymeric host material poly(9,9-dioctylfluorene) (PFO) was adopted to: 1) enhance the horizontal alignment by more rigid matrix; 2) avoid unnecessary host-guest aggregation; and 3) improve the solution-processability. PFO itself features a low orientation factor of *a* = 0.06 after annealing, indicating a strong

preference for horizontal TDM. As a result, doped emitters can inherit this horizontal alignment tendency. In particular, OPV7 doped at 5 wt% in PFO showed a significantly enhanced horizontal TDM ($a = 0.10$), offering potential to improve outcoupling efficiency in OLED devices.[165]

Collectively, these examples demonstrate that macromolecular organization provides an additional level of photophysical control, beyond what is achievable in small molecules. The interplay between sequence, structure, and electronic coupling is central to the design of programmable emissive materials, and ongoing developments in synthetic precision continue to expand the landscape of functional macromolecular dyes.

2.3 Sequence-Defined Macromolecules

2.3.1 Necessity of Sequence Definition

Macromolecular chemistry has historically been dominated by the use of homo- or statistical and block copolymers, which are synthesized through chain-growth or step-growth polymerizations. While such polymers have enabled numerous advances in materials science, they inherently suffer from molecular-level heterogeneity, including variations in chain length, monomer arrangement, and end-group fidelity.[4]

In contrast, sequence-defined macromolecules offer a level of molecular control that is analogous to that found in some of nature's biopolymers, such as nucleic acids and proteins, and thus open a new pathway toward the rational design of functional materials. This structural precision allows researchers to modulate and isolate the influence of individual building blocks, enabling a deeper understanding of the interplay between monomer identity, sequence, and macromolecular function.[5] Characterization techniques such as mass spectrometry, NMR, and SEC benefit from sequence-defined materials, as their uniformity enables high-resolution, interpretable data.[10] Similarly, the interpretation of UV-Vis and fluorescence spectra becomes significantly more reliable

when the emitting species is structurally homogeneous, as is the case with precisely synthesized π-conjugated systems.

An obvious sought-after application for sequence definition in macromolecular systems is digital information storage.[166–171] In this sense, information is "written" during the controlled synthesis by selecting the sequence of monomers, where the number of possible combinations, *i.e*. the possible permutations, represent stored data. The sequence can be "read" mainly by the analytical method tandem mass spectrometry, where fragmentation patterns enable re-establishment of the sequence and thus decoding of the stored data, often supported by dedicated software tools.[172,173]

A further highly anticipated application of sequence-defined molecules, also inspired by protein chemistry, is their use in catalysis.[4,5] A breakthrough in this field was reported in 2019, when Gellman and co-workers demonstrated the catalytic effect of sequence-defined foldamers in macrocyclic aldol condensation reactions. One specific sequence of the designed foldamer series achieved an 18-membered ring product in 97% yield, whereas the corresponding small-molecule catalyst pair, pyrrolidine-*n*-butylamine, produced only 8% of the macrocycle as detected by LC-MS analysis.[174] Another notable study involves grafting sequenced-defined oligomers bearing multiple active sites onto silica particles. Analogous to enzymes, the resulting spatial arrangement creates cooperative "pockets" that enable efficient catalytic oxidation of alcohols.[175] Their follow-up work in 2022 further highlighted the importance of the sequence in tuning catalytic activity, with the findings rationalized by molecular dynamics simulations.[176] In this sense, sequence definition offers a means to circumvent random distribution of catalytic components that can prevent the full pairing of all its effects, hence the full exploitation of the catalytic potential.

Furthermore, recent studies have shown that the sequence definition of synthetic macromolecules also holds substantial promise for practical applications. For instance, Ober *et al.* reported three sequence-defined peptoid 10-mers (S1, S2, and S3 in Figure 22a), each containing different sequences of two types of monomers: one with a phenolic side chain protected by *tert*-butoxycarbonyl (Boc) group (blue) and the other with a

terminal alkyne (yellow). These peptoid materials were prepared via solid-phase synthesis and employed as positive-tone photoresists in photolithography. After spin-coating onto the silicon wafer and pre-exposure processing, the 10-mers were patterned under deep ultraviolet light (248 nm) using a photomask, where phenolic groups were generated through Boc deprotection (Figure 22b). The exposed regions were subsequently dissolved by iso-propanol and rinsed away, leaving the unexposed material as the photoresist pattern on the silicon surface. As demonstrated by scanning electron microscopy (SEM) images (Figure 22c-e), different sequences exhibited different lithographic performances, highlighting the significance of sequence definition in nanoscale applications.[2]

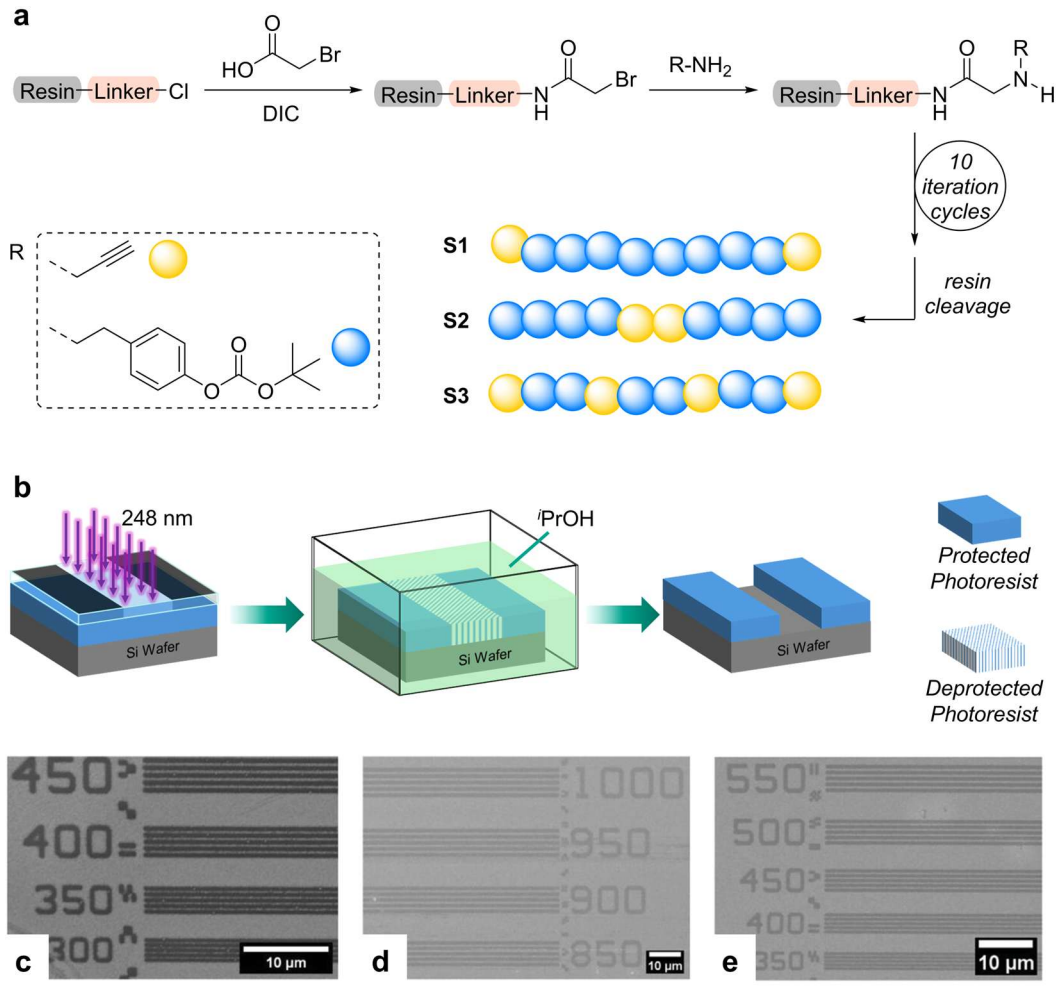

Figure 22. Use of sequence-defined macromolecules as photoresist for extreme-ultraviolet lithography. a) Solid-phase synthesis of sequence-defined polypeptoids; b) schematic illustration of photolithography process; c)-e) SEM images of different sized patterns obtained with samples S1, S2, and S3, respectively, reprinted from Ref. [2] with permission from Adv. Mater. Technol. 2023, 8, 2301104. Copyright ©, license no. 6278160030062.[2]

In general, the advantage of uniform sequence-defined materials is grounded in reduced stochastic effects: by controlling the arrangement of monomers, the material's properties are more uniform, minimizing random variations. In imaging, this becomes particularly significant for small patterns approaching molecular scales. As the semiconductor industry approaches the fundamental limits of conventional photolithography, the demand for materials capable of supporting extreme nanoscale patterning has become increasingly urgent. In this context, sequence-defined photoresists may offer promising innovations. This new class of lithographic materials designed with molecular-level precision can offer a pathway to overcoming several critical challenges that threaten to slow the progress of Moore's Law.[3]

The demand for sequence control is particularly evident in π-conjugated macromolecules, where optoelectronic function depends critically on backbone planarity, conjugation length, and electronic coupling between chromophore units. In such systems, dispersity and random sequence distributions can lead to inhomogeneous broadening of absorption and emission features, unpredictable aggregation behavior, and difficulties in device integration. In contrast, sequence-defined π-conjugated oligomers offer the ability to systematically control the placement of donor and acceptor units, enabling fine-tuning of photophysical properties and excited-state dynamics.

In summary, sequence-defined macromolecules provide a molecular-level design strategy that overcomes the limitations of traditional polymer systems. Their necessity arises both from the desire to understand fundamental structure-property relationships and from the practical need for reproducible, high-performance materials in advanced applications.

2.3.2 Synthetic Strategies for Sequence Definition

Unlike statistical polymers, sequence-defined macromolecules feature a precisely controlled monomer arrangement, often realized through stepwise, iterative synthetic methods. The chain growth follows either an exponential one or a linear one (Figure 23).

While the exponential iterative growth enables faster chain elongation, linear iterative growth allows more precise control over the sequence. In both cases, the relative orthogonality of the employed protecting groups is crucial. This concept is central to solid- and liquid-phase synthesis, as well as to fluorous-supported and polymer-tethered approaches.[6]

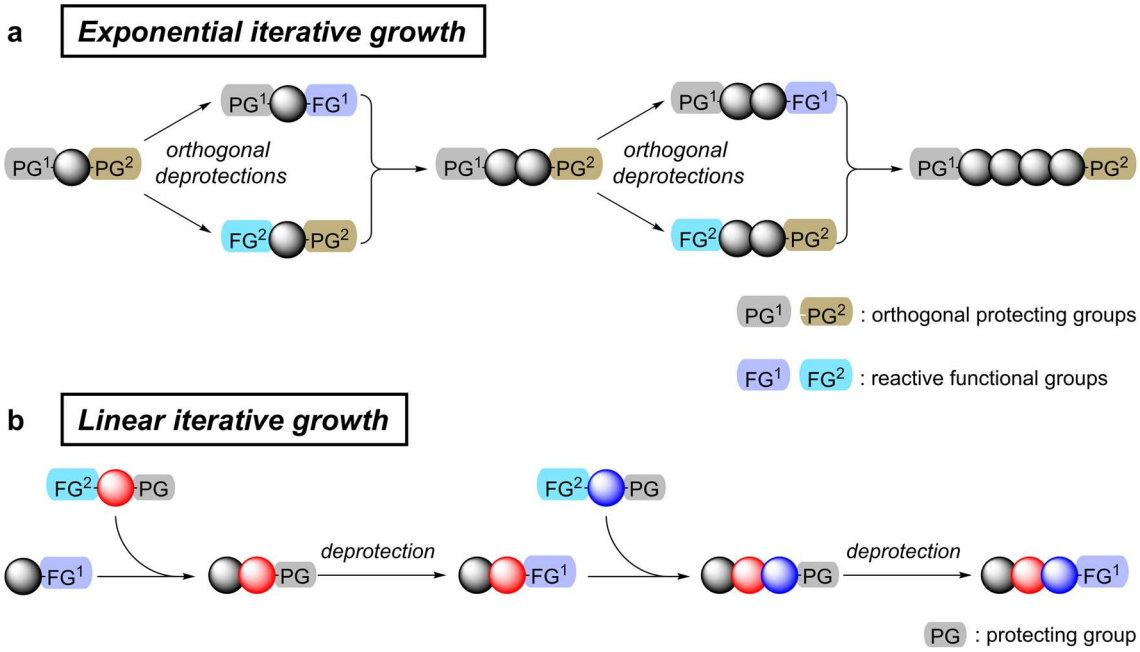

Figure 23. Conventionally employed iterative synthetic strategies towards sequence-definition in macromolecular systems. a) Iterative exponential growth (IEG). b) Monodirectional linear growth.[5,6]

While this thesis focuses on conjugated sequence-defined oligomers, the following overview starts by outlining synthetic strategies for their non-conjugated counterparts in order to provide a comprehensive overview.

2.3.2.1 Sequence-Defined Synthesis of Non-Conjugated Macromolecules

Sequence definition in organic chemistry traces back to the solid phase peptide synthesis (SPPS) introduced by Merrifield in the 1960s.[177] In this approach, an *N*-protected amino acid is anchored to an insoluble resin and the synthesis proceeds in a linear fashion.

Through iterative cycles of deprotection and coupling steps, the sequence of amino acids can be accurately defined. To improve efficiency, an excess of coupling reagents is typically required. To achieve longer sequences and improve reliability, an automated apparatus for SPPS was reported in 1966.[178] This development has since enabled extensive preparation works towards sequence-defined biomimetic oligomers.[179–184] As discussed in Section 2.3.1, Figure 22, the sequence-defined samples used for photolithography were prepared in such a manner.[2]

Even though SPPS is regarded as the go-to method to obtain sequence-defined oligomers, it has considerable drawbacks in terms of sustainability and scalability. In addition to the requirement for excess coupling reagents, extensive solvent consumption is necessary for resin washing, and scale-up procedures are challenging. Therefore, commercial applications of sequence-defined products are mostly limited to biological fields.[185] Applications in materials science typically demand larger quantities to investigate the bulk properties adequately.

To address these issues, several groups combined sequence definition with multicomponent reactions (MCRs), which can be conducted in solution-phase.[168,170,186–191] Owing to their high atom economy and modularity MCRs are regarded as effective coupling strategies towards iterative chain growth. In particular, the Passerini three-component reaction (P-3CR) and the Ugi four-component reaction (U-4CR) have been extensively employed over the past decade to synthesize sequence-defined peptoid-like oligomers. For example, in a 2016 publication, the Meier group reported the synthesis of a sequence-defined decamer (10-mer) through iterative cycles of the P-3CR followed by a deprotection step (Figure 23). This approach allows for the gram-scale preparation of sequence-defined oligomers with high purity, as confirmed by SEC analysis.[186]

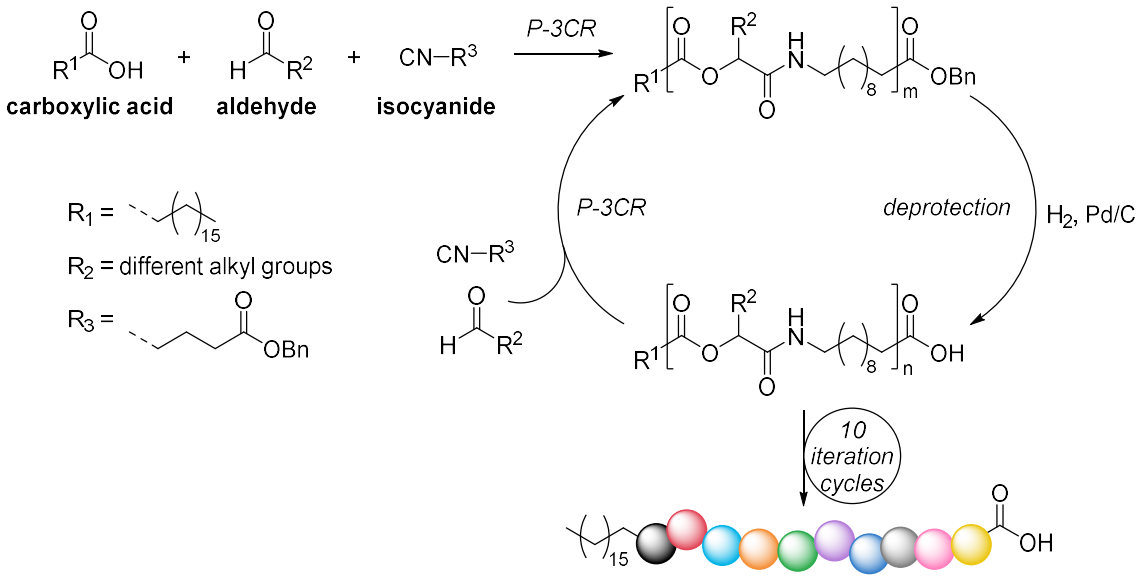

Figure 24. Iterative two-step synthesis of sequence-defined oligopeptides utilizing the Passerini three component reactions (P-3CR). [186]

By modifying or varying the reaction components, further reaction types can be directly applied to the resulting MCR products. This enables, on the one hand, a protection-group-free workflow, further improving the synthetic efficiency, on the other hand, the combination of IEG and linear strategies to accelerate the chain growth.[190,187,189,192] As was further demonstrated in a joint study with the Du Prez group, the terminal double bond of 10-undecenal enabled the subsequent thiol-ene addition, while the thiolactone moiety is used for a *thia*-Michael addition after aminolysis reaction (Figure 25). This way, up to 15 individually selectable side chains were incorporated in a single molecule successfully.[187]

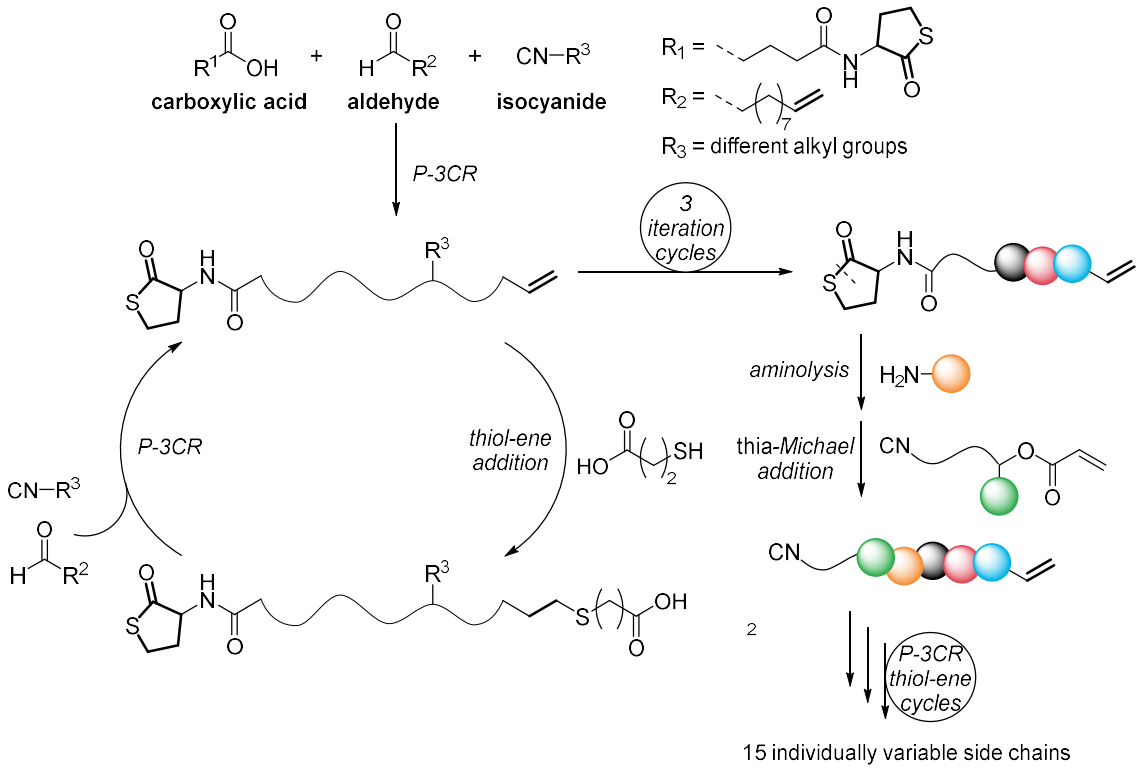

Figure 25. Protection-group-free sequence-defined synthesis combined P-3CR, thiol-ene chemistry, and thiolactone chemistry.[187]

Protection-group-free coupling can also be achieved by using wavelength-orthogonal photochemistry. In 2019, Barner-Kowollik *et al.* reported a photochemical protocol of sequence-defined macromolecules using nitrile imine-carboxylic acid ligation (NICAL) at 410 nm and photoinduced Diels-Alder cycloaddition at 365 nm (Figure 26).

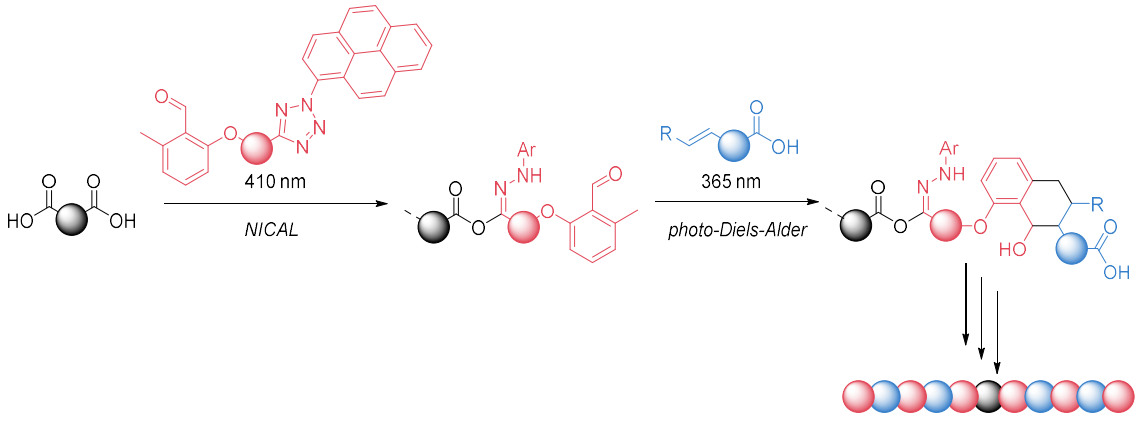

Figure 26. Orthogonal photochemical coupling steps.[193]

2.3.2.2 Sequence-Defined Synthesis of Conjugated Macromolecules

Their chemical structures dictate that conjugated sequence-defined macromolecules are mainly synthesized using cross-coupling reactions[194] and/or olefination reactions.[89]

In a recent study, Koeckelberghs *et al.* developed a combined synthetic strategy involving the Suzuki-Miyaura cross-coupling and the Horner-Wadsworth-Emmons (HWE) reaction.[89] Two types of orthogonally bifunctional building blocks were alternately employed for step-wise, protection-group-free chain growth: one bearing a boronic ester and an aldehyde group, and the other featuring a bromine substitution and a phosphonate moiety (Figure 27). The obtained oligomers consist of phenylene- and phenylvinylene monomer units, offering valuable insights into accurate sequence definition of conjugated cooligomers.

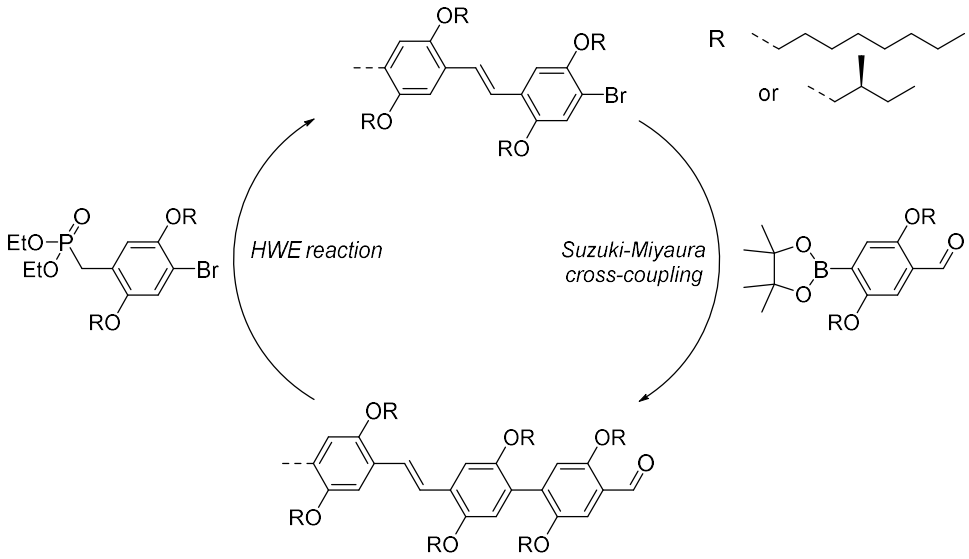

Figure 27. Synthetic strategy using Suzuki-Miyaura cross-coupling and subsequent Horner-Wadsworth-Emmons (HWE) reaction.[89]

As mentioned in Section 2.1.2, P3HT has attracted considerable interest due to its broad application in organic electronics. However, chain lengths dispersity in "traditionally" synthesized conjugated polymers leads to inconsistent solid-state packing, thereby affecting electronic properties and undermining the reproducibility of device performance.[195,196] To address this issue, Seferos *et al.* demonstrated that the

homogeneous step-growth conventionally initiated by Ni catalyst reaction could be controlled by temperature to yield monodisperse oligo(3-hexylthiophene)s (Figure 28).[197]

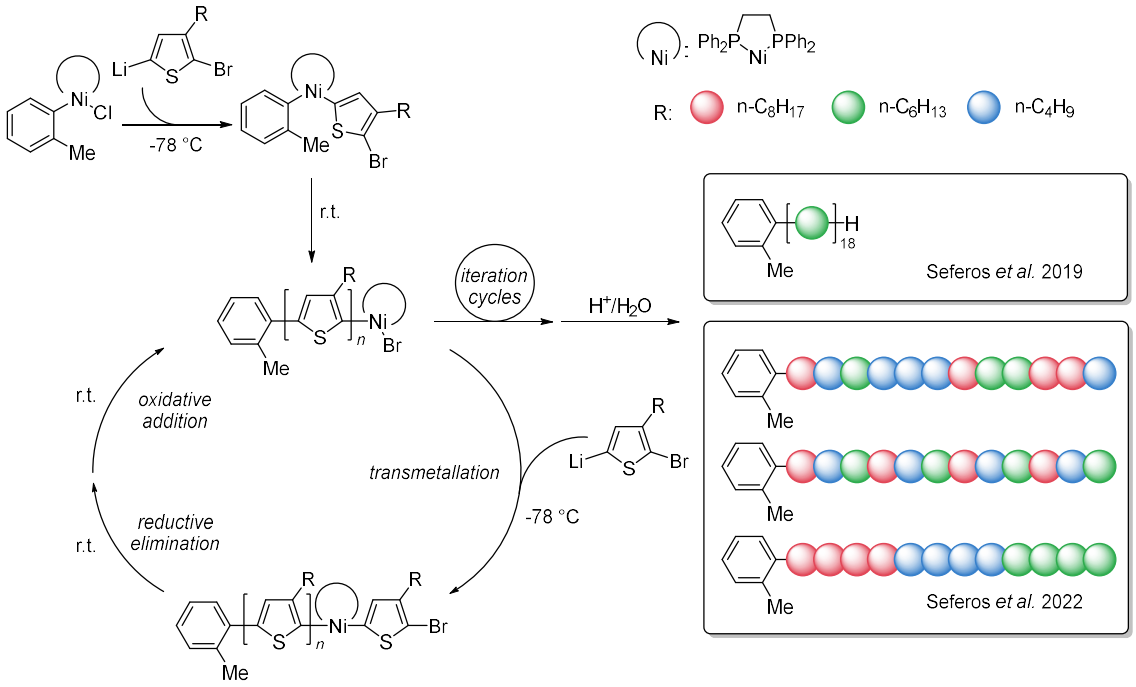

Figure 28. Catalyst-transfer oligomerization to obtain sequence-defined oligothiophenes via temperature cycling.[197,198]

To achieve single-monomer additions, the transmetalation step was carried out at cryogenic temperature (-78 °C), effectively suppressing undesired reductive elimination. To maintain coupling efficiency at such low temperature, highly reactive lithiated thiophene monomers were employed. After the excess monomers were quenched with butylated hydroxytoluene (BHT), the mixture was warmed to room temperature to trigger reductive elimination, followed by oxidative addition. As a result, the active Ni species was regenerated and thus one coupling cycle of Murahashi-type catalyst transfer polymerization was finished. After 15 cycles, gelation of the reaction mixture was observed at low temperature, which impaired further reaction. Nevertheless, oligomers of high purity were successfully obtained up to 18-mer. In a subsequent study, the same group synthesized a series of sequence-defined oligomers with up to 12 thiophene units

with alkyl side chains of different lengths, including a random cooligomer, an alternating/periodic cooligomer, and a triblock cooligomer.[198]

In the 1990s, Tour *et al.* presented multiple synthetic approaches towards monodisperse OPEs.[199–201] Using the Sonogashira cross-coupling reaction as the key step for chain growth, they investigated the synthetic strategies from IEG to stepwise (linear and bidirectional) approaches both in solution and on solid support. Main building blocks employed in the iterative synthesis towards linear OPEs are summarized in Figure 29. In linear approaches, the terminal alkyne is typically protected with a trimethylsilyl (TMS) group, allowing the halide (X) to react with a free terminal alkyne on the other coupling partner. On the other side, the N-containing functionalities can be used as anchoring points for solid-phase synthesis, or substituted with halides, serving as orthogonal protection relative to the TMS group.

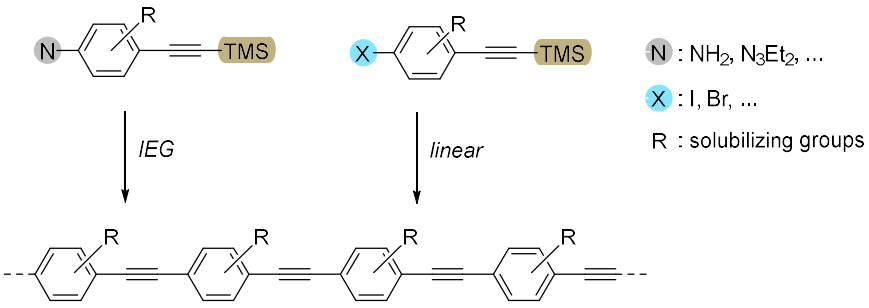

Figure 29. Building blocks to afford monodisperse OPEs employed in different synthetic strategies.[199–201]

To address the limited solubility commonly observed for conjugated molecules, the aromatic units are often substituted with long or branched alkyl chains. However, unsubstituted OPEs remain attractive as a model system to study intrinsic structure-property relationships. To overcome their poor solubility during synthesis, Lutz *et al.* proposed a polymer supported strategy in 2017.[202] In this approach, a pyridine-containing building block was introduced additionally to illustrate sequencing. The thus resulting structures are more accurately termed as oligo(arylene ethynylene)s (OAEs) rather than OPEs and synthesis was demonstrated up to tetramer stage. However, once cleaved from the polymer support, the characterization of the OAEs was again hindered

by poor solubility, which limited further investigations into their structure-property relationships. In this regard, a rational molecular design towards sufficient solubility was required in the context of sequence-defined conjugated systems.

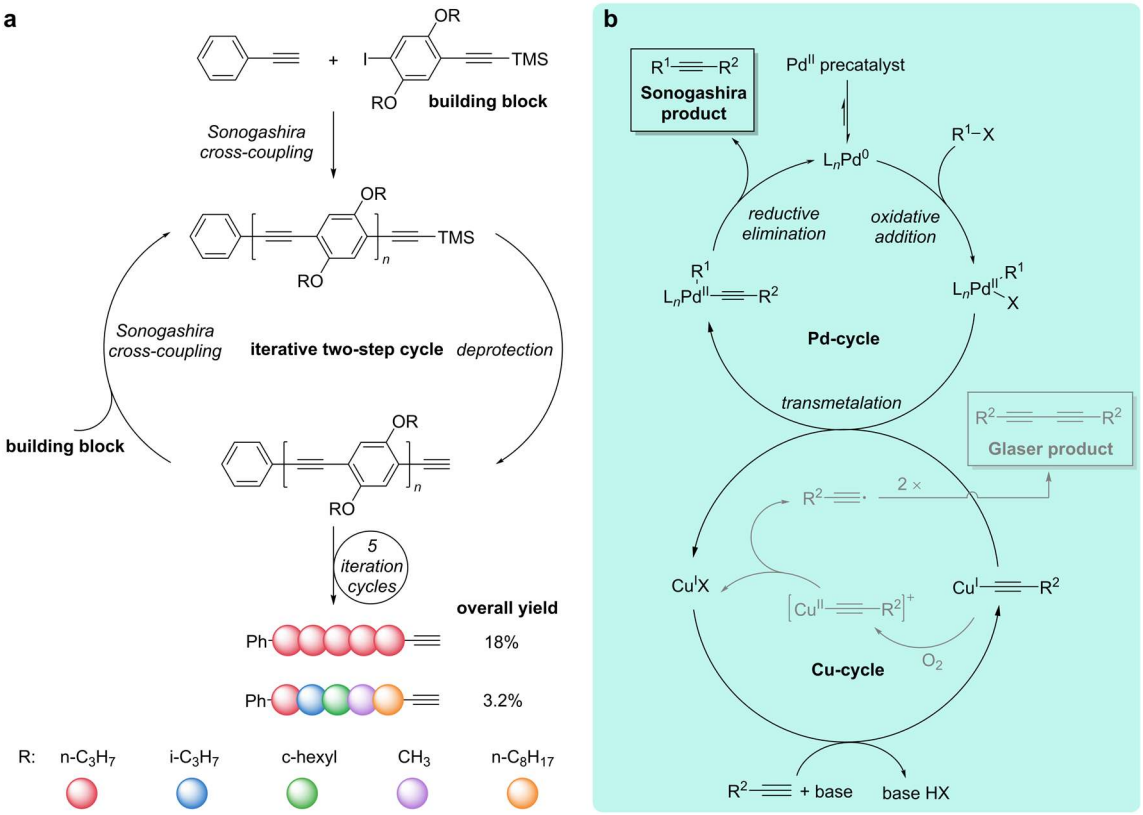

Figure 30. a) Adopted sequence-defined synthesis of monodisperse OPEs based on iterative two-step cycle of Sonogashira cross-coupling reaction and deprotection reaction.[7] b) Adopted mechanistic cycles of the Sonogashira cross-coupling reaction with Glaser homocoupling reaction greyed out.[126]

In 2018, Meier *et al.* demonstrated precise control on sequence in OPE systems by synthesizing a monodisperse pentamer bearing five distinct alkoxyl side chains (Figure 30a).[7] A linear approach was employed, where phenyl acetylene and an iodinated building block were used to initialize the sequence. The purification of the oligomers was particularly difficult attributed to the formation of a major side product, an alkyne homocoupling (Glaser coupling) product generated in the presence of trace oxygen (Figure 30b), which is structurally highly similar to the desired cross-coupling product. Thus, extensive efforts were made to isolate the targeted oligomers, until the high purity was confirmed by SEC. One cannot complain about an overall yield of 3.2% across 10

reaction steps, yet the time and solvent consumption associated with purification could be addressed more consciously through further optimization.

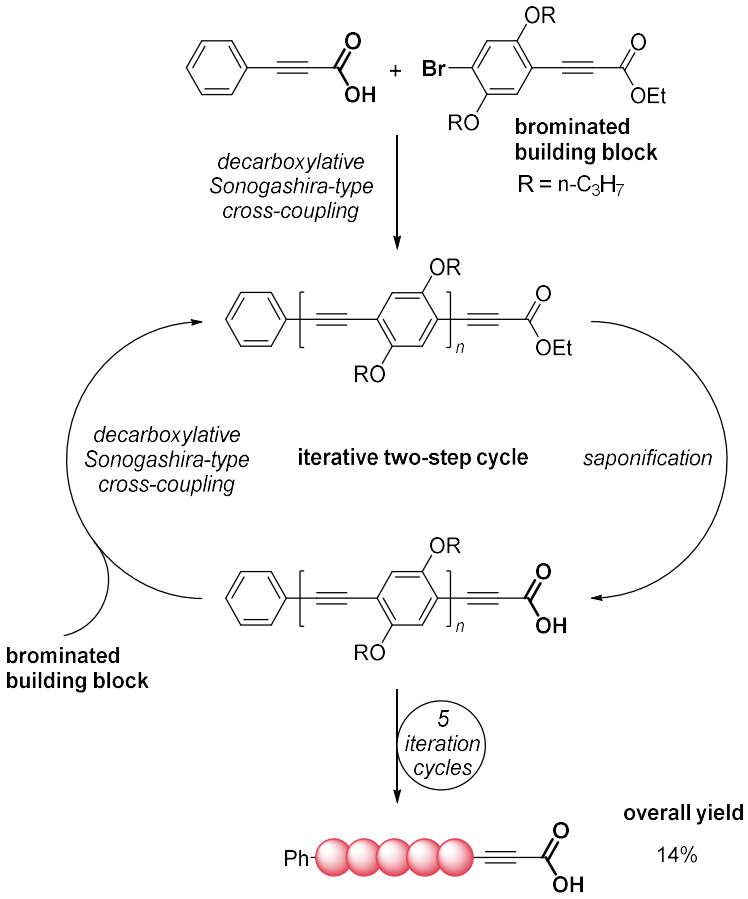

Figure 31. Adopted illustration of streamlined iterative two-step synthesis of OPE based on decarboxylative Sonogashira coupling and saponification.[9]

With this motivation in mind, Meier *et al.* adjusted the synthetic procedure by employing a decarboxylative variant of the Sonogashira coupling as the chain growth step (Figure 31).[9] Optimization began at the level of OPE building blocks. The use of a *para*-bromoiodobenzene instead of the diiodo analogue enabled the selective installation of TMS acetylene. Despite the fact that the decarboxylative coupling still suffers from the homo-coupling side reaction, the higher reactivity of the bromine substituent compensates for this limitation to a certain extent in comparison with conventional Sonogashira reactions.[203] Subsequently, the traditional TMS deprotection was replaced by a saponification step, which introduced a polarity shift to the oligomers and thereby

facilitated purification. The overall yield for the resulting OPE pentamer composed only of monomers bearing propoxy side chains was not improved, though it was not compromised significantly either. However, the new method saved 68 hours of purification time compared to the previous strategy, greatly improving the synthetic efficiency.[9]

3 Aim

Over the past decade, our research group has explored the structural motif of oligo(phenylene ethynylene)s (OPEs), with the underlying goal of studying structure-property relationships in sequence-defined conjugated macromolecules. This long-term goal was partially achieved on the "structure" side, with important progress being made by demonstrating the feasibility of sequence definition through side-chain variation and by improving the iterative synthesis strategy.[7,9]

These foundations allow the present thesis to shift the focus onto the "property" side. With emphasis on optoelectronic applications, two strategies are to be employed to investigate the excited-state properties of sequence-defined OPEs through both *in-silico* and experimental approaches. First, symmetric donor-acceptor-donor (D-A-D) architectures are introduced, in which systematic variation of the central acceptor strength and modification of the backbone conjugation degree were sought to enable a controlled tuning of the electronic band gap and emission color. Second, donor-OPE-acceptor (D-OPE-A) sequences with variable OPE bridge length were to be investigated to correlate the impact of conjugated length on the balance between charge-transfer and locally excited dominated excited-state character.

Beyond exploring their optoelectronic properties, a further strategy aims to utilize the stiffness of the OPE rods. In the context of developing structure-property relationships in sequence-defined macromolecules, size-exclusion chromatography (SEC) has shown high sensitivity to structural changes in rod-shaped OPE systems,[10] which motivated an investigation into whether SEC could also reliably resolve *E*/*Z* isomers. Thus, a defined bending position is to be introduced to uniform OPE rods by incorporating a photoswitchable azobenzene unit, capable of isomerizing between the extended linear *E*-form and the more compact bent *Z*-form. SEC should subsequently be evaluated as a quantitative tool method to characterize and monitor the *E*/*Z* isomerization.

By integrating these perspectives, this thesis aims to establish OPEs as an excellent model system for disentangling electronic and geometric contributions to structure-property

relationships in sequence-defined conjugated architectures, thereby providing design principles for further functional organic systems.

4 Tuning the Emission-Color of Sequence-Defined OPEs

***OPE-b'**, **OPE-g'**, and **OPE-y'** were synthesized within the bachelor's thesis of Lars Boller, which was co-supervised by the doctoral candidate.*

4.1 Motivation

π-Conjugated molecules that combine electron-donor (D) and electron-acceptor (A) units have become an important class of functional materials in organic electronics.[91,204–206] Targeting optoelectronic applications, the precisely defined sequence of D and A in oligomeric architectures, like D-A,[207,208] D-A-D,[209,210] or A-D-A,[211,212] has proven advantageous for achieving accurate control over photophysical properties. Tailoring the emission wavelength through donor-acceptor engineering has become a widely adopted strategy to provide full color coverage within visible spectrum.[204,213,214]

This chapter focuses on systematically tuning the optical properties of sequence-defined oligo(p-phenylene ethynylene)s (OPE). Building on the work of Usta *et al.*, who demonstrated the feasibility of employing A-D-A-sequenced OPEs with an alkoxylated donor core for solution-processed OLED devices,[122,123] we investigate structure-property relationships towards emission color tuning. To further enhance the solubility and therefore the processibility, the number of alkyl side chains was increased by adopting a D-A-D sequence design.

Accordingly, a modular series of eight oligomeric emitters was developed and synthesized (Figure 32), applying four different central acceptor units and two donor units with different conjugation length. For each emission color, two derivatives were synthesized: a classical D-A-D architecture (**OPE-*x***) and an extended analogue bearing two additional terminal phenyl groups flanking the donor units (**OPE-*x*'**). The extended

donor-groups were introduced to modulate the conjugation length and the molecular aspect ratio.

4.2 Results and Discussion

4.2.1 Molecular Design and Synthetic Access

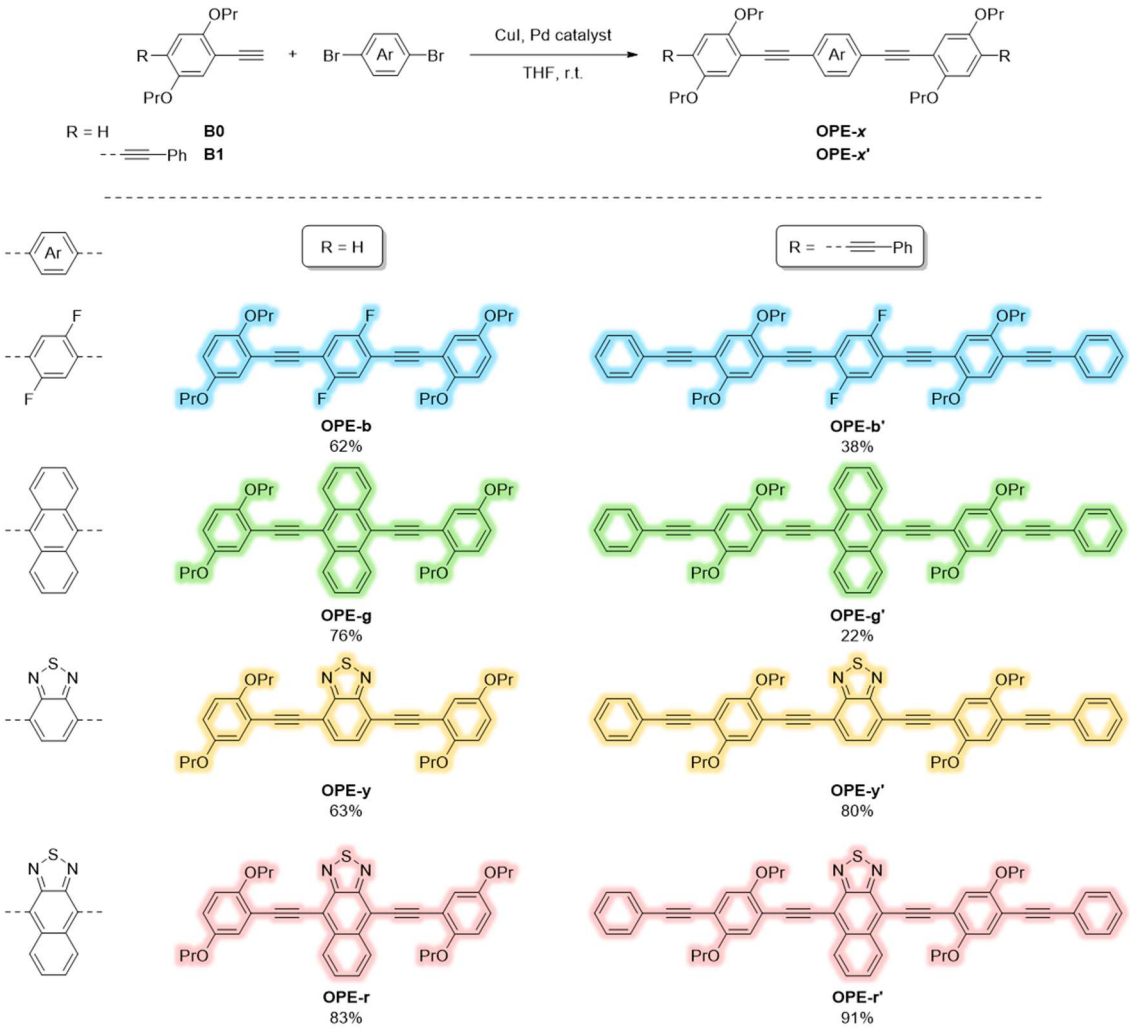

*Figure 32. Top: general reaction for the synthesis of D-A-D-type **OPE-x** and **OPE-x'** molecules. Bottom: Structure and isolated yield of **OPE-x** and **OPE-x'** derivatives, each highlighted in their corresponding observed emission wavelength.*

The **OPE-*x*** and **OPE-*x*'** series of emitters were synthesized starting from donor building units **B0** and **B1**, respectively, which were prepared based on the earlier reports.[15] Each OPE series comprises a library of molecules incorporating different acceptor cores, including *para*-difluorobenzene, anthracene, benzothiadiazole (BTD), and naphthothiadiazole (NTD). The complete set of synthesized D-A-D molecules is shown in Figure 32, along with the general reaction scheme.

The synthesis was performed on a preparative scale using established Sonogashira cross-coupling conditions.[7] Purification via Celite® filtration and flash column chromatography yielded **OPE-b** as a white cotton-like solid in a yield of 62%. The structure was confirmed by ^{1}H, ^{13}C, and ^{19}F NMR spectroscopy (provided in Section 8.3), and the purity was verified by size-exclusion chromatography (SEC, summarized in Figure 33a). In contrast, the same purification procedure proved insufficient for its π-extended derivative **OPE-b'**. Size-exclusion chromatography (SEC) of the purified **OPE-b'** showed a small peak (13% integration) at higher retention time next to the main product peak, indicating a species of possibly lower molecular weight (Figure 33a). Electrospray ionization mass spectrometry (ESI-MS) identified this species of similar polarity and solubility as a Glaser-coupling product (**GB1**, m/z = 634.306), likely formed due to traces of contamination with oxygen (Figure 33b). Due to difference in ionization efficiency, the higher signal intensity of **GB1** compared to the target compound **OPE-b'** in the mass spectrum does not reflect its actual abundance. As confirmed by the ^{1}H NMR spectroscopy of the chromatographically purified substance (Figure 33c), **OPE-b'** remained the predominant species in the mixture after careful validation.

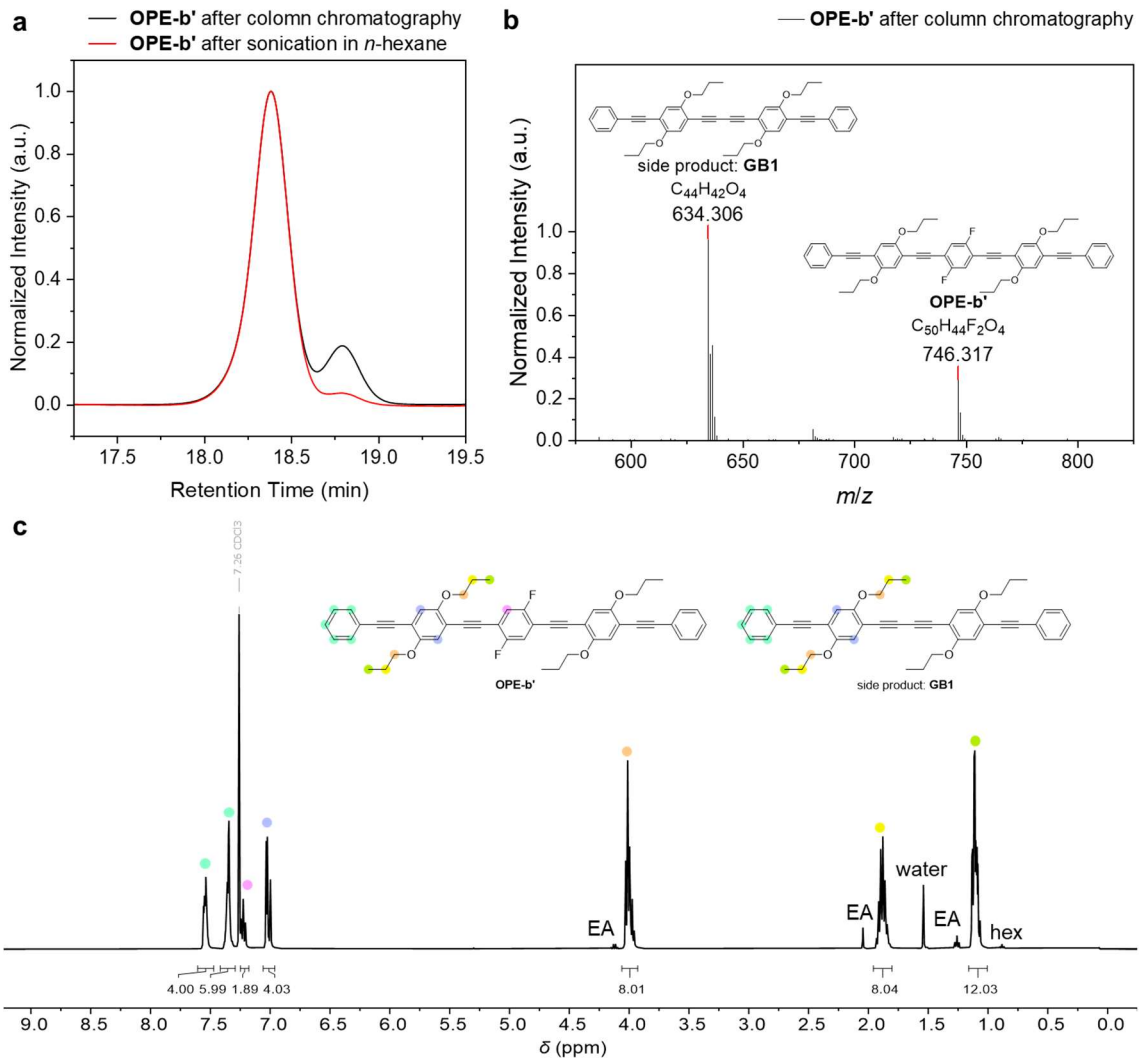

*Figure 33. a) SEC analysis of **OPE-b'** after flash column chromatography (black) and subsequent purification by sonication in n-hexane (red), showing the removal of impurities of lower molecular weight. b) ESI-MS spectrum of chromatographically purified **OPE-b'**, indicating the presence of a Glaser-type homocoupling side product **GB1**. c) ^{1}H NMR spectrum of chromatographically purified **OPE-b'** in $CDCl_3$. Identified impurities: ethyl acetate (EA) and n-hexane (hex).*

As an additional purification step, sonification in *n*-hexane, was conducted. The red trace in the SEC diagram (Figure 33a) showed that this treatment reduced the impurity to less than 3%, as determined by peak integration. **OPE-b'** was thereby isolated as a neon yellow powder in a moderate yield of 38% in a purity of 97%. This approach of sonification of the material in *n*-hexane was thus employed consistently as the final purification step to remove the Glaser-coupling side-product.

For all the other derivatives, precipitation from the reaction mixture was observed during stirring. After complete conversion, as indicated by TLC, the crude solids were collected by filtration over Celite®, washed with hexane(s), and taken up in dichloromethane. The ^{1}H NMR spectroscopy confirmed the precipitates as the target molecules, and their purity was further confirmed by SEC (Figure 34). **OPE-g**, **OPE-g'**, **OPE-y**, **OPE-y'** were obtained as orange powders in yields ranging from 20% to 80%, while **OPE-r** and **OPE-r'** were isolated as dark purple powders in 83% and 91% yield, respectively.

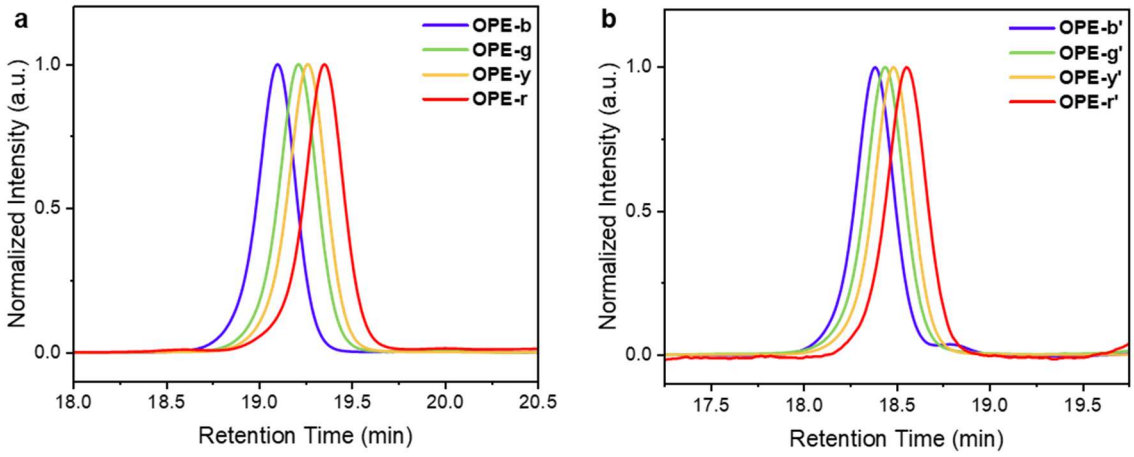

Figure 34. SEC traces of the purified products of a) the OPE-x series and b) the OPE-x' series.

All compounds were fully characterized by NMR spectroscopy, infrared spectroscopy, and high-resolution mass spectrometry (HRMS). The corresponding analytical data are provided in Section 8.3. With the exception of **OPE-b'**, all compounds exhibited SEC purities above 99%.

4.2.2 Theoretical Investigations

To assess the electronic impact of the selected acceptor units and anticipate the photophysical behavior of the resulting D-A-D systems, computational methods were employed. First, density functional theory (DFT) calculations were performed at the D3-PBE0/6-31G(d,p) level of theory to optimize the ground-state geometries, followed by wavefunction analysis to provide insight into spatial distribution and energy levels of the

frontier molecular orbitals (FMOs).[215,216] To reduce computational cost, the *n*-propyl chains were substituted with methyl groups, as their electronic effect on the conjugated core was expected to be minimal. Representative results for **OPE-*x*** and **OPE-*x*'** are shown in Figure 35 and Figure 36, respectively.

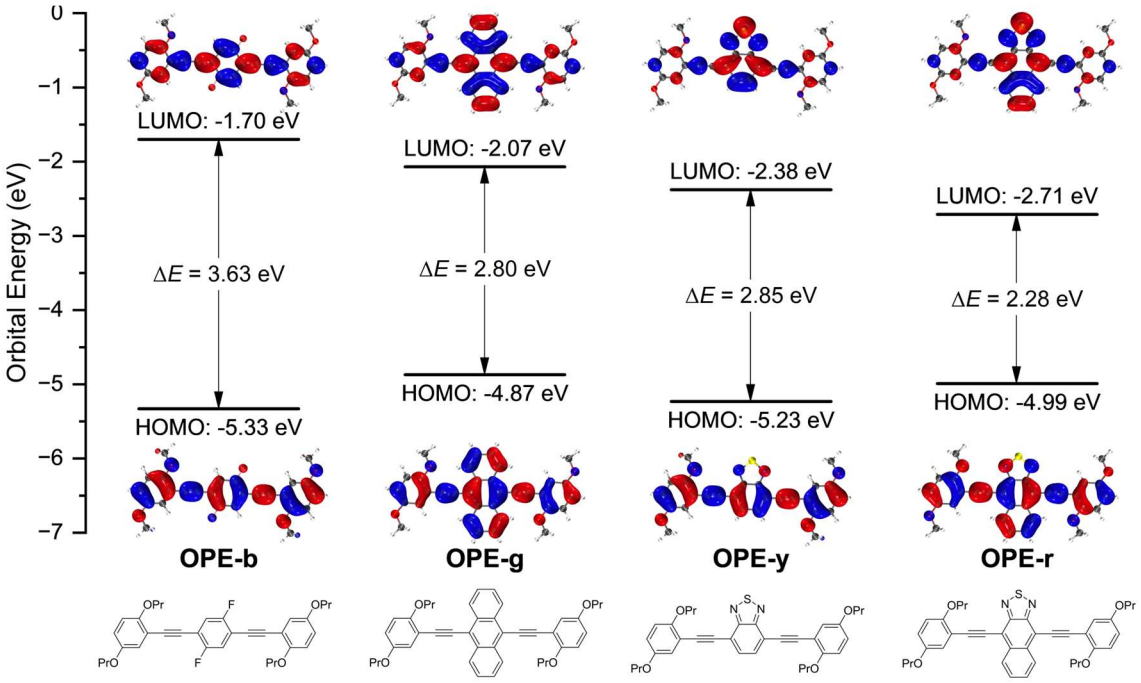

*Figure 35. Calculated FMO energy levels and corresponding molecular orbital distributions for the optimized geometries of **OPE-x** molecules. The calculations were performed at the D3-PBE0/6-31G(d,p) level of theory. HOMO: highest occupied molecular orbital; LUMO: lowest unoccupied molecular orbital. The orbital pictures are plotted with an isovalue of 0.02.*

The electron-accepting strength of the central unit increases in the order *para*-difluorobenzene < anthracene < BTD < NTD. Accordingly, the energy level of the lowest unoccupied molecular orbital (LUMO) decreases progressively from -1.70 eV to -2.71 eV in the **OPE-*x*** series. In line with this trend, the energy level of the highest occupied molecular orbital (HOMO) does not remain constant, despite the defined donor segment being unchanged throughout the series. This phenomenon can be attributed to the extended π-conjugation introduced by the more delocalized central units, *i.e.*, anthracene, BTD, and NTD. Particularly **OPE-g** and **OPE-r**, which contain the largest conjugated systems as acceptor motifs (anthracene and NTD, respectively), exhibit elevated HOMO levels above -5 eV, leading to a narrowing of the HOMO-LUMO gap

(Δ*E*). Correspondingly, the resulting Δ*E* of **OPE-g** (2.80 eV) is slightly smaller than **OPE-y** (2.85 eV) at this level of theory, which is expected to lead to a red-shift of the UV-Vis absorption and/or photoluminescence spectrum.

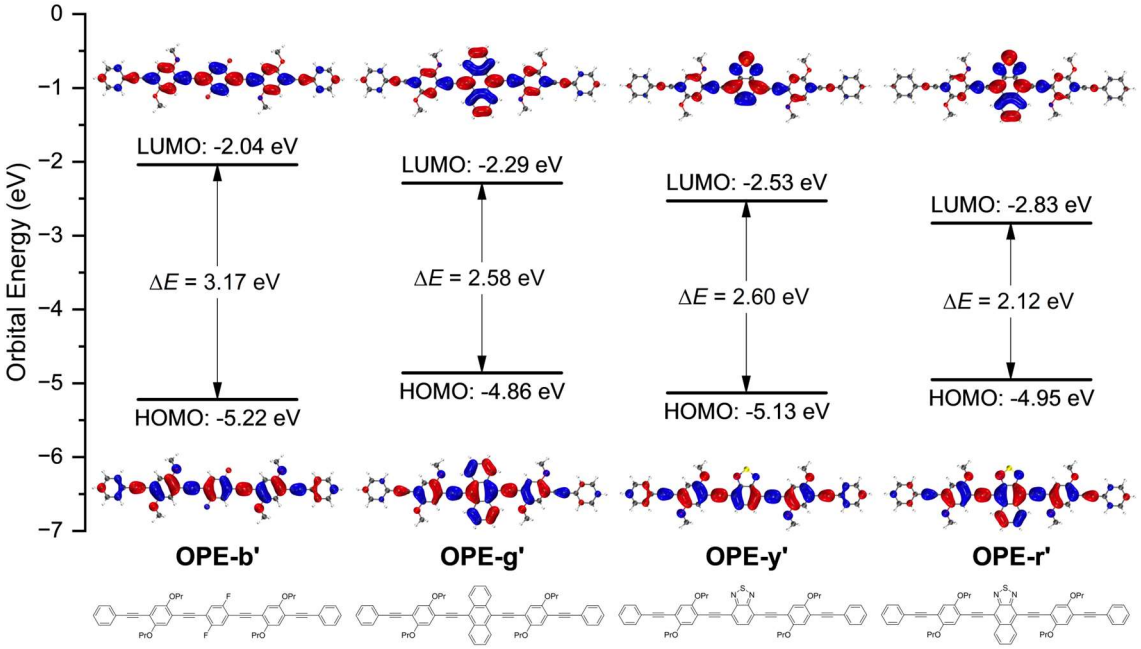

*Figure 36. Calculated FMO energy levels and corresponding molecular orbital distributions for the optimized geometries of **OPE-x'** molecules. The calculations were performed at the D3-PBE0/6-31G(d,p) level of theory. HOMO: highest occupied molecular orbital; LUMO: lowest unoccupied molecular orbital. The orbital pictures are plotted with an isovalue of 0.02.*

A similar trend in FMO levels is observed in the **OPE-*x*'** series, where the donor segment is extended by terminal phenyl ethynyl units. Compared to the **OPE-*x*** series, the additional π-conjugation leads to further stabilization of the π*-orbitals, which results in lower LUMO energies ranging from -2.04 eV to -2.83 eV, following the same trend of increasing acceptor strength. In addition, the effect of the central unit on the overall molecular electronic structure is attenuated in the π-extended series. For instance, the LUMO energy difference between **OPE-b** and **OPE-r** is 1.01 eV, whereas it decreases to 0.79 eV for **OPE-b'** and **OPE-r'**. The HOMO levels are likewise slightly elevated, consistent with the increased delocalization introduced by the extended conjugation. As a result, **OPE-*x*'** molecules exhibit smaller HOMO-LUMO gaps than their **OPE-*x*** analogues, and a general red-shift in the optical transitions is expected.

To gain further insight into the optical properties of the OPE-*x* and OPE-*x*' series, time-dependent DFT (TDDFT) calculations were performed at the same level of theory (D3-PEB0/6-31G(d,p)) using Tamm-Dancoff approximation (TDA). Vertical excitation energies were computed for the lowest 10 singlet and 10 triplet excited states of each molecule. For clarity, only the most relevant low-lying excited states are shown in Figure 37 and Figure 38, corresponding to the **OPE-*x*** and **OPE-*x*'** series, respectively. For each lowest singlet excited state (S_1), a geometry optimization was carried out, followed by wavefunction analysis. The hole-electron character of the $S_1 \rightarrow S_0$ transition was visualized in the form of natural transition orbitals (NTOs).[217] To quantitatively assess the extent of hole-electron separation, the orbital overlap index S_r was employed. It is defined as

$$S_r = \int \sqrt{\rho^{hole}(\boldsymbol{r})\rho^{ele}(\boldsymbol{r})}d\boldsymbol{r} \quad (4)$$

where $\rho^{hole}(\mathbf{r})$ and $\rho^{ele}(\mathbf{r})$ denote the spatial distributions of hole and electron densities, respectively.[218] Based on the value of S_r, the nature of the excited states is conventionally classified as charge transfer (CT) for 0-0.4, hybridized local excitation and charge transfer (HLCT) for 0.4-0.75, and local excitation (LE) for 0.75-1.[219–221]

With increasing acceptor strength, both the vertical excitation energies and the relaxed levels of S_1 states decrease across the series from **OPE-b** to **OPE-r**. The first vertical excitation energies range from 3.26 eV to 2.10 eV, while the relaxed S_1 levels lie between 3.02 eV and 1.89 eV. The latter corresponds to the emission wavelengths, spanning from 410 nm to 655 nm, thus covering the visible light spectrum from deep blue to red. Although **OPE-g** exhibits a similar HOMO-LUMO gap to **OPE-y** (Figure 35b-c), its S_1 level, especially after relaxation, lies significantly higher at 2.45 eV (507 nm) compared to 2.16 eV (575 nm) for **OPE-y** (Figure 37b-c). When translated into wavelength, it corresponds to a difference of approximately 70 nm, shifting the emission from the green to the yellow region. All molecules in the series show S_r values above 0.5, indicating a considerable LE character. Especially **OPE-g**, containing an anthracene core, exhibits an S_r index of 0.80 for the relaxed S_1 geometry, which corresponds to a pure LE state

according to the classification mentioned above. In contrast, **OPE-y** and **OPE-r**, two molecules with heterocyclic acceptors (BTD and NTD), show lower S_r values of 0.57 and 0.65, respectively. Their increased CT character is attributed to the polarizability and electron-withdrawing nature of the heterocycles.

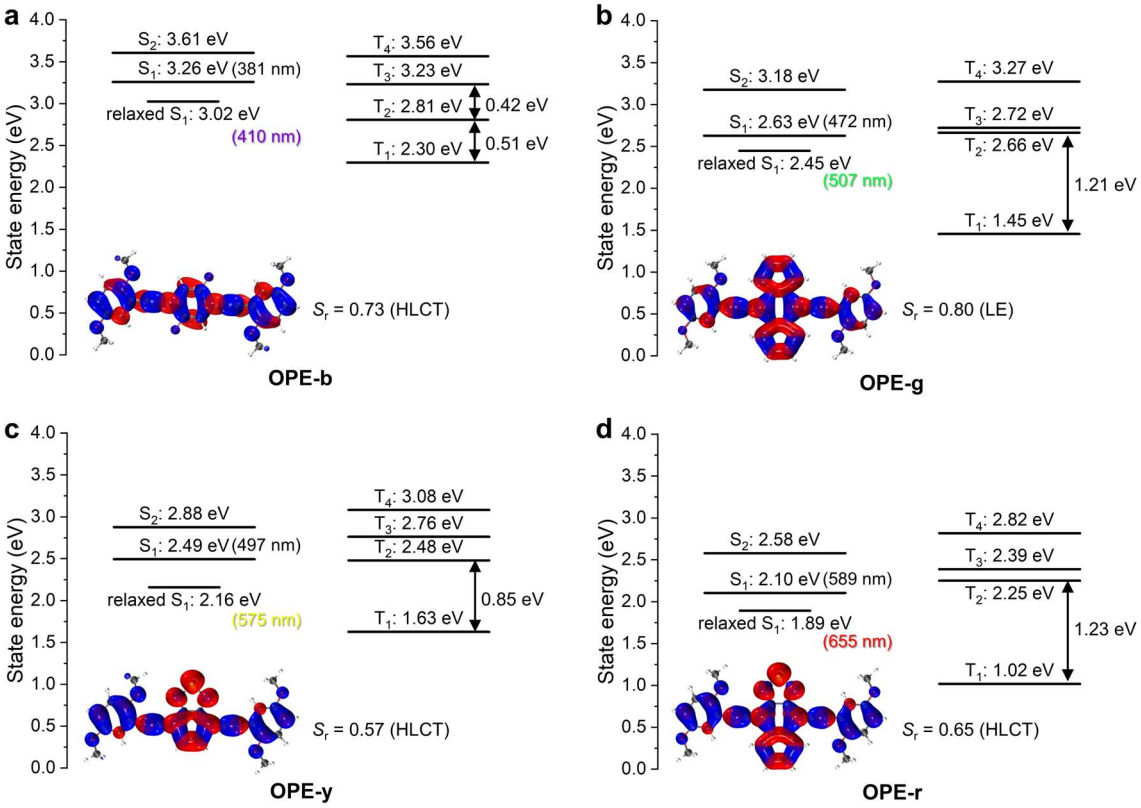

*Figure 37. Vertical excitation energies of representative excited states and the energy of relaxed S_1 geometry for a) **OPE-b**, b) **OPE-g**, c) **OPE-y**, and d) **OPE-r**, calculated at the D3-PBE0/6-31G(d,p) level of theory. For the S_1 levels, the corresponding wavelengths are given in parentheses. The spatial distributions of the hole (blue) and electron (red) in the relaxed S_1 states are shown as natural transition orbitals (NTOs), along with the corresponding S_r index for each molecule. The orbital pictures are plotted with an isovalue of 0.02.*

To evaluate the potential for triplet harvesting, the singlet and triplet excited-state energies are compared. If the energy levels of certain S_n ($n \geq 1$) and T_m ($m \geq 1$) states are close in energy (e.g., $\Delta E_{Sn\text{-}Tm} < 0.1$ eV), reverse intersystem crossing (RISC) becomes energetically feasible.[146,222] It can occur in the case of sufficient spin-orbit coupling to facilitate the spin-flipping process. For **OPE-b**, although the calculation suggests a small S_1-T_3 gap of 0.03 eV, its T_3-T_2 gap of 0.42 eV and T_2-T_1 gap of 0.51 eV may lead to stepwise relaxation via IC transitions, which are usually significantly faster than

RISC/ISC. The other three molecules exhibit relatively large T_2-T_1 energy gaps at the employed level of theory. The energy gaps of 1.21 eV (**OPE-g**), 0.85 eV (**OPE-y**), and 1.23 eV (**OPE-r**), may render the internal conversion less favorable, potentially facilitating RISC.[146] However, these interpretations are based exclusively on theoretical investigations and should be considered as preliminary insights.

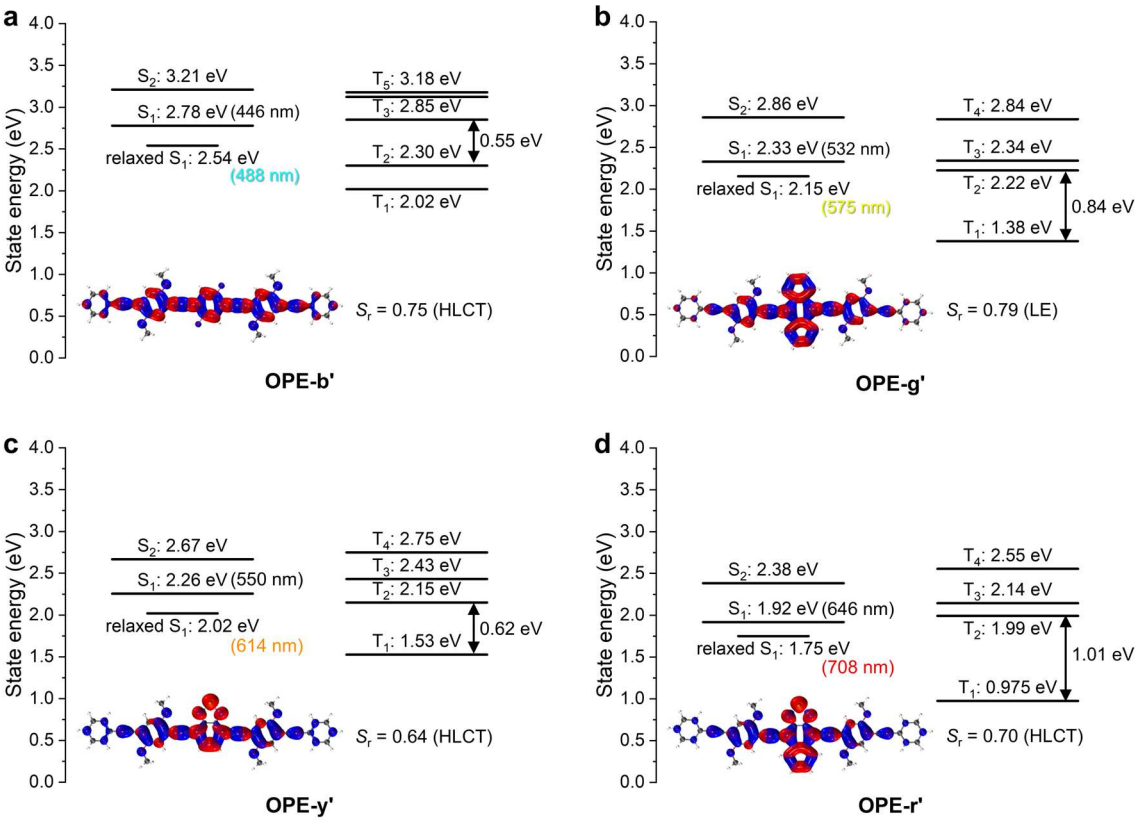

*Figure 38. Vertical excitation energies of representative excited states and the energy of relaxed S_1 geometry for a) **OPE-b'**, b) **OPE-g'**, c) **OPE-y'**, and d) **OPE-r'**, calculated at the D3-PBE0/6-31G(d,p) level of theory. For the S_1 levels, the corresponding wavelengths are given in parentheses. The spatial distributions of the hole (blue) and electron (red) in the relaxed S_1 states are shown as NTOs, along with the corresponding S_r index for each molecule.*

As depicted in Figure 38, TDDFT calculations revealed similar trends for the **OPE-*x*'** series. Due to the increased degree of π-conjugation, the energies of excited states are generally lower than their **OPE-*x*** analogues. Therefore, red-shifted vertical excitation and emission are predicted. The excited-state characteristics remain largely unaffected, as only a minor portion of the electron density is localized on the additional terminal phenyl rings.

4.2.3 Steady-State Optical Characterization

UV-Vis absorption, photoluminescence (PL), and (absolute) quantum yield (Φ_{PL}) measurements were carried out in dilute toluene solution (10 µM). As a non-polar solvent that mimics the environment of typical host materials in OLED devices,[223–225] toluene provided sufficient solubility for the **OPE-*x*** and **OPE-*x*'** series at the required concentration. The normalized absorption and PL spectra are plotted in Figure 39.

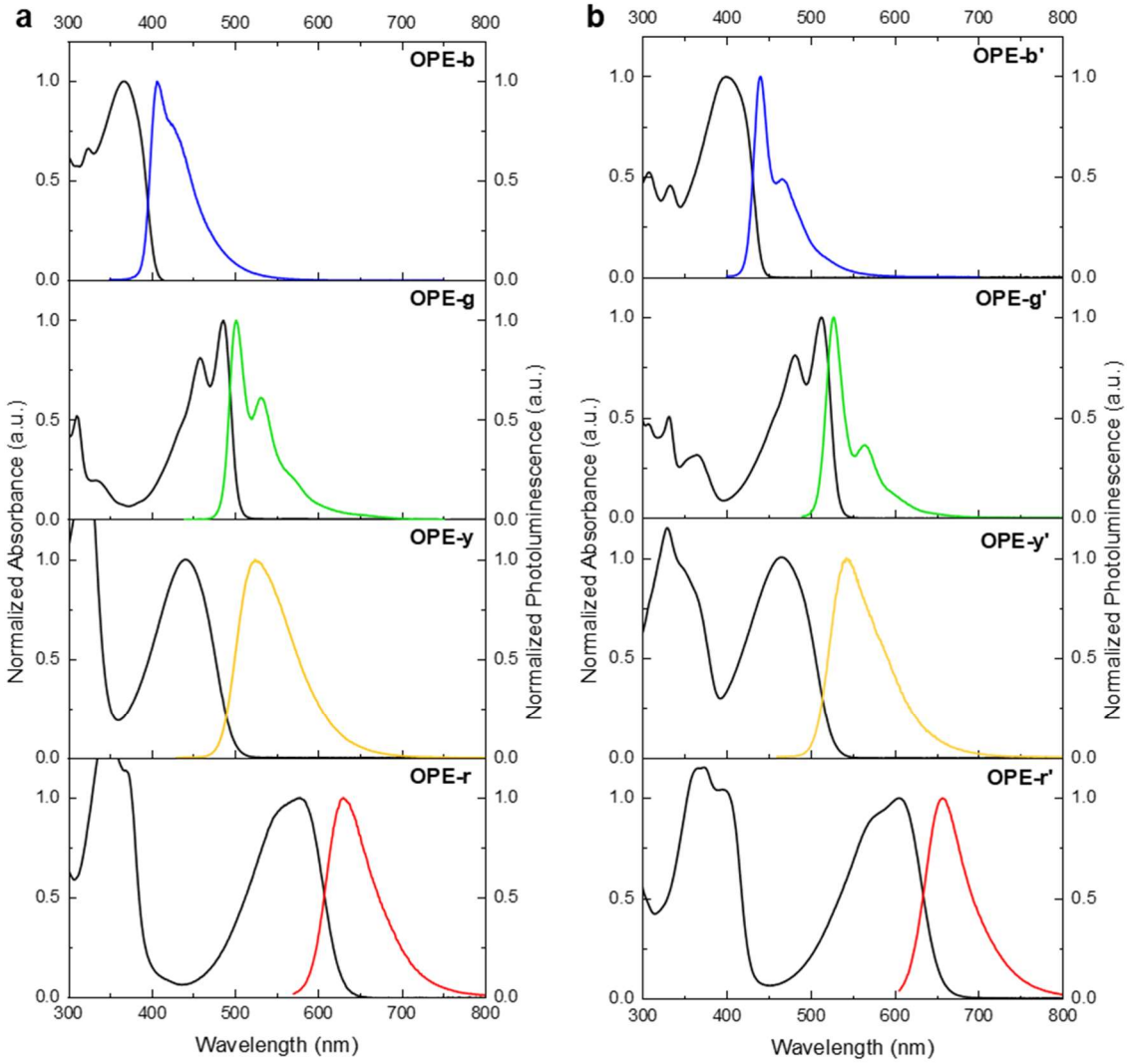

*Figure 39. Normalized absorption and PL spectra of a) the OPE-x series and b) the OPE-x' series. From top to bottom: a) **OPE-b**, **OPE-g**, **OPE-y**, and **OPE-r**; b) **OPE-b'**, **OPE-g'**, **OPE-y'**, and **OPE-r'**. Absorption spectra (black lines) were normalized with respect to the lowest-energy absorption band to enable direct comparison with the corresponding PL spectra (colored lines).*

In general, the **OPE-*x*'** series showed a red-shift of approximately 20-30 nm in both absorption and PL maxima compared to **OPE-*x***, respectively. This observation is consistent with the slightly reduced HOMO-LUMO gaps attributed to the extended π-conjugation. In addition, the increased conjugation led to narrower photoluminescence spectra, as indicated by the reduced full width at half maximum (FWHM) values summarized in Table 1. Notably, the FWHM of **OPE-b** (51 nm) decreased to 23 nm for **OPE-b'**. This can be associated with a weaker vibronic coupling, as displayed by the reduced shoulder peak in the emission profile.[223,226] As a result, an enhanced quantum yield (Φ_{PL}) was obtained which increased from 93% (**OPE-b**) to 97% (**OPE-b'**).

*Table 1. Summary of steady-state photophysical properties and TDDFT calculations for **OPE-x** and **OPE-x'** derivatives. The experiments were conducted in 10 μM toluene solutions.*

Entry	λ_{abs} / nm	λ_{PL}[a] / nm	$\Delta\tilde{\nu}_{exp}$ / cm^{-1}	$\lambda_{S0\text{-}S1}$[b] / nm	$\lambda_{S1\text{-}S0}$[c] / nm	$\Delta\tilde{\nu}_{calc}$ / cm^{-1}	Φ_{PL}[d]
OPE-b	368	407 (51)	2600	381 (1.85)	410 (2.09)	1860	93%
OPE-g	486	501 (48)	616	472 (1.42)	507 (1.52)	1460	83%
OPE-y	441	524 (77)	3590	497 (0.91)	575 (0.73)	2730	-
OPE-r	578	630 (66)	1430	589 (0.90)	655 (0.81)	1710	65%
OPE-b'	399	440 (23)	2340	446 (3.67)	488 (4.11)	1930	97%
OPE-g'	512	527 (24)	556	532 (2.96)	576 (3.28)	1440	83%
OPE-y'	464	542 (71)	3100	550 (2.11)	614 (1.96)	1900	79%
OPE-r'	605	658 (60)	1330	646 (1.90)	708 (1.82)	1360	68%

[a] Full width at half maximum (FWHM) of the emission peak, given in parentheses.
[b] Vertical excitation energy from S_0 to S_1, converted to wavelength (nm); oscillator strength given in parentheses.
[c] Vertical emission energy of relaxed S_1 geometry to S_0, converted to wavelength (nm); oscillator strength given in parentheses.
[d] Absolute photoluminescence quantum yield measured in non-degassed toluene solution. The PLQY for **OPE-y** was measured to exceed 100%, which is physically implausible and likely results from experimental inaccuracies, such as reabsorption effects, scattering artifacts, or calibration errors.

Subsequently, the Stokes shift was compared both between and within the two series. **OPE-g** (616 cm^{-1}) and **OPE-g'** (556 cm^{-1}) exhibited the smallest Stokes shifts among all derivatives, accompanied by mirror-like symmetric vibronic progressions. This indicates minimal structural reorganization between the ground and excited states. As exemplarily illustrated for **OPE-g** in Figure 40a, the overlay of the optimized S_0 geometry (blue) and relaxed S_1 geometry (red) reveals a high degree of structural consistency. In contrast, **OPE-y** showed the largest Stokes shift (2730 cm^{-1}) within the series. Upon excitation, its peripheral donor units exhibit a pronounced bending towards the heterocyclic acceptor, whereas the ground-state structure shows a more linear OPE-backbone (Figure 40b). This substantial structural deviation also explains the observation that the emission maximum of **OPE-y** was red-shifted by 23 nm relative to **OPE-g**, whereas its absorption maximum was blue-shifted by 45 nm.

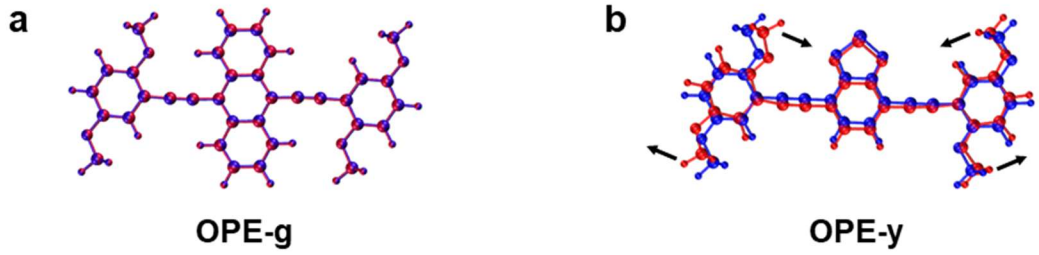

*Figure 40. Overlayed structures of optimized S_0 (blue) geometry and S_1 (red) geometry for a) **OPE-g** and b) **OPE-y**.*

To evaluate the chromaticity of both **OPE-x** and **OPE-x'** series, the Comission International de L'Eclairage (CIE) color coordinates (x,y) were obtained from the emission spectra of their toluene solutions and plotted onto the CIE 1931 diagram (Figure 41). The emission of **OPE-b** (0.157, 0.051) and **OPE-b'** (0.150, 0.084) is located in the deep blue region. Both coordinates closely match the "bluest" blue (0.150, 0.060) defined in the standard Red Green Blue (sRGB) color space.[227] **OPE-r** (0.682, 0.318) lies in the red region, while **OPE-r'** (0.715, 0.292) falls into the deep red region. **OPE-r'** aligns well with the red standard (0.708, 0.292) in the BT.2020 color space, which was more recently suggested for high-end displays.[228] The other derivatives showed green to yellow emission in toluene. **OPE-g** (0.240, 0.627) is situated in the green-cyan gamut.

OPE-g' (0.315, 0.656) and **OPE-y** (0.325, 0.614) fall into the yellow-green region, whereas **OPE-y'** (0.400,0.508) approaches the yellow domain. This distribution of emission colors demonstrates the modular tunability of chromaticity across the visible spectrum.

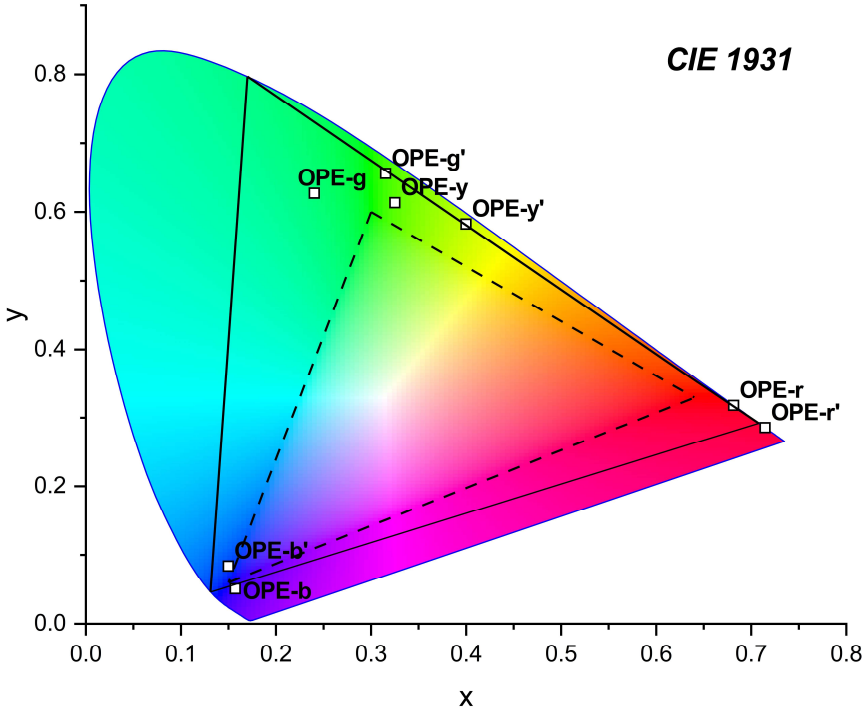

*Figure 41. The emission color coordinates of **OPE-x** and **OPE-x'** derivatives plotted on the CIE 1931 diagram. The dashed triangle denotes the standard sRGB color gamut, while the solid black triangle outlines the wider BT.2020 color gamut.*

4.3 Summary and Outlook

In summary, two series of D-A-D type OPE emitters, **OPE-*x*** and **OPE-*x*'**, covering different emitting colors, were successfully synthesized. Their steady-state photophysical properties were investigated in toluene and analyzed with the aid of DFT/TDDFT calculations. Compared to their **OPE-*x*** counterparts, the extended conjugation in the **OPE-*x*'** derivatives resulted narrower emission peaks and smaller Stokes shift, reflecting higher rigidity of the backbone. Notably, the green emitter **OPE-g'**, incorporating an anthracene moiety for further extended conjugation, displayed the narrowest emission spectrum (FWHM = 24 nm) and the smallest Stokes shift (556 cm^{-1}) in toluene among

the investigated molecules. All emitters showed high absolute quantum yields exceeding 65%. In particular, the blue emitters (**OPE-b**: 93%, **OPE-b'**: 97%) and green emitters (**OPE-g**: 83%, **OPE-g'**: 83%) exhibited excellent quantum yields in both series. In terms of chromaticity, **OPE-b** and **OPE-b'** well matched the sRGB blue coordinate, while **OPE-r'** aligned closely with the red primary suggested by BT.2020.

While the TADF mechanism can be elucidated by time-resolved photophysical measurements, unambiguous identification of a "hot exciton" pathway, as predicted theoretically for some of the discussed molecules, remains challenging using standard spectroscopic techniques. Often, evidence is obtained indirectly when the external quantum efficiency (EQE) of the resulting OLED devices exceeds 5%.[146] However, manufacturing of OLEDs was not feasible within the scope of this work.

In device contexts such as OLEDs, where light outcoupling efficiency (η_{out}) plays a significant role, the orientation of the transition dipole moment (TDM) is a further critical factor. Molecules that preferentially align horizontally within polymer matrices or vacuum-deposited films can substantially improve device performance by enhancing light extraction.[165,164] Thus, molecular design strategies often address not only the electronic structure, but also the shape anisotropy and packing tendencies. To confirm a preferential horizontal orientation of the TDM, angular dependent photoluminescence spectroscopy measurements are usually performed.[161,229,230]

A preferential horizontal orientation of the transition dipole moment (TDM) is characteristic of rod-shaped molecules like those presented in this thesis.[163–165] Experimental confirmation of this property would thus significantly enhance their appeal for optoelectronic applications. Investigating any impact of the π-extension would be of particular interest to this matter.

5 Donor-OPE-Acceptor Architectures

The synthetic work and the initial structural characterizations were carried out by Till Paha during his master's thesis. The transient absorption spectroscopy measurements were conducted by Marianne Armbruster, supervised by Prof. Dr. Andreas-Neil Unterreiner. Project design, advanced characterization and data interpretation are work of the author of this thesis.

5.1 Motivation

The control over intramolecular charge transfer (CT) versus locally excited (LE) character in the singlet excited state is a decisive factor governing fundamental properties like emission color, photoluminescence quantum yield (PLQY, Φ_{PL}), and excited-state lifetime.[231,232] In π-conjugated donor-acceptor systems, the balance is governed not only by the strength of the respective donor and acceptor, but also by their relative spatial arrangement and the effective conjugation length that mediates electronic coupling between them.[233–235]

For instance, this delicate interplay between LE and CT states is crucial for the development of "hot exciton" materials, a class of OLED emitters featuring hybridized local and charge-transfer (HLCT) states. The term HLCT was introduced by Ma *et al.* and describes an excited state in which the transition characteristics of LE and CT are closely combined and mutually compatible. One of the typical characteristics of an HLCT state is its solvent-dependent behavior, which often manifests as a two-slope linear correlation in a Lippert-Mataga plot.[146] In contrast to the well-established design rules for thermally activated delayed fluorescence (TADF) materials, guidelines for HLCT materials remains less clear. Many HLCT emitters rely on extended conjugated scaffold to tune the LE/CT balance.[236,237] However, studies that identify the exact donor–acceptor distance at which HLCT character emerges, are still lacking. Such investigations are therefore essential to

deepen the fundamental understanding, which may aid the development of HLCT emitters.

While the previous chapter focused on tuning the emission color of the D-A-D sequences by varying the acceptor strength and only hinted at conjugation-length dependence of LE/CT character, the present chapter offers a more systematic approach of investigating how the conjugation length and the distance between the same donor and acceptor units in D-OPE-A systems impact the CT and LE excited state characteristics. To this end, four new structures were thus synthesized, in which OPE segments of varied lengths connect a di-*tert*-butylcarbazole (D*t*BCb) donor and a triphenyltriazine (Trz) acceptor (Figure 42). The photophysical properties of the resulting structures are investigated both experimentally and theoretically.

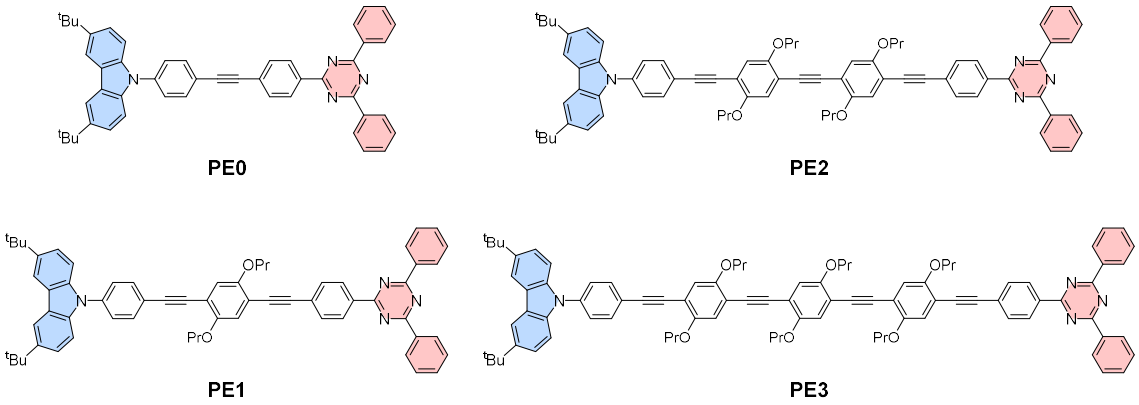

Figure 42. Structures studied in this chapter.

5.2 Results and Discussion

5.2.1 Synthesis of D-OPE-A Oligomers

The D-OPE-A oligomers were synthesized in an iterative manner based on a two-step cycle involving decarboxylative coupling followed by saponification (Figure 43). This modular synthetic strategy enables precise control over the oligomer length and has previously been established for the preparation of **OPE1a**-**OPE4a** molecules. The index

n in the nomenclature denotes the repeating number of propoxylated phenylene ethynylene (PE) units.

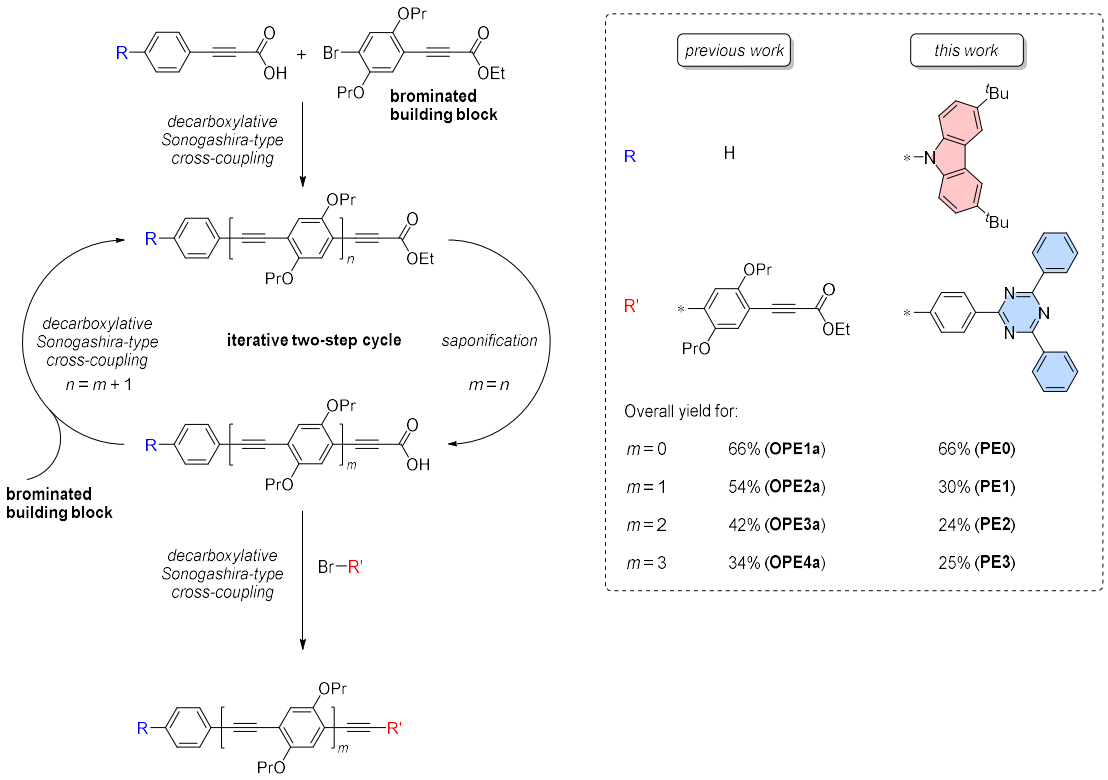

*Figure 43. Iterative synthesis of employed for **PEn** oligomers.*[9]

The direct decarboxylative coupling reaction between the donor-bearing unit 3-(4-(3,6-di-*tert*-butyl-9*H*-carbazol-9-yl)phenyl)propiolic acid **C4** and the acceptor-bearing unit 2-(4-bromophenyl)-4,6-diphenyl-1,3,5-triazine yielded **PE0** in 66%. The higher oligomers, **PE1**-**PE3** were obtained via iterative coupling-saponification cycles. The ^{1}H NMR spectra of flash-column-purified D-OPE-A oligomers are compared in Figure 44. The appearance of an additional aromatic resonance at 7.1 ppm, along with the distinct aliphatic signals in the regions of 4.1 – 4.0 ppm (OCH_2), 2.0 – 1.8 ppm (CH_2), and 1.2 – 1.1 ppm (CH_3), confirmed the successful incorporation of the propoxylated PE units. The integrals of these signals increased proportionally with the oligomer length, while the signals corresponding to the terminal donor and acceptor units remained constant, thus verifying the stepwise elongation of the conjugated backbone.

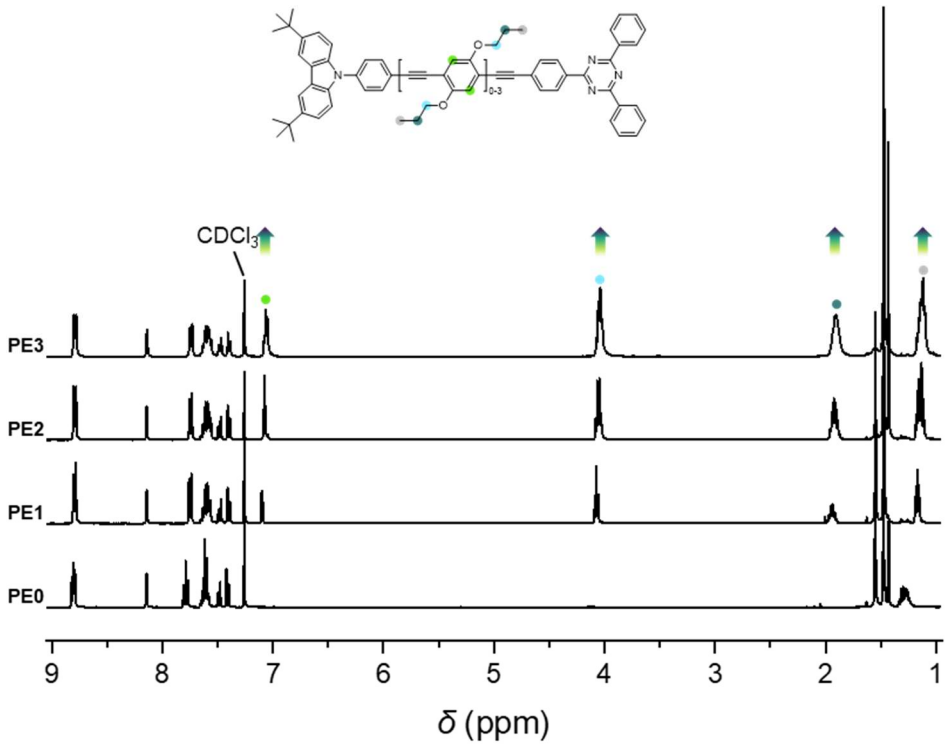

*Figure 44. ^{1}H NMR spectra of **PE0-PE3** recorded in $CDCl_3$. For comparison purposes, all spectra were normalized to the aromatic doublet at 8.1 ppm, belonging to the carbazole moiety.*

SEC confirmed the high purity of the flash-column-purified products **PE0** and **PE1** (Figure 45). In contrast, the SEC traces of the thus obtained **PE2** and **PE3** revealed impurity signals at lower retention times that could not be clearly identified by ^{1}H NMR spectroscopy. Therefore, further purification of these two higher oligomers was performed by preparative thin-layer chromatography (prep-TLC) in cyclohexane and DCM. The reduction of impurity peaks in the subsequent SEC traces demonstrated the effectiveness of this additional purification step and confirmed the successful isolation of the target oligomers. Consequently, **PE1-PE3** were obtained in 24-30% overall yields. These values are comparable with those reported for **OPE2a-OPE4a** (34-54%), which were prepared by the same reaction steps, thereby confirming the general applicability of this modular synthetic approach to OPE oligomer.[9] All synthesized molecules were fully characterized by ^{1}H and ^{13}C NMR spectroscopy, IR spectroscopy, and HRMS analysis. Further details can be found in Section 8.3.

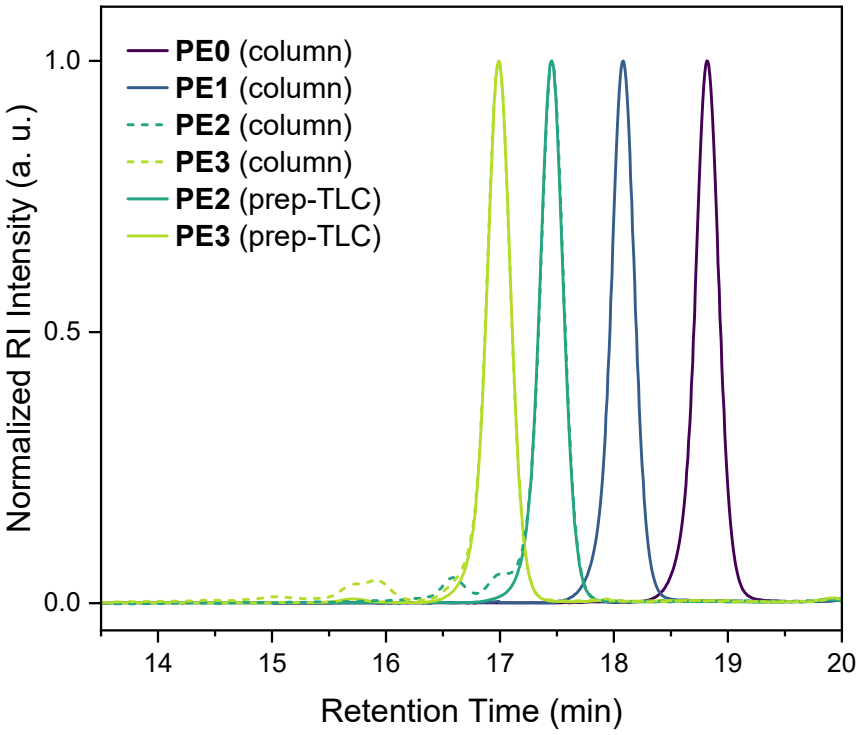

*Figure 45. Normalized SEC traces of **PE0-PE3** after different purification steps.*

5.2.2 Computational Investigation

To elucidate the nature of the lowest-energy excited states in dependence of the conjugation length, quantum mechanical calculations were carried out.[215,216] Ground-state geometries of the **PE*n*** oligomers were optimized at the D3-PBE0/6-31G(d,p) level of theory in the gas phase to probe their intrinsic electronic properties. The resulting frontier molecular orbitals (FMO) energy levels and the corresponding orbital distributions are depicted in Figure 46.

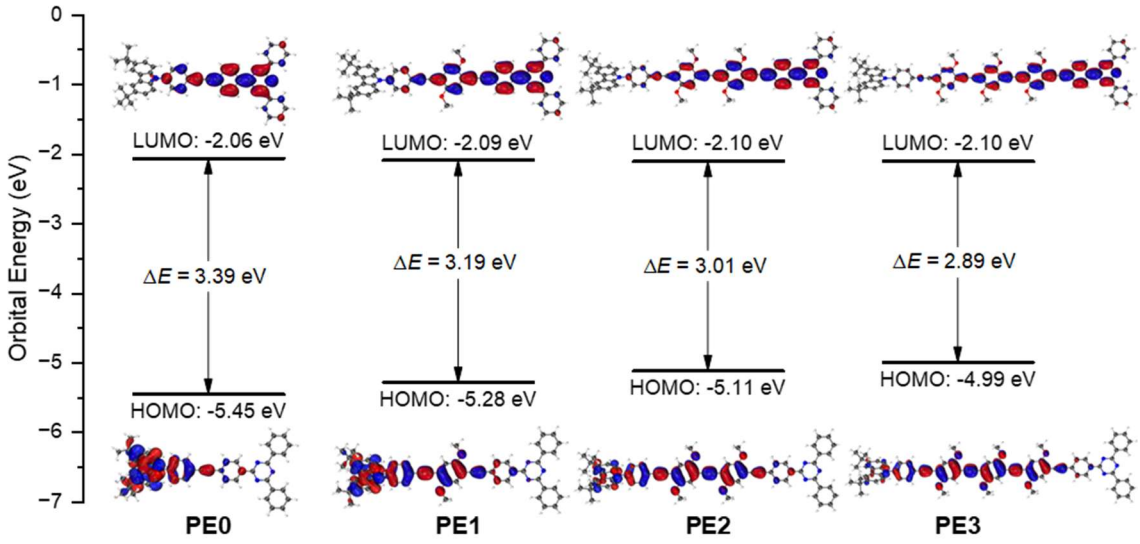

*Figure 46. FMO levels of **PE0-PE3** calculated at the D3-PBE0/6-31G(d,p) level of theory. The corresponding electron density distributions of the HOMO and LUMO are visualized with an isovalue of 0.02.*

While the lowest unoccupied molecular orbitals (LUMOs) are mainly distributed over the conjugated OPE backbone and their energy levels remain almost consistent across the series, the highest occupied molecular orbital (HOMO) energy levels show a clear increase in energy with *n*, from -5.45 eV to -4.99 eV. This trend reflects the increased conjugation introduced by the extended PE units, which generally both destabilizes the HOMO and delocalizes its distribution from the D*t*BCb donor towards the OPE backbone. Moreover, the alkoxy groups attached to the incorporating PE units exert an additional electron-donating effect, further contributing to the delocalization of the HOMO distributions. The resulting HOMO-LUMO gaps (ΔE) accordingly decrease from 3.39 eV to 2.89 eV, indicating a red-shifted trend with increasing chain length.

Time-dependent DFT (TDDFT) calculations were performed to obtain further insight into the photophysical properties of the **PE*n*** oligomers. Vertical excitation energies were computed from geometries optimized with a toluene polarizable continuum model (PCM), providing a more realistic description of the absorption process. To predict the nature of the emissive states, geometry optimizations of the first singlet excited state (S_1) were conducted applying the same solvent model. Both predicted absorption and emission

energies follow the same trend as the HOMO-LUMO gap evolution (Figure 47), however much less pronounces, as the S_1 levels (both vertically excited and relaxed) showed a decreasing trend in contrast to the LUMO levels discussed above.

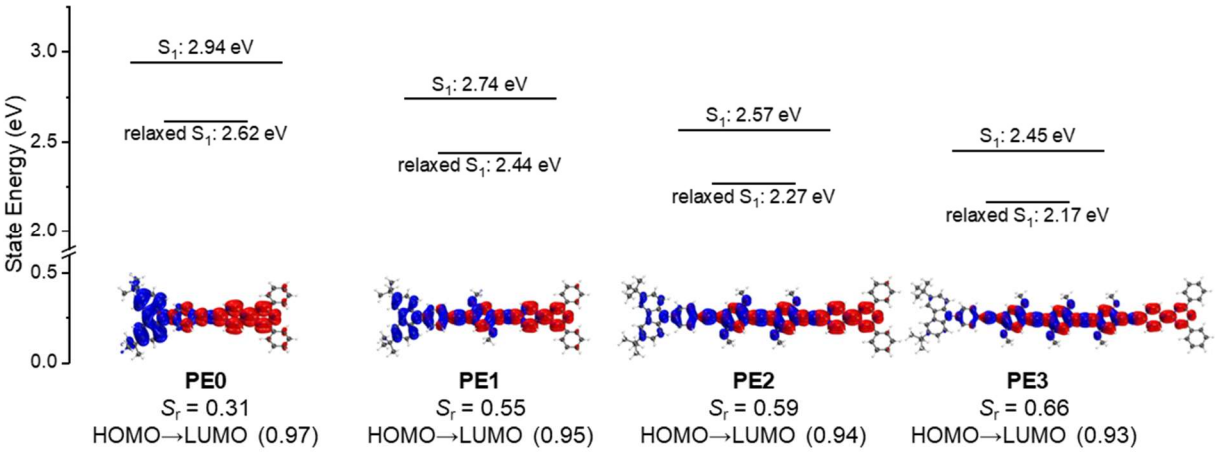

Figure 47. The vertical excitation energies (towards S_1) and vertical emission energies from the relaxed S_1 states calculated at the D3-PBE0/6-31G(d,p) level with TDA. NTO images illustrate the hole (blue) and electron (red) distributions for each oligomer, shown at an isovalue of 0.02. The corresponding S_r values, together with the probabilities of the most dominant transitions, are given below.

With increasing conjugation length, the natural transition orbital (NTO) images reveal a progressively greater spatial overlap between the hole and particle densities for the relaxed S_1 states. This trend is quantified by the corresponding overlap index (S_r), which increases from 0.31 (**PE0**) to 0.66 (**PE3**), indicating increasing LE character of the excited state.[217,218,220,221,238] Consequently, the shorter oligomers exhibit more CT character.

5.2.3 Steady State Photophysics

The steady-state optical properties of the **PE*n*** oligomers were first investigated in toluene solution. Figure 48 presents the UV-Vis absorption and photoluminescence (PL) spectra, whereas key spectral features together with the PLQY results are summarized in Table 2.

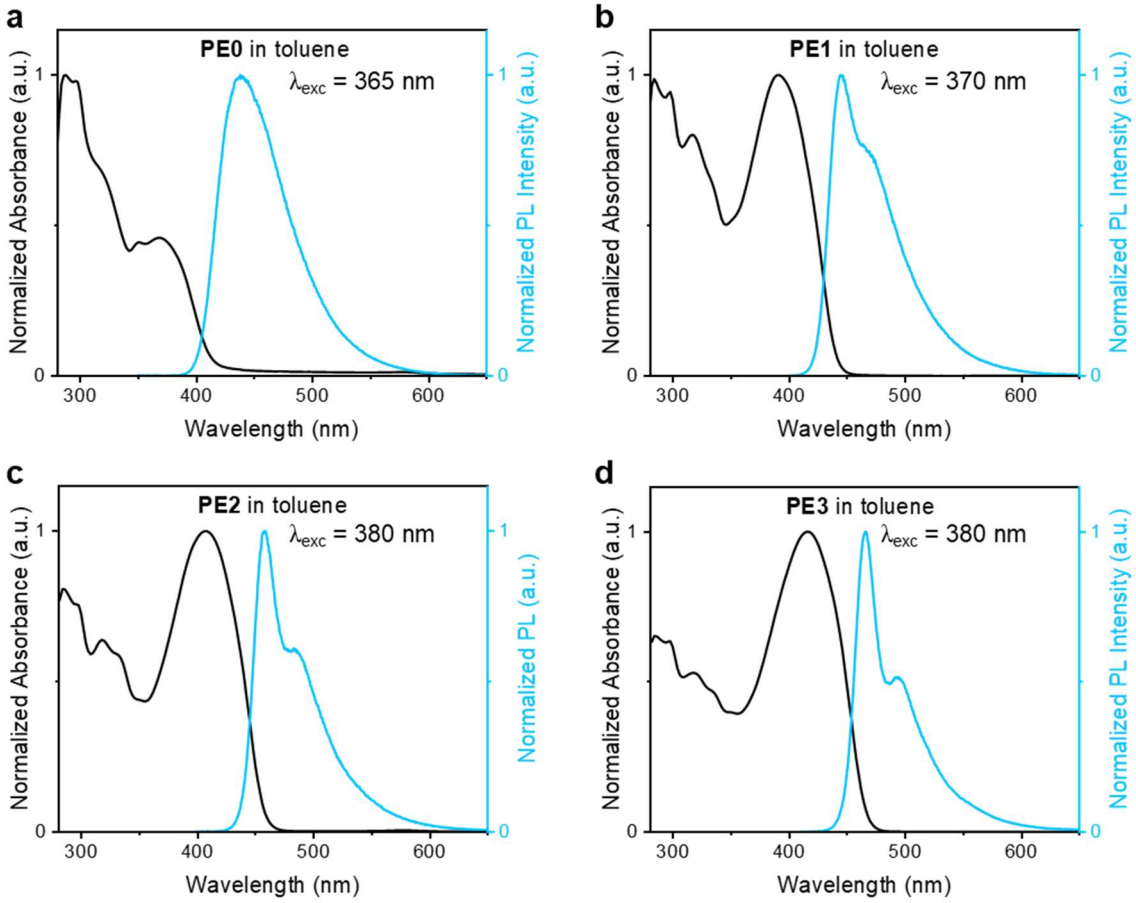

*Figure 48. Normalized UV-Vis absorption and photoluminescence spectra of a) **PE0**, b) **PE1**, c) **PE2**, and d) **PE3** in 10 µM solution of toluene. Excitation wavelengths (λ_{exc}) were chosen based on the respective lowest-energy absorption maxima.*

From **PE0** to **PE3**, the lowest-energy absorption band increased with respect to the higher-energy bands, reflecting enhanced π-electron delocalization along the conjugated backbone. The peak position red-shifted from 368 nm to 416 nm, consistent with the progressive narrowing of the HOMO-LUMO gap, as predicted by DFT calculations (Figure 46). A corresponding red-shift was also observed in the PL spectra, with the emission maxima shifting gradually from 438 nm to 466 nm across the series. All oligomers exhibited Φ_{PL} close to unity, in agreement with values reported for similar structures.[239]

*Table 2. Summary of optical and parameters of **PEn** series in toluene.*

Entry	λ_{abs} / nm (toluene)	λ_{PL} [a] / nm (toluene)	$\Delta\tilde{\nu}_{exp}$ [b] / cm^{-1}	Φ_{PL} [c]
PE0	368	438 (65)	4340	95%
PE1	390	445 (58)	3170	99%
PE2	408	458 (50)	2680	98%
PE3	416	466 (27)	2580	95%

[a] Full width at half maximum (FWHM) of the emission peak, given in parentheses.
[b] Stokes shift $\Delta\tilde{\nu} = \tilde{\nu}_{abs} - \tilde{\nu}_{PL}$.
[c] Measured in non-degassed toluene solution.

The narrowing of the PL peaks (Figure 48) from **PE0** to **PE3** (with FWHM decreasing from 65 nm to 27 nm, as shown in Table 2) indicates an increasing contribution of LE character. This trend arises from enhanced π-electron delocalization along the extended OPE backbone and is further supported by the reduced conformational relaxation between the S_0 and S_1 geometries. While the OPE backbone and the triazine acceptor remain coplanar, the carbazole donor twists out of the plane due to steric congestion. The dihedral angle φ(C3-N4-C14-C19) between the latter and the adjacent phenylene ring is exemplarily depicted for the S_1 geometry of **PE0** in Figure 49.

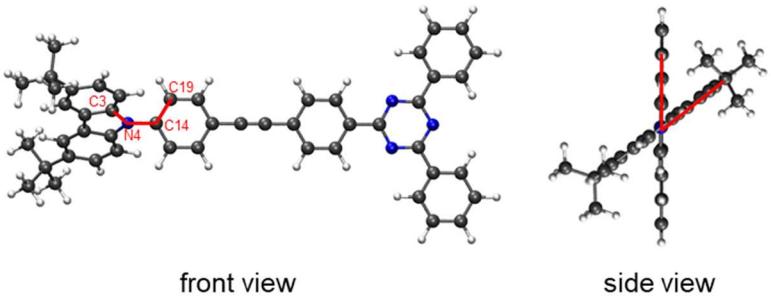

*Figure 49. Front and side views of the S_1 state geometry of **PE1**, showing the torsional angle φ(C3-N4-C14-C19).*

The computed values of φ(C3-N4-C14-C19) and their changes between the S_0 and S_1 states ($\Delta\varphi$) are compared in Table 3. A decreasing trend in $\Delta\varphi$ with increasing conjugation

length confirmed the reduced structural relaxation in the emissive state for longer oligomers. A stronger LE character in higher DP oligomers is again verified.

*Table 3. Computed torsional angles in the S_0 and S_1 states for **PE0-PE3**, calculated at the PBE0/6-31G(d,p) level with a toluene polarizable continuum model (PCM).*

Entry	φ in S_0 / °	φ in S_1 / °	$\Delta\varphi$ / °
PE0	48.8	42.0	6.8
PE1	49.7	44.1	5.6
PE2	50.2	46.2	4.0
PE3	50.2	48.1	1.9

The conformational deviation between the S_0 and the S_1 states further influences the optical behavior in terms of the Stokes shift ($\tilde{\nu}_{abs}$ - $\tilde{\nu}_{PL}$). For instance, in toluene, the increased similarity between the S_0 and S_1 geometries corresponds to smaller Stokes shifts (Table 2). The change in the Stokes shift became less pronounced with an increasing number of propoxylated PE units, indicating a decreased sensitivity to the employed solvent environment.

To further investigate the polarity-dependent behavior of the first singlet excited state in the **PE*n*** oligomers, a solvatochromic study was carried out in various solvents, ranging from non-polar *n*-hexane to moderately polar acetone. Representative absorption and PL spectra are shown in Figure 50. The complete data set for the solvatochromic study is provided in the Appendix (Figure S32-S33 and Table S1).

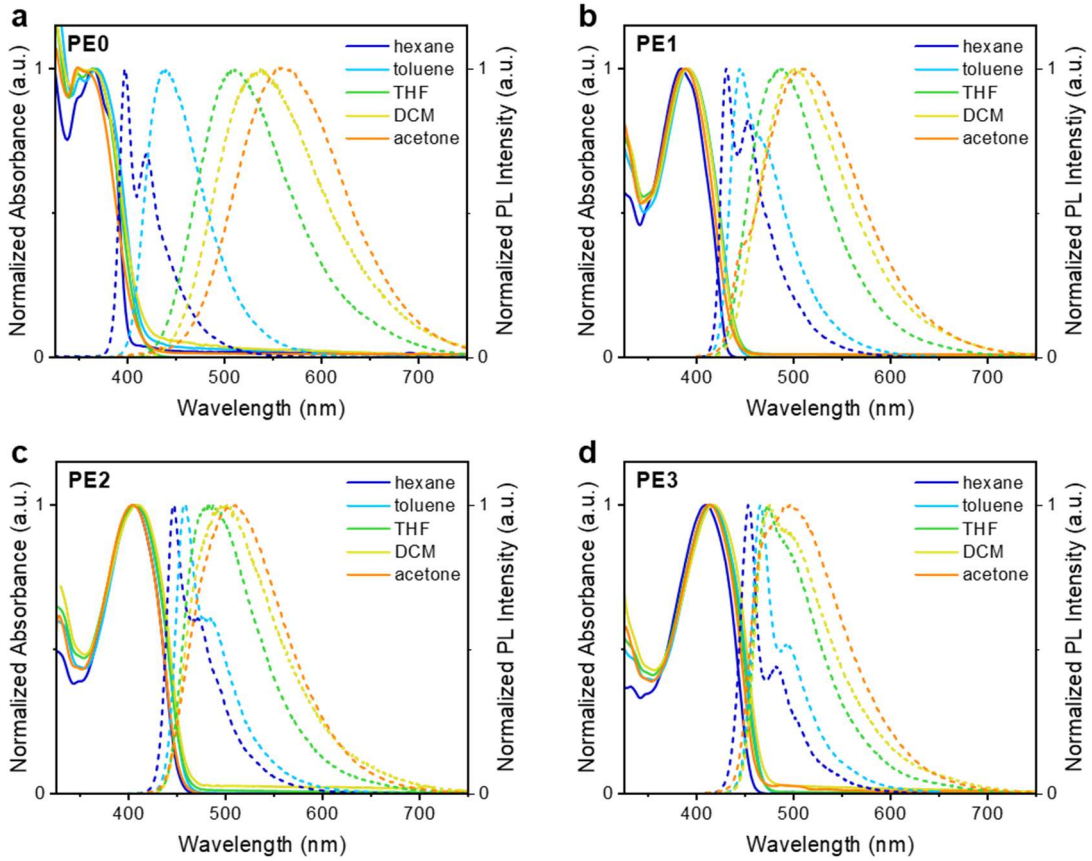

*Figure 50. Normalized photoluminescence spectra of a) **PE0**, b) **PE1**, c) **PE2**, and d) **PE3** in 10 µM solutions of n-hexane, toluene, THF, DCM, and acetone respectively.*

The absorption maxima of the lowest-energy band remained practically constant in all investigated solvents ($\Delta\lambda_{abs}$ < 8 nm) for the whole series. In contrast, the PL spectra showed a decreasing trend of polarity-induced red-shift with increasing conjugation length. **PE0** exhibited pronounced solvatochromism, with emission ranging from deep blue in *n*-hexane (397 nm) to yellow in acetone (559 nm). By comparison, **PE3** remained blue emissive in the sequence from *n*-hexane (454 nm) to DCM (475 nm), while a significant red-shift in acetone altered the emission towards the green region (496 nm), likely reflecting distinct excited-state characteristics in solvents of different polarity. The emission spectra for all investigated oligomers in low-polarity solvents like *n*-hexane and toluene display pronounced shoulder peaks, reflecting a high resolution of the vibronic band structure, which is typical for LE-dominated excited states. For **PE3**, these vibronic features persist in more polar solvents reflecting the significantly higher LE admixture in its emissive state compared to the shorter oligomers.

To better understand the length-dependent solvatochromic behavior of the **PE*n*** oligomers, the Stokes shifts, corresponding to the influence of the respective solvents, were plotted against the Lippert-Mataga orientation polarizability Δf (Figure 51), which is determined from their dielectric constant (ε) and refractive index (n) according to Equation 2 in Section 2.2.1.[240,241] Linear fits were applied to the data, and the resulting slopes (m) along with the coefficients of determination (R^2) are summarized in Table S2. By employing the Onsager radius (a) obtained based on the van der Waals volume, the change in dipole moment between the ground and excited states was calculated. The resulting excited-state dipole moment (μ_{es}) is indicated in each plot.

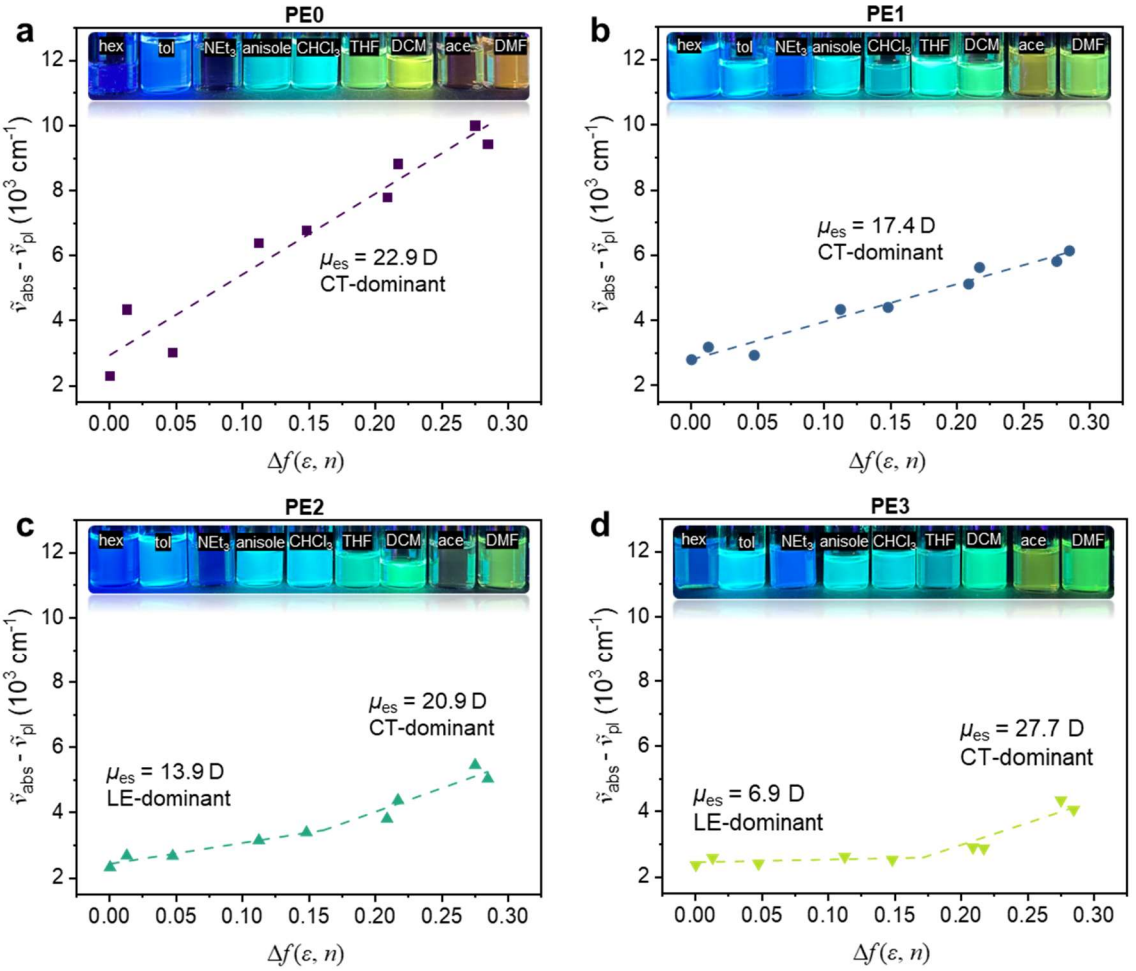

*Figure 51. Lippert-Mataga solvatochromic analysis of a) **PE0**, b) **PE1**, c) **PE2**, and d) **PE3**. Dashed lines represent the fitted linear correlations. Insets show photographs of each **PEn** oligomers in investigated solvents under UV excitation (365 nm).*

For shorter oligomers **PE0** and **PE1**, the solvatochromic results display an almost uniform linear correlation throughout the tested solvents, from *n*-hexane (Δf = 0.0005) to acetone (Δf = 0.28). **PE0** exhibited a more CT-dominant character with a large excited-state dipole moment (μ_{es}) for S_1 of 22.9 D, whereas **PE1** showed reduced CT contribution with a smaller μ_{es} value of 17.4 D. In contrast, **PE2** and **PE3** displayed distinct excited-state characteristics depending on solvent polarity. In the first segment of low-to-medium polarities, μ_{es} values of 13.9 D (**PE2**) and 6.9 D (**PE3**) are consistent with an LE-dominant HLCT excited state. At higher solvent polarity region, μ_{es} increased to 20.9 D for **PE2** and 27.7 D for **PE3**, respectively, indicating a transition towards a more CT-dominant HLCT state. The transition point between LE- and CT-dominant regimes shifted towards higher solvent polarity region with increasing oligomer length from **PE2** to **PE3**.

5.2.4 Transient Absorption Spectroscopy

To further elucidate the excited-state dynamics, transient absorption (TA) spectroscopy was carried out for all **PE*n*** oligomers in more polar toluene and less polar cyclohexane. A full comparison of all TA spectra is shown in Figure 52.

In both solvents, increased stimulated emission (SE, $\Delta OD < 0$) was observed along with elongation of the conjugated backbone, accompanied by a slight red shift, consistent with the λ_{PL} values of this series ($\approx$ 400-500 nm). Due to limited solubility, **PE3** in cyclohexane gave a much weaker signal in the TA measurement, but followed the general trend when comparing the relative intensities of SE and excited-state absorption (ESA, $S_1 \rightarrow S_n$, $n > 1$, $\Delta OD > 0$).

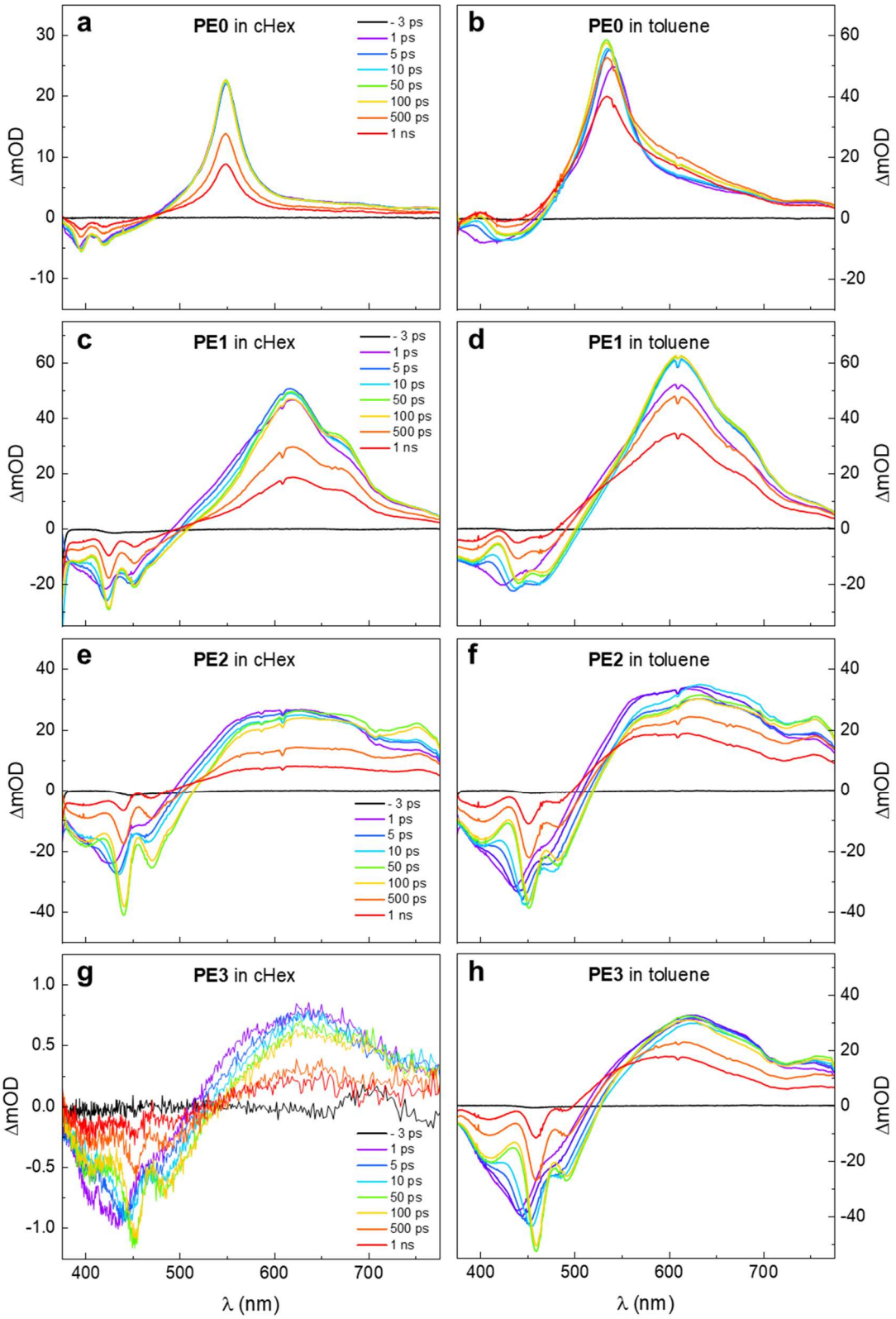

*Figure 52. Transient absorption spectra of **PE0** (a, b), **PE1** (c, d), **PE2** (d, f), and **PE3** (g, h) in 25 µM cyclohexane and toluene solution, excited by λ_{exc} = 370 nm.*

The sharp, symmetric ESA band of **PE0** at 550 nm in non-polar cyclohexane (Figure 52a) is characteristic for an excited state with LE admixture, in line with the TDDFT calculations.[242] In slight polar toluene, the ESA amplitude rises within 100 ps and shape became "less regular" (Figure 52b), suggesting additional contributions from charge-transfer (CT) character. The CT feature stabilized the S_1 energy level in toluene, leading to higher S_1-S_n energy gaps and therefore a blue-shifted ESA band. A similar blue-shift of ESA was observed for **PE1** from 616 nm (in cyclohexane) to 610 nm (toluene), consistent with the same CT stabilization effect. Compared to **PE0**, the ESA maximum of **PE1** is red-shifted in both solvents, which can be explained by reduced S_1-S_n energy gap due to the increased π-conjugation. For higher oligomers, the broadening of the ESA band, possibly attributed to a denser manifold of excited states or aggregations, renders the peak featureless, in agreement with the observations reported for comparable systems.[52]

Time constants derived from global fitting of the TA measurements are summarized in Table 4. The corresponding decay-associated difference spectra are provided in appendix (Figure S34).

*Table 4. The time constants of global fitting of TA data for all investigated **PEn** molecules.*

	cyclohexane			toluene		
entry	τ_1	τ_2	τ_3	τ_1	τ_2	τ_3
PE0	30 fs	12 ps	> 1 ns	57 fs	9.8 ps	>1 ns
PE1		1.9 ps	>1 ns	98 fs	1.5 ps	>1 ns
PE2		9.0 ps	700 ps	64 fs	2.5 ps	>1 ns
PE3	62 fs	0.2 ps	538 ps	88 fs	5.2 ps	847 ps

Ultrafast components (from the femtosecond to the early picosecond range) were observed for all the **PE*n*** oligomers. These can be assigned to relaxation processes

occurring within the initially populated excited state, such as vibrational cooling and solvent reorganization.[242–244] The longer-lived species on the nanosecond timescale (τ_3) may correspond to a stable S_1 state, which is stabilized by partial CT character.[7,242] With increasing PE units, τ_3 decreases for **PE2** and **PE3**, reflecting reduced CT stabilization. In cyclohexane, τ_3 falls below 1 ns for both **PE2** (700 ps) and **PE3** (538 ps), consistent with reduced CT stabilization of the excited state in the less polar environment.

5.3 Summary and Outlook

In this work, four new D-OPE-A type oligomers (**PE0**-**PE3**) were synthesized via an iterative strategy combining decarboxylative coupling and saponification reactions. Comparable overall yields to those of their unmodified derivatives (**OPE1a**-**OPE4a**) confirmed the broad compatibility of this approach. The high purity (>99%) of these oligomers was verified by SEC, ensuring a reliable basis for comparison of their photophysical properties. This is of particular importance in the context of fundamental research on conjugated oligomers, where even minor impurities can interfere with the structure-property relationships.

Solvatochromic studies combined with computational analysis demonstrated that the character of the lowest excited singlet state (S_1) evolves systematically with the OPE length. UV-Vis absorption spectroscopy revealed the growing LE contribution of the excited-state by showing a rise of the π-π* transition across the series. Consistently, PL investigations showed the gradual decay of CT character. While S_1 of **PE0** and **PE1** are CT-dominated, **PE2** and **PE3** exhibit stronger mixed character of CT and LE. More particularly in the case of **PE2** and **PE3**, the Lippert-Mataga plot indicates a clear switch between an initially LE-dominated state in non-polar solvents into a CT-dominated state in polar environments.

TA measurements in non-polar and less polar environments also reflect the shift from CT- towards LE-dominated excited states with increasing OPE length. Further measurements

could be conducted in polar environments, especially to verify a polarity-induced switch between LE and CT dominated states in higher conjugated oligomers. Overall, this series highlights that the hybridization of LE and CT (HLCT) is a delicate balance that can be precisely tuned through the OPE bridge length in D-OPE-A architectures.

6 OPE-based Photowitches

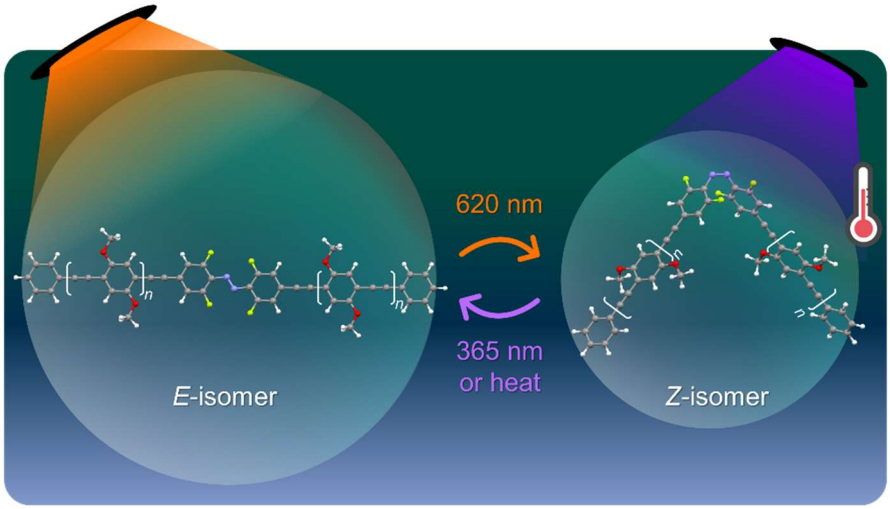

*The Sonogashira precursor **F_4I_2AB** was provided by Petko Stoychev, who also carried out the NMR analysis of the photoswitching behavior under the supervision of PD Dr. Zbigniew Pianowski at the Karlsruhe Institute of Technology.*

6.1 Motivation

As discussed in 2.1.3, the fully π-conjugated backbones of poly-/oligo(phenylene ethynylene)s (PPEs/OPEs) enable efficient electronic delocalization and facilitate a rapid charge and exciton transport on the nanometer scale.[245,246] This "molecular wire" effect manifests as an apparent amplification of the optical or electrochemical readout in sensing applications.[82,102,106,247,248]

Likewise, this amplification concept may also be applied to "size"-based readouts due to the stiffness: By incorporating a photoswitchable unit into the rigid OPE scaffold, the backbone rigidity may be utilized to magnify the geometric change of *E*/*Z* isomerization and translate it into a measurable hydrodynamic response.

Although size-exclusion chromatography (SEC) has been applied to main-chain macromolecular photoswitches, where the pronounced steric and conformational differences between the two isomers influence hydrodynamic volume, the inherent dispersity of polymers caused severe peak overlap, restricting those studies to qualitative confirmation of isomerization rather than quantitative determination of isomer distributions.[249–251] ^{1}H NMR spectroscopy, often regarded as the gold standard for monitoring photoisomerization, provides enriched structural information. However, our previous work in the field of sequence-defined oligomers has uncovered limitations, especially in resolving the sequence of isomers. We have therefore focused on alternative methods like MS fragmentation and SEC to identify isomers.[170,171,189] In the context of sequence-defined macromolecules developed for data storage, side-chain variation alone has proven insufficient to directly resolve differences by SEC, so that destructive methods such as MS fragmentation were often required. The underutilization of SEC can be attributed to excessive main-chain flexibility and the absence of defined secondary structure in typical sequence-defined oligomers.

Herein, we present a series of uniform, sequence-defined OPE molecules with varying length and an azobenzene unit embedded at the central position of the backbone, maximizing the geometric change upon photoisomerization (Figure 53).

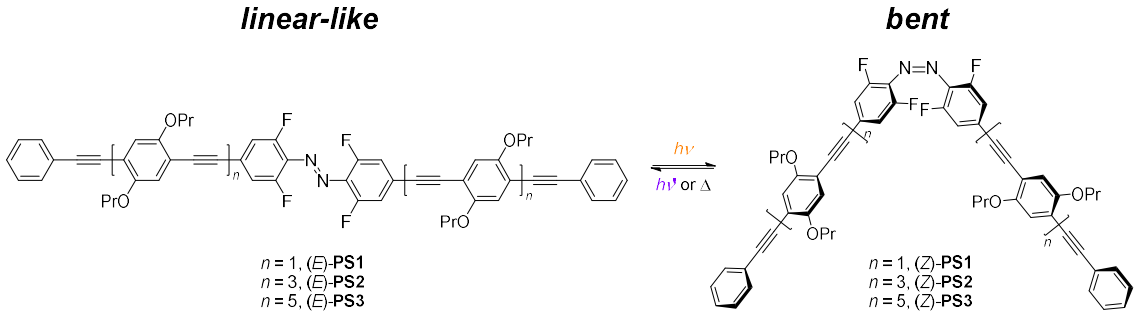

Figure 53. Switch-to-bent: photoisomerization between "linear" E*-isomers and bent* Z*-isomers.*

The lengths of the OPE backbones were varied with the repeating number of propoxylated phenylene ethynylene units by one (**PS1**), three (**PS2**), and five (**PS3**), respectively. The electron-rich OPE backbone in *para*-position to the diazo functionality can reduce the

lifetime of the *Z*-isomer, and thereby compromise the reliability of targeted SEC analysis.[252] Therefore, an *ortho*-tetrafluoroazobenzene (TFAB), reported with significantly enhanced thermal stability of its *Z*-form compared to the unsubstituted analogue, was employed to counterbalance the electronic influence of the OPE and ensure reliable SEC quantification.[253] Furthermore, the molecular design with fluorine substituents allows for rapid determination of the *E*/*Z* ratio by ^{19}F NMR spectroscopy, offering a practical advantage over the more information-rich ^{1}H NMR approach through its spectral simplicity and straightforward analysis.

6.2 Results and Discussion

6.2.1 Synthesis and Initial Characterization

To obtain the target structures, OPE building blocks (**OPE1-3**), constructed as previously described in an iterative synthetic protocol[7] and subsequently attached to the predominantly *E*-configured azobenzene derivative, 1,2-bis(2,6-difluoro-4-iodophenyl)diazene (**F$_4$I$_2$AB**), via Sonogashira cross coupling (Figure 54).

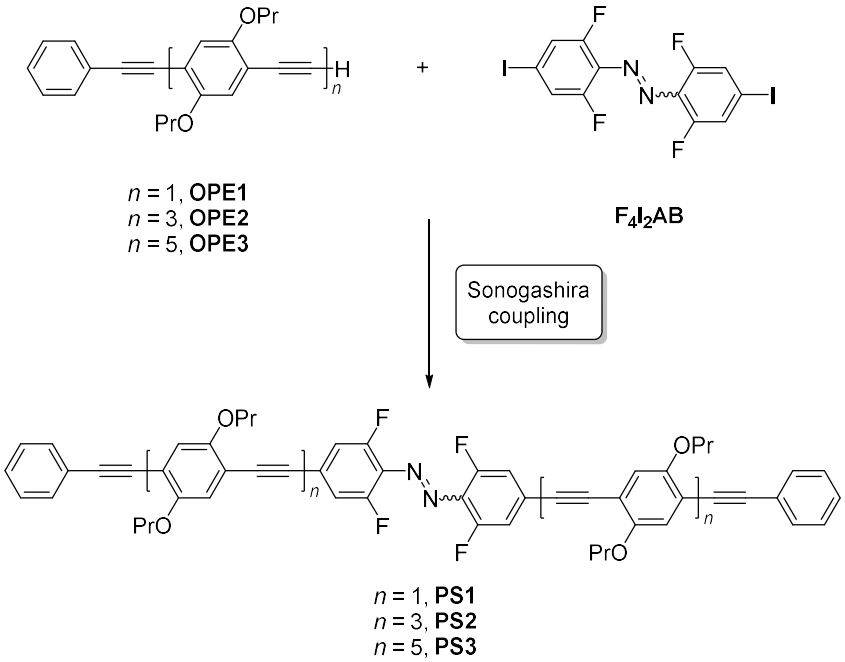

*Figure 54. Synthesis of **PS1-PS3** via Sonogashira cross coupling.*

To minimize undesired photoisomerization during the coupling step, the reactions were carried out under exclusion of light. All three compounds were obtained after flash column chromatography as red powders. The ^{1}H NMR spectra in deuterated chloroform ($CDCl_3$) are compared in Figure 55. The increasing integrals of resonances assigned to the propoxylated units with progressively longer OPE precursors, relative to those of the tetrafluoroazobenzene (TFAB) moiety, indicate the successful Sonogashira coupling.

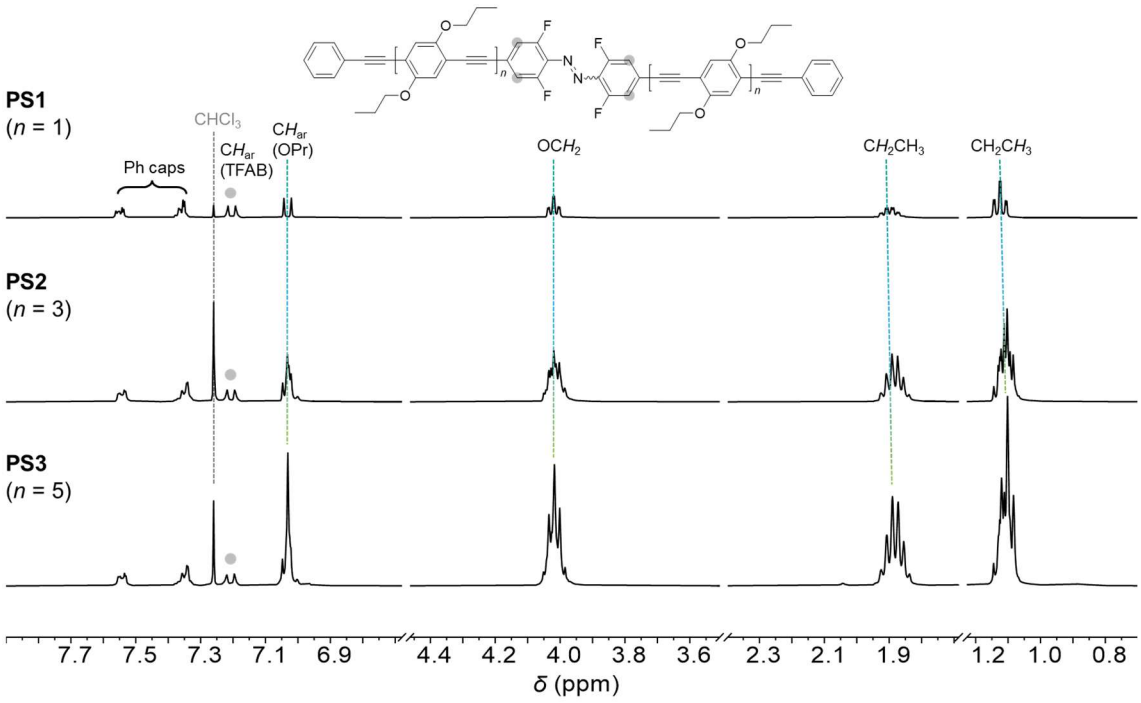

*Figure 55. Stacked ^{1}H NMR spectra of **PS1-PS3** in $CDCl_3$ recorded at 400 MHz. The integrals were normalized to the range of 7.23 – 7.19 ppm, corresponding to the aromatic resonances of the tetrafluoroazobenzene (TFAB) unit, highlighted in grey in the general structure displayed above the spectra. Ph caps = α,ω-phenyl endgroups.*

To investigate the initial degrees of isomerization in the obtained materials, ^{19}F NMR spectroscopy was employed due to its high sensitivity and the distinct chemical shifts of the *E*- and *Z*-isomers.[254] The ^{19}F spectra of **PS1-PS3** are shown in Figure 56a. For all three oligomers, the ^{19}F signal of the *E*-isomer appeared at -120.3 ppm, while that of the *Z*-isomer appeared downfield at -119.1 ppm. Integrations of the peaks revealed the initial *E*-contents of >99%, 98%, and 93% for **PS1**, **PS2**, and **PS3**, respectively.

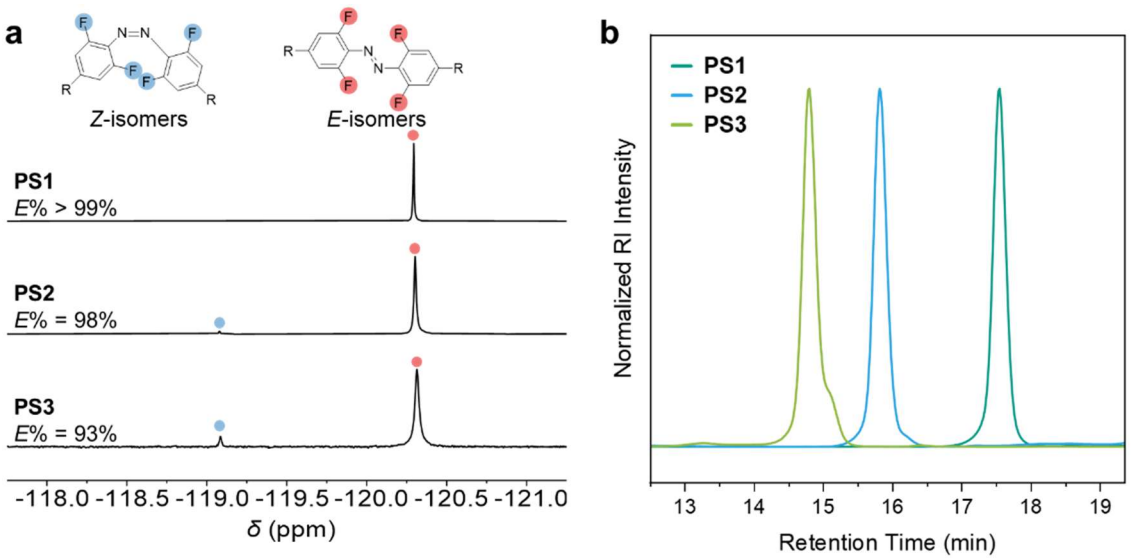

*Figure 56. a) Stacked ^{19}F NMR spectra of **PS1-PS3** in $CDCl_3$ recorded at 376 MHz. b) SEC traces of **PS1-PS3** in THF.*

To confirm these findings and to obtain complementary information on purity and size, the oligomers were further characterized by SEC (Figure 56b). **PS1** exhibited the longest retention time and **PS3** the shortest, in line with the expected order of hydrodynamic volumes of these rod-shaped oligomers. Both **PS1** and **PS2** displayed a single elution peak, consistent with high purity and the high *E*-contents obtained by ^{19}F NMR. In contrast, **PS3** showed a shoulder overlapping with its main elution peak at a slightly higher retention time. This shoulder was assigned to the *Z*-isomer, as its intensity decreased after heating at 50 °C overnight (Figure 57), corresponding the *Z*→*E* back-isomerization process. The retention times shown in Figure 57 differs from those in Figure 56b, as the measurements were conducted on a different SEC instrument. While the absolute values of the retention times are therefore not directly comparable, the relative elution trend remains consistent.

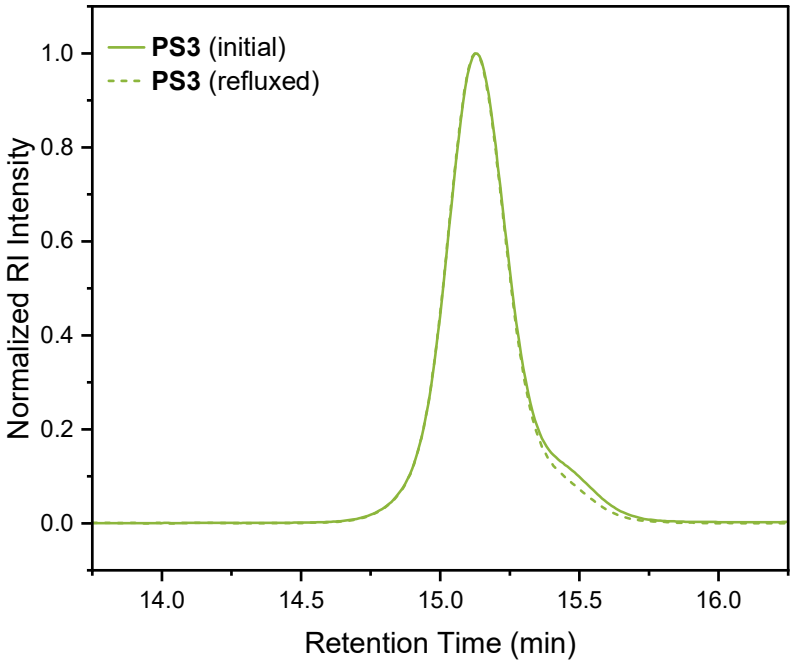

*Figure 57. SEC traces of **PS3** recorded before and after thermal relaxation.*

6.2.2 Characterization of Photoisomerization Behavior

With the aim of applying SEC as a complementary quantification method for *E* and *Z* isomers, samples used in the following experiments were prepared under SEC-compatible conditions (~1 mg/mL in THF). Prior to the photochemical characterization by UV-Vis spectroscopy, the photostationary states (PSS) upon irradiation at wavelengths ranging from 365 nm (UV) to 660 nm (red light) were investigated for all three oligomers. The *Z*-percentage (*Z*%) values in the respective PSS, as determined by ^{19}F NMR spectroscopy, are shown in Figure 58.

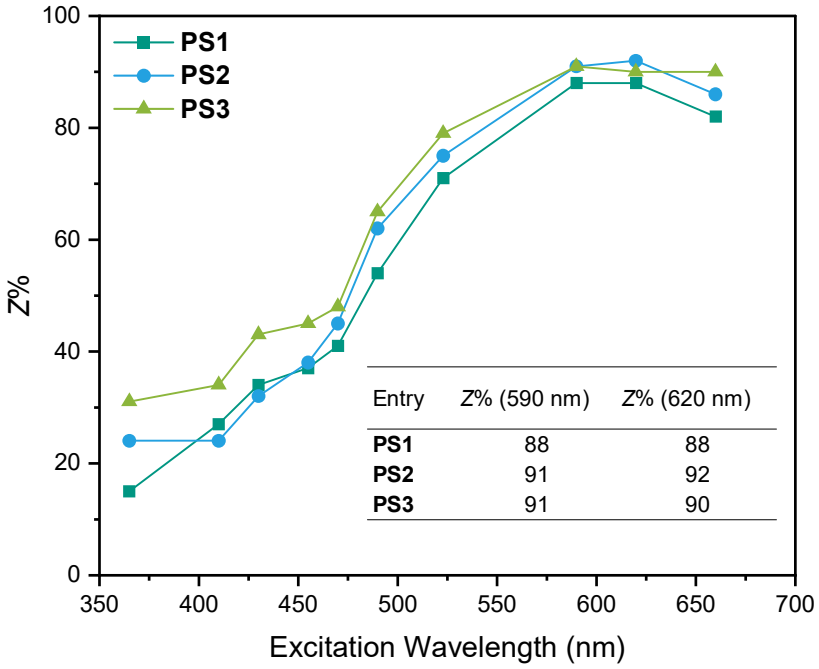

Figure 58. Percentage of Z-isomer (Z%) of photostationary state upon irradiation at different wavelengths (365-660 nm) in 1 mg/mL deuterated THF solution, determined by ^{19}F NMR spectroscopy. Inset: Table of Z% values at 590 nm and at 620 nm.

All three samples reached the highest *Z*% value of ~90% upon irradiation with 590 – 620 nm light. Below this range, especially in the UV to blue light region, **PS3** showed a significantly higher *Z*-content (*Z*%) than the other two derivatives. The OPE switches were further compared to a previously reported system with similar structure (entry **4** in the cited literature) that reached only 22% *Z*-content in the PSS at 436 nm. In contrast, the photoswitches developed in this work exhibited generally higher *Z*-contents at a comparable wavelength of 430 nm (**PS1**: 34%; **PS2**: 32%; **PS3**: 43%).[255] This result may reflect a conjunction degree-dependent photoswitching behavior. However, this issue lies beyond the scope of the present study and was not further investigated.

Next, the photoisomerization process was monitored by the UV-Vis absorption spectroscopy in 20 µM THF solutions (Figure 59). Irradiation at 590 nm was used to trigger the isomerization reaction, as this wavelength was shown to yield the highest Z%

among the tested conditions. The key features of the absorption spectra before and after the irradiation are summarized in Table 5.

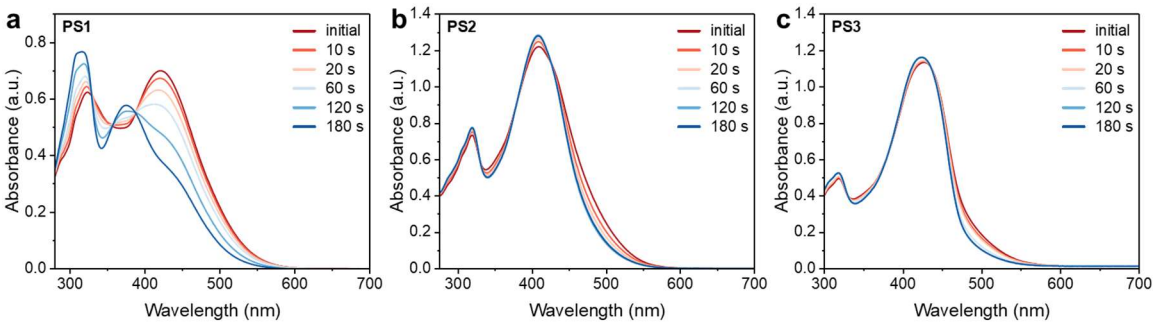

*Figure 59. UV-Vis absorption spectra of **PS1**-**PS3** showing the photoinduced transition from the initial E-isomer state to the E/Z photostationary state after 180 s of irradiation at 590 nm. Spectra were recorded in 20 μM THF solutions.*

Table 5. Key features of the UV-Vis spectra.

Entry	$\lambda_{initial,max}$[a] / nm	$\lambda_{irradiated,max}$[a] / nm
PS1	323 (3.1)	316 (3.8)
	421 (3.5)	375 (2.8)
PS2	319 (3.7)	319 (3.9)
	409 (6.1)	408 (6.4)
PS3	319 (2.5)	318 (2.6)
	427 (5.7)	424 (5.8)

[a] Molar extinction coefficients ($\times 10^4$ M^{-1} cm^{-1}) are given in paratheses.

PS1 showed a clear absorption profile change upon photoisomerization with three isosbestic points at 329 nm, 357 nm and 388 nm, respectively. For the initial dark state (predominantly *E*-form), the lowest-energy absorption maximum appeared at 421 nm. With increasing molar fraction of the *Z*-isomer upon orange light, the intensity of the 421 nm band decreased significantly, along with the formation of a new absorption at 376 nm.

For **PS2** and **PS3**, the photophysical properties are dominated by the longer OPE backbone. Therefore, any significant change in the absorption profile during the photoisomerization process seems to be masked by the strong absorbance of OPE.[7] Nevertheless, the recognizable isosbestic points indicated the isomerization process without detectable side reactions. In both cases, the lowest-energy bands exhibit high absorbance values of approximately 1.2, corresponding to molar extinction coefficients on the order of 6×10^4 M^{-1} cm^{-1}.

To further understand the different behaviors between **PS1** and **PS2**/**PS3** in the UV-Vis spectra, TDDFT calculations were carried out on the optimized ground state geometries at the CAM-B3LYP/6-31G(d,p) level of theory. Since this analysis was primarily directed at the change in the visible absorption spectrum, the discussion focuses on the two lowest vertically excited states, S_1 and S_2, which are presented in Figure 60a.

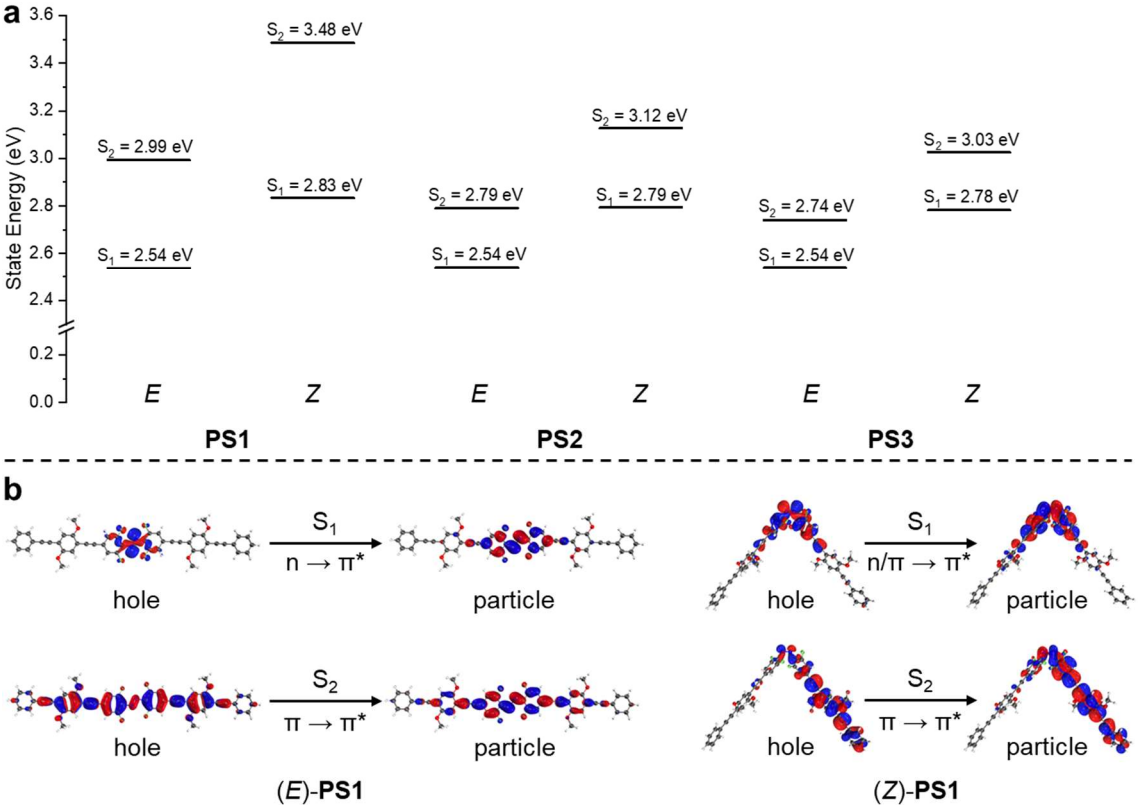

*Figure 60. a) Energy diagrams of calculated S_1 and S_2 states for the E- and Z-isomers of **PS1-PS3** at the CAM-B3LYP/6-31G(d,p) level of theory. b) NTO representations for **PS1**, illustrating the electronic character of S_1 and S_2 in the E- and Z-isomers. Hole and particle orbitals are visualized at an isovalue of 0.02.*

For all *E*-isomers, the S_1 state was predicted at an excitation energy of 2.54 eV corresponding to a "dark" n→π* transition localized primarily on the azobenzene moiety. This assignment is supported by the natural transition orbital (NTO) analysis, as exemplified for **PS1** in **Error! Reference source not found.**b, where the nitrogen lone-pair orbitals are orthogonal to the partially delocalized π* orbitals, resulting in insufficient orbital overlap. In contrast, the "bright" S_2 states correspond to a π→π* transition involving MOs delocalized over the conjugated backbone.

For the *Z*-isomers, both the S_1 and S_2 states are optically "bright" according to the calculations. As illustrated for (*Z*)-**PS1** in Figure 60b, the hole orbital of S_1 exhibits mixed non-bonding (n) and π character, which provides sufficient overlap with the antibonding π* orbital (particle). The S_2 state corresponds to a π→π* excitation that is predominantly localized on one half of the molecule, as a full conjugation across the backbone is disrupted by the bending of the N=N double bond. For **PS2** and **PS3**, the energetic alignment between the S_2 state of the *E*-isomer and the S_1 of the *Z*-isomer may help rationalize the minor change in the absorption maximum of the lowest-energy band (Figure 59 and Table 5).

6.2.3 Development of Quantification Using SEC

To assess the possibility of using SEC as a quantitative read-out of photoisomerization and to benchmark its accuracy against the established NMR approaches, samples irradiated with green light (525 nm) for 30 min in deuterated THF (THF-*d*8, 1 mg/mL) were analyzed on SEC, while the same solutions were measured by ^{1}H and ^{19}F NMR spectroscopy (Figure 61). For completeness, HPLC was also explored as an alternative. However, due to the insufficient separation of the *E*- and *Z*-isomers of **PS*x*** using a typical water/acetonitrile elution gradient, HPLC was considered unsuitable without elaborative method development for these highly conjugated oligomeric systems and was thus not further employed.

In the ^{1}H NMR spectra (Figure 61b-d), the aromatic protons in the TFAB moiety were utilized to estimate the ratio of the *E*- and *Z*-isomers. In the initial **PS1** sample, which contained exclusively the *E*-isomer, the protons of the TFAB unit (highlighted in red) appeared as a singlet at 7.13 ppm in THF-d_8 at 25 °C under the employed acquisition parameters. Upon isomerization, this resonance split into two distinct singlets that shifted upfield to 7.09 ppm and 7.05 ppm. In the higher oligomers **PS2** and **PS3**, the *E*-isomer already exhibited two separate peaks for these protons at 7.11 ppm and 7.13 ppm, most likely attributed to more restricted rotational freedom arising from the extended OPE backbones. In the corresponding *Z*-isomers, both the TFAB resonances and those of several propoxylated phenylene units are shifted upfield, leading to substantial signal overlaps. Thus, the quantification by ^{1}H NMR could only rely on the relative decrease of the *E*-TFAB resonances, which compromises the accuracy of the analysis. As a reference, the multiplet at 7.53 – 7.46 ppm, assigned to the terminal phenyl capping groups, were used for normalization.

In contrast, quantification using ^{19}F NMR spectroscopy was more straightforward, as it displayed non-overlapped signals for the *E*- and *Z*-isomers, allowing for reliable quantification by integration (Figure 61e-g). In parallel, SEC also revealed two partially resolved elution features corresponding to the *E*- and *Z*-isomers of the conjugated oligomers (Figure 61h-j). In the investigated systems, the effects of molecular size and polarity were expected to act in opposite directions. While the higher polarity of the *Z*-isomers would be expected to increase solvation in THF and thus its hydrodynamic volume, the pronounced size compaction dominates, resulting in a smaller hydrodynamic radius. Consequently, the *Z*-isomers eluted at a later retention time, compared to their corresponding *E*-isomers, which are more extended.

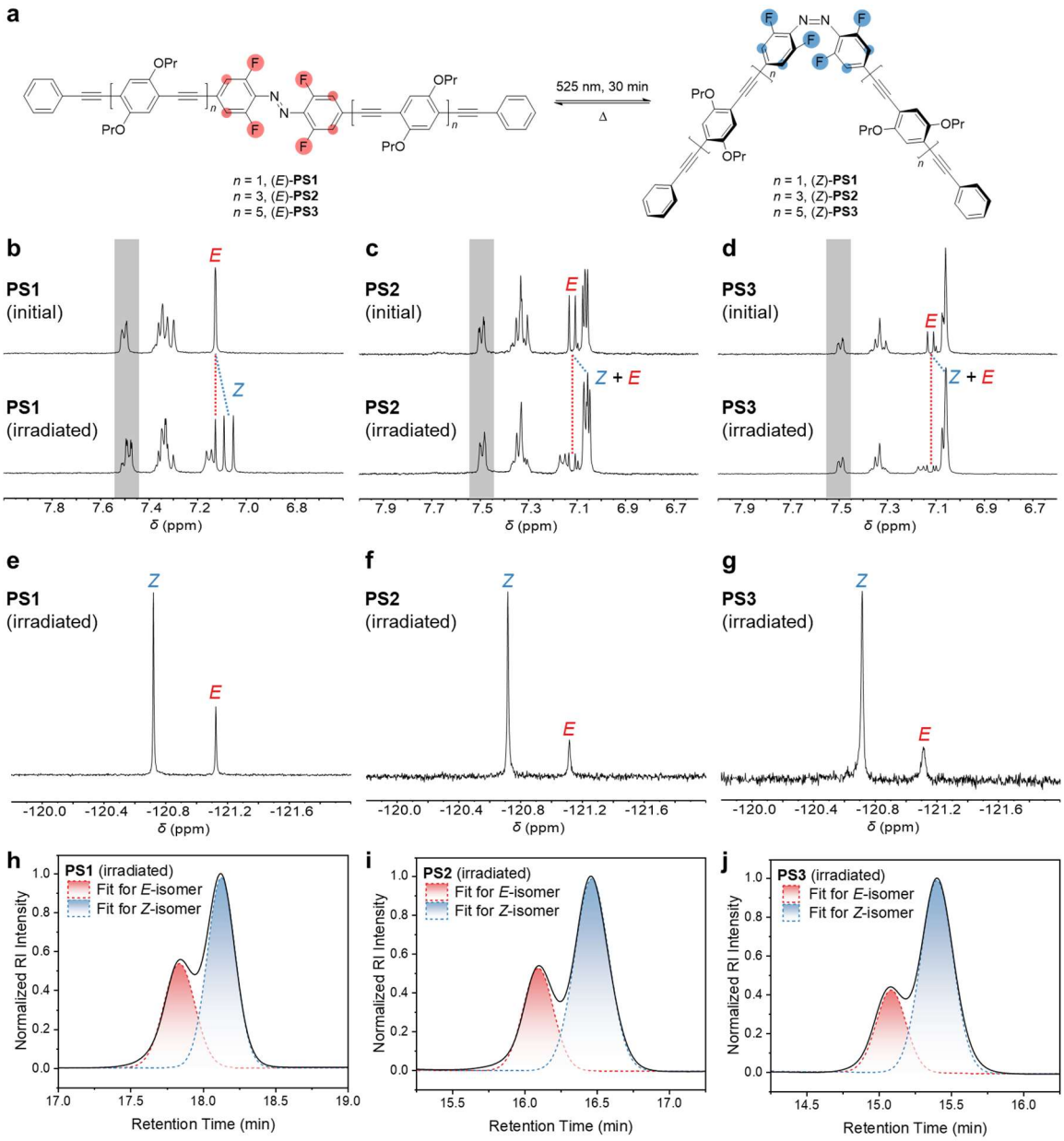

Figure 61. Benchmark of analytical methods for quantifying the photoisomerization of xxx. a) Reaction scheme of E→Z photoisomerization employing 525 nm light. b-d) ^{1}*H NMR spectra of the aromatic region, with the spectra recorded before irradiation shown as reference. The integral of the grey highlighted region, corresponding to the peripheral phenyl groups was normalized. e-g)* ^{19}*F NMR spectra. h-j) SEC traces with deconvoluted peak fitted for the E- and Z-isomers. All samples were dissolved in THF-*d_8 *(1 mg/mL) and filtered.*

The *Z*% values, determined from the previously discussed methods, are summarized in Table 6. Taking the ^{19}F NMR method as a benchmark, the SEC analysis (both by direct integration and by Gaussian deconvolution) reproduced the same increasing trend in

Z-content from **PS1** to **PS3**. However, an underestimation of the *Z*% value by 6-10% relative to ^{19}F NMR was observed consistently. This may point to the bias in the refractive index (RI) detector of the SEC setup. While the RI response is proportional to the concentration (*c*) of each eluting species according to

$$\text{RI Intensity} \propto c \cdot \left(\frac{dn}{dc}\right) \tag{5}$$

differences in specific refractive index increments (*dn*/*dc*) between the *E* and *Z* isomers can lead to unequal responses and thereby distort the apparent isomer ratio. To increase the accuracy of the SEC method, a calibration was performed against the ^{19}F NMR method using five **PS1** mixtures of varying *E*/*Z* composition (Figure 62a,b). The *Z*% values obtained by direct integration and by Gaussian deconvolution were plotted against the corresponding ^{19}F NMR-derived *Z*% values in Figure 62c and d, respectively.

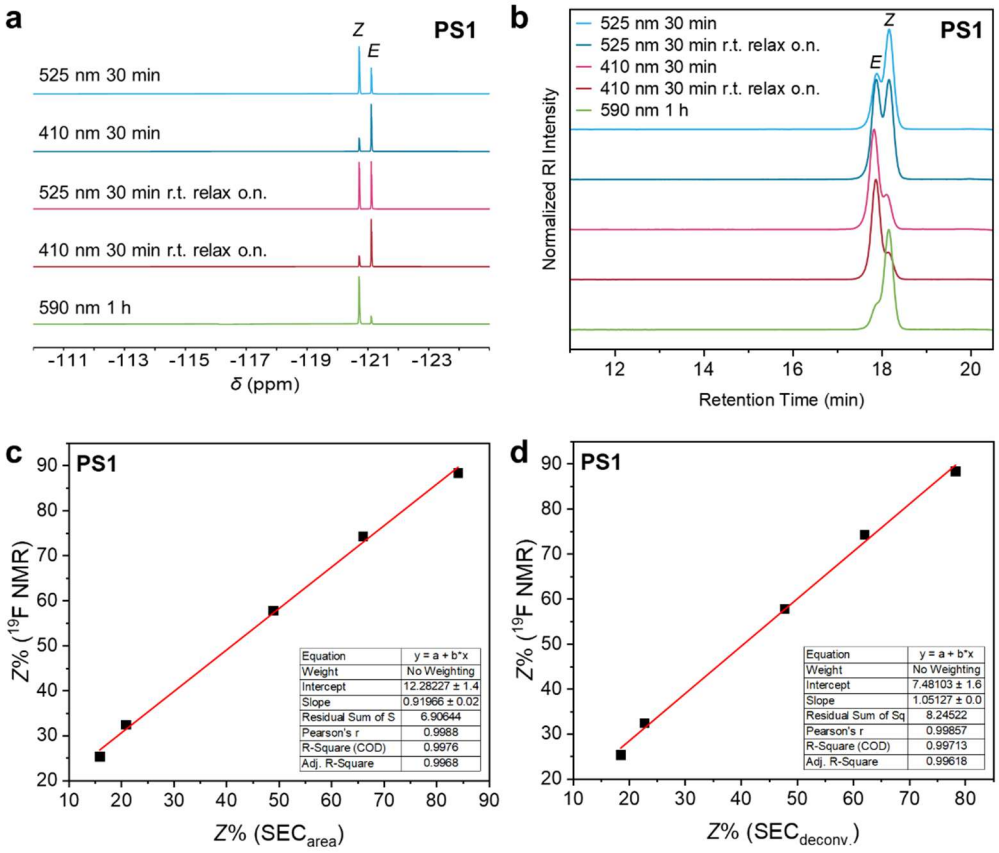

*Figure 62. Calibrations of the RI detector of the SEC setup against ^{19}F NMR for **PS1**. a) ^{19}F NMR spectra of **PS1** under different conditions of in THF-d8. b) SEC traces of corresponding samples. c) Plot of Z% determined by direct integration of SEC peaks against ^{19}F NMR. d) Plot of Z% determined by Gaussian deconvolution of SEC peaks against ^{19}F NMR.*

The R^2 values of both linear fits were close to unity, confirming a reliable linear correlation between the SEC-derived and ^{19}F NMR-determined *Z*% values for the chosen photoswitch molecule **PS1**. In principle, such calibration should be carried out individually for each isomeric pair. However, given the high structural similarity of **PS1**-**PS3**, the calibration fit obtained for **PS1** was applied to **PS2** and **PS3**. The corrected *Z*% values are presented in parentheses alongside the unprocessed data in Table 6. After this correction, the deviation for both **PS2** and **PS3** was reduced to <3%, bringing the SEC results into closer agreement with their ^{19}F NMR references.

Table 6. Z-isomer content (%) determined by ^{1}H NMR, ^{19}F NMR, and SEC.

Entry	^{1}H NMR	^{19}F NMR	SEC_{area} [c]	$SEC_{deconv.}$ [c]
PS1	69[a]	73	66 (73)	62 (73)
PS2	76[b]	78	68 (75)	68 (79)
PS3	67[b]	81	74 (80)	72 (83)

[a] *Z*% determined from the relative increase of the TFAB resonances at 7.09 and 7.05 ppm assigned to the *Z*-isomer.
[b] *Z*% determined from the relative decrease of the TFAB resonances at 7.13 and 7.11 ppm assigned to the *E*-isomer.
[c] Values obtained after calibration against ^{19}F NMR are given in parentheses.

For smaller oligomers **PS1** and **PS2**, ^{1}H NMR analysis agreed within 5% error compared to ^{19}F NMR. However, in the case of **PS3**, ^{1}H NMR suggested a lower *Z*% value than those of **PS1** and **PS2**, which contradicts the trends observed by ^{19}F NMR and SEC. This discrepancy (19% relative to the ^{19}F NMR determined *E*/*Z* ratio) was due to the severe overlap of the signals of *E*- and *Z*-isomers in the ^{1}H NMR spectra, leading to an inaccurate quantification.

Finally, SEC was employed to monitor the thermal back-isomerization. The SEC traces recorded during the thermal relaxation process at 60 °C are shown in Figure 63.

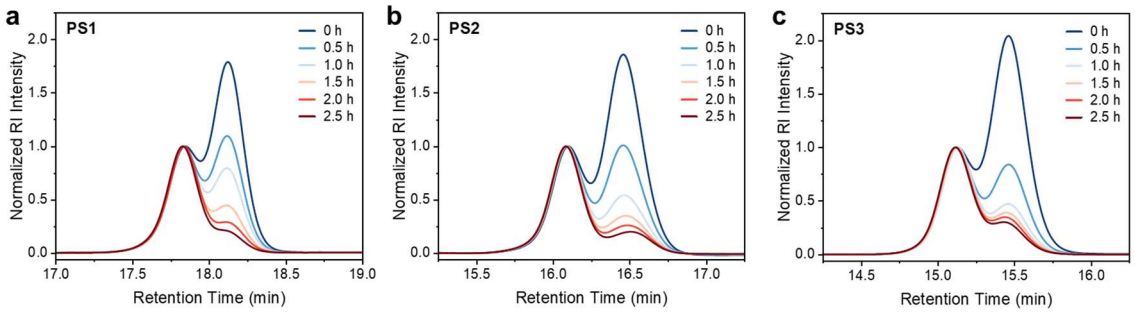

*Figure 63. Thermal relaxation study at 60 °C monitored by SEC for a) **PS1**, b) **PS2**, and c) **PS3**.*

As a first-order reaction, the *Z*-concentration ($[Z]$) in the mixture depending on relaxation time (t) is described by

$$[Z] = [Z_0]e^{-kt} \tag{6}$$

with $[Z_0]$ representing the initial *Z*-concentration and *k* representing the rate constant.[256] Linearization by taking the natural logarithm of $[Z]/[Z_0]$ yields

$$\ln\left(\frac{[Z]}{[Z_0]}\right) = -kt \tag{7}$$

so that k can be obtained from the slope of the linear fit (Figure S35) and the corresponding half-life time $\tau_{1/2}$ is given by

$$\tau_{1/2} = \frac{\ln(2)}{k} \tag{8}$$

The thus extracted $\tau_{1/2}$ values are summarized in Table 7 and compared with those obtained independently by ^{19}F NMR (Figure S36 – Figure S38). Here, the *Z*% results derived from SEC were used without calibration, since in Equation 7 only relative values were required.

Table 7. Comparison of the half-life values ($\tau_{1/2}$) estimated by the ^{19}F NMR spectroscopy and the SEC analysis.

Entry	$\tau_{1/2}$ by ^{19}F NMR/ min	$\tau_{1/2}$ by SEC_{area} / min	$\tau_{1/2}$ by SEC_{deconv} / min
PS1	54	59	68
PS2	65	78	87
PS3	67	84	104

Both the direct integration and the deconvolutional analysis of the SEC elution peaks reproduced the same increasing trend in $\tau_{1/2}$ from **PS1** to **PS3**, consistent with the ^{19}F NMR reference. Considering that the ^{19}F NMR and SEC experiments were performed independently, the deviation of 5-17 min from the integration method to ^{19}F NMR can be regarded acceptable. In contrast, the results derived from the deconvolution approach showed more substantial deviations. Due to the peak overlap, the two elution peaks were most distinguishable at *Z*% values of 30-70% for the investigated isomers. Outside this range, identification and quantification of the minor fraction became less reliable. However, for the investigated OPE-based azobenzene systems with $\tau_{1/2}$ values of approximately 1 h, as determined by ^{19}F NMR, only 2-3 data points could be collected under the employed SEC elution conditions (30 min pro sample). Additional data points often fell outside the reliable *Z*% window of 30-70%, thus limiting the accuracy of the kinetic analysis at 60 °C.

6.3 Summary and Outlook

In this work, three OPE-based azobenzene photoswitches (**PS1**-**PS3**) were synthesized. All three photoswitching oligomers were obtained predominantly in *E*-forms after synthesis and remained responsive to light irradiation up to 620 nm, enabling a maximum *Z*-content of approximately 90%.

The isomerization process was monitored by UV-Vis spectroscopy. While **PS1** exhibited a clear switching profile from *E* to *Z* isomer, the absorption spectra of **PS2** and **PS3** were largely dominated by the elongated OPE backbones.

Quantification of the *E*/*Z* ratio by SEC with an RI detector yielded *Z*% in close agreement with ^{19}F NMR after calibration, with the latter serving as a reference method. This approach could be further simplified by employing a UV detector targeting the isosbestic point of the absorption spectrum, thereby avoiding the need for calibration.

Thermal stability of a PSS was exemplarily assessed for the at 60°C by SEC, which reproduced the expected back-isomerization kinetics, albeit with limited accuracy compared to ^{19}F NMR. It is interesting to note that this thermal back isomerization to the thermodynamic *E*/*Z* equilibrium is clearly size and thus sequence dependent, as evidenced by the increasing half-life times in the series of **PS1** to **PS3**. Further investigations could address unsymmetric sequences incorporating the dynamic azobenzene unit at varied positions, as well as sequences containing multiple photoswitchable units.

7 Conclusions

Based on the synthetic foundations established in previous work in our group,[7,9] this thesis has explored three different systems of sequence-defined conjugated oligomers based on oligo(phenylene ethynylene). The experimental studies were complemented and guided by computational simulations, enabling a comprehensive exploration of their structure-property relationships.

First, donor-acceptor-donor (D-A-D) sequences were introduced to the OPE model systems. While the propoxylated units served simultaneously as weak donors and solubilizing enhancers, the central acceptor was systematically varied, enabling precise tuning of the electronic bandgap. Thus, four **OPE-*x*** emitters were developed, each targeting a distinct emission color in the visible spectrum, spanning from deep blue (407 nm for **OPE-b**) to red (630 nm for **OPE-r**) in toluene. All **OPE-*x*** emitters exhibited high PLQYs exceeding 65%. To investigate the influence of extended conjugation on photophysical properties, the **OPE-*x*'** series comprising four additional compounds with elongated OPE backbones was synthesized and analyzed. Compared to their **OPE-*x*** analogues, the **OPE-*x*'** oligomers displayed narrower emission bands and further enhanced PLQYs. Together with *in-silico* investigations, these results point to a stronger contribution of LE character in the emissive states, arising from the increased length of π-conjugation.

Subsequently, the conjugation length-dependent effect on the excited-state properties was further investigated using a donor-OPE-acceptor (D-OPE-A) system. Herein, the number of the alkoxylated phenylene ethylene (PE) units bridging a di-*tert*-butylcarbazole donor and a triphenyltriazine acceptor was varied. Four new compounds, **PE0**-**PE3**, were synthesized via an iterative decarboxylative coupling strategy. The high purity of these length-defined oligomers was confirmed by SEC to ensure suitability for high-sensitivity photophysical characterizations. Solvent-dependent photophysics were analyzed via Lippert-Mataga plots. A uniform correlation between the solvent orientation polarizability

(Δ*f*) and the Stokes shifts could be concluded for the shorter oligomers **PE0** and **PE1**, yielding a single dipole moment of the first singlet excited state across all tested solvents. With increasing donor-acceptor distance, **PE2** and **PE3** exhibited a two-segment response with two distinct excited-state dipole moments, separated at $\Delta f \approx 0.15$-0.20, indicating a switch from CT-dominated excited-state character in less polar solvents to a stronger LE character in more polar environments. Transient absorption spectroscopy further confirmed the presence of more LE admixture in longer OPE structures. A decreased lifetime of the CT-state was observed with increasing OPE length, providing direct experimental evidence for the growing LE character in the extended oligomers.

The third part of this thesis focused on exploring geometric control in sequence-defined OPE systems by incorporating *ortho*-tetrafluoroazobenzene as a dynamic element capable of reversible *E*/*Z* photoisomerization. Three photoswitchable molecules, **PS1**-**PS3**, which remained responsive to light irradiation up to 620 nm, were introduced. The rigidity of OPE backbones amplified the volume change of linear *E*-form and the bent *Z*-form, rendering the two isomers distinguishable by SEC and enabling their approximate quantification through comparison of the elution peak areas. Benchmarking with ^{19}F NMR revealed that the SEC-derived *E*/*Z* ratios fell within an acceptable range. Application of SEC to monitor thermal relaxation yielded half-lives that followed the trend to those obtained by ^{19}F NMR, further confirming the feasibility of SEC as a complementary method for studying photoisomerization processes.

In conclusion, this thesis advanced the study of OPE-based systems towards a deeper understanding of their photophysics and photochemistry. While previous work within this research group focused primarily on sequencing via side-chain variation and supramolecular assembly,[7,113] the present study extended the field by altering the electronic sequence via targeted donor-acceptor engineering and introducing dynamic geometric modulation to the π-conjugated backbone. In this way, OPEs were confirmed as an excellent model system for elucidating structure-property relationships in conjugated, organic materials.

8 Experimental Section

8.1 Materials

The following chemicals were used as received: acetic anhydride (97%, Sigma-Aldrich) 1,4-benzoquinone (98%, TCI); 3,6-bis(*tert*-butyl)carbazole (98%, ChemPur); [1,1′-bis(diphenylphosphino)ferrocene] dichloropalladium(II) complex with dichloromethane ($Pd(dppf)Cl_2 \cdot CH_2Cl_2$, 98%, fluoro chem); bis(triphenylphosphine)palladium(II) chloride ($Pd(PPh_3)_2Cl_2$, >99.99%, Sigma-Aldrich); 1-bromo-4-fluorobenzene (95%, ChemPur); 1-bromopropane (99%, Sigma-Aldrich); cesium carbonate (Cs_2CO_3, 99.5%, Fisher Chemical); cesium fluoride (CsF, 99.9%, Acros Organics); 9,10-dibromoanthracene (98%, Sigma-Aldrich); copper(I) iodide (CuI, 99.9%, abcr); 1,4-dibromo-2,5-difluorobenzene (98%, BLDpharm); dicyclohexyl(2′,6′-dimethoxy[1,1′-biphenyl]-2-yl)phosphane (SPhos, 98%, Sigma-Aldrich); 4,7-dibromobenzo[*c*][1,2,5]thiadiazole (98%, BLDpharm); 4,9-dibromonaphtho[2,3-*c*][1,2,5]thiadiazole (98%, BLDpharm); dichloromethane (DCM, anhydrous, ≥99.8%, contains 40-150 ppm amylene as stabilizer, Sigma-Aldrich); diisopropylamine (DIPA, >99.5%, Sigma-Aldrich); diisopropylethylamine (DIPEA, >99%, abcr); hydrochloric acid (HCl, 37% solution in water, Acros Organics); potassium hydroxide (KOH, for analysis, Bernd Kraft); sodium hydrogencarbonate ($NaHCO_3$, laboratory reagent grade, Fisher Scientific); sodium hydroxide (NaOH, for analysis, Bernd Kraft); sodium sulfate (Na_2SO_4, pure, Bernd Kraft); tetrahydrofuran (THF, anhydrous, ≥99.5%, Thermo Scientific Chemicals); tetrakis(triphenylphosphine)palladium(0) ($Pd(PPh_3)_4$, 99%, Sigma-Aldrich); triethylamine (TEA, anhydrous, fluoro chem); trimethylsilylacetylene (98%, TCI); toluene (anhydrous, 99.85%, Thermo Scientific Chemicals); tris(dibenzylideneacetone)dipalladium(II) ($Pd_2(dba)_3$, >98%, fluoro chem) zinc bromide ($ZnBr_2$, 99%, abcr). Solvents like acetone, cyclohexane, dichloromethane, ethanol, ethyl acetate, methanol, *n*-pentane were used in HPLC grade without further purification. Flash column chromatography was performed using Silica gel (pore size 60 Å, 230-400 mesh

particle size, 40-63 µm particle size, Sigma-Aldrich), Celite® 545 (Thermo Scientific Chemicals), and quartz sand (glowed and purified with hydrochloric acid, abcr).

(*E*)-1,2-Bis(2,6-difluoro-4-iodophenyl) (**F_4I_2AB**) was provided by Petko Stoychev, which was synthesized following the procedure reported by John and Ling.[257]

The OPE building blocks **OPE1** (**B1**), **OPE2**, and **OPE3** were obtained from archived materials and had been synthesized previously according protocols developed within the group.[7]

8.2 Instrumentation

Nuclear Magnetic Resonance (NMR)

^{1}H and ^{13}C NMR spectra were recorded at the Karlsruhe Institute of Technology (KIT, Germany) on a Bruker Avance 400 NMR instrument at 400 MHz for ^{1}H NMR and 101 MHz for ^{13}C NMR or on a Bruker AVANCE DRX at 500 MHz for ^{1}H-NMR and 126 MHz for ^{13}C NMR. $CDCl_3$, CD_3OD, DMSO-d_6, and THF-d_8 used as solvent. Chemical shifts are presented in parts per million (δ) relative to residual solvent signals: δ = 7.26 ppm (^{1}H, $CDCl_3$) and δ = 77.16 ppm (^{13}C, $CDCl_3$); δ = 3.31 ppm (^{1}H, CD_3OD) and δ = 49.00 ppm (^{13}C, CD_3OD); δ = 2.50 ppm (^{1}H, DMSO-*d*6) and δ = 39.52 ppm (^{13}C, DMSO-*d*6); δ = 1.71 ppm (^{1}H, THF-*d*8) and δ = 25.31 ppm (^{13}C, THF-*d*8). The spin multiplicity and corresponding signal patterns were abbreviated as follows: s = singlet, d = doublet, t = triplet, q = quartet, quint = quintet, sext = sextet, m = multiplet, dd = doublet of doublets, and br = broad signal. Coupling constants (*J*) are reported in Hertz (Hz). All measurements were recorded in a standard fashion at 25 °C unless otherwise stated. Full assignment of structures was aided by 2D NMR analysis (COSY, HSQC and HMBC).

Orbitrap Electrospray-Ionization Mass Spectrometry (ESI-MS)

Mass spectra were recorded on a Q Exactive (Orbitrap) mass spectrometer (Thermo Fisher Scientific, San Jose, CA, USA) equipped with an atmospheric pressure ionization

source operating in the nebulizer assisted electrospray mode. The instrument was calibrated in the m/z-range 150-2000 using a standard containing caffeine, Met-Arg-Phe-Ala acetate (MRFA) and a mixture of fluorinated phosphazenes (Ultramark 1621, all from Sigma-Aldrich). A constant spray voltage of 3.5 kV, a dimensionless sheath gas of 6, and a sweep gas flow rate of 2 were applied. The capillary voltage and the S-lens RF level were set to 68.0 V and 320 °C, respectively.

Thin Layer Chromatography (TLC)

All TLC experiments were performed on silica gel coated aluminum foil (silica gel 60 F_{254}, SIGMA-ALDRICH). Compounds were visualized first by fluorescence quenching ($\lambda = 254$ nm and 365 nm) or staining with Seebach-solution (mixture of phosphomolybdic acid hydrate, cerium(IV)-sulfate, sulfuric acid and water).

Preparative Thin Layer Chromatography (prep-TLC)

Prep-TLC was performed on glass-backed silica gel 60 F_{254} plates (20 × 20 cm, 2 mm thickness, MACHEREY-NAGEL). The crude material was applied as a narrow band approximately 3 cm from the bottom edge of the plate. Plates were developed using a mixture of cyclohexane/dichloromethane as the eluent. The eluent composition was optimized based on analytical TLC to achieve sufficient separation between the target product and impurities. After development, the product band was visualized under UV light (254 nm), scraped off, and taken off with dichloromethane (3 × 50 mL). The combined extracts were filtered and concentrated under reduced pressure to afford the purified compound.

Flash Column Chromatography

Flash column chromatography was performed on silica gel (see description above) as the stationary phase packed using the chosen eluent under positive pressure. The crude products were loaded onto the column as a concentrated solution in a minimal volume of eluent or adsorbed onto Celite® for dry loading.

For automatic flash column chromatography, a Biotage® Isolera™ One Flash Column equipped with a UV-Vis detector (200 × 800 nm) with Biotage® Sfär Silica HC Duo Columns was used. All solvents were used in HPLC grade.

Size-Exclusion Chromatography (SEC)

The SEC measurements were performed on two different systems: a Shimadzu system equipped with an isocratic pump (LC-20AD), a refractive index detector (RID-20A, 24 °C), an autosampler (SIL-20A), and a Varian column oven (510, 50 °C). Separation was achieved using a three-column setup consisting of one SDV 3 µm, 8 × 50 mm precolumn and two SDV 3 µm, 1000 Å, 3 × 300 mm columns (PSS, Germany). Tetrahydrofuran (THF) stabilized with 250 ppm butylated hydroxytoluene (BHT, ≥99.9%, Sigma-Aldrich) was employed as the eluent at a flow rate of 1.0 mL min^{-1}. Calibration was performed with eight narrow polymethyl methacrylate (PMMA) standards ranging from 102 to 58 300 Da.

For Chapter 6, the SEC measurements shown in Figure 56 were performed in THF on a PSS SECcurity^2 GPC system based on Agilent infinity 1260 II hardware. The system was equipped with an autosampler SECcurity^2, a SECcurity^2 isocratic pump, a column oven (Bio)SECcurity^2 column compartment TCC6500, and a refractive index detector SECcurity^2 RI. Analysis was performed using two PSS SDV analytical columns (3 µm, 300 × 8.0 mm^2, 1000 Å) with a PSS SDV analytical precolumn (3 µm, 50 × 8.0 mm^2). The flow rate for measurements was set to 1 mL·min^{-1}. The system was calibrated with narrow linear poly(methyl methacrylate) standards (Polymer Standards Service, PSS, Germany) ranging from 102 to 62200 Da.

Infrared Spectroscopy (IR)

The infrared spectra were recorded on a Bruker Alpha-p spectrometer equipped with attenuated total reflection (ATR) technology in the range of 4000 – 500 cm^{-1}, using 24 scans per measurement at a resolution of 4 cm^{-1}.

UV-Vis spectroscopy

The UV-Vis spectra were recorded at 20 °C using a Cary 3500 UV-Vis spectrophotometer equipped with a multicell Peltier temperature controller. All spectra were background-corrected against the corresponding solvent baseline.

Photoluminescence spectroscopy

The photoluminescence spectra were recorded on a Jobin-Yvon Fluoromax-4 fluorimeter equipped with a Peltier element (LFI3751) at 20 °C. Spectra were corrected for Raman scattering of the pure solvent. Calibration was performed using the Raman peak of water.

Quantum Yield Determination

The absolute quantum yields (Φ_{PL}) were determined in dilute, non-degassed toluene solution using a Quantaurus QY C11347 spectrometer (Hamamatsu). The excitation wavelength was selected based absorption maxima.

8.3 Synthetic procedures

All the procedures described in Section 8.3.1 were adopted from previously reported methods, with references provided accordingly. Structural verification was carried out by ^{1}H NMR spectroscopy. Procedures for the novel molecules presented in this thesis are provided in Section 8.3.2-8.3.4. Structural elucidation was performed using ^{1}H and ^{13}C NMR spectroscopy, IR spectroscopy, and HRMS analysis; for fluorine-containing compounds, ^{19}F NMR spectroscopy was additionally employed. The corresponding ^{1}H NMR spectra are included directly after the respective procedures.

8.3.1 Modification of OPE Building Blocks

2-Bromobenzene-1,4-diol (compound **1)**

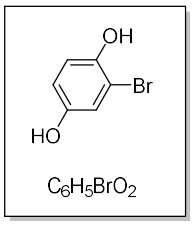

The title compound was synthesized in two steps from 1,4-benzoquinone, following a reported protocal.[258]

1,4-Benzoquinone (8.00 g, 74.0 mmol, 1.00 equiv.) was added to a suspension of anhydrous zinc bromide (20.8 g, 92.5 mmol, 1.25 equiv.) in acetic anhydride (10.4 mL, 22.7 g, 110 mmol) at 100 °C and stirred for 3 h. After cooling, the reaction mixture was poured into water (50 mL), filtrated, and recrystallized in ethanol/water (1:1). The white crystalline solid was given to a solution of sodium hydroxide (8.88 g, 222 mmol, 3.00 equiv.) in 400 mL water. The mixture was stirred at room temperature for 18 h, then acidified with concentrated hydrochloric acid to pH 6. The solution was extracted with diethyl ether (3 × 150 mL). The combined organic layers were washed with brine (200 mL), then dried over anhydrous sodium sulfate. After removal of solvent under reduced pressure the product was yielded as a light brown solid (8.81 g, 46.2 mmol, 63%).

TLC (cyclohexane/DCM 7:3): R_f = 0.63.

^{1}H NMR (400 MHz, CD_3OD): δ (ppm) = 6.90 (d, J = 2.9 Hz, 1H, H_{ar}), 6.73 (d, J = 8.7 Hz, 1H, H_{ar}), 6.61 (dd, J = 8.7, 2.9 Hz, 1H, H_{ar}).

^{13}C NMR (101 MHz, CD_3OD): δ (ppm) = 152.00, 148.22, 120.25, 117.73, 116.36, 110.71.

HRMS (ESI, m/z): $[M+H]^+$ calcd for $C_6H_5BrO_2$ 188.9546; found 188.9545.

IR (ATR): $\tilde{\nu}$ (cm^{-1}) = 3205 (m), 3182 (m), 3112 (m), 3061 (w), 3044 (w), 2966 (w), 2923 (w), 2886 (w), 2859 (w), 2849 (w), 2841 (w), 2832 (w), 2816 (w), 2779 (w), 2744 (w), 2668 (w), 2577 (w), 2569 (w), 1598 (w), 1518 (w), 1448 (vs), 1393 (w), 1370 (m), 1362 (m), 1275 (w), 1228 (vs), 1197 (vs), 1135 (w), 1123 (m), 1037 (s), 893 (m),

876 (w), 854 (s), 817 (m), 806 (m), 771 (vs), 724 (w), 699 (w), 677 (m), 666 (m), 642 (m), 631 (m), 623 (m), 572 (s), 541 (m), 525 (s), 518 (s), 483 (m), 448 (w), 438 (w), 430 (w).

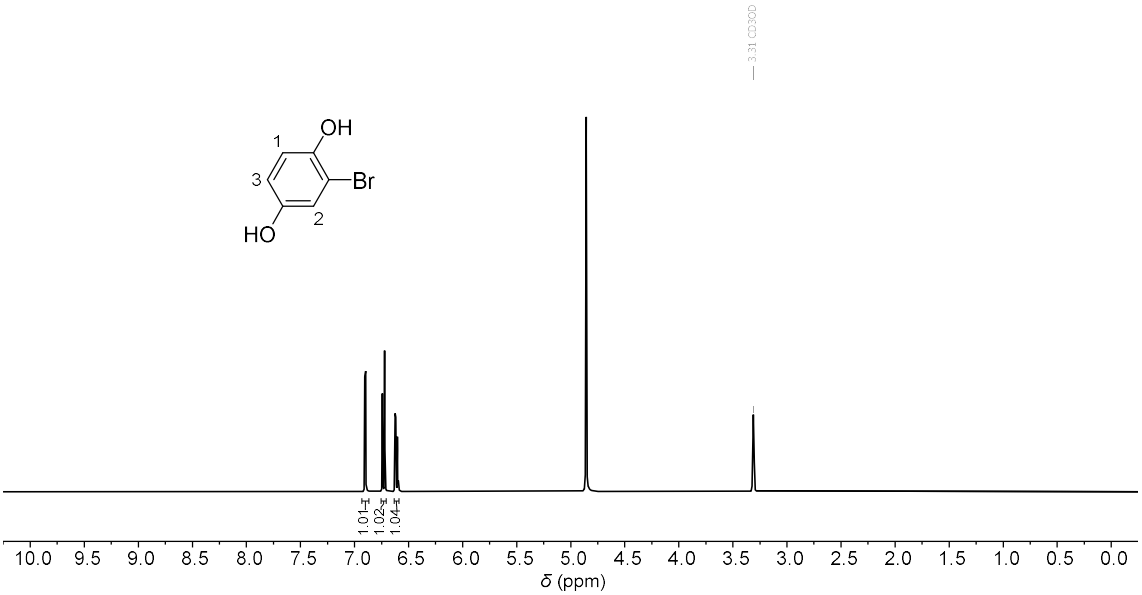

*Figure S1. ^{1}H NMR spectrum of compound **1**, measured in CD_3OD at 400 MHz.*

2-Bromo-1,4-dipropoxybenzene (compound **2)**

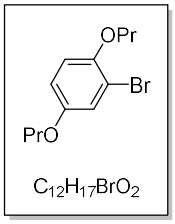

The title compound was synthesized via a Williamson ether-synthesis according to a reported procedure.[9]

Compound **1** (3.78 g, 20.0 mmol, 1.00 equiv.) was dissolved in 20 mL absolute ethanol. KOH (2.81 g, 50.0 mmol, 2.50 equiv.) was added and the mixture was stirred for 30 min under reflux. Subsequently, 1-bromopropane (3.53 mL, 6.15 g, 50.0 mmol, 2.50 equiv.) was added over a 50-minute period and stirred under reflux for another 2 h. Ethanol was removed under reduced pressure and the residue was taken up in 50 mL DCM. The organic phase was washed with water (3 × 50 mL) and saturated $NaHCO_3$ solution (50 mL) and dried over anhydrous Na_2SO_4. The solvent was removed under reduced pressure and the crude product was purified via flash column chromatography (cyclohexane/ethyl acetate 40:1) to yield a colorless liquid (3.91 g, 14.3 mmol, 72%).

TLC (cyclohexane/ethyl acetate 20:1): R_f = 0.53.

^{1}H NMR (400 MHz, $CDCl_3$): δ (ppm) = 7.11 (d, J = 2.7 Hz, 1H, CH_{ar}), 6.83 (d, J = 8.9 Hz, 1H, CH_{ar}), 6.79 (dd, J = 8.9, 2.7 Hz, 1H, CH_{ar}), 3.92 (t, J = 6.5 Hz, 2H, OCH_2), 3.85 (t, J = 6.6 Hz, 2H, OCH_2), 1.83 (overlapped, 2H, $CH_2CH_2CH_3$), 1.76 (overlapped, 2H, $CH_2CH_2CH_3$), 1.06 (t, J = 7.4 Hz, 3H, CH_2CH_3), 1.02 (t, J = 7.4 Hz, 3H, CH_2CH_3).

^{13}C NMR (101 MHz, $CDCl_3$): δ (ppm) = 153.73, 149.90, 119.66, 114.90, 114.57, 112.95, 71.85, 70.49, 22.80, 22.73, 10.71, 10.62.

HRMS (ESI, m/z): $[M]^+$ calcd for $C_{12}H_{17}BrO_2$ 272.0406; found 272.0404.

IR (ATR): $\tilde{\nu}$ (cm^{-1}) = 2964 (w), 2935 (w), 2878 (w), 1604 (vw), 1574 (vw), 1491 (vs), 1467 (s), 1388 (w), 1269 (s), 1205 (vs), 1148 (vw), 1135 (vw), 1107 (vw), 1065 (m), 1049 (m), 1035 (w), 1022 (w), 979 (vs), 909 (vw), 884 (w), 860 (w), 841 (w), 798 (w), 765 (vw), 736 (w), 677 (vw), 440 (vw).

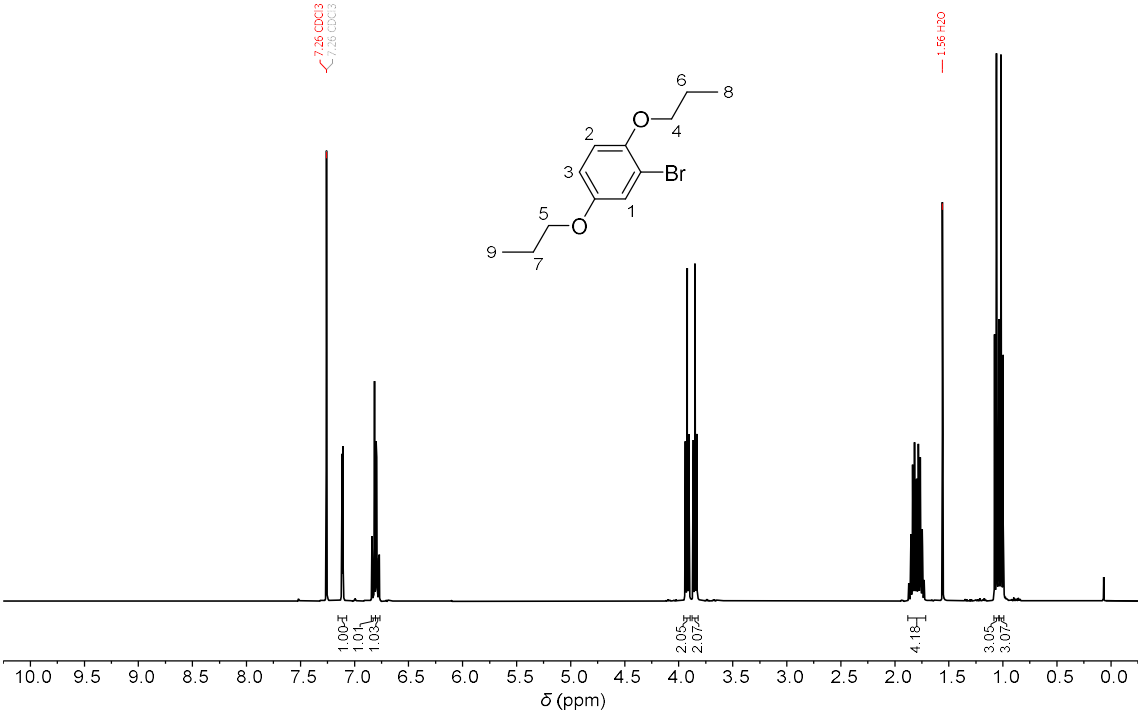

*Figure S2. ^{1}H NMR spectrum of compound **2**, measured in $CDCl_3$ at 400 MHz.*

((2,5-Dipropoxyphenyl)ethynyl)trimethylsilane (compound **3)**

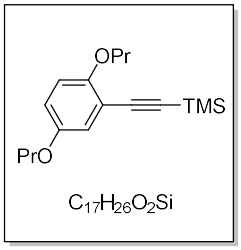

The title compound was synthesized according to an adapted literature procedure for Sonogashira cross coupling.[259]

Compound **2** (1.12 g, 4.10 mmol, 1.00 equiv.), copper(I) iodide (39.0 mg, 205 µmol, 0.05 equiv.), and $Pd(PPh_3)_2Cl_3$ (78.0 mg, 103 µmol, 0.025 equiv.) were degassed and dissolved in 10 mL anhydrous diisopropylamine and stirred at 50 °C for 15 min. Trimethylsilylacetylene (0.68 mL, 0.48 g, 1.2 equiv.) was added dropwise under argon atmosphere and the reaction mixture was stirred at 80°C for 20 h. After cooling down to room temperature, the mixture was filtered through a pad of Celite® and washed with diethyl ether. The solvent was removed under reduced pressure. The residue was purified via flash column chromatography (cyclohexane → cyclohexane/ethyl acetate 95:5). The title compound was obtained as a white wax (955 mg, 3.29 mmol, 80%).

TLC (cyclohexane/ethyl acetate 20:1): R_f = 0.36.

^{1}H NMR (400 MHz, $CDCl_3$): δ (ppm) = 6.96 (d, J = 2.9 Hz, 1H, H_{ar}), 6.82 (dd, J = 8.9 Hz, J = 2.8 Hz, 1H, H_{ar}), 6.77 (d, J = 8.9 Hz, 1H, H_{ar}), 3.93 (t, J = 6.4 Hz, 2H, OCH_2CH_2), 3.86 (t, J = 6.6 Hz, 2H, OCH_2CH_2), 1.84 (h, J = 5.9 Hz, 2H, $CH_2CH_2CH_3$), 1.77 (h, J = 7.1 Hz, 2H, $CH_2CH_2CH_3$), 1.08 (t, J = 7.4 Hz, 3H, CH_2CH_3), 1.02 (t, J = 7.4 Hz, 3H, CH_2CH_3), 0.26 (s, 9H, $SiCH_3$).

^{13}C NMR (126 MHz, $CDCl_3$): δ (ppm) = 154.79, 152.82, 118.77, 117.12, 114.32, 113.59, 101.51, 98.34, 71.34, 70.33, 22.92, 22.76, 10.68, 10.63, 0.14.

HRMS (ESI, m/z): $[M]^+$ calcd for $C_{17}H_{26}O_2Si$ 290.1702; found 290.1692.

IR (ATR): $\tilde{\nu}$ (cm^{-1}) = 2962 (w), 2937 (vw), 2900 (vw), 2878 (vw), 2154 (vw), 1602 (vw), 1574 (vw), 1495 (w), 1469 (w), 1411 (vw), 1388 (w), 1306 (vw), 1271 (w), 1263 (w), 1249 (w), 1226 (m), 1209 (w), 1168 (w), 1129 (w), 1119 (w), 1065 (w), 1049 (w), 1024

(w), 993 (w), 979 (w), 948 (w), 839 (vs), 757 (m), 722 (vw), 697 (w), 654 (w), 625 (vw), 541 (vw).

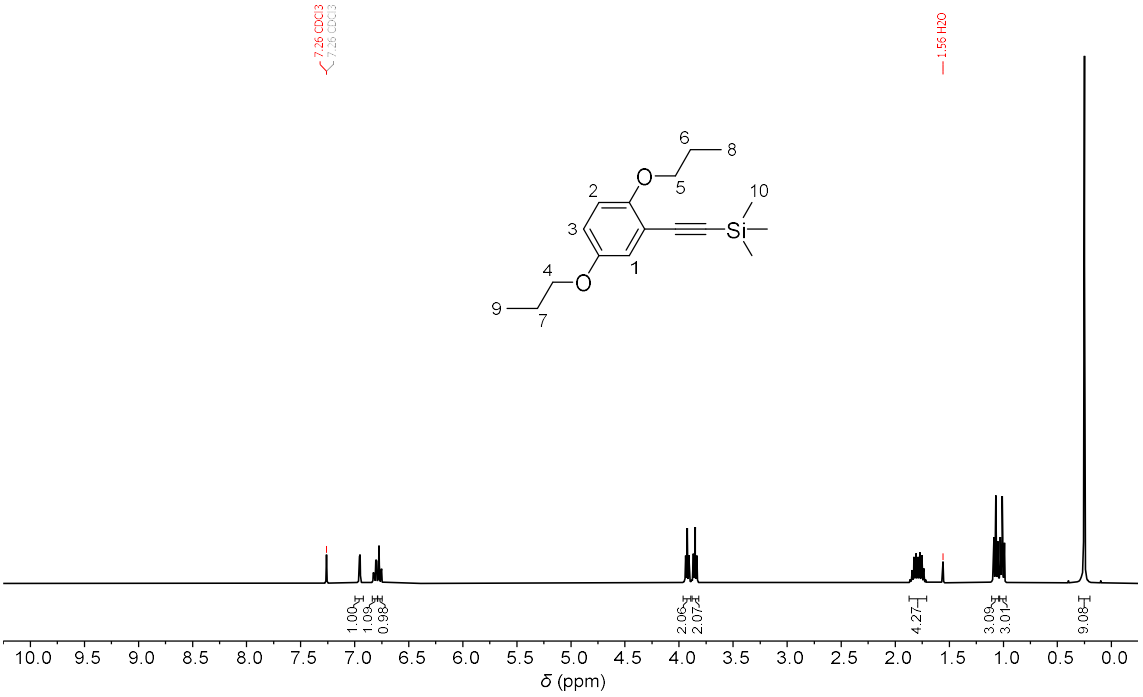

*Figure S3. ^{1}H NMR spectrum of compound **3**, measured in $CDCl_3$ at 400 MHz.*

1-Bromo-4-iodo-2,5-dipropoxybenzene (compound **4)**

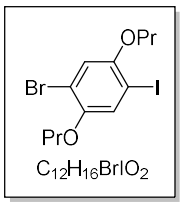

The title compound was synthesized according to a reported procedure.[9]

Periodic acid (1.84 g, 8.09 mmol, 0.34 eq.), iodine (4.05 g, 15.9 mmol, 0.67 eq.), and compound **3** (6.50 g, 23.8 mmol, 1.00 equiv.) were stirred at 65 °C for 4 h. After quenching with 250 mL aqueous potassium metabisulfite (10.6 g, 47.8 mmol, 2.00 equiv.), the precipitate was washed with methanol and dissolved in dichloromethane. The solution was filtered, and the filtrate was concentrated under reduced pressure. The residue was purified by recrystallization from methanol to yield the product as a white solid (8.55 g, 21.4 mmol, 90%).

TLC (cyclohexane/ethyl acetate 20:1): R_f = 0.65.

^{1}H NMR (400 MHz, $CDCl_3$): δ (ppm) = 7.55 (s, 1H, H_{ar}), 7.53 (s, 1H, H_{ar}), 4.19 (t, J = 6.5 Hz, 2H, OCH_2CH_2), 4.18 (t, J = 6.4 Hz, 2H, OCH_2CH_2), 2.17 – 2.03 (m, 4H, $CH_2CH_2CH_3$), 1.35 (overlapped, 3H, CH_2CH_3), 1.33 (overlapped, 3H, CH_2CH_3).

^{13}C NMR (101 MHz, $CDCl_3$): δ (ppm) = 152.66, 150.55, 124.44, 117.23, 112.69, 84.93, 71.99, 71.93, 22.72, 10.84, 10.67.

HRMS (ESI, m/z): $[M]^+$ calcd for $C_{12}H_{16}BrIO_2$ 397.9373, found 397.9370.

IR (ATR): $\tilde{\nu}$ (cm^{-1}) = 2962 (w), 2911 (w), 2871 (w), 1489 (s), 1467 (m), 1452 (vs), 1395 (m), 1376 (w), 1353 (vs), 1267 (m), 1244 (w), 1207 (vs), 1127 (w), 1059 (vs), 1039 (s), 1008 (vs), 909 (m), 850 (vs), 831 (w), 800 (vs), 771 (vs), 627 (w), 438 (w).

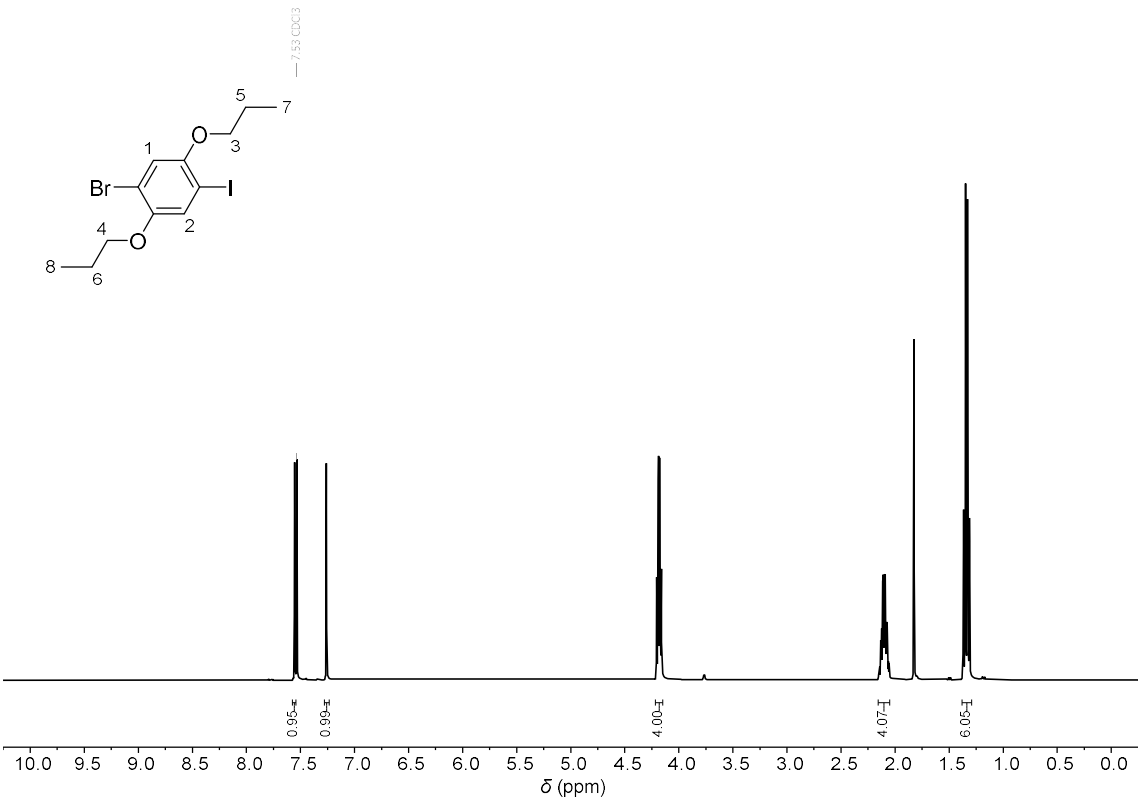

*Figure S4. ^{1}H NMR spectrum of compound **4**, measured in $CDCl_3$ at 400 MHz.*

((4-Bromo-2,5-dipropoxyphenyl)ethynyl)trimethylsilane (compound **5)**

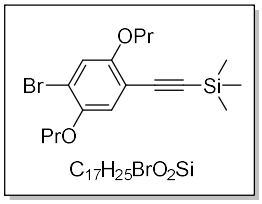

The title compound was synthesized following the procedure reported by Meier *et al.*[9]

Compound **4** (4.50 g, 11.2 mmol, 1.00 equiv.), copper(I) iodide (215 mg, 1.12 mmol, 0.10 equiv.) and $PdCl_2(PPh_3)_2$ (396 mg, 564 µmol, 0.05 equiv.) were degassed and added to 80 mL diisopropylamine (56.8 g, 561 mmol, 50.0 equiv.) under argon flow. At 0°C, trimethylsilylacetylene (1.56 mL, 1.11 g, 11.3 mmol, 1.01 equiv.) was added dropwise. The reaction mixture was stirred for 30 min at 0°C and then for 2 h at room temperature. After filtration through a pad of Celite® and washed with diethyl ether. The volatiles were removed under reduced pressure and the residue was purified by flash column chromatography (cyclohexane/DCM 9:1) to yield the title compound as a white solid (3.92 g, 10.6 mmol, 93%).

TLC (cyclohexane/ethyl acetate 20:1): R_f = 0.65.

^{1}H NMR (400 MHz, $CDCl_3$): δ (ppm) = 7.05 (s, 1H, H_{ar}), 6.94 (s, 1H, H_{ar}), 3.92 (t, J = 6.5 Hz, 2H, OCH_2), 3.91 (t, J = 6.4 Hz, 2H, OCH_2), 1.89 – 1.75 (m, 4H, $CH_2CH_2CH_3$), 1.07 (t, J = 7.4 Hz, 2H, CH_2CH_3), 1.04 (d, J = 7.4 Hz, 2H, CH_2CH_3), 0.25 (s, 9H, $SiCH_3$).

^{13}C NMR (101 MHz, $CDCl_3$): δ (ppm) = 154.87, 149.46, 118.25, 118.06, 113.73, 112.66, 100.73, 99.39, 71.69, 71.43, 22.80, 22.73, 10.68, 10.62, 0.07.

HRMS (ESI, m/z): $[M+H]^+$ calcd for $C_{17}H_{25}BrO_2Si$ 369.0880, found 369.0874.

IR (ATR): $\tilde{\nu}$ (cm^{-1}) = 2958 (m), 2911 (w), 2900 (w), 2874 (w), 2162 (w), 1504 (m), 1489 (s), 1458 (s), 1421 (vw), 1397 (w), 1380 (s), 1372 (s), 1292 (vw), 1267 (m), 1255 (m), 1244 (m), 1216 (vs), 1203 (vs), 1166 (m), 1127 (w), 1041 (s), 1033 (m), 1018 (vs), 981 (w), 907 (w), 858 (vs), 831 (vs), 757 (vs), 697 (w), 669 (m), 642 (m), 613 (w), 570 (w), 502 (w), 494 (w), 471 (vw).

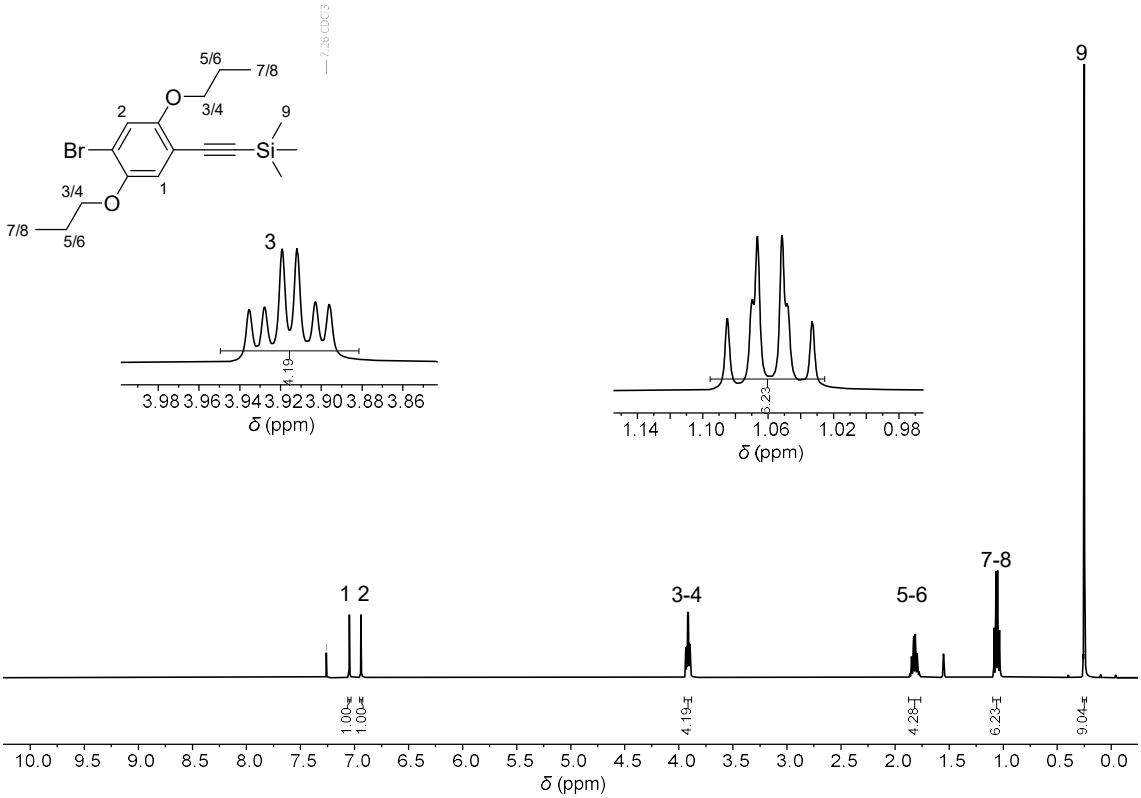

*Figure S5. ^{1}H NMR spectrum of compound **5**, measured in $CDCl_3$ at 400 MHz.*

Ethyl 3-(4-bromo-2,5-dipropoxyphenyl)propiolate (compound **6)**

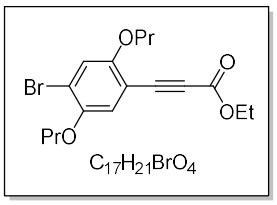

The title compound was synthesized following the procedure reported by Meier *et al.*[9]

Compound **5** (3.50 g, 9.47 mmol, 1.00 equiv.) and cesium fluoride (1.73 g, 11.4 mmol, 1.20 equiv.) were degassed, backfilled with CO_2, and dissolved in anhydrous DMSO (30 mL). The mixture was stirred at room temperature for 3 h, after which iodoethane (1.00 mL, 1.77 g, 11.4 mmol, 1.00 equiv.) was added dropwise. After overnight stirring at room temperature, the reaction was quenched with saturated ammonium chloride solution (150 mL). The mixture was extracted with ethyl acetate (3 × 150 mL). The combined organic layers were washed with water (150 mL) and brine (150 mL), drying over Na_2SO_4, and concentrated under reduced pressure. Purification by flash column chromatography (cyclohexane/ethyl acetate 40:1 → 30:1) yielded the title compound as a white solid (2.80 g, 7.58 mmol, 80%).

TLC (cyclohexane/ethyl acetate 40:1): R_f = 0.18.

^{1}H NMR (400 MHz, $CDCl_3$): δ (ppm) = 7.11 (s, 1H, H_{ar}), 7.01 (s, 1H, H_{ar}), 4.29 (q, J = 7.1 Hz, 2H, OCH_2CH_3), 3.94 (overlapped t, J = 6.3 Hz, 2H, OCH_2CH_2), 3.91 (overlapped t, J = 6.5 Hz, 2H, OCH_2CH_2), 1.94 – 1.74 (m, 4H, $CH_2CH_2CH_3$), 1.34 (t, J = 7.1 Hz, 3H, CH_2CH_3), 1.06 (t, J = 7.4 Hz, 3H, CH_2CH_3), 1.06 (t, J = 7.4 Hz, 3H, CH_2CH_3).

^{13}C NMR (101 MHz, $CDCl_3$): δ (ppm) = 155.79, 154.26, 149.52, 118.45, 118.24, 116.76, 108.85, 85.04, 82.64, 71.67, 71.50, 62.17, 22.63, 22.62, 14.23, 10.64, 10.50.

HRMS (ESI, *m*/*z*): $[M+H]^+$ calcd for $C_{17}H_{21}BrO_4$ 369.0696, found 369.0692.

IR (ATR): $\tilde{\nu}$ (cm^{-1}) = 2962 (w), 2939 (w), 2878 (w), 2209 (s), 1699 (vs), 1559 (w), 1497 (s), 1465 (s), 1403 (w), 1382 (m), 1366 (m), 1323 (w), 1304 (w), 1242 (vs), 1214 (vs), 1156 (vs), 1129 (m), 1117 (w), 1109 (w), 1068 (w), 1037 (s), 1016 (vs), 989 (m), 975 (m), 965 (m), 907 (w), 850 (s), 829 (s), 802 (w), 769 (w), 745 (m), 736 (m), 726 (w), 687 (vw), 652 (w), 422 (vw).

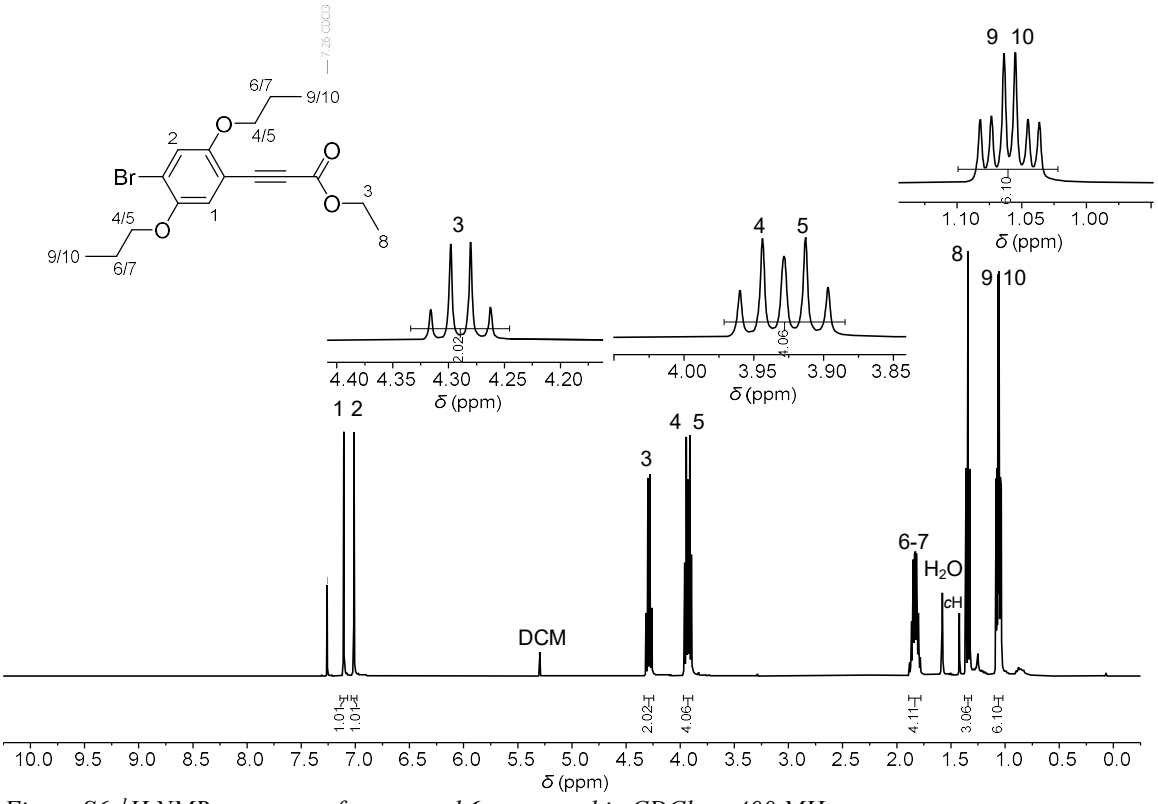

*Figure S6. ^{1}H NMR spectrum of compound **6**, measured in $CDCl_3$ at 400 MHz.*

2-Ethynyl-1,4-dipropoxybenzene (B0)

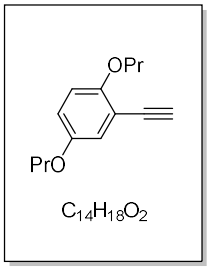

Compound **3** (1.51 g, 5.20 mmol, 1.00 equiv.) and K_2CO_3 (2.87 g, 20.8 mmol, 4.00 equiv.) were stirred in a solvent mixture of 30 mL methanol and 30 mL dichloromethane at 21 °C for 2 h. After the complete conversion was confirmed by TLC, 40 mL water was added to the mixture. The aqueous phase was extracted with dichloromethane (3 × 30 mL). The combined organic phases were dried over anhydrous Na_2SO_4. After removal of the volatiles under reduced pressure, 2-ethynyl-1,4-dipropoxybenzene was obtained as a colorless liquid (1.09 g, 5.01 mmol, 96%).

TLC (cyclohexane/ethyl acetate 10:1): R_f = 0.51.

^{1}H NMR (400 MHz, $CDCl_3$): δ (ppm) = 6.99 (d, J = 3.0 Hz, 1H, H_{ar}), 6.85 (dd, J = 9.0 Hz, J = 3.0 Hz, 1H, H_{ar}), 6.80 (d, J = 9.0 Hz, 1H, H_{ar}), 3.95 (t, J = 6.6 Hz, 2H, OCH_2CH$_2$), 3.86 (t, J = 6.6 Hz, 2H, OCH_2CH$_2$), 3.24 (s, 1H, CCH), 1.82 (overlapped h, J = 7.0 Hz, 2H, CH$_2$CH_2CH$_3$), 1.77 (overlapped h, J = 7.0 Hz, 2H, CH$_2$CH_2CH$_3$), 1.05 (t, J = 7.4 Hz, 3H, CH$_2$CH_3), 1.02 (t, J = 7.4 Hz, 3H, CH$_2$CH_3).

^{13}C NMR (100 MHz, $CDCl_3$): δ (ppm) = 154.6 (C_q), 152.7 (C_q), 119.3 (CH$_{ar}$), 117.0 (CH$_{ar}$), 114.0 (CH$_{ar}$), 112.3 (C_q), 80.8 (CH), 80.1 (C_q), 71.2 (OCH$_2$), 70.2 (OCH$_2$), 22.6 (CH$_2$), 22.6 (CH$_2$), 10.5 (CH$_3$), 10.5 (CH$_3$).

HRMS (ESI, m/z): $[M+H]^+$ calcd for $C_{14}H_{18}O_2$ 219.1380, found 219.1381.

IR (ATR): $\tilde{\nu}$ (cm^{-1}) = 3287 (vw), 2964 (w), 2935 (w), 2878 (w), 2112 (vw), 1609 (vw), 1578 (vw), 1495 (vs), 1469 (s), 1438 (vw), 1409 (w), 1388 (w), 1302 (w), 1273 (s), 1222 (vs), 1162 (w), 1119 (w), 1065 (m), 1047 (w), 1020 (w), 991 (m), 979 (m), 936 (vw), 924 (vw), 909 (vw), 874 (w), 854 (w), 802 (w), 765 (vw), 745 (vw), 722 (w), 695 (vw), 642 (w), 613 (m), 541 (w) cm^{-1}.

9 10

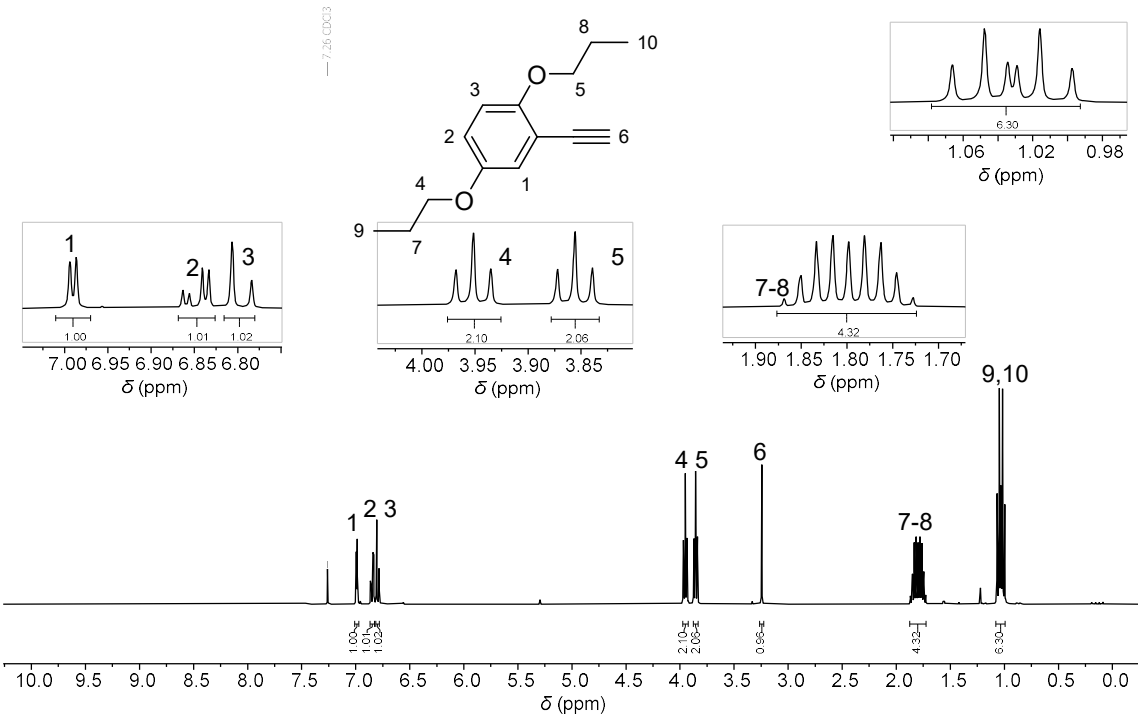

*Figure S7. ^{1}H NMR spectrum of compound **B0**, measured in $CDCl_3$ at 400 MHz.*

3,6-Di-*tert*-butyl-9-(4-((trimethylsilyl)ethynyl)phenyl)-9*H*-carbazole (C2)

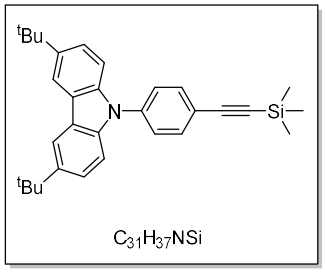

The title compound was synthesized according to reported conditions.[260]

9-(4-Bromophenyl)-3,6-di-*tert*-butyl-9*H*-carbazole (900 mg, 2.07 mmol, 1.00 equiv), $Pd(PPh_3)_2Cl_2$ (72.7 mg, 103 µmol, 0.05 equiv), and copper(I) iodide (39.5 mg, 207 µmol, 0.10 equiv) were degassed and added to diisopropylethylamine (4.23 mL, 3.21 g, 24.9 mmol, 12.0 equiv) and anhydrous THF (15 mL) under argon. After purging with argon for 15 min, trimethylsilylacetylene (0.72 mL, 0.51 g, 5.2 mmol, 2.5 equiv.) was added dropwise, and the reaction mixture was stirred at 65 °C for 24 h. After cooling to room temperature, the mixture was diluted with DCM and filtered through a pad of Celite®. The DCM solution was washed with washed with water and brine, dried over anhydrous Na_2SO_4. After removal of the volatiles under reduced pressure, purification via flash column chromatography (cyclohexane → cyclohexane/ethyl acetate 40:1) yielded the title compound as off-white solid (685 mg, 1.52 mmol, 73%).

TLC (cyclohexane): R_f = 0.37 in cyclohexane.

^{1}H NMR (400 MHz, $CDCl_3$): δ (ppm) = 8.13 (d, J = 1.2 Hz, 2H, H_{ar}), 7.71 – 7.64 (m, 2H, H_{ar}), 7.54 – 7.49 (m, 2H, H_{ar}), 7.46 (dd, J = 8.7, 2.0 Hz, 2H, H_{ar}), 7.35 (dd, J = 8.7, 0.6 Hz, 2H, H_{ar}), 1.46 (s, 18H, CCH_3), 0.29 (s, 9H, SiCH_3).

^{13}C NMR (101 MHz, $CDCl_3$): δ (ppm) = 143.20, 138.87, 138.31, 133.43, 126.27, 123.74, 123.58, 121.50, 116.30, 109.17, 104.44, 95.10, 34.77, 32.01, 0.00.

HRMS (ESI, m/z): $[M]^+$ calcd for $C_{31}H_{37}NSi$ 451.2690, found 451.2688.

IR (ATR): $\tilde{\nu}$ (cm^{-1}) = 2956 (m), 2927 (w), 2900 (w), 2861 (w), 2158 (w), 1600 (w), 1510 (s), 1497 (m), 1489 (m), 1471 (s), 1362 (m), 1325 (w), 1294 (m), 1263 (m), 1247 (s), 1236 (m), 1220 (w), 1203 (w), 1168 (w), 1103 (w), 1035 (w), 860 (vs), 839 (vs), 810 (vs), 757 (s), 740 (w), 699 (w), 656 (m), 644 (w), 611 (m), 597 (w), 574 (w), 543 (m), 424 (w).

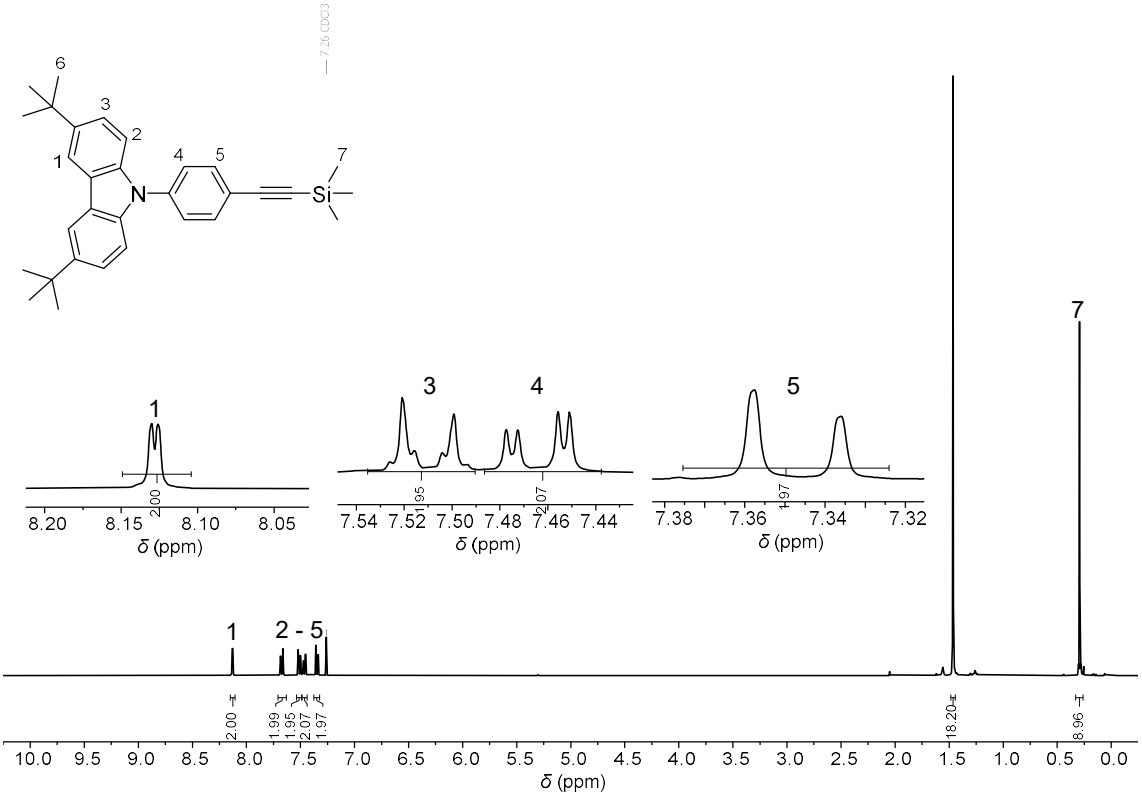

*Figure S8. ^{1}H NMR spectrum of compound **C2**, measured in $CDCl_3$ at 400 MHz.*

8.3.2 Synthesis of D-A-D OPEs

2,2'-((2,5-Difluoro-1,4-phenylene)bis(ethyne-2,1-diyl))bis(1,4-dipropoxybenzene) (OPE-b)

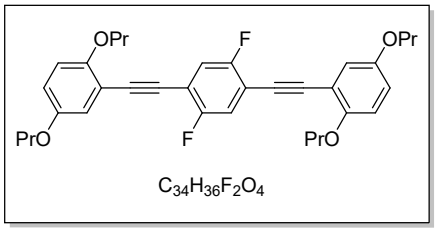

1,4-Dibromo-2,5-difluorobenzene (109 mg, 400 µmol, 1.00 equiv.), **B0** (218 mg, 1.00 mmol, 2.50 equiv.), copper(I) iodide (3.8 mg, 20 µmol, 0.05 equiv.), and $Pd(PPh_3)_2Cl_2$ (8.4 mg, 12 µmol, 0.03 equiv.) were degassed and added to 2.00 mL anhydrous THF and 1.12 mL anhydrous triethylamine under argon. After 18 h stirring at room temperature, a complete conversion was indicated by TLC. The volatiles were removed under reduced pressure and the residue was purified by column chromatography (cyclohexane → cyclohexane/ethyl acetate 30:1) to yield a white solid (62%).

TLC (cyclohexane/ethylacetate 20:1): R_f = 0.45.

^{1}H NMR (500 MHz, $CDCl_3$): δ (ppm) = 7.21 (t, J = 7.4 Hz, 2H, H_{ar}), 7.03 (d, J = 2.9 Hz, 2H, H_{ar}), 6.88 (dd, J = 9.0 Hz, J = 3.0 Hz, 2H, H_{ar}), 6.83 (d, J = 9.0 Hz, 2H, H_{ar}), 3.98 (t, J = 6.4 Hz, 4H, OCH_2CH_2), 3.89 (t, J = 6.6 Hz, 4H, OCH_2CH_2), 1.91–1.75 (m, 8H, $CH_2CH_2CH_3$), 1.09 (t, J = 7.4 Hz, 6H, CH_2CH_3), 1.03 (t, J = 7.4 Hz, 6H, CH_2CH_3).

^{13}C NMR (126 MHz, $CDCl_3$): δ (ppm) = 158.23 (dd, J = 249.8 Hz, J = 3.6 Hz, C_qF), 154.54 (C_q), 152.92 (C_q), 119.45–119.12 (m, *C*H), 118.55 (*C*H), 117.73 (*C*H), 114.15 (2C, *C*H), 113.58–113.35 (m, C_q), 112.72 (*C*H), 93.85 (C_q), 85.70 (C_q), 71.38 (OCH_2), 70.42 (OCH_2), 22.79 (CH_2), 10.66 (CH_3).

HRMS (ASAP, *m*/*z*): $[M+H]^+$ calcd for $C_{34}H_{36}F_2O_4$ 547.2654, found 547.2653.

IR (ATR): $\tilde{\nu}$ (cm^{-1}) = 2962 (w), 2937 (w), 2876 (w), 2217 (w), 1602 (w), 1510 (s), 1493 (vs), 1469 (s), 1456 (m), 1430 (s), 1403 (m), 1388 (s), 1308 (w), 1269 (vs), 1238 (s), 1212 (vs), 1179 (vs), 1160 (s), 1140 (vs), 1109 (m), 1065 (vs), 1031 (w), 991 (vs), 973 (vs),

950 (s), 930 (m), 870 (vs), 845 (vs), 812 (vs), 775 (m), 747 (m), 724 (s), 646 (m), 599 (w), 463 (w).

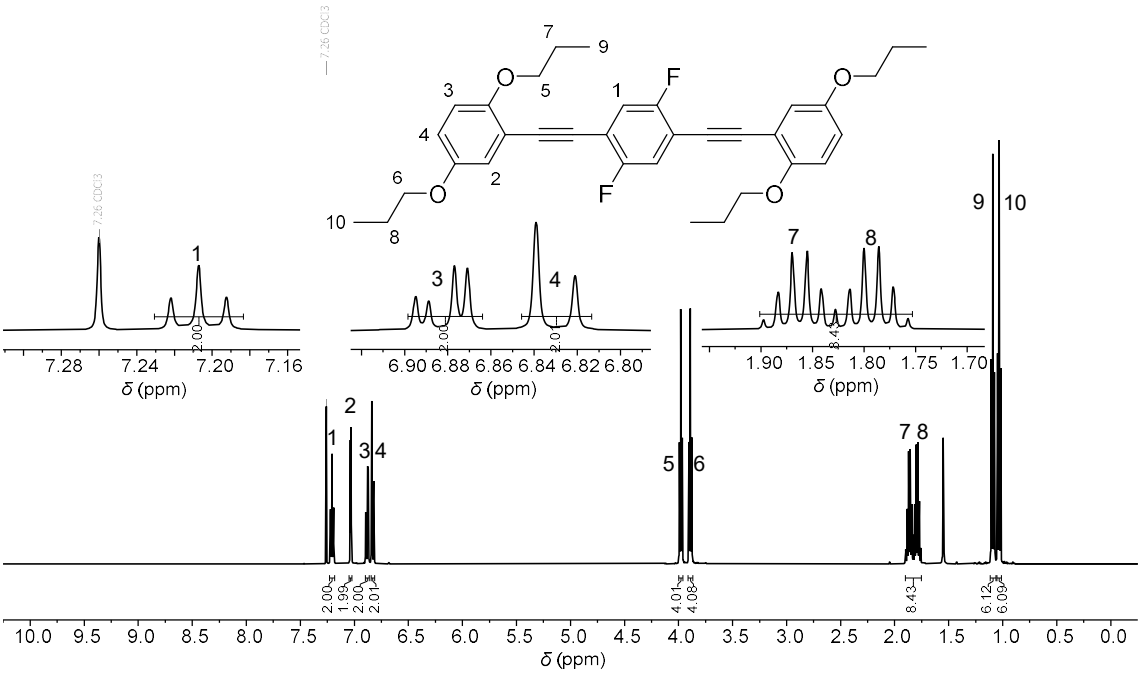

*Figure S9. ^{1}H NMR spectrum of compound **OPE-b**, measured in $CDCl_3$ at 500 MHz.*

9,10-Bis((2,5-dipropoxyphenyl)ethynyl)anthracene (OPE-g)

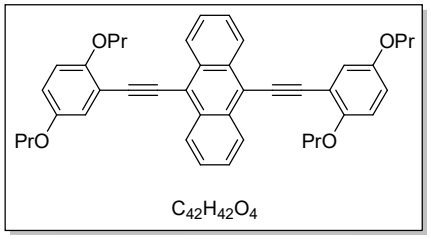

9,10-Dibromanthracene (168 mg, 500 µmol, 1.00 equiv.), Pd_2dba_3 (4.8 mg, 5.0 µmol, 0.01 equiv.), triphenylphosphine (3.9 mg, 15 µmol, 0.03 equiv.), and copper(I) iodide (2.9 mg, 15 µmol, 0.03 equiv.) were degassed and suspended under continuous argon flow in 10 mL anhydrous THF and 1.4 mL anhydrous triethylamine (1.0 g, 10 mmol, 20 equiv.). After flushing with argon for 10 min, **B0** (240 mg, 1.10 mmol, 2.20 equiv.) was added dropwise, and the reaction mixture was stirred at 65 °C for 20 h. The reaction mixture was cooled down to room temperature and poured onto a short silica gel plug (5 cm) and washed with cyclohexane. Purification by flash column chromatography (cyclohexane → cyclohexane/DCM 1:2) yielded the title compound as an orange solid (78.2 mg, 138 µmol, 69%).

TLC (cyclohexane/DCM 3:2): R_f = 0.35.

^{1}H NMR (400 MHz, $CDCl_3$): δ (ppm) = 8.84 (m, 4H, H_{ar}), 7.62 (m, 4H, H_{ar}), 7.30 – 7.24 (m, 2H, H_{ar}), 6.95 – 6.88 (m, 4H, H_{ar}), 4.10 (t, J = 6.5 Hz, 4H, OCH_2CH_2), 3.98 (t, J = 6.5 Hz, 4H, OCH_2CH_2), 2.06 (h, J = 7.1 Hz, 4H, $CH_2CH_2CH_3$), 1.85 (h, J = 7.1 Hz, 4H, $CH_2CH_2CH_3$), 1.18 (t, J = 7.4 Hz, 6H, CH_2CH_3), 1.08 (t, J = 7.4 Hz, 6H, CH_2CH_3).

^{13}C NMR (101 MHz, $CDCl_3$): δ (ppm) = 154.40 (C_q), 152.77 (C_q), 132.07 (C_q), 127.55 (*C*H), 126.52 (*C*H), 118.59 (*C*H), 116.62 (*C*H), 113.53 (*C*H), 112.89 (C_q), 99.28 (C_q), 90.81 (C_q), 70.91 (OCH_2), 70.40 (OCH_2), 23.00 (CH_2), 22.75 (CH_2), 10.89 (CH_3), 10.60 (CH_3).

HRMS (ASAP, *m*/*z*): $[M]^+$ calcd for $C_{42}H_{42}O_4$ 610.3083, found 610.3071.

IR (ATR): $\tilde{\nu}$ (cm^{-1}) = 2966 (w), 2935 (w), 2917 (w), 2874 (w), 1600 (w), 1497 (s), 1467 (m), 1434 (m), 1393 (w), 1384 (w), 1296 (w), 1267 (s), 1226 (vs), 1207 (m), 1193 (s), 1160 (m), 1127 (w), 1121 (m), 1041 (vs), 1020 (vs), 959 (w), 936 (w), 903 (w), 850 (s), 812 (s), 802 (w), 775 (s), 761 (vs), 720 (w), 691 (w), 638 (s), 605 (m), 574 (w), 475 (w).

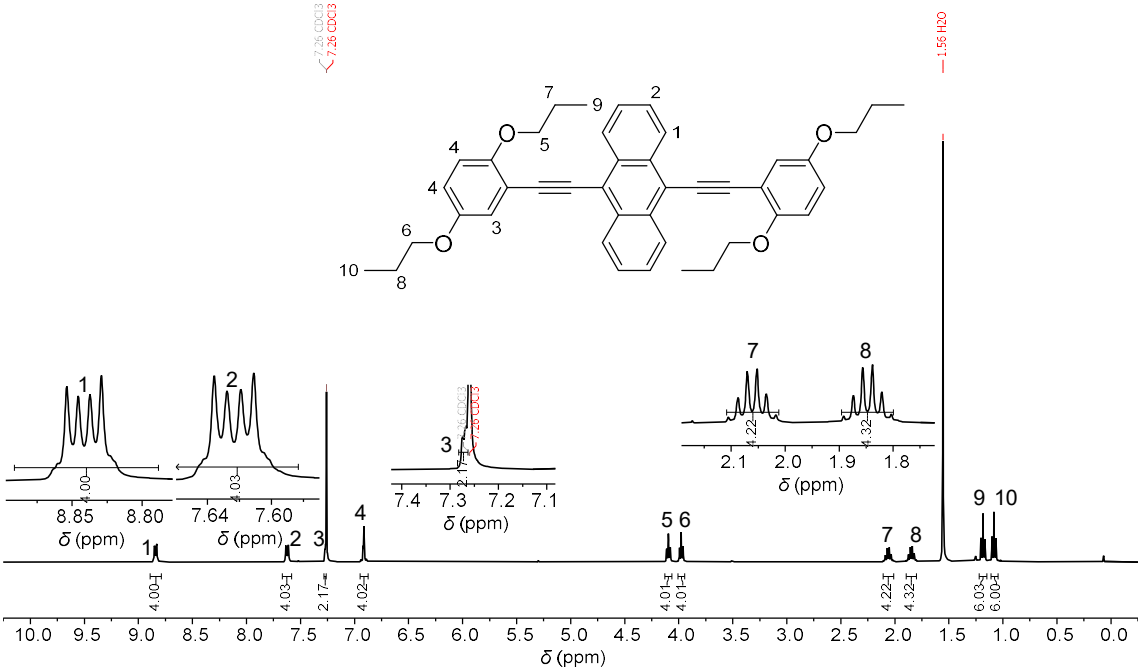

*Figure S10. ^{1}H NMR spectrum of **OPE-g**, measured in $CDCl_3$ at 400 MHz.*

4,7-Bis((2,5-dipropoxyphenyl)ethynyl)benzo[*c*][1,2,5]thiadiazole (OPE-y)

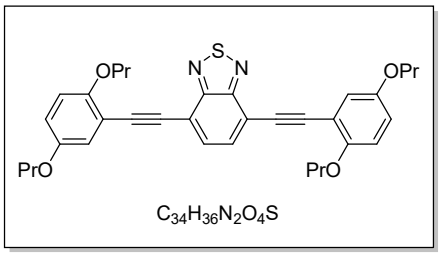

4,7-Dibromobenzo[*c*][1,2,5]thiadiazole (96.0 mg, 440 µmol, 1.00 equiv.), **B0** (96.0 mg, 440 µmol, 2.21 equiv.), $Pd(PPh_3)_4$ (9.9 mg, 8.6 µmol, 0.04 equiv.), and copper(I) iodide (3.8 mg, 20 µmol, 0.10 equiv.) were degassed and suspended under continuous argon flow in 2.0 mL anhydrous THF and 1.4 mL anhydrous diisopropylamine (405 mg, 3.96 mmol, 19.9 equiv.). The reaction mixture was stirred at room temperature for 20 h. After a complete conversion confirmed by TLC, the reaction mixture was poured onto a short silica gel plug (5 cm) and washed with cyclohexane. Purification by flash column chromatography (cyclohexane → cyclohexane/DCM 1:2) yielded the title compound as an orange solid (78.2 mg, 138 µmol, 69%).

TLC (cyclohexane/ethyl acetate 5:1): $R_f = 0.42$.

^{1}H NMR (400 MHz, $CDCl_3$): δ (ppm) = 7.76 (s, 2H, H_{ar}), 7.15 (d, J = 2.9 Hz, 2H, H_{ar}), 6.90 (dd, J = 9.0 Hz, J = 2.9 Hz, 2H, H_{ar}), 6.86 (dd, 2H, H_{ar}), 4.03 (t, J = 6.5 Hz, 4H, OCH_2), 3.91 (t, J = 6.6 Hz, 4H, OCH_2), 1.92 (h, J = 7.3 Hz, 4H, $CH_2CH_2CH_3$), 1.80 (h, J = 7.2 Hz, 4H, $CH_2CH_2CH_3$), 1.12 (t, J = 7.4 Hz, 6H, CH_2CH_3), 1.04 (t, J = 7.4 Hz, 6H, CH_2CH_3).

^{13}C NMR (101 MHz, $CDCl_3$): δ (ppm) = 154.60 (C_q), 154.45 (C_q), 152.82 (C_q), 132.19 (CH), 118.51 (CH), 117.71 (CH), 117.36 (C_q), 114.05 (CH), 112.89 (C_q), 94.32 (C_q), 89.28 (C_q), 71.32 (OCH_2), 70.32 (OCH_2), 22.82 (CH_2), 22.67 (CH_2), 10.66 (CH_3), 10.54 (CH_3).

HRMS (ESI, *m*/*z*): $[M+H]^+$ calcd for $C_{34}H_{36}N_2O_4S$ 569.2469, found 569.2471.

IR (ATR): $\tilde{\nu}$ (cm^{-1}) = 2960 (m), 2931 (m), 2874 (m), 2205 (w), 1600 (w), 1547 (w), 1500 (vs), 1477 (w), 1462 (s), 1417 (w), 1413 (w), 1393 (m), 1308 (w), 1271 (vs), 1236 (s), 1214 (vs), 1168 (w), 1140 (s), 1119 (s), 1070 (s), 1049 (m), 1020 (s), 985 (vs), 975 (vs),

938 (w), 880 (w), 843 (vs), 810 (vs), 802 (vs), 771 (w), 743 (m), 736 (m), 634 (m), 601 (w), 541 (s), 508 (s), 479 (w).

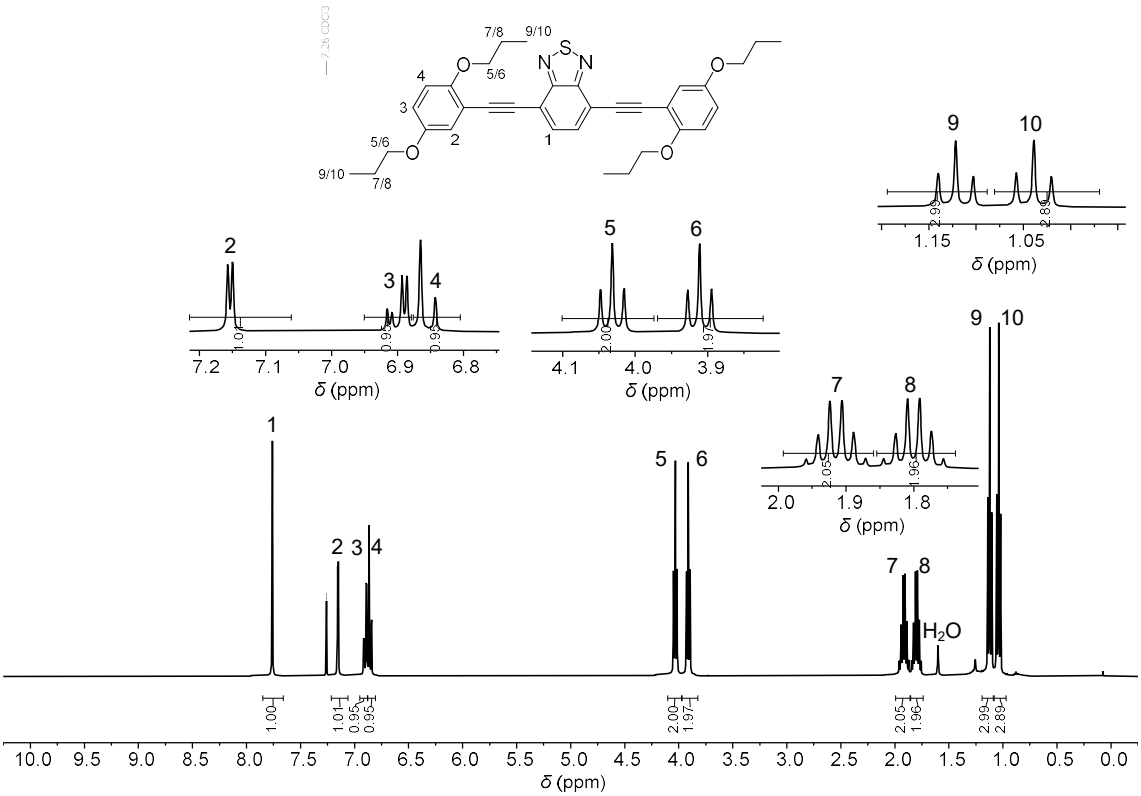

*Figure S11. ^{1}H NMR spectrum of **OPE-y**, measured in $CDCl_3$ at 400 MHz.*

4,9-Bis((2,5-dipropoxyphenyl)ethynyl)naphtho[2,3-*c*][1,2,5]thiadiazole (OPE-r)

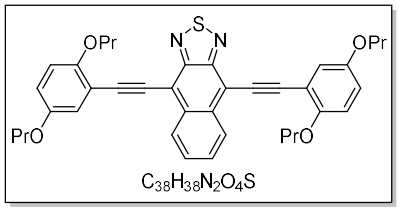

4,9-Dibromonaphtho[2,3-*c*][1,2,5]thiadiazole (50.0 mg, 145 µmol, 1.00 equiv.), **B0** (95.2 mg, 436 µmol, 3.00 equiv.), $Pd_2(dba)_3$ (1.3 mg, 1.5 µmol, 0.01 equiv.), triphenylphosphine (1.1 mg, 4.4 µmol, 0.03 equiv.) and copper(I) iodide (1.4 mg, 7.3 µmol, 0.05 equiv.) were degassed and suspended under continuous argon flow in 3.0 mL anhydrous THF and 0.41 mL anhydrous triethylamine (0.29 g, 2.9 mmol, 20 equiv.). Under argon atmosphere, the reaction mixture was stirred for 20 h at 65 °C. After a complete conversion confirmed by TLC, the reaction mixture was poured onto a short silica gel plug (5 cm) and washed with cyclohexane. Purification

by flash column chromatography (cyclohexane → cyclohexane/DCM 1:2) and subsequent washing with methanol yielded the title compound as an orange solid (74.8 mg, 121 µmol, 83%).

TLC (cyclohexane/DCM 3:2): R_f = 0.55.

^{1}H NMR (400 MHz, $CDCl_3$): δ = 8.85 – 8.80 (m, 2H, H_{ar}), 7.58 – 7.54 (m, 2H, H_{ar}), 7.29 (d, J = 2.8 Hz, 2H, H_{ar}), 6.94 (dd, J = 9.0 Hz, J = 3.0 Hz, 2H, H_{ar}), 6.89 (d, J = 9.0 Hz, 2H, H_{ar}), 4.09 (t, J = 6.5 Hz, 4H, OCH_2), 3.95 (t, J = 6.6 Hz, 4H, OCH_2), 2.03 (h, J = 7.3 Hz, 4H, $CH_2CH_2CH_3$), 1.83 (h, J = 7.3 Hz, 4H, $CH_2CH_2CH_3$), 1.17 (t, J = 7.4 Hz, 6H, CH_2CH_3), 1.06 (t, J = 7.4 Hz, 6H, CH_2CH_3).

^{13}C NMR (101 MHz, $CDCl_3$): δ = 154.7 (C_q), 152.8 (C_q), 152.5 (C_q), 134.9 (C_q), 128.1 (CH), 127.6 (CH), 118.4 (CH), 117.8 (CH), 113.2 (CH), 112.9 (C_q), 112.9 (C_q), 101.2 (C_q), 89.6 (C_q), 71.0 (OCH_2), 70.4 (OCH_2), 23.0 (CH_2), 22.7 (CH_2), 10.8 (CH_3), 10.6 (CH_3).

HRMS (ESI, m/z): $[M]^+$ calcd for $C_{38}H_{38}N_2O_4S$ 618.2552, found 618.2546.

IR (ATR): ν (cm^{-1}) = 2960 (m), 2935 (w), 2909 (w), 2871 (w), 2189 (vw), 1600 (w), 1539 (vw), 1497 (vs), 1481 (m), 1469 (s), 1456 (s), 1413 (w), 1390 (m), 1265 (s), 1228 (vs), 1207 (vs), 1131 (m), 1119 (m), 1043 (s), 1024 (vs), 1010 (vs), 948 (m), 905 (m), 856 (vs), 804 (s), 796 (vs), 778 (m), 767 (m), 753 (vs), 738 (s), 708 (w), 629 (w), 619 (w), 601 (w), 586 (w), 522 (vs), 479 (w).

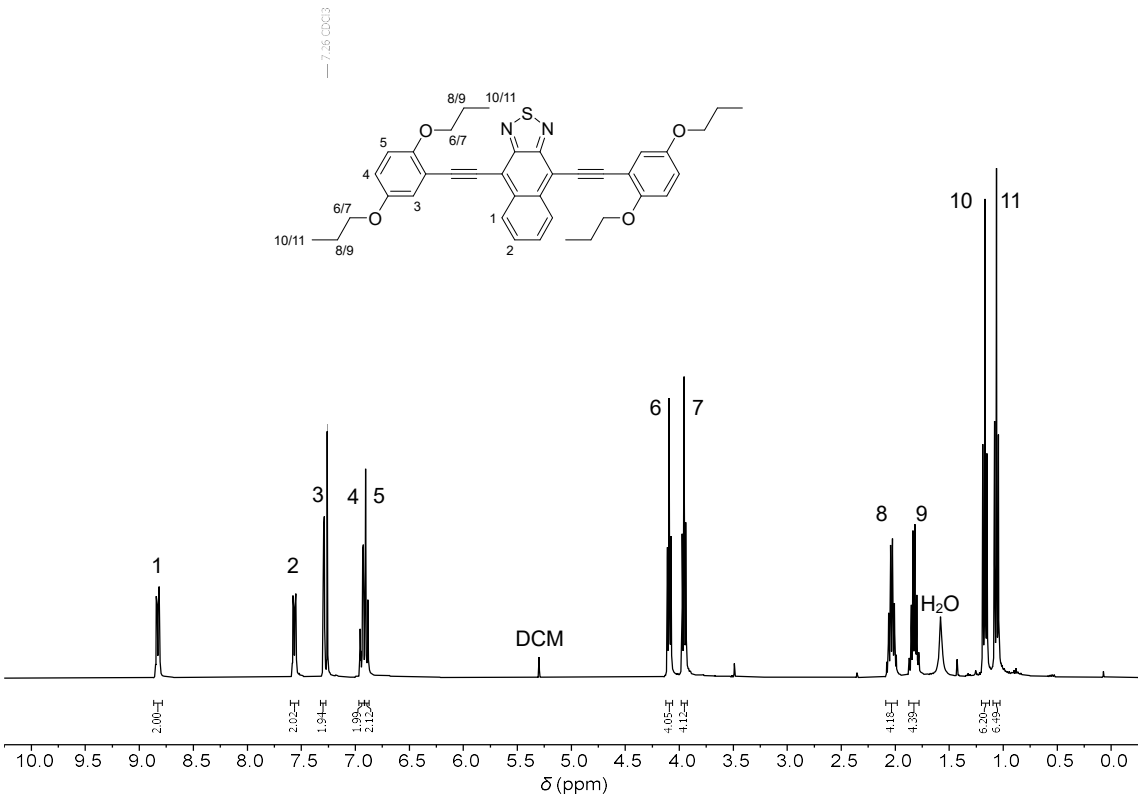

*Figure S12. ^{1}H NMR spectrum of **OPE-r**, measured in $CDCl_3$ at 400 MHz.*

5,5'-((2,5-Difluoro-1,4-phenylene)bis(ethyne-2,1-diyl))bis(2-(phenylethynyl)-1,4-dipropoxybenzene) (OPE-b')

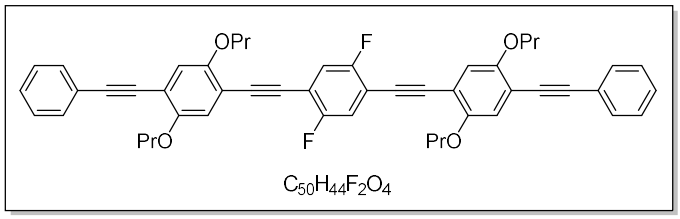

The synthesis of the title compound was carried out by Lars Boller as part of his bachelor's thesis.

A mixture of **B1** (131 mg, 411 µmol, 2.06 equiv.), 1,4-dibromo-2,5-difluorobenzene (54.3 mg, 200 µmol, 1.00 equiv.), $Pd(PPh_3)_4$ (13.9 mg, 12.0 µmol, 0.06 equiv.) and copper(I) iodide (4.70 mg, 24.7 µmol, 0.12 equiv.) was degassed and then dissolved in 4 mL anhydrous toluene. After purging with argon for 5 minutes, 0.60 mL diisopropylamine

(0.43 g, 4.3 mmol, 10 equiv.) were added. The reaction mixture was stirred under argon at room temperature for 23 h. The solvent was removed under reduced pressure. The residue was taken up with DCM, washed with water and brine. The organic phase was dried over Na_2SO_4 and concentrated under reduced pressure. The crude product was purified by flash column chromatography (cyclohexane to cyclohexane/ethyl acetate 20:1) and further by prep-TLC (cyclohexane/dichloromethane 3:1). The title compound was obtained after sonication in *n*-hexane as a neon-yellow solid (57.6 mg, 76.6 µmol, 38%).

TLC (cyclohexane/DCM 1:1): R_f = 0.32.

^{1}H NMR (400 MHz, $CDCl_3$): δ (ppm) = 7.56 – 7.53 (m, 4H, H_{ar}), 7.37 – 7.34 (m, 6H, H_{ar}), 7.23 (t, J = 7.6 Hz, 2H, FCCH_{ar}), 7.03 – 7.00 (m, 4H, H_{ar}), 4.03 – 3.96 (m, 8H, OCH_2), 1.93 – 1.84 (m, 8H, $CH_2CH_2CH_2CH_3$), 1.13 – 1.07 (m, 12H, CH_2CH_3).

^{13}C NMR (101 MHz, $CDCl_3$): δ (ppm) = 158.2 (dd, J = 249.8 Hz, J = 3.6 Hz, C_qF) 153.9 (C_qO), 153.6 (C_qO), 131.6 (CH), 128.4 (CH), 123.4 (C_q), 119.3–119.0 (*C*H), 117.8 (*C*H) 117.0 (*C*H), 117.0 (*C*H), 116.9 (*C*H), 115.2 (C_q), 115.1 (C_q), 112.8 (C_q, *C*CF), 95.4 (C_q), 95.7 (C_q), 87.1 (C_q), 85.8 (C_q), 71.2 (O*C*H2), 71.1 (O*C*H_2), 22.7 (*C*H_2), 22.7 (*C*H_2), 10.6 (*C*H_3), 10.5 (*C*H_3).

HRMS (ESI, *m*/*z*): M^+ calcd for $C_{50}H_{44}F_2O_4$ 746.3208, found 746.3167.

IR (ATR) $\tilde{\nu}$ (cm^{-1}) = 2962 (w), 2937 (w), 2921 (w), 2874 (w), 2211 (vw), 1596 (vw), 1514 (m), 1495 (m), 1487 (s), 1469 (m), 1425 (m), 1407 (m), 1386 (s), 1275 (s), 1249 (w), 1214 (vs), 1179 (m), 1148 (w), 1127 (w), 1107 (w), 1065 (m), 1047 (w), 1016 (m), 985 (s), 905 (w), 891 (w), 870 (m), 858 (s), 841 (w), 827 (w), 751 (vs), 734 (w), 685 (vs), 629 (w), 570 (w), 527 (w), 461 (w).

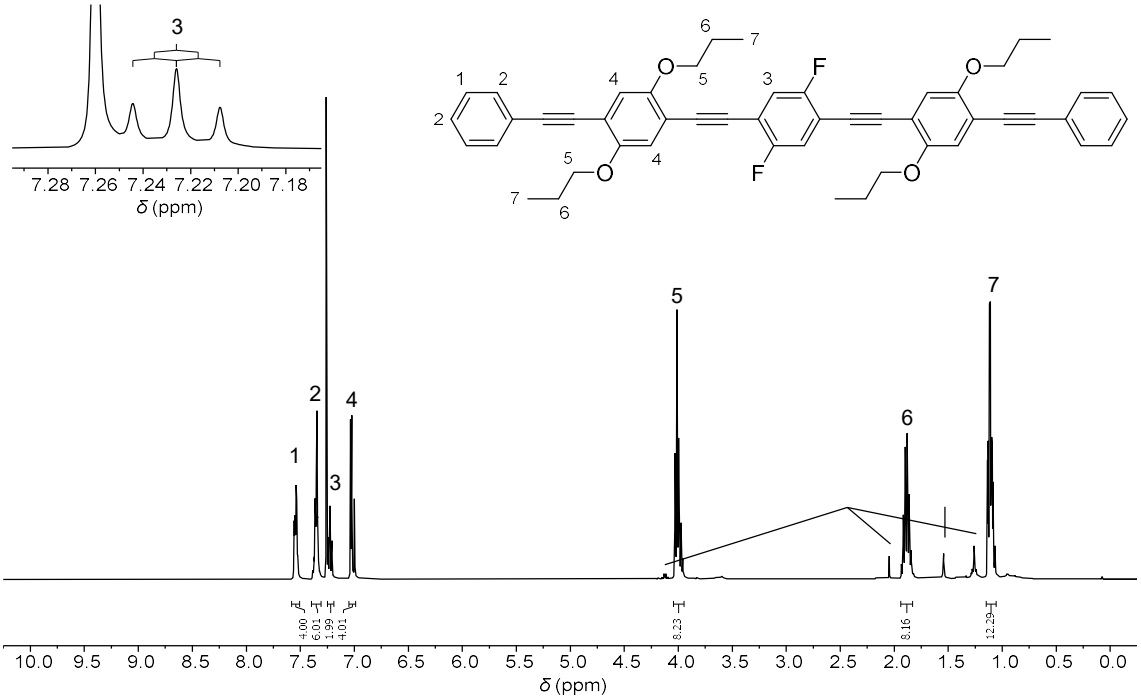

*Figure S13. [1]H NMR spectrum of **OPE-b'**, measured in $CDCl_3$ at 400 MHz.*

9,10-Bis((4-(phenylethynyl)-2,5-dipropoxyphenyl)ethynyl)anthracene (OPE-g')

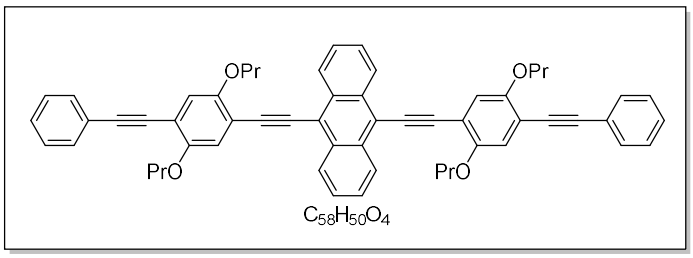

The synthesis of the title compound was carried out by Lars Boller as part of his bachelor's thesis.

A mixture of **B1** (129 mg, 404 µmol, 2.02 equiv.), 9,10-dibromoanthracene (67.1 mg, 200 µmol, 1.00 equiv.), $Pd(PPh_3)_4$ (14.1 mg, 12.2 µmol, 0.06 equiv.) and copper(I) iodide (4.80 mg, 25.2 µmol, 0.13 equiv.) was degassed and added to 4.0 mL anhydrous toluene and 0.60 mL diisopropylamine (0.43 g, 4.3 mmol, 11 equiv.). The reaction mixture was

stirred under argon at 21 °C for 3 days. After a complete conversion confirmed by TLC, the reaction mixture was poured onto a short silica gel plug (5 cm), washed with cyclohexane, and eluted with DCM. The crude product was subsequently washed with methanol and cyclohexane. After removal of the volatiles under reduced pressure, the title compound was obtained as an orange solid (35.8 mg, 44.1 μmol 22%).

TLC (cyclohexane/DCM 1:1): R_f = 0.24.

^{1}H NMR spectra was attempted in several deuterated solvents ($CDCl_3$, C_6D_6 and THF-d_8). However, well-resolved spectra could not obtained due to insufficient solubility. The following assignment is based on measurements in THF-d_8 at 500 MHz: δ (ppm) = 8.90 (dd, J = 6.6, 3.3 Hz, 4H, H_{ar}), 7.67 (dd, J = 6.7, 3.3 Hz, 4H, H_{ar}), 7.59 – 7.49 (m, 4H, H_{ar}), 7.43 – 7.31 (m, 8H, H_{ar}), 7.20 (s, 2H, H_{ar}), 4.17 (t, J = 6.5 Hz, 4H, OCH_2CH_2), 4.12 (t, J = 6.3 Hz, 4H, OCH_2CH_2), 2.15 – 1.99 (m, 8H, $CH_2CH_2CH_3$), 41.21 (t, J = 7.5 Hz, 7H), 1.16 (t, J = 7.4 Hz, 6H).

^{13}C NMR: not available; spectra suffered from poor resolution under the conditions tested.

HRMS (ESI, m/z): $[M+H]^+$ calcd for $C_{58}H_{50}O_4$ 811.3782; found 811.3743.

IR (ATR): $\tilde{\nu}$ (cm^{-1}) = 2964 (w), 2946 (w), 2904 (w), 2874 (w), 1504 (s), 1487 (w), 1471 (w), 1454 (w), 1440 (w), 1425 (m), 1386 (s), 1273 (m), 1216 (vs), 1197 (m), 1154 (w), 1041 (m), 1022 (vs), 905 (w), 876 (vw), 860 (s), 775 (w), 761 (vs), 691 (m), 640 (s), 613 (w), 531 (w).

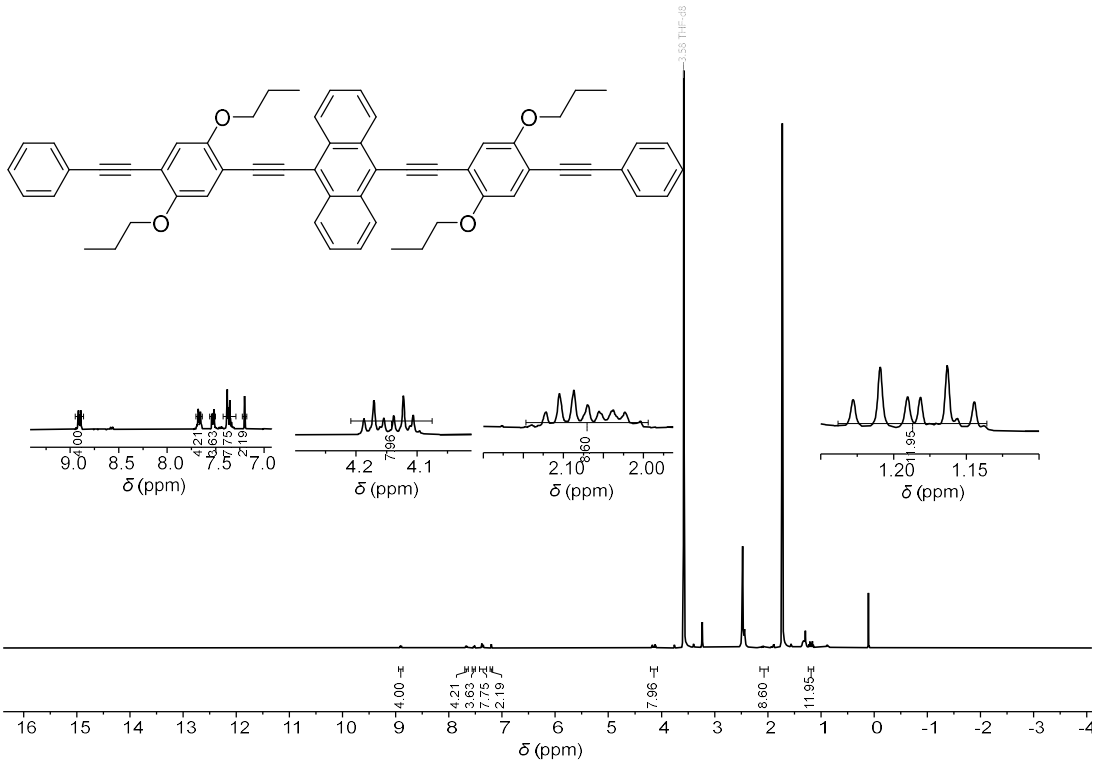

*Figure S14. [1]H NMR spectrum of **OPE-g'**, measured in $CDCl_3$ at 400 MHz.*

4,7-Bis((4-(phenylethynyl)-2,5-dipropoxyphenyl)ethynyl)benzo[*c*][1,2,5]thiadiazole (OPE-y')

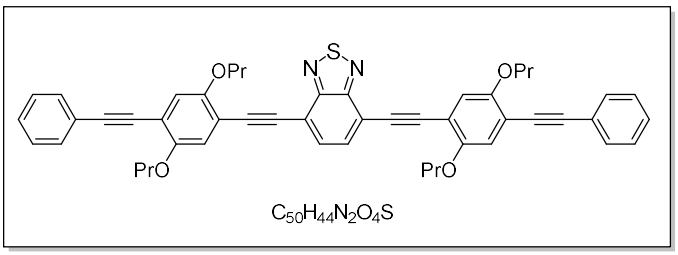

The synthesis of the title compound was carried out by Lars Boller as part of his bachelor's thesis.

A mixture of **B1** (124 mg, 390 µmol, 2,05 equiv.), 1,4-dibromo-2,5-difluorobenzene (55.9 mg, 190 µmol, 1.00 equiv.), $Pd(PPh_3)_4$ (13.9 mg, 12.0 µmol, 0.06 equiv.) and copper(I) iodide (4.57mg, 24.0 µmol, 0.13 equiv.) was degassed and added to 4.0 mL

anhydrous toluene and 0.60 mL diisopropylamine (0.43 g, 4.3 mmol, 11 equiv.). After stirring at room temperature for 2 days, a complete conversion was indicated by TLC. The reaction mixture was poured onto a short silica gel plug (5 cm), washed with cyclohexane, and eluted with DCM. After removal of the volatiles under reduced pressure, the title compound was obtained as orange-red solid (117 mg, 15.2 µmol, 80%).

TLC: R_f = 0.48 in cyclohexane/DCM (1:1).

^{1}H NMR (400 MHz, $CDCl_3$): δ (ppm) = 7.78 (s, 2H, H_{ar}), 7.57–7.54 (m, 4H, H_{ar}), 7.39–7.32 (m, 6H, H_{ar}), 7.15 (s, 2H, H_{ar}), 7.06 (s, 2H, H_{ar}), 4.06 (t, J = 6.4 Hz, 4H, OCH_2CH$_2$), 4.04 (t, J = 6.4 Hz, 4H, OCH_2CH$_2$), 1.99–1.85 (m, 8H, CH$_2$CH_2CH$_3$), 1.14 (overlapped t, J = 7.6 Hz, 6H, CH$_2$CH_3), 1.12 (overlapped t, J = 7.7 Hz, 6H, CH$_2$CH_3).

^{13}C NMR (100 MHz, $CDCl_3$): δ (ppm) = 154.4 (2C, C_q), 154.1 (2C, C_q), 153.6 (2C, C_q), 132.3 (4C, *C*H), 131.6 (2C, *C*H), 128.4 (6C, *C*H), 123.4 (2C, C_q), 117.3 (2C, C_q), 117.2 (2C, *C*H), 116.9 (2C, *C*H), 115.1 (2C, C_q), 113.1 (2C, C_q), 95.4 (2C, C_q), 94.4 (2C, C_q), 90.8 (2C, C_q), 85.9 (2C, C_q), 71.2 (2C, *C*H$_2$), 71.2 (2C, *C*H$_2$), 22.8 (4C, *C*H$_2$), 10.7 (2C, *C*H$_3$), 10.6 (2C, *C*H$_3$).

HRMS (ESI, *m*/*z*): $[M+H]^+$ calcd for $C_{50}H_{44}N_2O_4S$ 769.3095, found 769.3082.

IR (ATR): $\tilde{\nu}$ (cm^{-1}) = 2958 (w), 2933 (w), 2874 (w), 2203 (w), 1594 (w), 1510 (s), 1485 (s), 1469 (m), 1440 (w), 1415 (s), 1388 (s), 1362 (w), 1323 (w), 1277 (s), 1216 (vs), 1191 (s), 1148 (w), 1127 (w), 1105 (w), 1065 (w), 1045 (m), 1024 (s), 1014 (s), 985 (w), 967 (m), 913 (w), 893 (m), 858 (s), 835 (s), 753 (vs), 689 (vs), 631 (m), 588 (w), 527 (w), 508 (w), 469 (w).

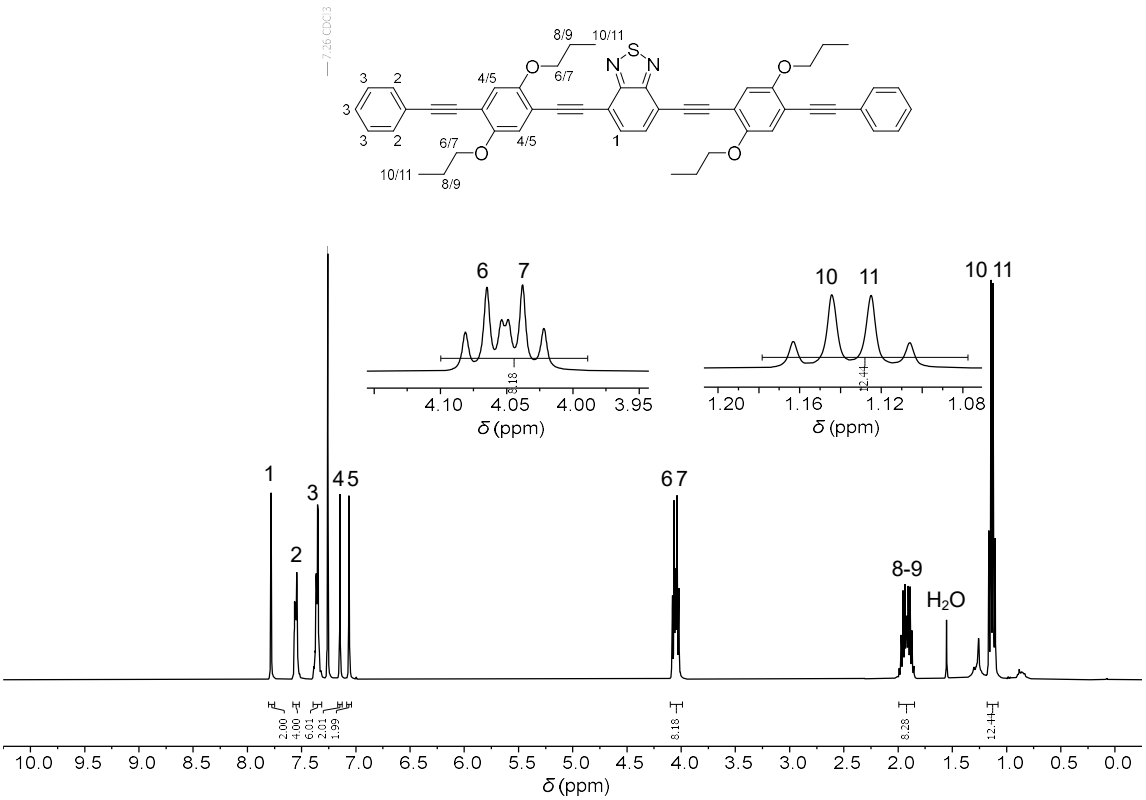

*Figure S15. ^{1}H NMR spectrum of **OPE-y'**, measured in $CDCl_3$ at 400 MHz.*

4,9-bis((4-(phenylethynyl)-2,5-dipropoxyphenyl)ethynyl)naphtho[2,3-*c*][1,2,5]thiadiazole (OPE-r')

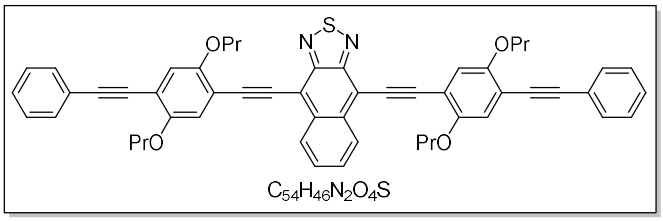

4,9-Dibromonaphtho[2,3-*c*][1,2,5]thiadiazole (60.5 mg, 176 µmol, 1.00 equiv.), **B1** (127 mg, 400 µmol, 2.28 equiv.), 5 mol% of $Pd(PPh_3)_4$ (9.9 mg, 8.6 µmol), and 10 mol% of copper(I) iodide (3.3 mg, 18 µmol) were degassed and suspended in 5 mL THF. Under continuous argon flow, diisopropylamine (0.50 mL, 0.36 g, 3.5 mmol, 20 equiv.) was added and the reaction mixture was stirred at room temperature for 20 h. The mixture was poured onto a short silica gel plug (5 cm) and washed with cyclohexane. Purification by

flash column chromatography (cyclohexane → cyclohexane/DCM 1:3) yielded the title compound as a dark purple solid (78.2 mg, 138 µmol, 69%).

TLC (cyclohexane/DCM 5:1)**.:** R_f = 0.09.

^{1}H NMR (400 MHz, $CDCl_3$): δ = 7.67 – 7.53 (m, 4H, H_{ar}), 7.44 – 7.32 (m, 4H, H_{ar}), 7.32 – 7.18 (m, overlapped with solvent signal, H_{ar}), 7.10 (s, 2H, H_{ar}), 7.00 (s, 2H, H_{ar}), 4.14 (t, J = 6.5 Hz, 4H), 4.09 (t, J = 6.5 Hz, 4H), 2.13 – 1.99 (m, 4H), 1.99 – 1.82 (m, 4H), 1.19 (t, J = 7.4 Hz, 6H), 1.15 (t, J = 7.4 Hz, 6H).

^{13}C NMR: not available; spectra suffered from poor resolution under the conditions tested.

HRMS (ESI, m/z): $[M]^+$ calcd for $C_{54}H_{46}N_2O_2S$ 818.3178, found 818.3181.

IR (ATR): $\tilde{\nu}$ (cm^{-1}) = 2964 (w), 2909 (w), 2874 (w), 2184 (vw), 1539 (w), 1504 (m), 1483 (w), 1471 (w), 1467 (w), 1444 (w), 1411 (m), 1390 (s), 1314 (w), 1275 (m), 1212 (vs), 1041 (m), 1022 (vs), 926 (w), 907 (w), 860 (s), 757 (vs), 691 (m), 650 (w), 529 (m).

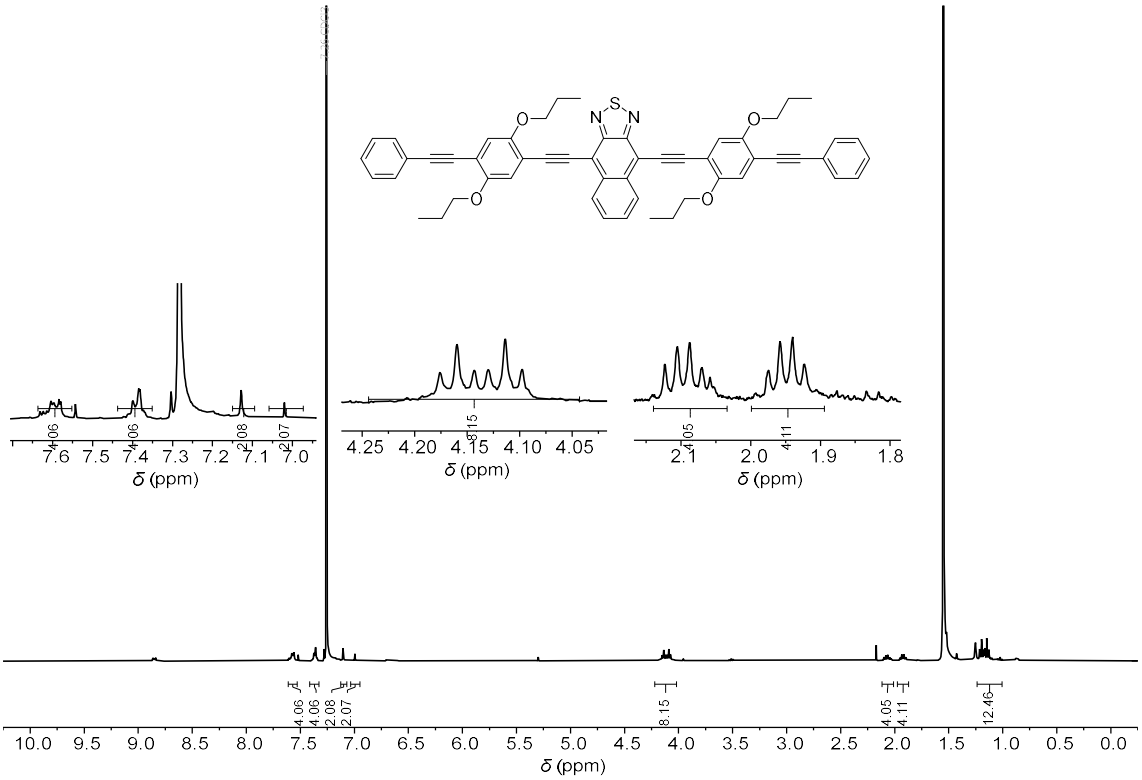

*Figure S16. ^{1}H NMR spectrum of **OPE-r'**, measured in $CDCl_3$ at 400 MHz.*

8.3.3 Iterative Synthesis of D-OPE-A Systems

The synthesis presented in this section was primarily conducted by Till Paha during his master's thesis. The compounds **PE2** and **PE3** were further purified by the author.

General procedure of saponification reaction (GP1): An ester-protected product was dissolved in a mixture of THF/MeOH/water (3:1:1), and equimolar sodium hydroxide was added. After stirring over night at ambient temperature, the reaction mixture was diluted with DCM and neutralized with hydrochloric acid. The phases were separated, and the aqueous phase was extracted with DCM. The combined organic layers were washed with brine, dried over anhydrous Na_2SO_4, and concentrated under reduced pressure. The product was used without further purification.[9]

General procedure of decarboxylative coupling reaction (GP2): An alkynyl carboxylic acid (1.00 equiv.), an aryl bromide (0.90 – 1.10 equiv.), SPhos (0.05 equiv.), cesium carbonate (1.20 equiv.), and $Pd(dppf)Cl_2 \cdot CH_2Cl_2$ (0.025 equiv.) were degassed and dissolved in a solvent mixture of toluene/THF (7:3). The solution was stirred overnight at 65°C under argon atmosphere. After TLC confirmed complete conversion, the mixture was diluted with THF and washed with water. The aqueous phase was extracted with DCM (4 ×). The combined organic layers were washed with brine, dried over Na_2SO_4, filtered, and concentrated under reduced pressure. The crude product was purified by flash column chromatography (cyclohexane/ethyl acetate).[9]

Ethyl 3-(4-(3,6-di-*tert*-butyl-9*H*-carbazol-9-yl)phenyl)propiolate (C3)

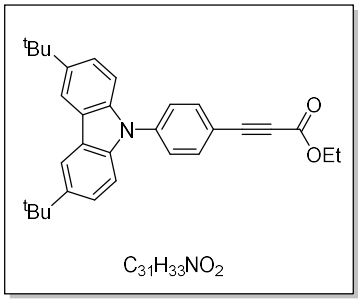

C2 (2.50 g, 5.53 mmol, 1.00 equiv.) and CsF (1.00 g, 6.64 mmol, 1.20 equiv.) were degassed, backfilled with CO_2 and added to 25 mL anhydrous DMSO. After stirring at ambient temperature for 3 h, iodoethane (0.53 ml, 1.1 g, 6.6 mmol, 1.2 equiv.) was added dropwise and the mixture was stirred over night at room temperature. The reaction

was quenched 15 mL saturated NH_4Cl solution. The aqueous phase was extracted with DCM (3 × 40 mL) and the combined organic layers were washed with brine (100 mL). After drying over anhydrous Na_2SO_4, the solvent was removed under reduced pressure, and the crude product was purified with flash column chromatography (cyclohexane/ethyl acetate 40:1). The title compound was obtained as an off-white solid (2.10 g, 4.65 mmol, 85%).

TLC (cyclohexane/ethyl acetate (40:1) R_f = 0.29.

^{1}H NMR (400 MHz, $CDCl_3$): δ (ppm) = 8.13 (d, J = 1.9 Hz, 2H, H_{ar}), 7.80 (d, J = 8.5 Hz, 2H, H_{ar}), 7.61 (d, J = 8.5 Hz, 2H, H_{ar}), 7.48 (dd, J = 8.7, 1.9 Hz, 2H, H_{ar}), 7.40 (d, J = 8.7 Hz, 2H, H_{ar}), 4.34 (q, J = 7.1 Hz, 2H, OCH_2CH_3), 1.47 (s, 18H, CCH_3), 1.39 (t, J = 7.2 Hz, 3H, CH_2CH_3).

^{13}C NMR (101 MHz, $CDCl_3$): δ (ppm) = 154.19, 143.77, 140.62, 138.67, 134.72, 126.38, 124.00, 117.68, 116.53, 109.34, 85.64, 81.42, 62.35, 34.91, 32.11, 14.28.

HRMS (ESI, m/z): $[M]^+$ calcd for $C_{31}H_{33}NO_2$ 451.2506, found 451.2503.

IR (ATR): $\tilde{\nu}$ (cm^{-1}) = 2956 (m), 2902 (w), 2865 (w), 2232 (w), 2201 (m), 1699 (vs), 1600 (m), 1512 (vs), 1500 (m), 1491 (m), 1471 (vs), 1444 (m), 1364 (s), 1325 (w), 1290 (vs), 1275 (s), 1263 (s), 1234 (m), 1187 (vs), 1166 (vs), 1129 (w), 1107 (w), 1092 (m), 1080 (w), 1035 (w), 1008 (m), 944 (w), 917 (w), 893 (m), 858 (w), 841 (m), 810 (vs), 765 (w), 751 (m), 743 (w), 720 (w), 654 (w), 642 (w), 613 (m), 597 (w), 564 (w), 541 (m), 469 (w), 426 (w), 407 (w).

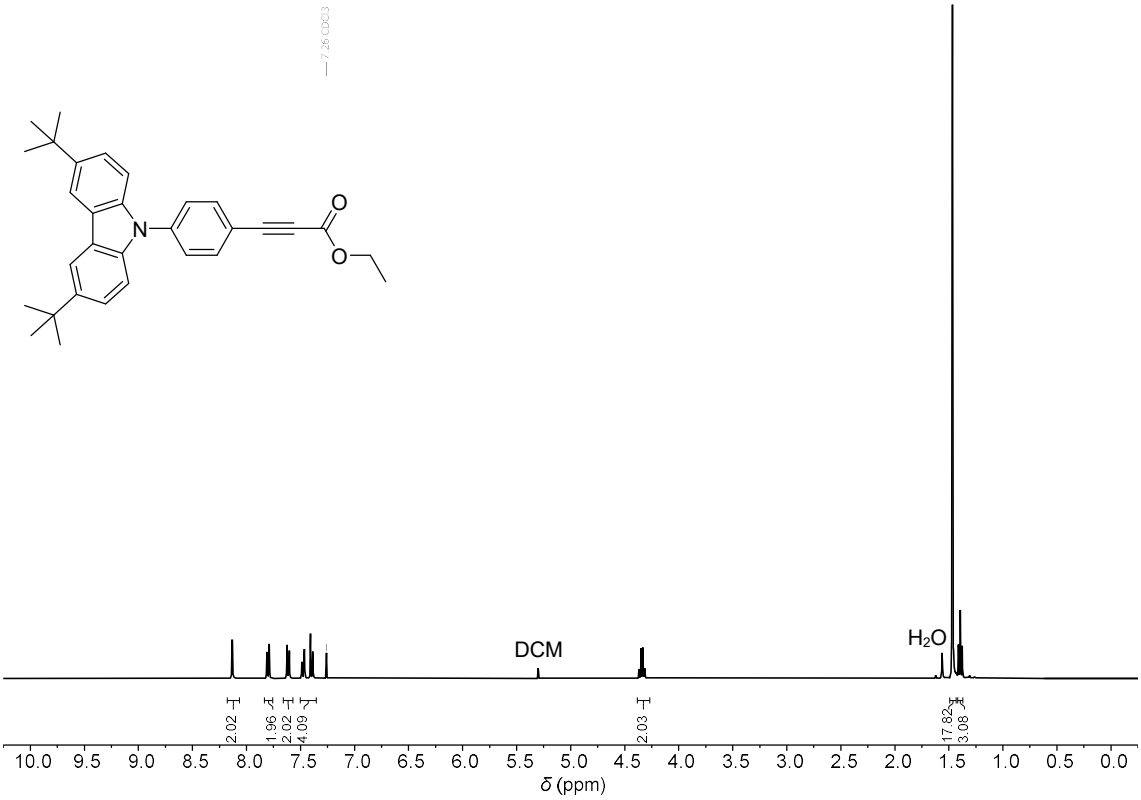

*Figure S17. ^{1}H NMR spectrum of **C3**, measured in $CDCl_3$ at 400 MHz.*

3-(4-(3,6-Di-*tert*-butyl-9*H*-carbazol-9-yl)phenyl)propiolic acid (C4)

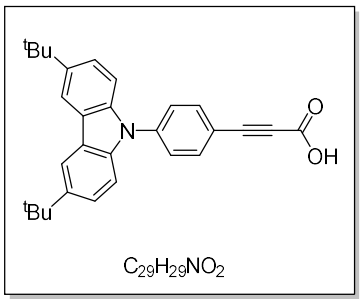

According to *GP1*, **C3** (2.00 g, 4.42 mmol, 1.00 equiv.) was dissolved in 100 ml solvent mixture and reacted with NaOH (354 mg, 8.85 mmol, 2.00 equiv.) overnight. After work-up, the title compound was obtained as a yellow solid (1.88 g, 14.42 mmol, quantitative yield).

^{1}H NMR (400 MHz, $CDCl_3$): δ (ppm) = 8.14 (d, J = 1.9 Hz, 2H, H_{ar}), 7.74 (d, J = 8.5 Hz, 2H, H_{ar}), 7.58 (d, J = 8.5 Hz, 2H, H_{ar}), 7.48 (dd, J = 8.7, 1.9 Hz, 2H, H_{ar}), 7.40 (d, J = 8.7 Hz, 2H, CH_{Ar}), 7.07 (d, J = 2.1 Hz, 2H, CH_{Ar}), 4.02 (dt, J = 9.0, 6.5 Hz, 4H, OCH_2), 1.98 – 1.83 (m, 4H, CH_2), 1.47 (s, 18H, CH_3), 1.12 (dt, J = 15.0, 7.4 Hz, 6H, CH_3)

^{13}C NMR (101 MHz, $CDCl_3$): δ (ppm) = 157.62, 143.76, 141.00, 138.46, 134.92, 126.26, 123.93, 116.91, 116.44, 109.22, 88.38, 80.59, 34.79, 31.98, 29.73.

HRMS (ESI, *m*/*z*): $[M]^+$ calcd for $C_{29}H_{29}NO_2$ 423.2193, found 423.2189.

IR (ATR): $\tilde{\nu}$ (cm^{-1}) = 2956 (m), 2902 (w), 2865 (w), 2228 (m), 2199 (w), 1740 (w), 1681 (vs), 1598 (m), 1512 (vs), 1489 (s), 1471 (vs), 1413 (s), 1393 (w), 1362 (vs), 1325 (m), 1292 (vs), 1261 (vs), 1234 (s), 1212 (vs), 1170 (vs), 1107 (w), 1082 (w), 1037 (w), 919 (w), 878 (s), 841 (m), 810 (vs), 759 (w), 743 (w), 718 (w), 654 (w), 642 (w), 631 (w), 611 (s), 599 (m), 539 (w), 471 (w).

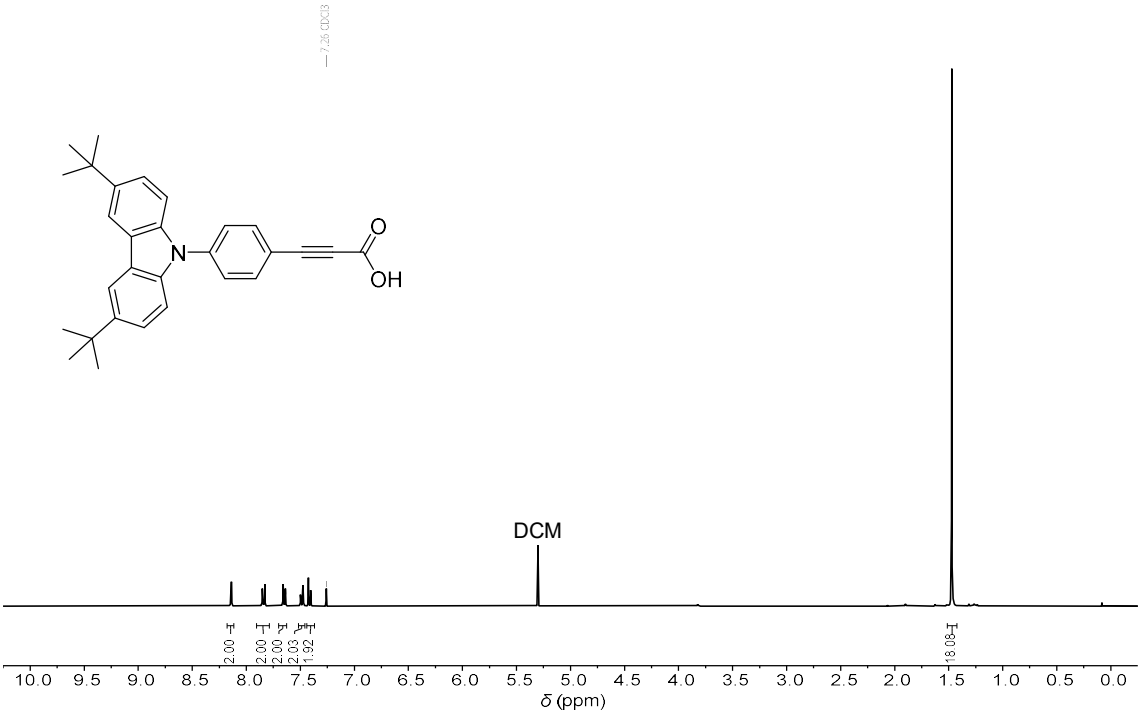

*Figure S18. ^1H NMR spectrum of **C4**, measured in $CDCl_3$ at 400 MHz.*

Ethyl 3-(4-((4-(3,6-di-*tert*-butyl-9*H*-carbazol-9-yl)phenyl)ethynyl)-2,5-dipropoxyphenyl)propiolate (C5)

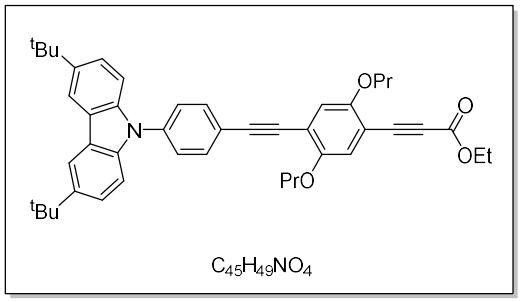

According to GP2, **C4** (1.40 g, 3.30 mmol, 1.00 equiv.), compound **6** (1.16 g, 3.14 mmol, 0.95 equiv.), $Pd(dppf)Cl_2 \cdot CH_2Cl_2$ (67.5 mg, 82.6 µmol, 0.025 equiv.), SPhos (67.9 mg, 165 µmol, 0.05 equiv.) and Cs_2CO_3 (1.29 g, 3.96 mmol, 1.20 equiv.) were reacted 10 mL toluene/THF (7:3) at 65 °C overnight. Purification by manual flash column chromatography (cyclohexane → cyclohexane/ethyl acetate 40:1), followed by automated flash column chromatography on a Biotage® Sfär Silica HC cartridge (cyclohexane → ethyl acetate/cyclohexane 2%), afforded the title compound as a yellow solid. (1.50 g, 2.25 mmol, 70%).

TLC (cyclohexane/ethyl acetate (40:1): R_f = 0.20.

^{1}H NMR (400 MHz, $CDCl_3$): δ (ppm) = 8.14 (d, J = 1.9 Hz, 2H, H_{ar}), 7.73 (d, J = 8.5 Hz, 2H, H_{ar}), 7.57 (d, J = 8.5 Hz, 2H, H_{ar}), 7.48 (dd, J = 8.6, 2.0 Hz, 2H, H_{ar}), 7.39 (d, J = 8.7 Hz, 2H, H_{ar}), 7.06 (d, J = 1.5 Hz, 2H, H_{ar}), 4.31 (q, J = 7.1 Hz, 2H, CH_2CH_3), 4.08 – 3.89 (m, 4H, OCH_2CH_3), 1.98 – 1.74 (m, 4H, $CH_2CH_2CH_3$), 1.47 (s, 18H, CCH_3), 1.36 (t, J = 7.1 Hz, 3H, CH_2CH_3), 1.16 – 1.05 (m, 6H, CH_2CH_3).

^{13}C NMR (101 MHz, $CDCl_3$): δ (ppm) = 155.38, 154.31, 153.53, 143.40, 138.98, 138.53, 133.21, 126.52, 123.87, 123.75, 121.58, 117.98, 117.07, 116.89, 116.45, 110.15, 109.35, 95.61, 86.34, 85.67, 83.11, 71.32, 71.23, 62.18, 34.89, 32.13, 27.06, 22.80, 22.70, 14.26, 10.72, 10.57.

HRMS (ESI, m/z): $[M]^+$ calcd for $C_{45}H_{49}NO_4$ 667.3662, found 667.3661.

IR (ATR): $\tilde{\nu}$ (cm^{-1}) = 2960 (m), 2902 (w), 2869 (w), 2213 (m), 1703 (vs), 1598 (w), 1514 (vs), 1489 (s), 1471 (vs), 1415 (m), 1386 (m), 1366 (s), 1325 (w), 1294 (w), 1277 (m), 1261 (s), 1218 (vs), 1172 (s), 1152 (vs), 1103 (m), 1080 (w), 1063 (w), 1043 (w), 1033

(m), 1016 (m), 983 (m), 944 (w), 876 (w), 860 (w), 841 (m), 808 (s), 745 (w), 718 (w), 654 (w), 611 (w), 597 (w).

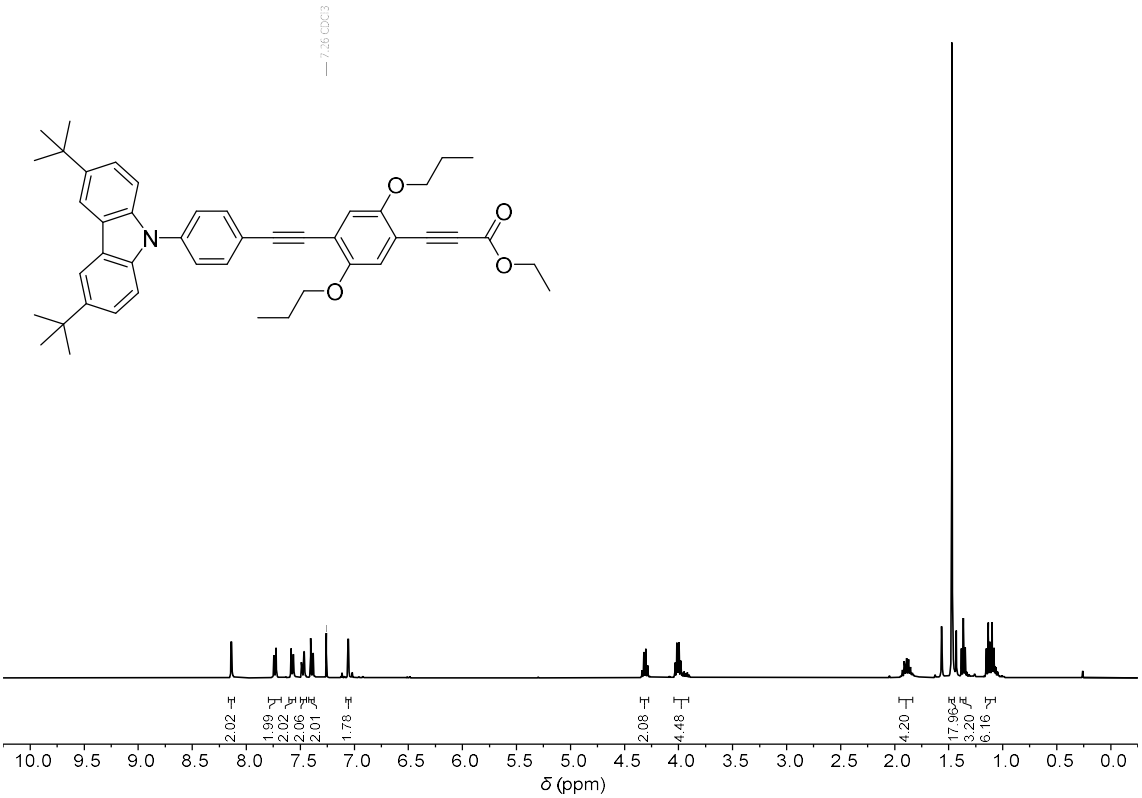

*Figure S19. ^{1}H NMR spectrum of **C5**, measured in $CDCl_3$ at 400 MHz.*

3-(4-((4-(3,6-Di-*tert*-butyl-9*H*-carbazol-9-yl)phenyl)ethynyl)-2,5-dipropoxyphenyl)propiolic acid (C6)

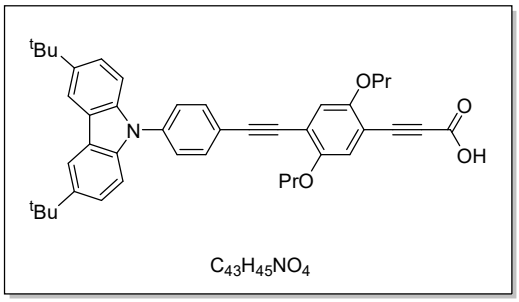

According to *GP1*, **C5** (1.30 g, 1.95 mmol, 1.00 equiv.) was dissolved in 36 ml THF and 12 ml MeOH and reacted with NaOH (156 mg, 3.89 mmol, 1.00 equiv.) in 12 ml water overnight. After work-up, the title compound was obtained as a yellow solid (1.25 g, 1.95 mmol, quantitative yield).

^{1}H NMR (400 MHz, $CDCl_3$): δ (ppm) = 8.14 (d, J = 1.9 Hz, 2H, H_{ar}), 7.74 (d, J = 8.5 Hz, 2H, H_{ar}), 7.58 (d, J = 8.5 Hz, 2H, H_{ar}), 7.48 (dd, J = 8.7, 1.9 Hz, 2H, H_{ar}), 7.40 (d, J = 8.7 Hz, 2H, H_{ar}), 7.07 (d, J = 2.1 Hz, 2H, H_{ar}), 4.03 (t, J = 6.5 Hz, 2H, OCH_2), 4.01 (t, J = 6.5 Hz, 2H, OCH_2), 1.98 – 1.83 (m, 4H, $CH_2CH_2CH_3$), 1.47 (s, 18H, CCH_3), 1.14 (t, J = 7.4 Hz, 3H, CH_2CH_3), 1.10 (t, J = 7.4 Hz, 3H, CH_2CH_3).

^{13}C NMR (101 MHz, $CDCl_3$): δ (ppm) = 156.63, 155.59, 153.56, 143.42, 138.97, 138.61, 133.24, 126.53, 123.88, 123.76, 121.49, 118.09, 117.50, 117.07, 116.47, 109.58, 109.35, 95.93, 86.27, 85.67, 84.91, 71.37, 71.27, 34.90, 32.14, 22.80, 22.69, 10.72, 10.58.

HRMS (ESI, m/z): $[M]^+$ calcd for $C_{43}H_{45}NO_4$ 639.3343, found 639.3350.

IR (ATR): $\tilde{\nu}$ (cm^{-1}) = 2960 (m), 2935 (m), 2867 (w), 2213 (s), 1676 (vs), 1516 (vs), 1497 (s), 1489 (s), 1471 (vs), 1421 (m), 1409 (s), 1388 (s), 1364 (s), 1284 (vs), 1263 (vs), 1218 (vs), 1170 (s), 1063 (m), 1014 (w), 985 (s), 917 (w), 874 (m), 860 (m), 841 (m), 817 (s), 804 (s), 611 (s), 597 (w).

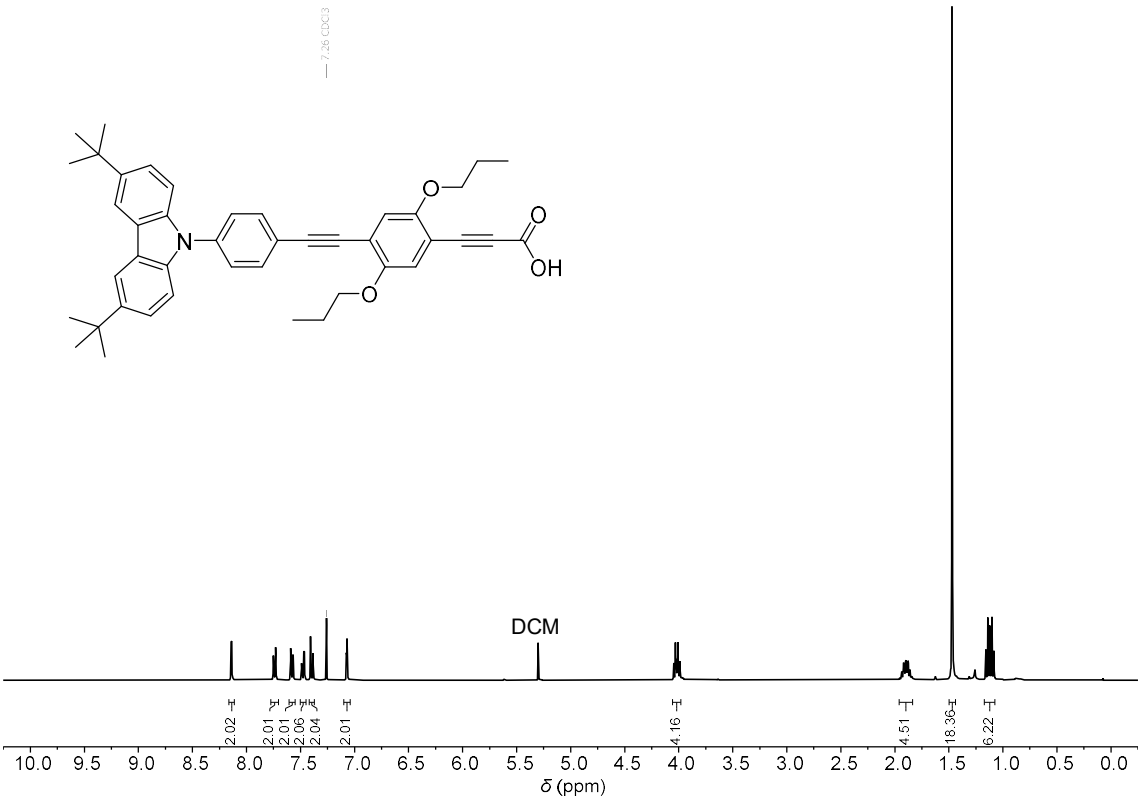

*Figure S20. ^{1}H NMR spectrum of **C6**, measured in $CDCl_3$ at 400 MHz.*

Ethyl 3-(4-((4-((4-(3,6-di-*tert*-butyl-9*H*-carbazol-9-yl)phenyl)ethynyl)-2,5-dipropoxyphenyl)ethynyl)-2,5-dipropoxyphenyl)propiolate (C7)

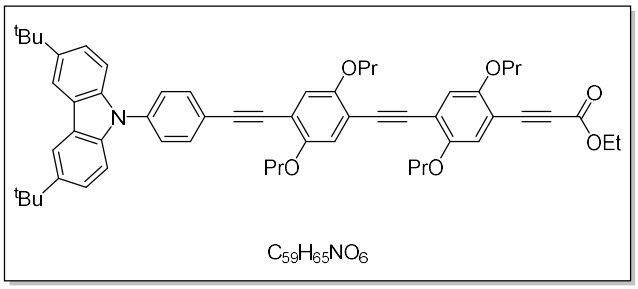

Accoding to *GP2*, **C6** (1.00 g, 1.56 mmol, 1.00 equiv.), compound **6** (548 mg, 1.48 mmol, 0.95 equiv.), $Pd(dppf)Cl_2 \cdot CH_2Cl_2$ (31.9 mg, 39.1 µmol, 0.025 equiv.), SPhos (32.1 mg, 78.1 µmol, 0.05 equiv.) and Cs_2CO_3 (611 mg, 1.87 mmol, 1.20 equiv.) were used in the general procedure. Purification by automated flash column chromatography on a 25 g Biotage® Silica Fär HC cartridge (ethyl acetate/cyclohexane 2% → 10%) yielded the title compound as an orange solid. (994 mg, 1.12 mmol, 75%).

TLC (cyclohexane/ethyl acetate 40:1): R_f = 0.10.

^{1}H NMR (400 MHz, $CDCl_3$): δ (ppm) = 8.14 (d, J = 1.9 Hz, 2H, H_{ar}), 7.80 – 7.69 (m, 2H, H_{ar}), 7.61 – 7.53 (m, 2H, H_{ar}), 7.48 (dd, J = 8.7, 1.9 Hz, 2H, H_{ar}), 7.39 (d, J = 8.6 Hz, 2H, H_{ar}), 7.09 – 6.99 (m, 4H, H_{ar}), 4.31 (q, J = 7.1 Hz, 2H, OCH_2CH_3), 4.09 – 3.84 (m, 8H, OCH_2CH_2), 2.02 – 1.79 (m, 8H, $CH_2CH_2CH_3$), 1.47 (s, 18H, CCH_3), 1.36 (t, J = 7.1 Hz 3H, CH_2CH_3), 1.19 – 0.97 (m, 12H, CH_2CH_3).

^{13}C NMR (101 MHz, $CDCl_3$) δ(ppm) = 155.22, 154.19, 153.67, 153.62, 153.18, 143.21, 138.89, 138.15, 132.98, 126.39, 123.73, 123.59, 121.80, 118.03, 117.28, 117.22, 117.16, 117.13, 116.31, 114.27, 114.07, 109.87, 109.23, 94.49, 92.73, 91.01, 86.70, 85.51, 83.07, 77.23, 71.11, 62.03, 34.76, 32.01, 22.76, 22.69, 22.60, 22.55, 14.13, 10.63, 10.59, 10.54, 10.42.

HRMS (ESI, m/z): $[M]^+$ calculated for $C_{59}H_{65}NO_6$ = 883.4806, found 883.4808

IR (ATR): $\tilde{\nu}$ (cm^{-1}) = 2960 (m), 2935 (w), 2902 (w), 2874 (w), 2211 (w), 1703 (s), 1514 (s), 1504 (m), 1489 (s), 1471 (vs), 1421 (m), 1384 (m), 1364 (s), 1325 (w), 1294 (w), 1273 (s), 1261 (s), 1236 (s), 1212 (vs), 1172 (s), 1148 (vs), 1105 (m), 1061 (m), 1043 (m),

1035 (m), 1014 (s), 981 (s), 946 (w), 919 (w), 876 (w), 858 (m), 841 (m), 808 (s), 745 (w), 718 (w), 611 (w).

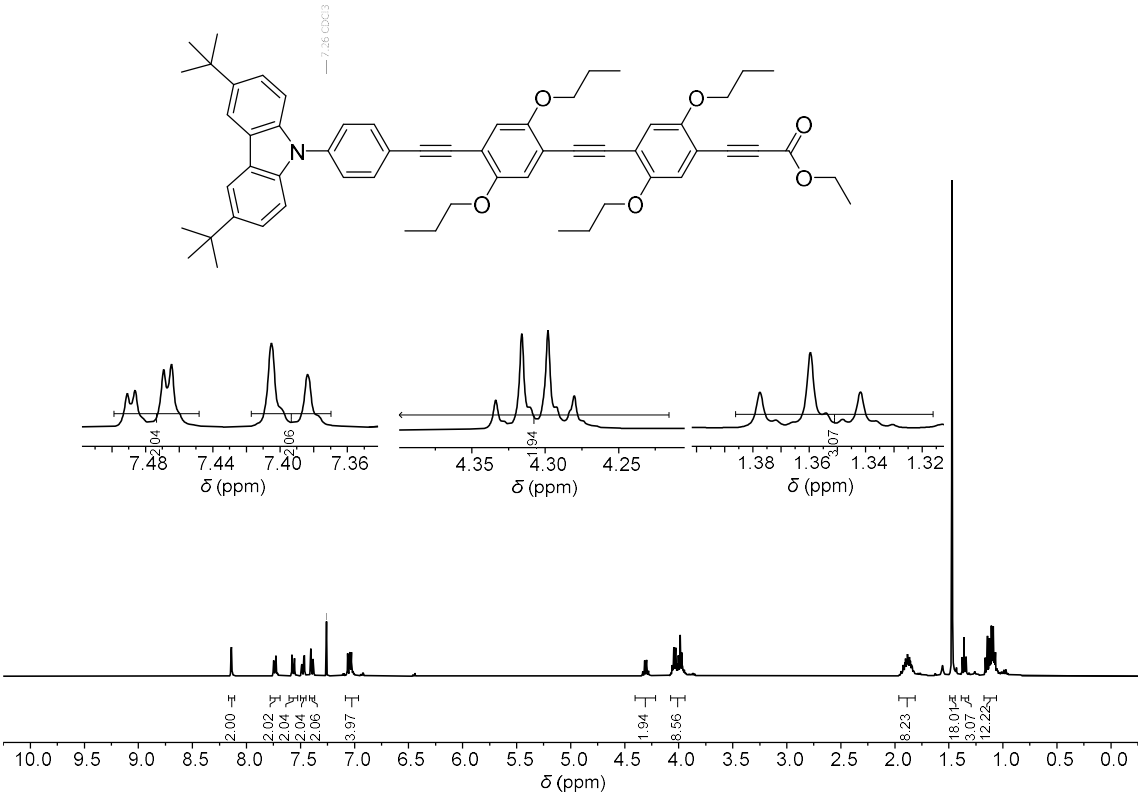

*Figure S 21. ^{1}H NMR spectrum of **C7**, measured in $CDCl_3$ at 400 MHz.*

3-(4-((4-((4-(3,6-di-*tert*-butyl-9*H*-carbazol-9-yl)phenyl)ethynyl)-2,5-dipropoxyphenyl)ethynyl)-2,5-dipropoxyphenyl)propiolic acid (C8)

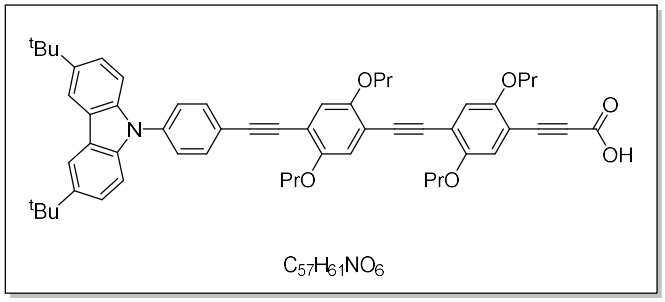

According to *GP1*, **C7** (900 mg, 1.02 mmol, 1.00 equiv.) was dissolved in 15 ml THF and 5 ml MeOH and reacted with NaOH (82.4 mg, 2.04 mmol, 2.00 equiv.)

in 5 ml water over night. After work-up, the title compound was obtained as a yellow solid (870 mg, 1.02 mmol, quant. yield).

^{1}H NMR (400 MHz, $CDCl_3$): δ (ppm) = 8.14 (d, J = 1.9 Hz, 2H, H_{ar}), 7.79 – 7.69 (m, 2H, H_{ar}), 7.63 – 7.53 (m, 2H, H_{ar}), 7.48 (dd, *J* = 8.7, 1.9 Hz, 2H, H_{ar}), 7.39 (d, *J* = 8.6 Hz, 2H, H_{ar}), 7.09 – 7.01 (m, 4H, H_{ar}), 4.08 – 3.93 (m, 8H, OCH_2CH_2), 1.97 – 1.81 (m, 8H, $CH_2CH_2CH_3$), 1.47 (s, 18H, CCH_3), 1.19 – 1.03 (m, 12H, CH_2CH_3).

^{13}C NMR (101 MHz, $CDCl_3$): δ (ppm) = 156.62, 155.58, 153.80, 153.78, 153.31, 143.35, 139.03, 133.12, 126.53, 123.87, 123.73, 118.26, 117.42, 117.29, 117.24, 116.45, 109.42, 109.37, 77.36, 71.34, 71.26, 34.90, 32.14, 22.89, 22.82, 22.73, 22.67, 10.76, 10.72, 10.67, 10.56.

HRMS (ESI, *m*/*z*): $[M]^+$ calculated for $C_5H_{61}NO_6$ = 855.4493, found 855.4496.

IR (ATR): $\tilde{\nu}$ (cm^{-1}) = 2960 (m), 2937 (m), 2904 (w), 2874 (w), 2205 (m), 1711 (w), 1676 (m), 1602 (w), 1514 (vs), 1504 (m), 1489 (s), 1471 (vs), 1421 (s), 1384 (s), 1366 (s), 1325 (w), 1292 (m), 1273 (s), 1263 (s), 1203 (vs), 1105 (w), 1061 (m), 1043 (m), 1012 (m), 981 (s), 915 (w), 874 (w), 860 (m), 841 (m), 808 (s), 763 (w), 751 (w), 740 (w), 712 (w), 679 (w), 654 (w), 611 (m), 597 (w).

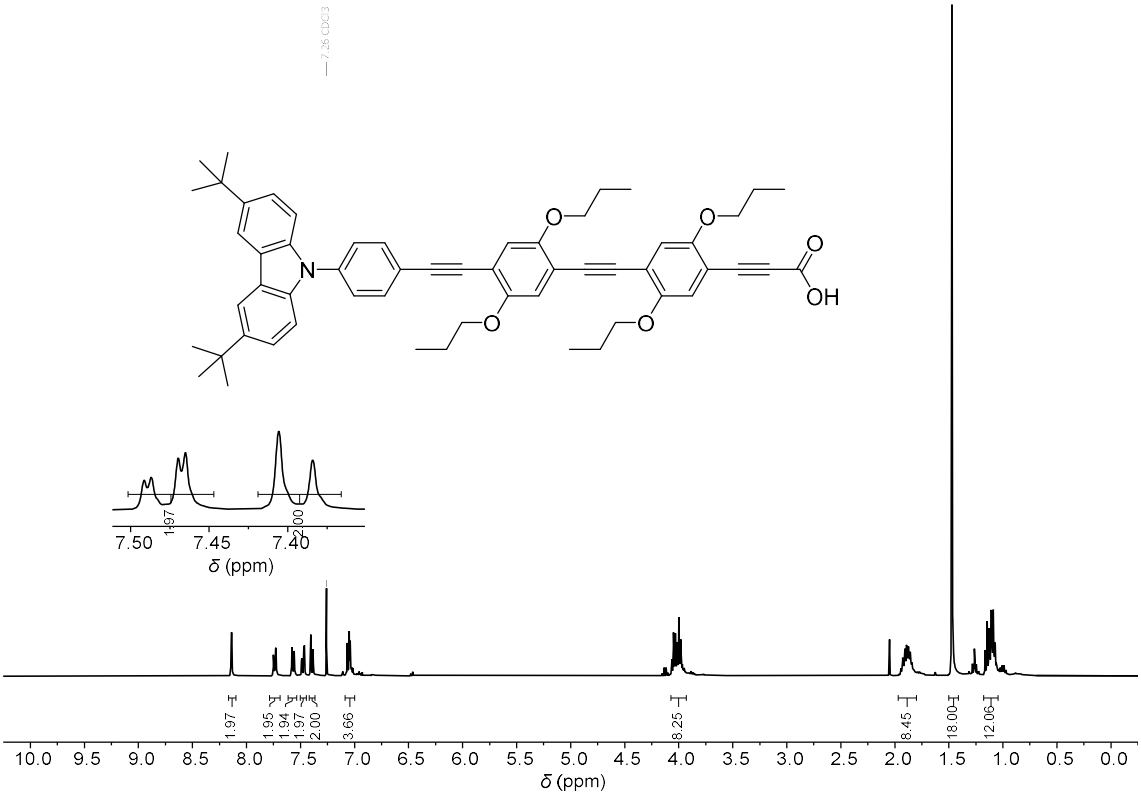

*Figure S22. ^{1}H NMR spectrum of **C8**, measured in $CDCl_3$ at 400 MHz.*

Ethyl 3-(4-((4-((4-((4-(3,6-di-*tert*-butyl-9*H*-carbazol-9-yl)phenyl)ethynyl)-2,5-dipropoxyphenyl)ethynyl)-2,5-dipropoxyphenyl)ethynyl)-2,5-dipropoxyphenyl)propiolate (C9)

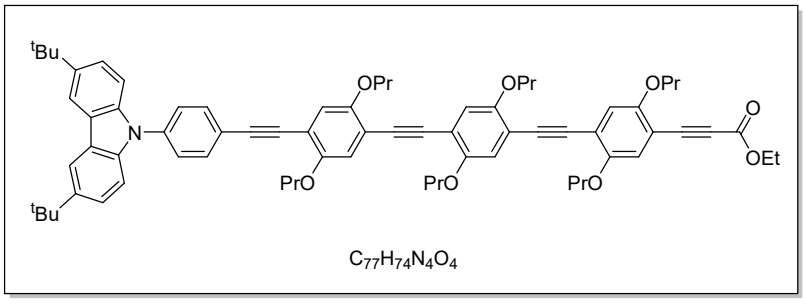

According to *GP2*, **C8** (350 mg, 408 µmol, 1.00 equiv.), compound **6** (136 mg, 367 µmol, 0.90 equiv.), $Pd(dppf)Cl_2 \cdot CH_2Cl_2$ (8.4 mg, 10 µmol, 0.025 equiv.), SPhos (8.4 mg, 20 µmol, 0.05 equiv.), and Cs_2CO_3 (160 mg, 490 µmol, 1.20 equiv.) were reacted in

20 mL solvent mixture. Purification by flash column chromatography (cyclohexane/ethyl acetate 30:1 → 10:1), followed by prep-TLC (cyclohexane/DCM 1:3) yielded the title compound as a yellow solid. (325 mg, 295 µmol, 80%).

TLC (cyclohexane/ethyl acetate 40:1): R_f = 0.20.

^{1}H NMR (400 MHz, $CDCl_3$): δ (ppm) = 8.14 (d, J = 1.9 Hz, 2H, H_{ar}), 7.74 (d, J = 8.5 Hz, 2H, H_{ar}), 7.56 (d, J = 8.5 Hz, 2H, H_{ar}), 7.48 (dd, J = 8.7, 1.9 Hz, 2H, H_{ar}), 7.39 (d, J = 8.6 Hz, 2H, H_{ar}), 7.08 – 6.99 (m, 6H, H_{ar}), 4.30 (q, J = 7.1 Hz, 2H, OCH_2CH_3), 4.09 – 3.93 (m, 12H, OCH_2CH_2), 1.98 – 1.79 (m, 12H, $CH_2CH_2CH_3$), 1.47 (s, 18H, CCH_3), 1.36 (t, J = 7.1 Hz, 3H, CH_2CH_3), 1.18 – 1.05 (m, 18H, CH_2CH_3).

^{13}C NMR (101 MHz, $CDCl_3$): δ (ppm) = 143.20, 138.90, 132.97, 126.39, 123.73, 123.58, 117.24, 116.31, 115.54, 109.24, 77.23, 71.18, 71.11, 34.76, 32.01, 29.72, 22.77, 22.68, 22.65, 22.59, 22.54, 14.13, 10.63, 10.57, 10.53, 10.41.

HRMS (ESI, m/z): $[M]^+$ calculated for $C_{73}H_{81}NO_8$ = 1099.5957, found 1099.5958

IR (ATR): $\tilde{\nu}$ (cm^{-1}) = 2962 (w), 2935 (w), 2871 (w), 2211 (w), 1705 (m), 1602 (w), 1514 (s), 1493 (m), 1471 (s), 1421 (s), 1390 (s), 1366 (m), 1325 (w), 1292 (w), 1275 (m), 1261 (m), 1249 (m), 1214 (vs), 1150 (m), 1096 (w), 1080 (w), 1061 (w), 1043 (m), 1016 (s), 985 (w), 973 (w), 946 (w), 907 (w), 889 (w), 878 (w), 858 (s), 841 (w), 833 (w), 808 (m), 775 (w), 749 (w), 732 (w), 720 (w), 697 (w), 654 (w), 611 (w).

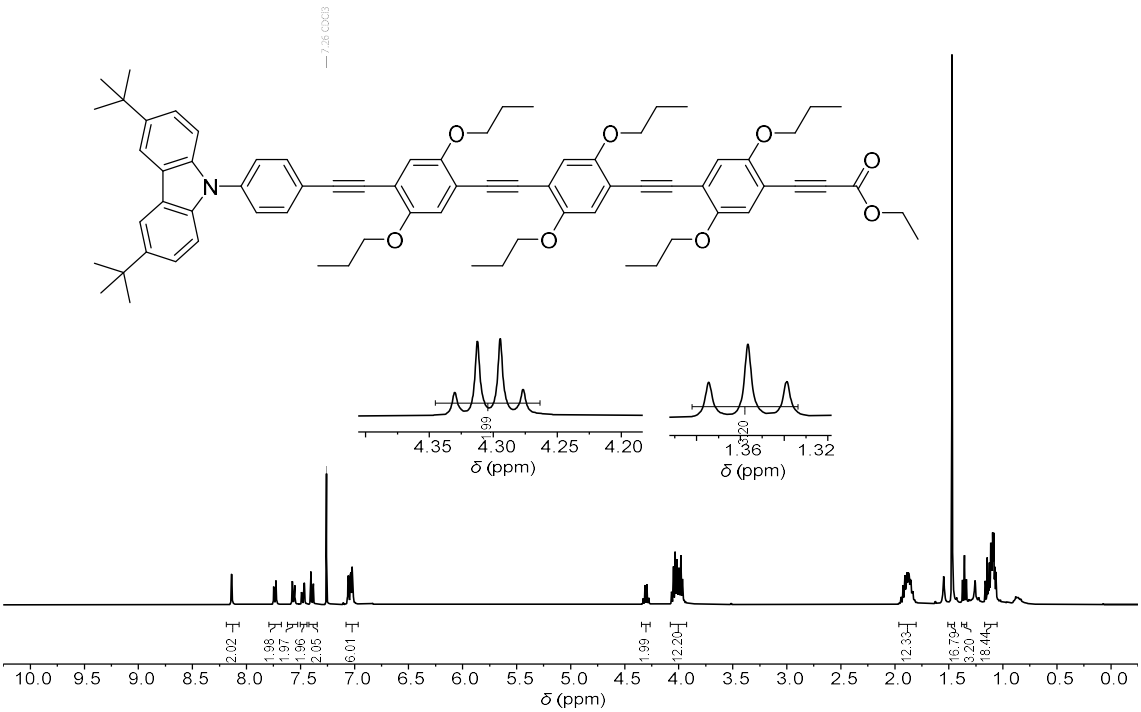

*Figure S23. ^{1}H NMR spectrum of **C9**, measured in $CDCl_3$ at 400 MHz.*

3-(4-((4-((4-((4-(3,6-di-tert-butyl-9H-carbazol-9-yl)phenyl)ethynyl)-2,5-dipropoxyphenyl)ethynyl)-2,5-dipropoxyphenyl)ethynyl)-2,5-dipropoxyphenyl)propiolic acid (C10)

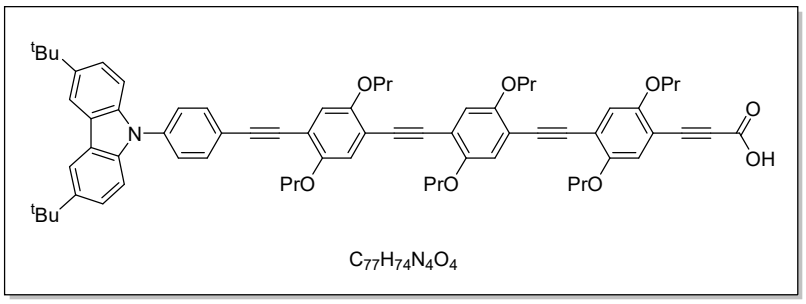

According to *GP1*, **C9** (199 mg, 181 µmol, 1.00 equiv.) was reacted with NaOH (30.0 mg, 726 µmol, 4.00 equiv.) in 10 mL of the solvent mixture. The title compound was obtained after work-up as a brawn solid (195 mg, 181 µmol, quantitative yield).

^{1}H NMR (400 MHz, $CDCl_3$): δ (ppm) = 8.14 (d, J = 1.9 Hz, 2H, H_{ar}), 7.77 – 7.71 (m, 2H, H_{ar}), 7.60 – 7.53 (m, 2H, H_{ar}), 7.48 (dd, J = 8.6, 2.0 Hz, 2H, H_{ar}), 7.39 (d, J = 8.6 Hz, 2H, H_{ar}), 7.08 – 7.01 (m, 6H, H_{ar}), 4.10 – 3.94 (m, 12H, OCH_2CH_2), 1.98 – 1.80 (m, 12H, $CH_2CH_2CH_3$), 1.47 (s, 18H, CCH_3), 1.19 – 1.02 (m, 18H, CH_2CH_3).

^{13}C NMR (101 MHz, $CDCl_3$): δ (ppm) = 155.87, 155.36, 153.69, 153.59, 153.52, 153.44, 153.17, 143.19, 138.89, 138.10, 132.96, 126.38, 123.73, 123.57, 121.84, 118.11, 117.45, 117.34, 117.25, 117.20, 117.10, 116.30, 114.43, 113.83, 109.23, 109.21, 104.52, 83.23, 71.25, 71.20, 71.19, 71.13, 61.85, 34.77, 32.01, 31.96, 29.71, 22.76, 22.71, 22.68, 22.66, 22.58, 22.53, 10.63, 10.60, 10.57, 10.56, 10.53, 10.42, 4.13.

HRMS (ESI, m/z): $[M]^+$ calcd for $C_{71}H_{77}NO_8$ = 1071.5644, found 1071.5640.

IR (ATR, $\tilde{\nu}$(cm^{-1})) = 2960 (w), 2929 (w), 2867 (w), 2205 (w), 1672 (m), 1514 (s), 1493 (m), 1471 (s), 1421 (s), 1388 (s), 1368 (m), 1275 (s), 1263 (s), 1216 (vs), 1164 (m), 1129 (w), 1103 (w), 1078 (w), 1061 (w), 1043 (s), 1022 (vs), 985 (w), 973 (w), 917 (w), 878 (w), 858 (s), 841 (w), 833 (w), 808 (s), 775 (w), 767 (w), 716 (w), 611 (w).

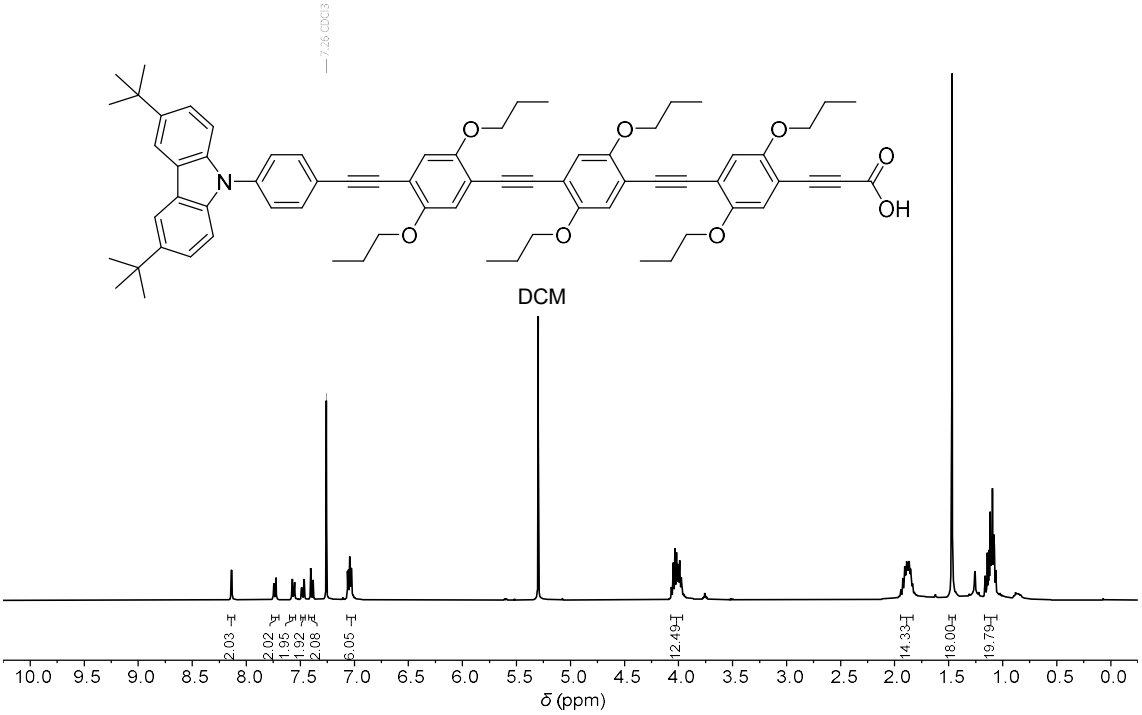

*Figure S24. ^{1}H NMR spectrum of **C10**, measured in $CDCl_3$ at 400 MHz.*

3,6-di-*tert*-butyl-9-(4-((4-(4,6-diphenyl-1,3,5-triazin-2-yl)phenyl)ethynyl)phenyl)-9*H*-carbazole (PE0)

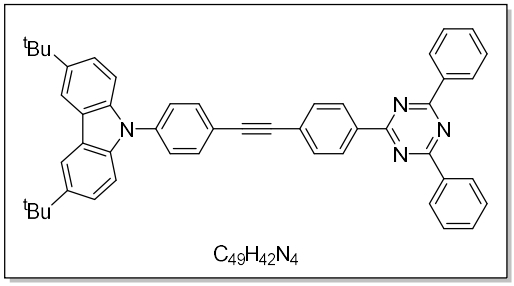

According to *GP2*, **C4** (200 mg, 472 µmol, 1.00 equiv.) 2-(4-bromophenyl)-4,6-diphenyl-1,3,5-triazine (165 mg, 425 µmol, 0.90 equiv.), $Pd(dppf)Cl_2 \cdot CH_2Cl_2$ (9.6 mg, 12 µmol, 0.025 equiv.), SPhos (9.6 mg, 24 µmol, 0.05 equiv.) and cesium carbonate (185 mg, 567 µmol, 1.20 equiv.) were degassed and reacted in 5 mL solvent mixture. Purification via flash column chromatography (cyclohexane/DCM 10:1) and following washing with cyclohexane yielded the title compound as a white solid. (195 mg, 283 µmol, 66%).

TLC (cyclohexane/DCM 40:1): $R_f = 0.45$.

^{1}H NMR (400 MHz, $CDCl_3$): δ (ppm) = 8.84 – 8.77 (m, 6H, H_{ar}), 8.15 (d, J = 1.9 Hz, 2H, H_{ar}), 7.85 – 7.75 (m, 4H, H_{ar}), 7.67 – 7.56 (m, 8H, H_{ar}), 7.49 (dd, J = 8.7, 1.9 Hz, 2H, H_{ar}), 7.41 (d, J = 8.7 Hz, 2H, H_{ar}), 1.48 (s, 18H, CCH_3).

^{13}C NMR (101 MHz, $CDCl_3$): δ (ppm) = 171.90, 171.15, 143.42, 138.99, 138.64, 136.30, 136.17, 133.34, 132.77, 132.03, 129.16, 129.08, 128.84, 127.43, 126.57, 123.91, 123.78, 121.39, 116.47, 109.36, 91.74, 90.14, 34.91, 32.15, 27.07.

HRMS (ESI, m/z): $[M]^+$ calcd for $C_{49}H_{42}N_4$ 686.3404, found 686.3405.

IR (ATR) $\tilde{\nu}$ (cm^{-1}) = 2962 (w), 1598 (w), 1588 (w), 1565 (w), 1518 (vs), 1489 (m), 1473 (m), 1446 (w), 1405 (vw), 1366 (vs), 1327 (w), 1294 (w), 1265 (w), 1236 (w), 1175 (w), 1137 (vw), 1105 (vw), 1024 (vw), 1014 (vw), 880 (w), 862 (vw), 835 (m), 815 (m), 769 (s), 736 (w), 691 (m), 662 (w), 650 (w), 638 (w), 613 (w), 599 (vw), 527 (w).

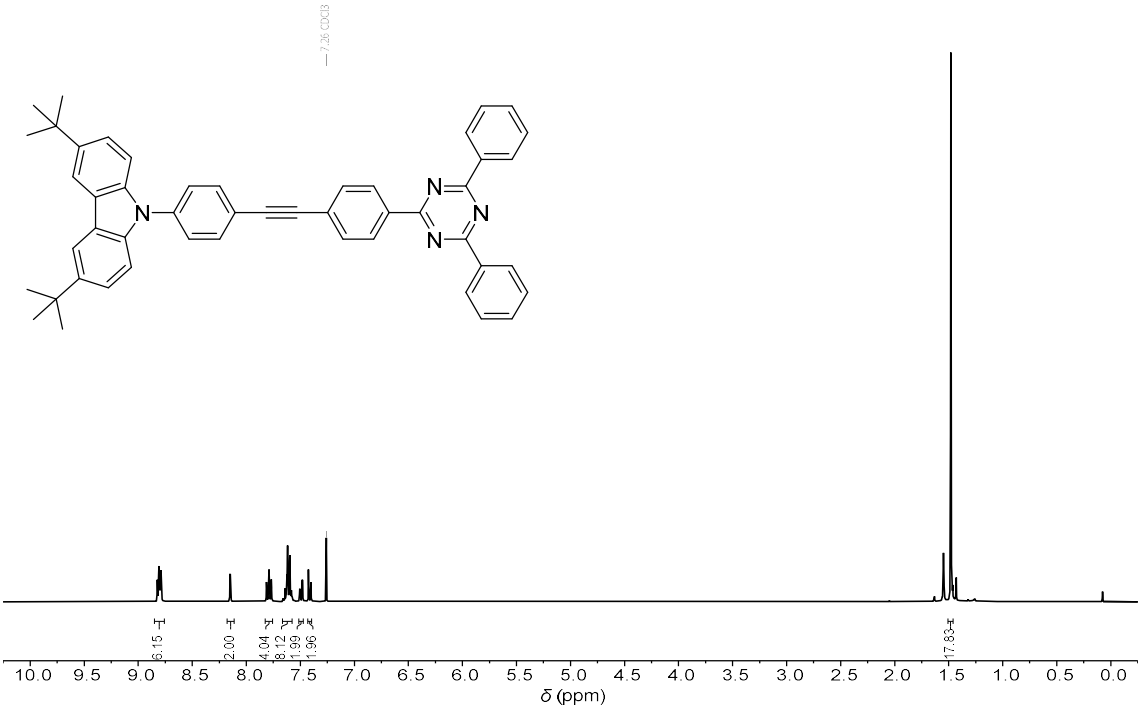

*Figure S25. ^{1}H NMR spectrum of **PE0**, measured in $CDCl_3$ at 400 MHz.*

3,6-Di-*tert*-butyl-9-(4-((4-((4,6-diphenyl-1,3,5-triazin-2-yl)ethynyl)-2,5-dipropoxyphenyl)ethynyl)phenyl)-9*H*-carbazole (PE1)

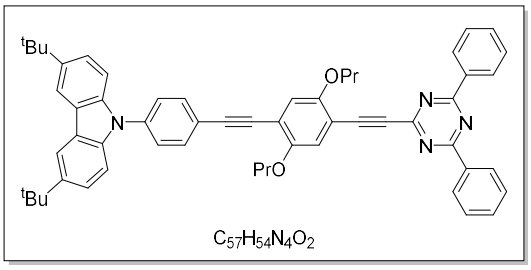

According to GP2, **C6** (150 mg, 234 µmol, 1.00 equiv.), 2-(4-bromophenyl)-4,6-diphenyl-1,3,5-triazine (100 mg, 257 µmol, 1.10 equiv.), Pd(dppf)Cl_2·CH_2Cl_2 (4.8 mg, 5.8 µmol, 0.025 equiv.), SPhos (4.8 mg, 12 µmol, 0.05 equiv.) and cesium carbonate (91.6 mg, 281 µmol, 1.20 equiv.) were reacted in 5 mL solvent mixture at 65 °C. Purification by automated flash column chromatography on a 10 g Biotage® Sfär Silica HC cartridge (ethyl acetate/cyclohexane 0% → 5%), followed by manual flash column

chromatography (cyclohexane/DCM/ethyl acetate 90:10:0 → 83:17:0 → 83:16:1), and subsequent sonication in acetonitrile yielded a neo-yellow solid. (122 mg, 135 µmol, 43%).

TLC (cyclohexane/ethyl acetate 40:1): R_f = 0.33.

^{1}H NMR (400 MHz, $CDCl_3$): δ (ppm) = 8.79 (dd, J = 8.3, 1.8 Hz, 6H, H_{ar}), 8.14 (d, J = 1.9 Hz, 2H, H_{ar}), 7.79 – 7.72 (m, 4H, H_{ar}), 7.67 – 7.55 (m, 8H, H_{ar}), 7.48 (dd, J = 8.7, 1.9 Hz, 2H, H_{ar}), 7.40 (d, J = 8.6 Hz, 2H, H_{ar}), 7.10 (d, J = 3.7 Hz, 2H, H_{ar}), 4.07 (t, J = 6.4 Hz, 4H, OCH_2CH_2), 2.00 – 1.89 (m, 4H, $CH_2CH_2CH_3$), 1.47 (s, 18H, CCH_3), 1.17 (t, J = 7.4 Hz, 3H, CH_2CH_3), 1.16 (t, J = 7.4 Hz, 3H, CH_2CH_3).

^{13}C NMR (101 MHz, $CDCl_3$): δ (ppm) = 171.73, 171.04, 153.88, 153.74, 143.22, 138.90, 138.16, 136.18, 135.86, 133.00, 132.61, 131.80, 129.01, 128.90, 128.69, 127.66, 126.40, 123.74, 123.60, 121.81, 117.03, 116.32, 114.36, 113.81, 109.25, 94.85, 94.54, 88.85, 86.71, 71.19, 34.77, 32.01, 26.93, 22.80, 10.66.

HRMS (ESI, m/z): $[M]^+$ calculated for $C_{63}H_{58}N_4O_2$ = 902.4554, found 902.4537.

IR (ATR) $\tilde{\nu}$ (cm^{-1}) = 2960 (w), 2904 (w), 2867 (w), 1600 (w), 1588 (w), 1563 (w), 1514 (vs), 1471 (s), 1446 (m), 1415 (w), 1390 (w), 1368 (vs), 1325 (w), 1294 (w), 1279 (w), 1263 (m), 1232 (w), 1218 (s), 1175 (w), 1148 (w), 1127 (w), 1103 (w), 1065 (w), 1045 (w), 1026 (m), 1016 (w), 987 (w), 975 (w), 876 (w), 858 (w), 841 (m), 833 (m), 808 (m), 784 (w), 769 (vs), 736 (m), 691 (s), 669 (w), 648 (w), 638 (w), 611 (w), 597 (w), 529 (w), 473 (w), 420 (w).

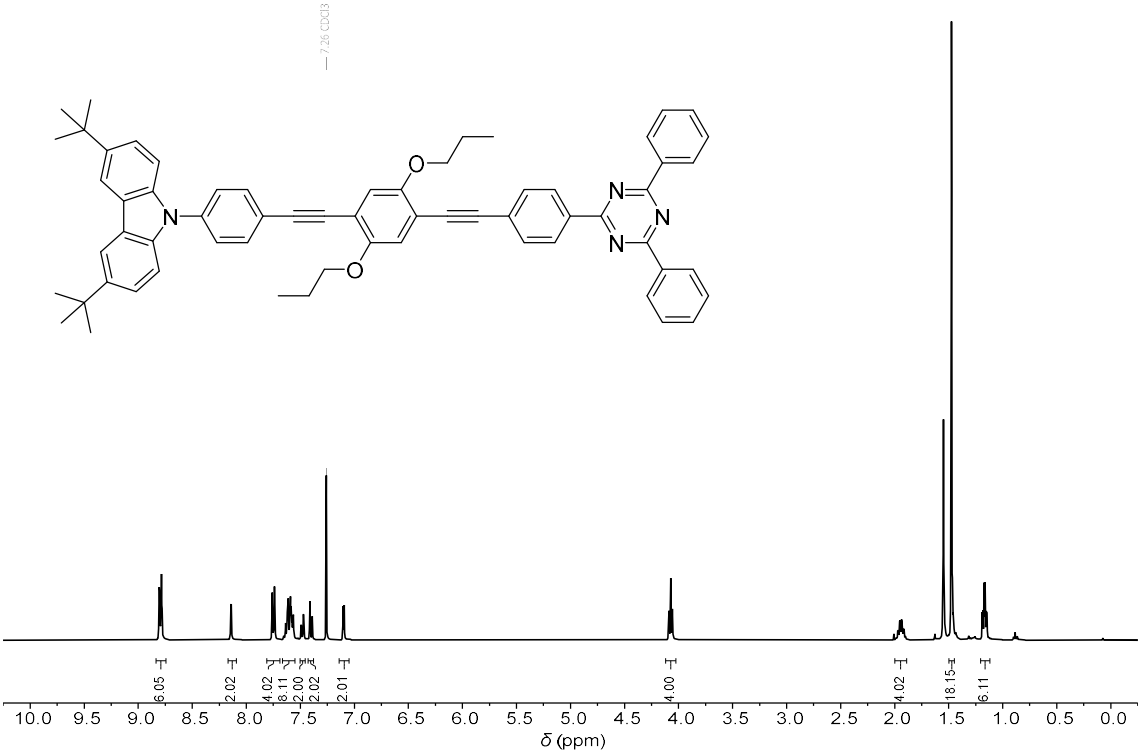

*Figure S26. ^1H NMR spectrum of **PE1**, measured in $CDCl_3$ at 400 MHz.*

3,6-Di-*tert*-butyl-9-(4-((4-((4-((4-(4,6-diphenyl-1,3,5-triazin-2-yl)phenyl)ethynyl)-2,5-dipropoxyphenyl)ethynyl)-2,5-dipropoxyphenyl)ethynyl)phenyl)-9*H*-carbazole (PE2)

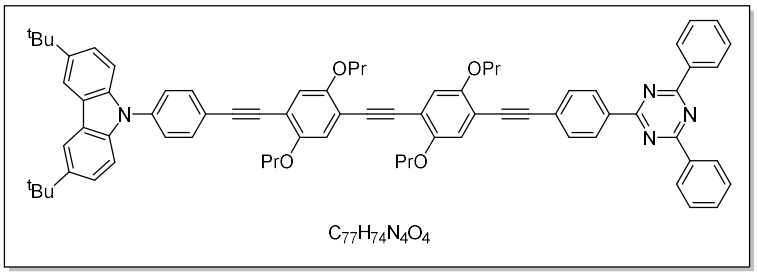

Accoding to *GP2*, **C8** (350 mg, 408 µmol, 1.00 equiv.), 2-(4-bromophenyl)-4,6-diphenyl-1,3,5-triazine (143 mg, 367 µmol, 0.9 equiv.), $Pd(dppf)Cl_2 \cdot CH_2Cl_2$ (8.4 mg, 10 µmol, 0.025 equiv.), SPhos (8.4 mg, 20 µmol, 0.05 equiv.) and Cs_2CO_3 (91.6 mg, 281 µmol, 1.20 equiv.) were reacted in 10 mL solvent mixture for 2 days. The crude product was purified by flash column chromatography (cyclohexane/ethyl acetate 40:1), recrystallized

in cyclohexane, and further purified with prep-TLC (cyclohexane/DCM 1:2). The title compound was obtained as a yellow solid (190 mg, 170 mg, 46%).

TLC (cyclohexane/ethyl acetate 40:1): R_f = 0.33.

^{1}H NMR (400 MHz, Chloroform-*d*): δ (ppm) = 8.84 – 8.74 (m, 6H, H_{ar}), 8.14 (d, J = 1.9 Hz, 2H, H_{ar}), 7.74 (d, J = 8.4 Hz, 4H, H_{ar}), 7.67 – 7.53 (m, 8H, H_{ar}), 7.48 (dd, J = 8.7, 1.9 Hz, 2H, H_{ar}), 7.40 (d, J = 8.6 Hz, 2H, H_{ar}), 7.10 (d, J = 3.7 Hz, 4H, H_{ar}), 4.13 – 3.98 (m, 8H, OCH_2CH_2), 1.99 – 1.83 (m, 8H, $CH_2CH_2CH_3$), 1.48 (s, 18H, CCH_3), 1.21 – 1.09 (m, 12H).

^{13}C NMR (101 MHz, Chloroform-*d*) δ(ppm) = 171.73, 171.04, 153.88, 153.74, 143.22, 138.90, 138.16, 136.18, 135.86, 133.00, 132.61, 131.80, 129.01, 128.90, 128.69, 127.66, 126.40, 123.74, 123.60, 121.81, 117.03, 116.32, 114.36, 113.81, 109.25, 94.85, 94.54, 88.85, 86.71, 71.19, 34.77, 32.01, 26.93, 22.80, 10.66.

IR (ATR, $\tilde{\nu}$(cm^{-1})) = 2960 (w), 2904 (w), 2867 (w), 1600 (w), 1588 (w), 1563 (w), 1514 (vs), 1471 (s), 1446 (m), 1415 (w), 1390 (w), 1368 (vs), 1325 (w), 1294 (w), 1279 (w), 1263 (m), 1232 (w), 1218 (s), 1175 (w), 1148 (w), 1127 (w), 1103 (w), 1065 (w), 1045 (w), 1026 (m), 1016 (w), 987 (w), 975 (w), 876 (w), 858 (w), 841 (m), 833 (m), 808 (m), 784 (w), 769 (vs), 736 (m), 691 (s), 669 (w), 648 (w), 638 (w), 611 (w), 597 (w), 529 (w), 473 (w), 420 (w).

HRMS (ESI, *m*/*z*): $[M]^+$ calculated for $C_{77}H_{74}N_4O_4$ = 1118.5705, found 1118.5697.

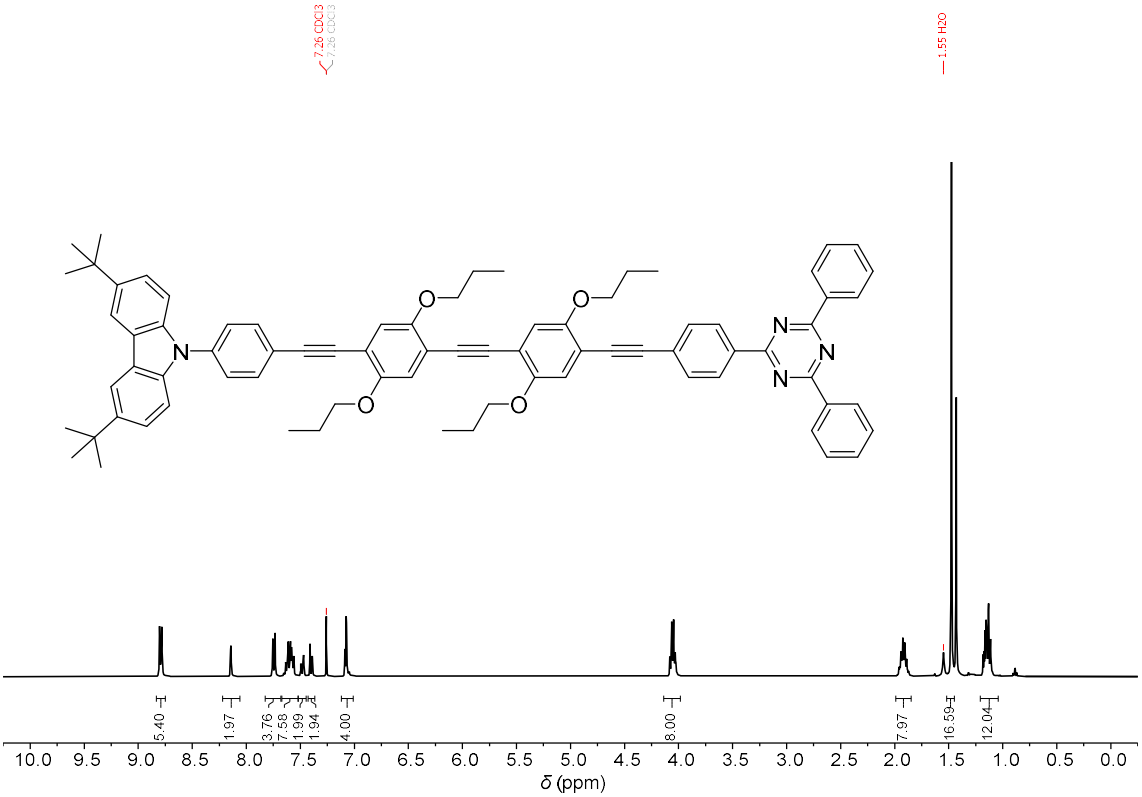

*Figure S27. ^{1}H NMR spectrum of **PE2**, measured in $CDCl_3$ at 400 MHz.*

3,6-Di-*tert*-butyl-9-(4-((4-((4-((4-((4-((4,6-diphenyl-1,3,5-triazin-2-yl)ethynyl)phenyl)ethynyl)-2,5-dipropoxyphenyl)ethynyl)-2,5-dipropoxyphenyl)ethynyl)-2,5-dipropoxyphenyl)ethynyl)phenyl)-9*H*-carbazole (PE3)

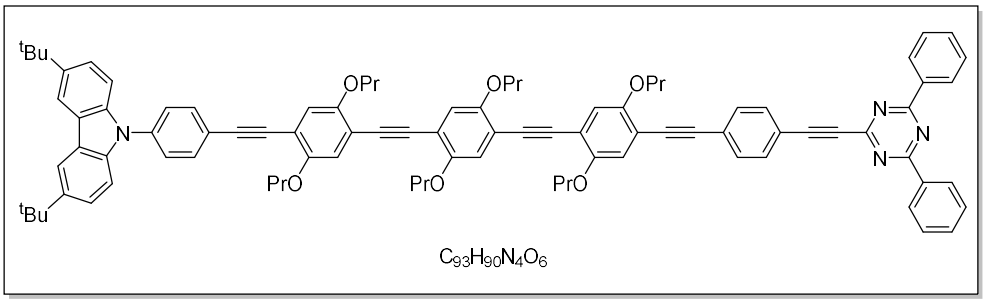

The synthesis follows the general procedure of the decarboxylative coupling. Acid protected trimer (150 mg, 139 µmol, 1.00 equiv.), 2-(4-bromophenyl)-4,6-diphenyl-

1,3,5-triazine (51.6 mg, 132.8 µmol, 0.95 equiv.), $PdCl_2(PPh_3)_3Fe$ dichloromethane complex (2.9 mg, 3.4 µmol, 0.025 eq), SPhos (2.9 mg, 6.9 µmol, 0.05 eq.), and cesium carbonate (54.7 mg, 168 µmol, 1.20 equiv.) were placed in a 50ml vial. After a reaction time of 48h the crude product was purified *via* column chromatography CH/EE (40:1) and was subsequently recrystallized in cyclohexane and washed with *n*-pentane. Yellow-orange crystals were received (103 mg, 77.4 µmol, 58%).

TLC (cyclohexane/ethyl acetate 40:1): R_f = 0.20.

^{1}H NMR (400 MHz, $CDCl_3$): δ(ppm) = 8.92 – 8.70 (m, 6H, H_{ar}), 8.14 (d, *J* = 1.9 Hz, 2H, H_{ar}), 7.74 (d, *J* = 8.1 Hz, 4H, H_{ar}), 7.70 – 7.53 (m, 8H, H_{ar}), 7.52 – 7.44 (m, 2H, H_{ar}), 7.40 (d, *J* = 8.6 Hz, 2H, H_{ar}), 7.13 – 6.98 (m, 6H, H_{ar}), 4.12 – 3.97 (m, 12H, OCH_2CH_2), 2.03 – 1.81 (m, 12H, $CH_2CH_2CH_3$), 1.47 (s, 18H, CCH_3), 1.22 – 1.06 (m, 18H, CH_2CH_3).

^{13}C NMR (101 MHz, $CDCl_3$): *δ* (ppm) = 171.72, 168.27, 167.71, 153.83, 153.70, 153.51, 143.19, 138.90, 138.09, 136.18, 135.82, 132.97, 132.60, 131.78, 129.00, 128.93, 128.89, 128.73, 128.68, 127.68, 126.43, 126.39, 123.73, 123.58, 121.87, 117.49, 117.41, 117.24, 117.22, 117.18, 116.30, 109.24, 103.16, 94.31, 91.84, 91.52, 91.42, 71.26, 71.19, 71.10, 62.32, 34.77, 32.06, 32.01, 22.78, 22.72, 22.70, 10.63, 10.62, 10.59.

HRMS (ESI, *m*/*z*): $[M]^+$ calculated for $C_{91}H_{90}N_4O_6$ = 1334.6855 found 1334.6865

IR (ATR): $\tilde{\nu}$ (cm^{-1}) = 2960 (w), 1514 (vs), 1471 (m), 1446 (w), 1421 (s), 1390 (m), 1366 (vs), 1325 (w), 1292 (w), 1277 (m), 1263 (w), 1214 (vs), 1175 (m), 1146 (w), 1125 (w), 1103 (w), 1061 (w), 1043 (m), 1024 (m), 1016 (s), 985 (w), 973 (w), 858 (m), 841 (w), 833 (m), 808 (m), 767 (s), 734 (w), 689 (m), 611 (w).

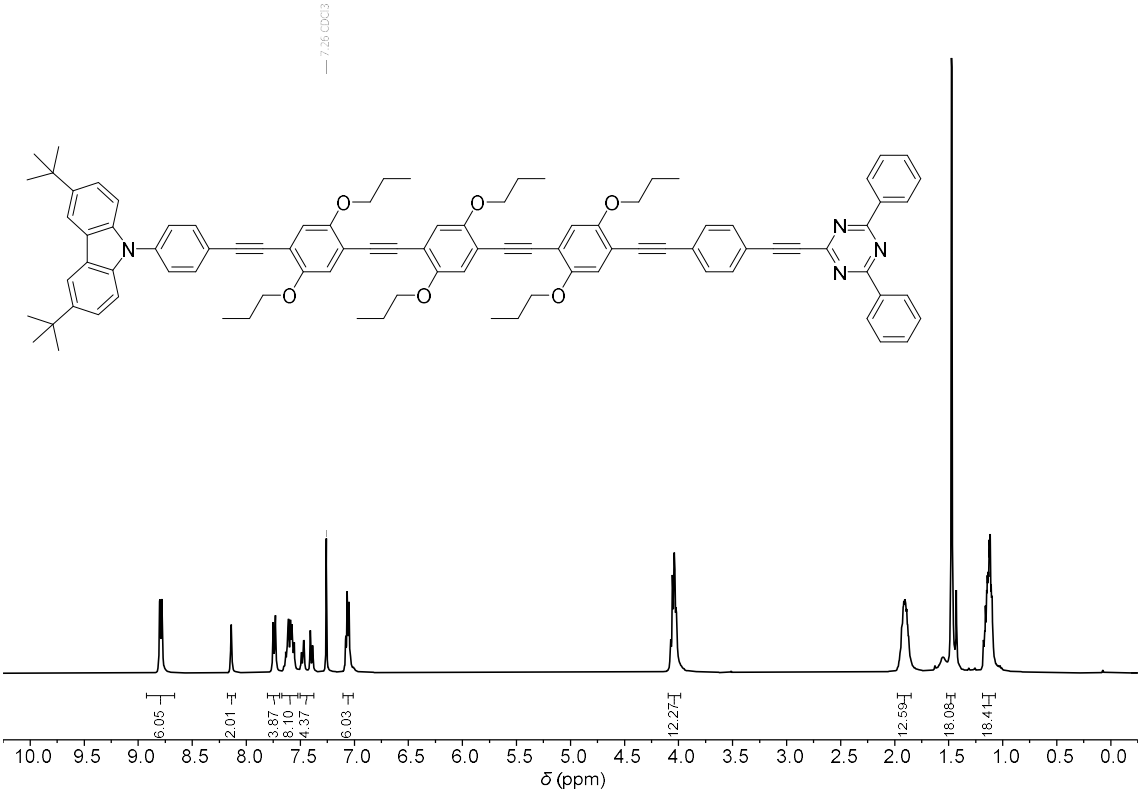

*Figure S28. ^{1}H NMR spectrum of **PE3**, measured in $CDCl_3$ at 400 MHz.*

8.3.4 Synthesis of OPE Photoswitches

General procedure of OPE-based azobenzene photoswitches (GP3): (*E*)-1,2-bis(2,6-difluoro-4-iodophenyl)diazene (1 equiv.), a terminal alkyne (2 equiv.), copper (I) iodide, and a palladium catalyst were sealed in a crimp vial and degassed three times. Under exclusion of light, anhydrous THF and diisopropylamine were added and the mixture was carefully degassed for three more times. The reaction mixture was stirred at room temperature. After TLC confirmed complete conversion, the reaction mixture was poured onto a short silica gel plug (5 cm) and washed with cyclohexane. The residue was purified by flash column chromatography (cyclohexane → cyclohexane/DCM).

(*E*)-1,2-bis(2,6-difluoro-4-((4-(phenylethynyl)-2,5-dipropoxyphenyl)ethynyl)phenyl)diazene (PS1)

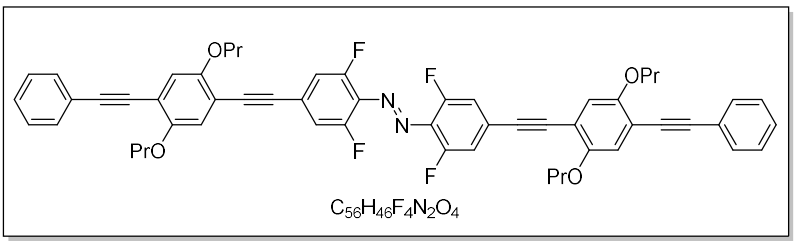

According to *GP3*, (*E*)-**F$_4$I$_2$AB** (99.8 mg, 197 µmmol, 1.00 equiv.), **OPE1** (128 mg, 402 mmol, 2.04 equiv.), copper(I) iodide (6.2 mg, 33 µmol, 0.17 equiv.), $Pd(PPh_3)_4$ (14.1 mg, 12.2 µmol, 0.06 equiv.), and diisopropylamine (300 µL, 215 mg, 2.13 mmol, 10.8 equiv.) were reacted in anhydrous THF (6.0 mL) for 1 h. Purification via flash column chromatography (cyclohexane/DCM 1:1 to 1:2) afforded the title compound as a red solid (164 mg, 185 µmol, 94%).

TLC (cyclohexane/ethyl acetate 40:1): R_f = 0.41.

^{1}H NMR (400 MHz, $CDCl_3$): δ (ppm) = 7.56 – 7.52 (m, 4H, H_{ar}), 7.39 – 7.33 (m, 6H, H_{ar}), 7.20 (d, J = 9.3 Hz, 4H, H_{ar}), 7.03 (d, J = 9.0 Hz, 4H, H_{ar}), 4.02 (t, J = 6.4 Hz, 4H, OCH_2), 4.02 (t, J = 6.4 Hz, 4H, OCH_2), 1.90 (h, J = 7.0 Hz, 4H, $CH_2CH_2CH_3$), 1.90 (h, J = 7.0 Hz, 4H, $CH_2CH_2CH_3$), 1.13 (t, J = 7.4 Hz, 6H, CH_3), 1.12 (t, J = 7.4 Hz, 6H, CH_3).

^{13}C NMR (101 MHz, $CDCl_3$): δ = 192.72, 173.18, 154.08, 153.80, 153.59, 153.57, 143.48, 142.30, 139.54, 138.73, 131.63, 128.45, 128.38, 127.53, 127.39, 125.72, 123.31, 122.89, 117.04, 116.83, 115.72, 115.50, 115.48, 112.34, 97.42, 95.58, 95.22, 91.00, 85.41, 72.53, 71.20, 71.03, 68.11, 67.84, 58.29, 52.83, 42.79, 34.53, 29.44, 26.57, 22.74, 22.71, 17.09, 14.44, 13.85, 10.58, 9.21, 1.58, 1.28, -1.76.

^{19}F NMR (376 MHz, $CDCl_3$): δ (ppm) = -120.3 ppm (E-isomer).

HRMS (ESI, *m*/*z*): $[M+H]^+$ calcd for $C_{56}H_{46}F_4N_2O_4$ 887.3467, found 887.3439.

IR (ATR): $\tilde{\nu}$ (cm^{-1}) = 2962 (w), 2933 (m), 2923 (m), 2904 (w), 2874 (w), 2853 (w), 2201 (m), 1613 (vs), 1602 (vs), 1559 (s), 1530 (w), 1508 (s), 1487 (m), 1467 (m), 1436 (m), 1421 (s), 1413 (vs), 1388 (s), 1314 (m), 1277 (s), 1212 (vs), 1119 (m), 1082 (w), 1065 (m), 1047 (vs), 1026 (m), 1010 (vs), 989 (vs), 963 (s), 926 (w), 909 (m), 870 (w), 852 (vs), 808 (w), 784 (w), 751 (vs), 685 (vs), 662 (m), 644 (s), 631 (m), 527 (s), 496 (w), 479 (m).

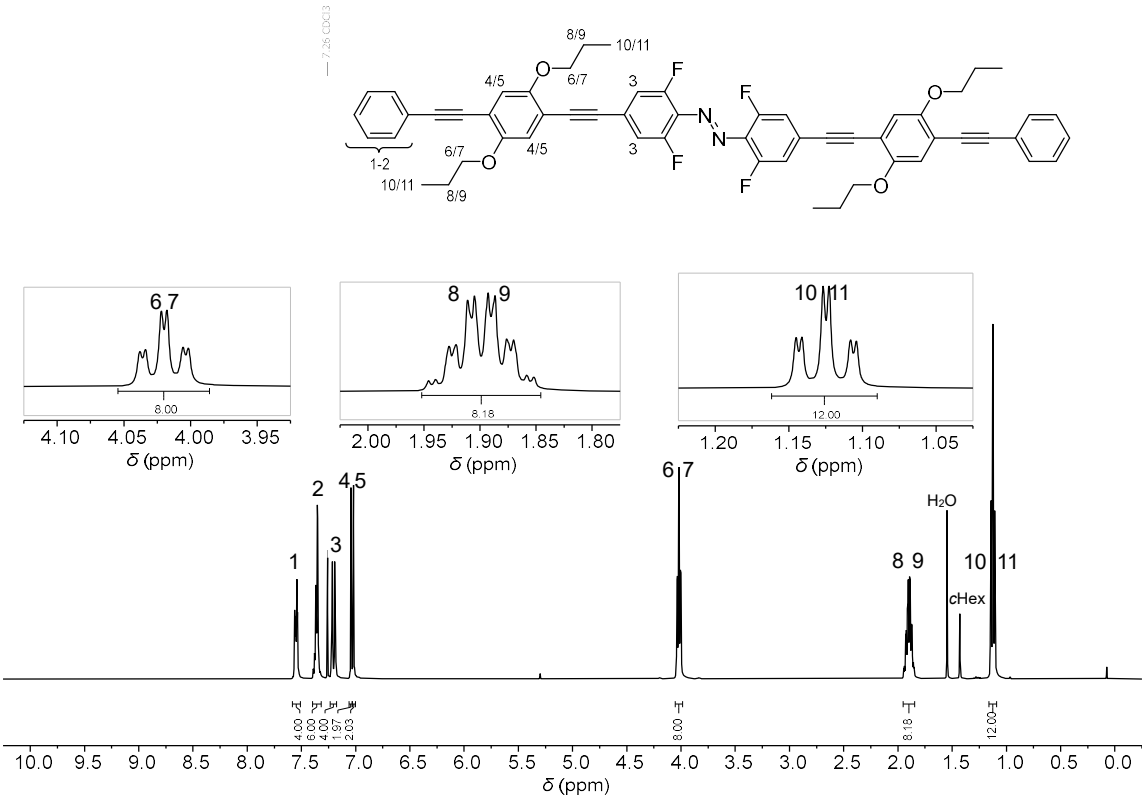

*Figure S29. ^{1}H NMR spectrum of **PS1**, measured in $CDCl_3$ at 400 MHz.*

(*E*)-1,2-bis(2,6-difluoro-4-((4-((4-((4-(phenylethynyl)-2,5-dipropoxyphenyl)ethynyl)-2,5-dipropoxyphenyl)ethynyl)-2,5-dipropoxyphenyl)ethynyl)phenyl)diazene (PS2)

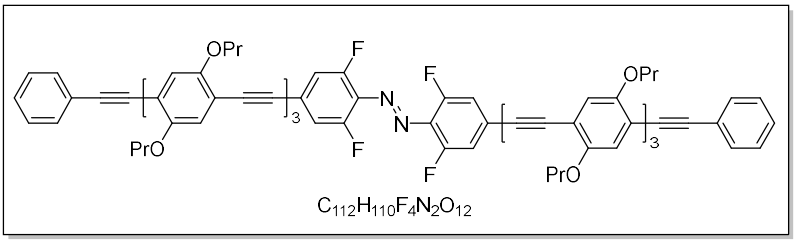

According to *GP3*, (*E*)-**F$_4$I$_2$AB** (26.1 mg, 51.6 µmmol, 1.00 equiv.), **OPE2** (78.2 mg, 104 µmol, 2.02 equiv.), copper(I) iodide (2.3 mg, 12 µmol, 0.23 equiv.), $Pd(PPh_3)_2Cl_2$ (2.7 mg, 3.8 µmol, 0.07 equiv.), and diisopropylamine (141 µL, 101 mg, 1.00 mmol, 19.4 equiv.) were reacted in anhydrous THF (3.0 mL) and were added to the mixture. The reaction mixture was stirred at 21 °C for 2 h. The volatiles were removed under reduced pressure and the residue was purified via flash column chromatography (cyclohexane/DCM 1:1 to 1:2). The title compound was obtained as a red solid (63 mg, 36.0 µmol, 70%).

TLC (cyclohexane/DCM 1:2): R_f = 0.33.

^{1}H NMR (400 MHz, $CDCl_3$): δ (ppm) = 7.56 – 7.53 (m, 4H, H_{ar}), 7.38 – 7.31 (m, 6H, H_{ar}), 7.21 (d, J = 9.1 Hz, 4H, $FCCH_{ar}$), 7.05 – 7.00 (m, 12H, H_{ar}), 4.05 – 3.97 (m, 24H, OCH_2CH_2), 1.94 – 1.84 (m, 24H, $CH_2CH_2CH_3$), 1.14 – 1.07 (m, 36H, CH_2CH_3).

^{13}C NMR (101 MHz, $CDCl_3$): δ (ppm) = 154.29, 154.24, 154.06, 153.62, 153.53, 153.51, 153.45, 153.40, 131.58, 131.54, 128.34, 128.30, 128.27, 123.49, 117.43, 117.36, 117.29, 117.19, 117.16, 117.00, 115.79, 115.72, 115.70, 115.68, 115.50, 115.47, 114.61, 114.28, 114.13, 114.11, 114.07, 112.34, 94.92, 92.32, 91.67, 91.47, 91.27, 91.08, 85.98, 71.26, 71.21, 71.19, 71.14, 71.12, 70.97, 22.75, 22.68, 22.60, 10.59, 10.57.

^{19}F NMR (376 MHz, $CDCl_3$): δ (ppm) = -119.1 (*Z*-isomer, 2%), -120.3 (*E*-isomer, 98%).

HRMS (ESI, *m/z*): $[M+H]^+$ calcd for $C_{112}H_{110}F_4N_2O_{12}$ = 1751.8073, found 1751.8168.

IR (ATR): $\tilde{\nu}$ (cm^{-1}) = 2962 (w), 2933 (w), 2874 (w), 2203 (w), 1615 (m), 1557 (w), 1530 (w), 1510 (s), 1489 (w), 1465 (w), 1423 (vs), 1386 (s), 1343 (w), 1275 (s), 1207 (vs), 1105 (w), 1084 (w), 1063 (s), 1043 (s), 1016 (s), 987 (s), 907 (w), 889 (w), 847 (vs), 786 (w), 757 (s), 691 (s), 664 (w), 629 (w), 611 (w), 580 (w), 529 (w), 508 (w), 485 (w), 463 (w), 442 (w).

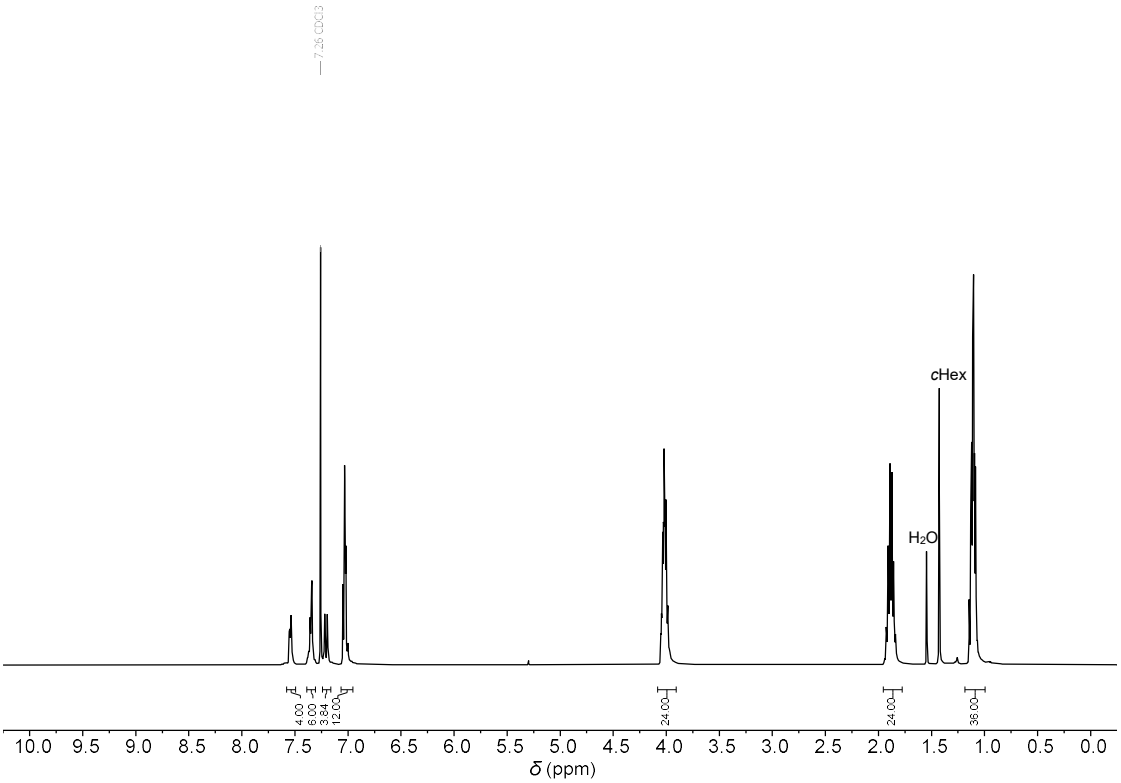

*Figure S30. ^1H NMR spectrum of **PS1**, measured in $CDCl_3$ at 400 MHz.*

(*E*)-1,2-bis(2,6-difluoro-4-((4-((4-((4-((4-((4-(phenylethynyl)-2,5-dipropoxyphenyl)ethynyl)-2,5-dipropoxyphenyl)ethynyl)-2,5-dipropoxyphenyl)ethynyl)-2,5-dipropoxyphenyl)ethynyl)-2,5-dipropoxyphenyl)ethynyl)phenyl)diazene (PS3)

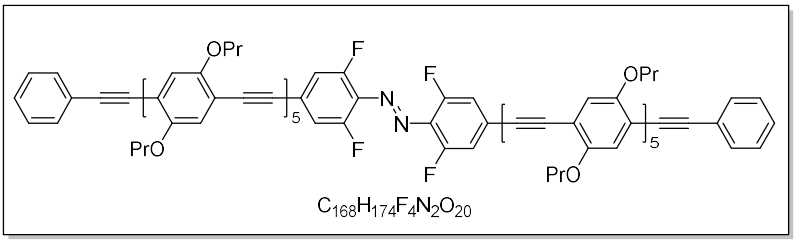

According to *GP3*, (*E*)-**F$_4$I$_2$AB** (7.6 mg, 15 µmol, 1.0 equiv.), **OPE3** (35.5 mg, 30 µmol, 2.0 equiv.), copper(I) iodide (0.29 mg, 1.5 µmol, 0.10 equiv.), $Pd(PPh_3)_4$ (0.87 mg, 0.75 µmol, 0.05 equiv.), and diisopropylamine (42 µL, 30 mg, 0.30 mmol, 20 equiv.) were reacted in anhydrous THF (3.0 mL) for 1.5 h. Purification via flash column chromatography (cyclohexane/DCM 1:1 to 1:2) afforded the title compound was obtained as a red solid (26.7 mg, 10.1 µmol, 67%).

TLC (cyclohexane/DCM (1:2): R_f = 0.25.

^{1}H NMR (400 MHz, $CDCl_3$): δ (ppm) = 7.55 – 7.53 (m, 4H, H_{ar}), 7.38 – 7.33 (m, 6H, H_{ar}), 7.22 – 7.20 (m, 4H, $FCCH_{ar}$), 7.05 – 7.00 (m, 20H, H_{ar}), 4.05 – 3.98 (m, 40H, OCH_2CH_2), 1.88 (h, J = 7.1 Hz, 40H), 1.14 – 1.08 (m, 60H).

^{13}C NMR (101 MHz, CDCl3): δ (ppm) = 154.06, 153.62, 153.53, 153.51, 153.46, 153.41, 131.58, 128.34, 117.47, 117.41, 117.36, 117.29, 117.20, 117.16, 117.01, 115.70, 114.63, 114.42, 114.37, 114.34, 114.29, 114.08, 112.34, 91.55, 91.53, 71.26, 71.22, 71.18, 71.12, 70.97, 22.75, 22.68, 10.57.

^{19}F NMR (376 MHz, $CDCl_3$): δ (ppm) = -119.1 (*Z*-isomer, 7%), -120.3 (*E*-isomer, 93%).

HRMS (ESI, *m*/*z*): $[M+H]^+$ calced for $C_{168}H_{174}F_4N_2O_{20}$ 2616.2669, found 2616.2729.

IR (ATR): $\tilde{\nu}$ (cm^{-1}) = 2964 (w), 2931 (w), 2874 (w), 2195 (vw), 1615 (w), 1557 (w), 1512 (s), 1465 (w), 1425 (vs), 1386 (s), 1275 (s), 1209 (vs), 1148 (w), 1065 (s), 1045 (s), 1016 (m), 987 (s), 905 (w), 889 (w), 854 (vs), 761 (m), 726 (w), 693 (m).

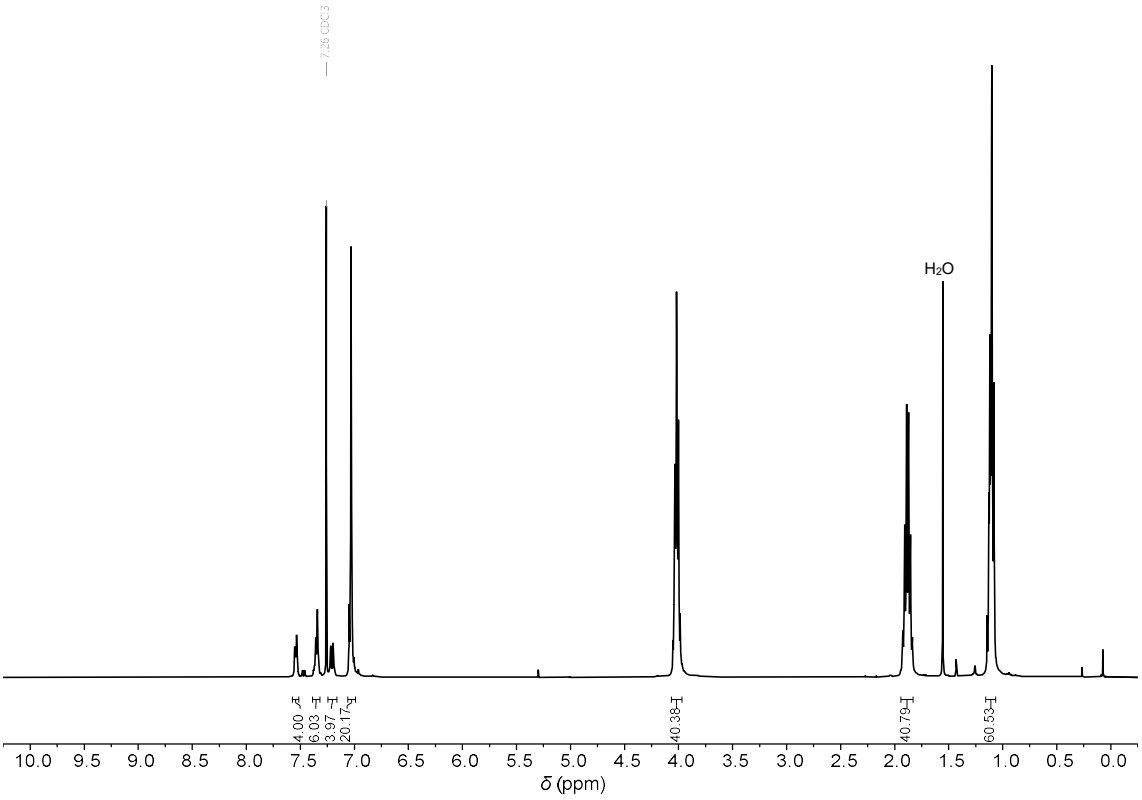

*Figure S31. ^{1}H NMR spectrum of **PS1**, measured in $CDCl_3$ at 400 MHz.*

9 Appendix

9.1 Computational Details

All quantum-chemical calculations were carried out using Gaussian 16 at the levels of theory specified in the respective chapters.[215] Computational tasks were in part managed through Digichem.[216] Natural transition orbital (NTO) analysis and overlap indices (S_r) were generated using Multiwfn.[217]

9.2 Additional Photophyisical Results

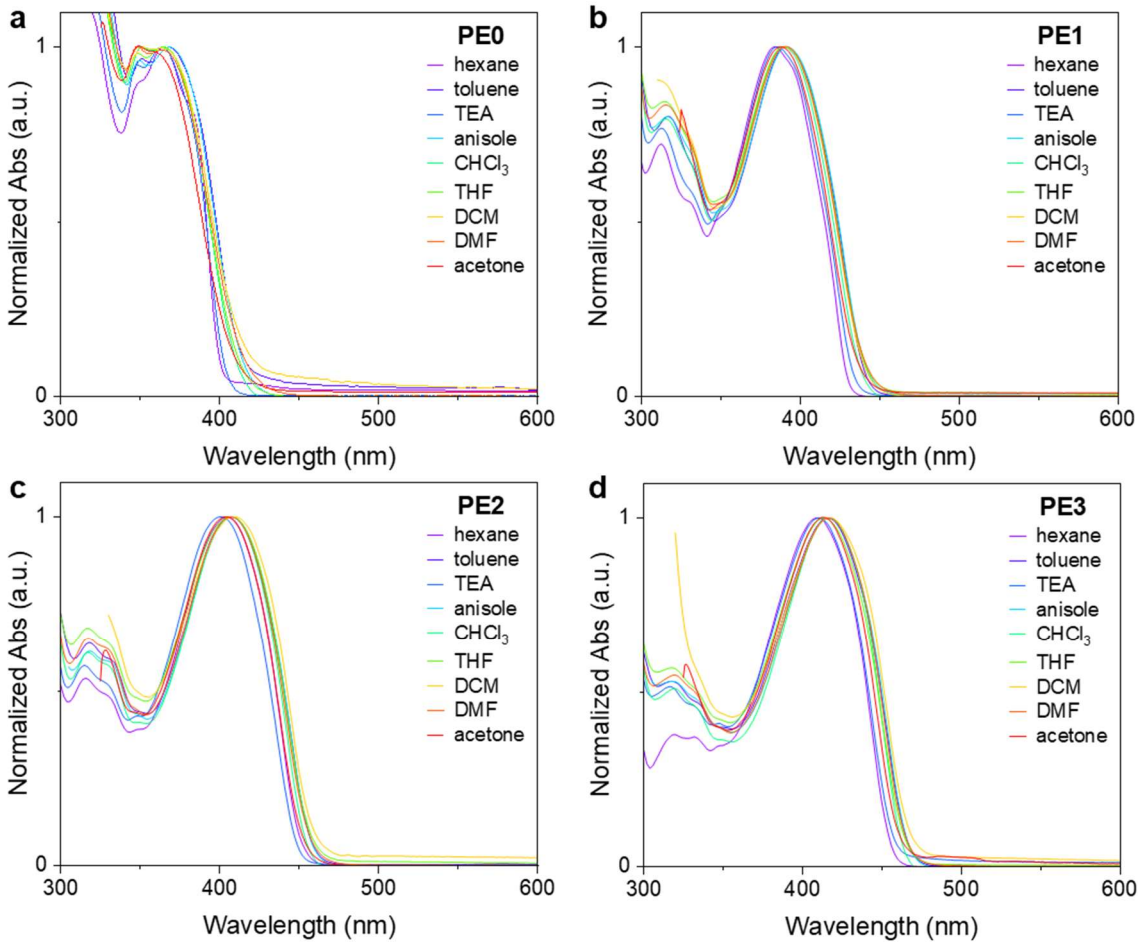

Figure S32. Normalized UV-Vis absorption spectra of in ~10 µM solution of various aprotic solvents.

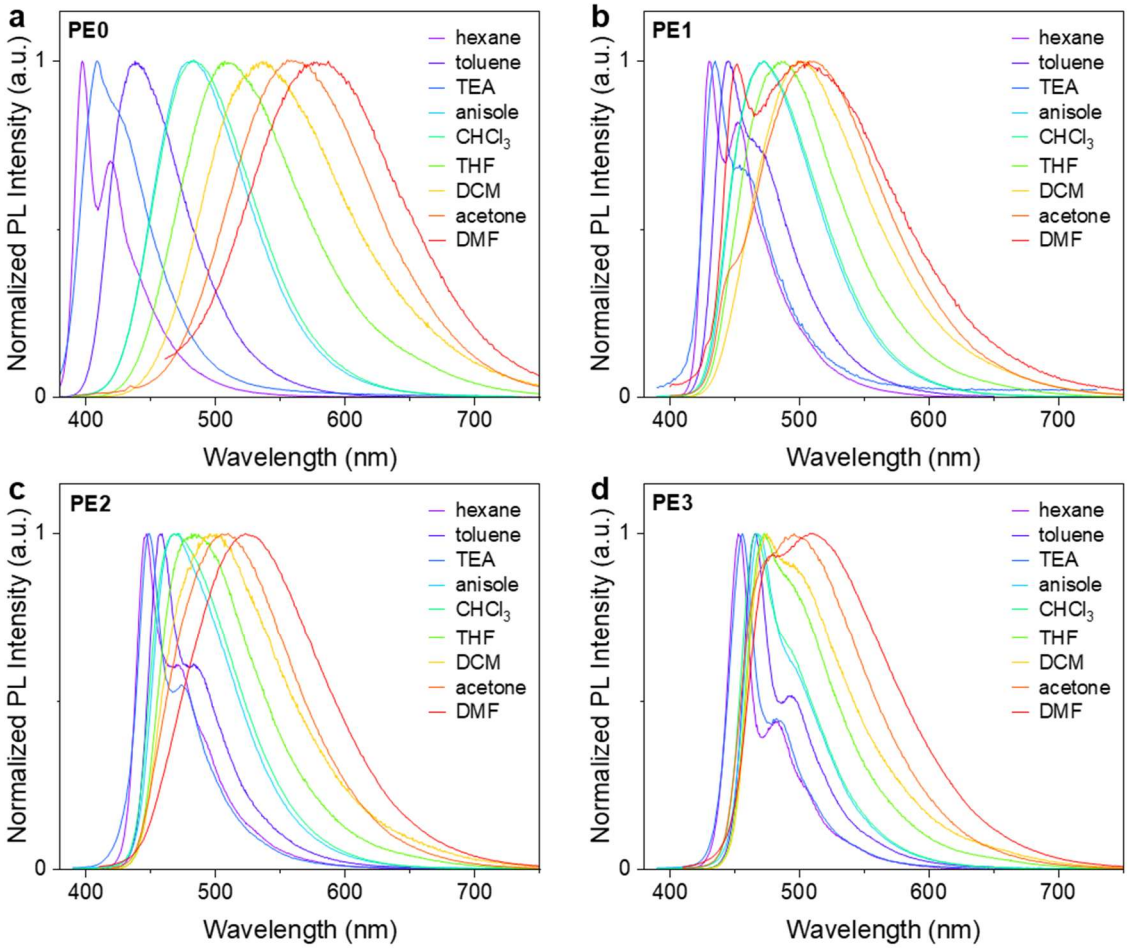

Figure S33. Normalized PL spectra in ~10 µM solution of various aprotic solvents. Excitation wavelength λ_{exc} *= 370 nm.*

*Table S1. Overview of absorption and photoluminescence maxima (λ_{abs} [nm] and λ_{PL} [nm]) and corresponding Stokes shifts ($\Delta\tilde{\nu}$ [10^3 cm^{-1}]) for **PE0-PE3** in various aprotic solvents.*

	PE0			**PE1**			**PE2**			**PE3**		
	λ_{abs}	λ_{PL}	$\Delta\tilde{\nu}$	λ_{abs}	λ_{PL}	$\Delta\tilde{\nu}$	λ_{abs}	λ_{PL}	$\Delta\tilde{\nu}$	λ_{abs}	λ_{PL}	$\Delta\tilde{\nu}$
hexane	364	397	2.28	384	430	2.79	405	447	2.32	410	454	2.36
toluene	368	438	4.34	390	445	3.17	408	458	2.68	416	466	2.58
TEA	364	409	3.02	386	435	2.92	401	449	2.67	411	456	2.40
anisole	368	481	6.38	392	472	4.32	408	468	3.14	417	468	2.61
$CHCl_3$	364	483	6.77	391	472	4.39	407	472	3.38	417	466	2.52
THF	365	510	7.79	390	487	5.11	408	483	3.81	416	473	2.90
DCM	364	536	8.82	391	501	5.62	409	498	4.37	418	475	2.87
DMF	366	577	9990	390	504	5800	407	523	5450	417	509	4.33
acetone	366	559	9430	388	509	6130	404	507	5030	413	496	4.05

Table S2. Additional data to Lipper-Mataga plot in Section 5.2.3.

R^2 (Lippert-Mataga)	Slope / cm^{-1}	a / Å	$\Delta\mu$/ D	μ_{gs} / D	μ_{es} / D

PE0	0.945	23156	5.90	22.5	0.36	22.9
PE1	0.987	11478	6.36	17.2	0.16	17.4
PE2	0.939	6409	6.69	13.8	0.12	13.9
	0.895	14498		20.76		20.9
PE3	0.235	829	7.02	7.00	0.08	6.9
	0.870	13532		27.61		27.7

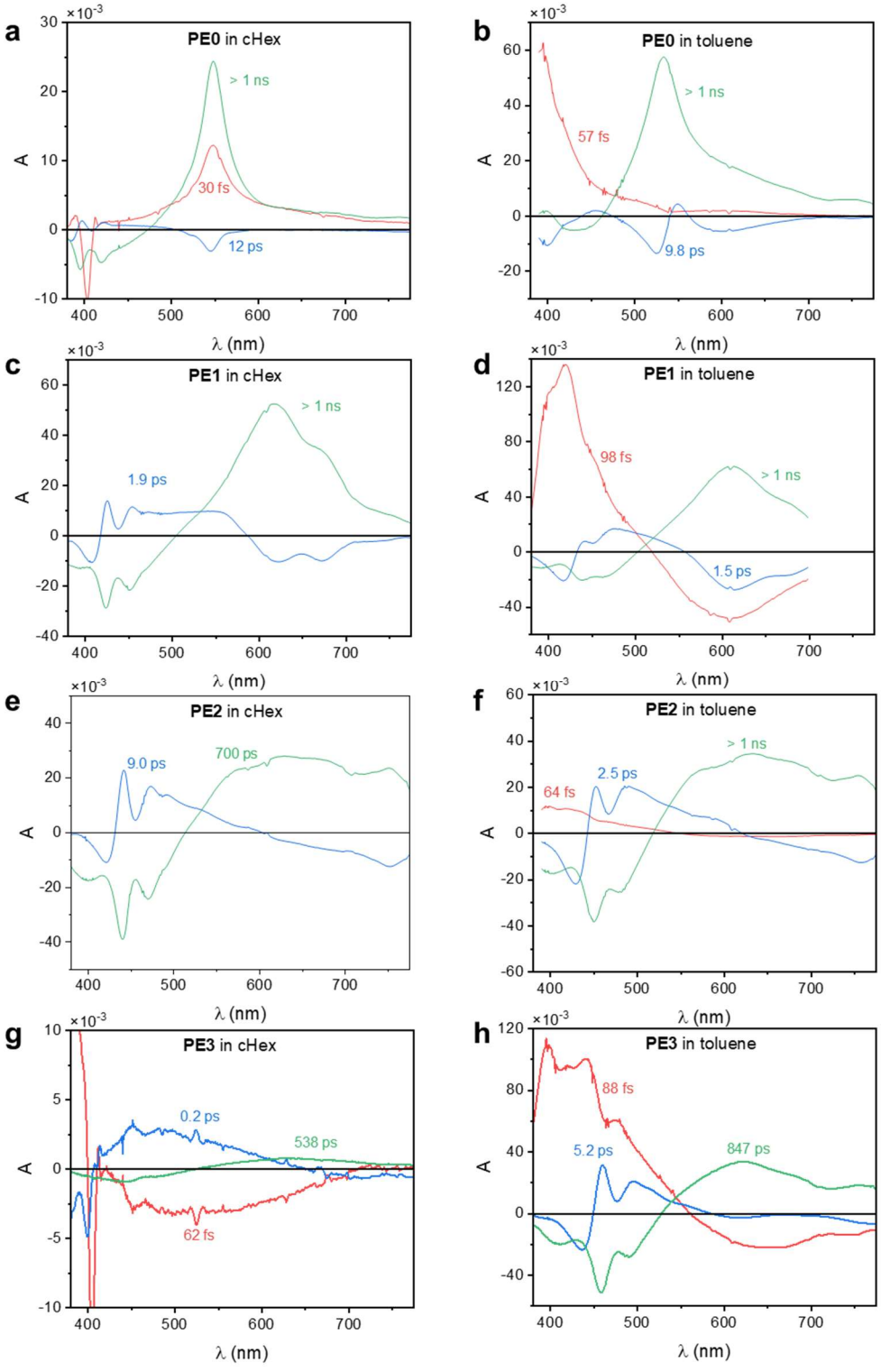

*Figure S34. Decay-associated difference (DAD) spectra of **PE0-PE3** in cyclohexane and toluene.*

9.3 Investigation of Photostationary State

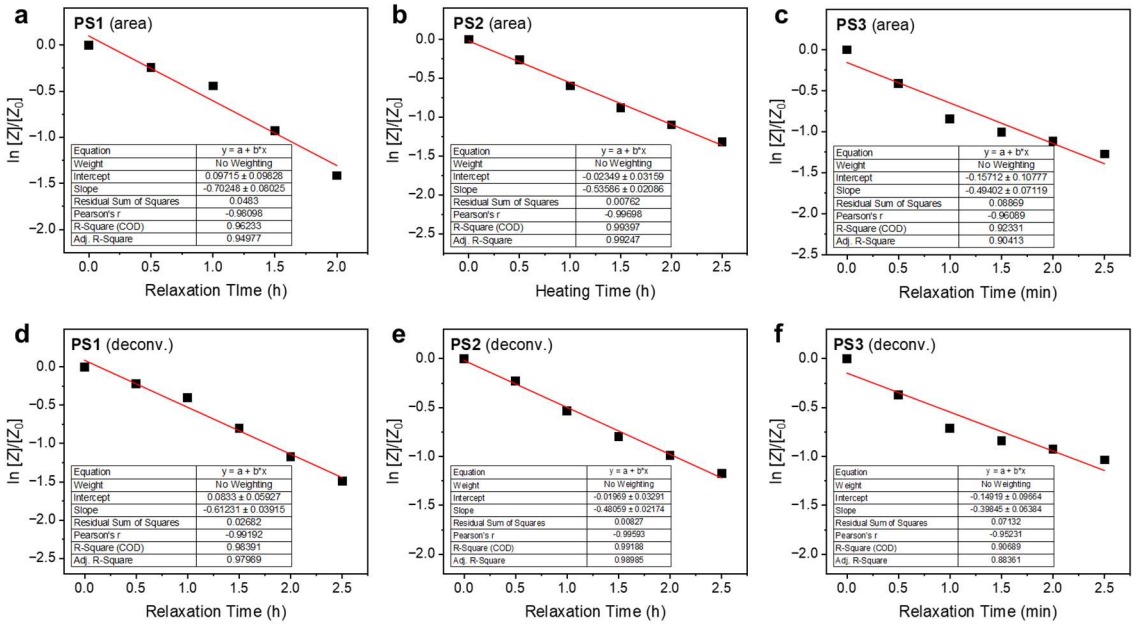

Figure S35. a-c) First-order kinetic plots derived from the SEC results evaluated using direct integration of the area below the curve. d-f) First-order kinetic plots derived from the SEC results evaluated using Gaussian peak deconvolution.

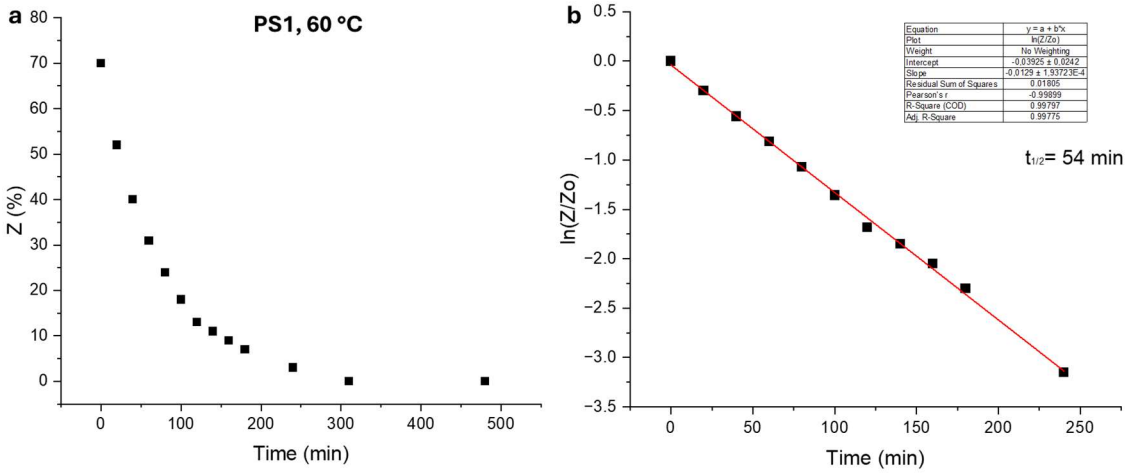

*Figure S36. Thermal stability characterization of **PS1** after 30 min irradiation with 525 nm, measured with ^{19}F NMR, THF-d8, 1 mg/mL, filtered, 60 °C.*

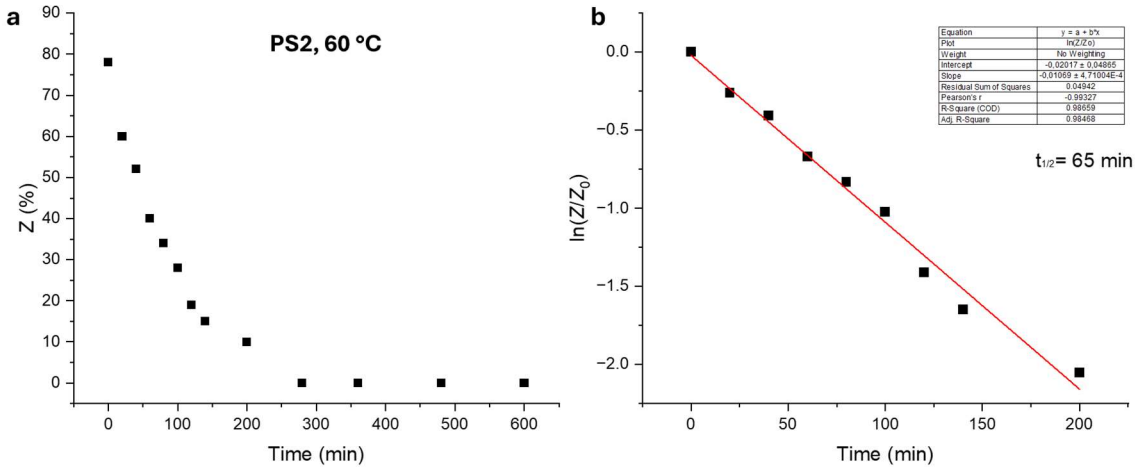

*Figure S37. Thermal stability characterization of **PS2** after 30 min irradiation with 525 nm, measured with ^{19}F NMR, THF-d8, 1 mg/mL, filtered, 60 °C.*

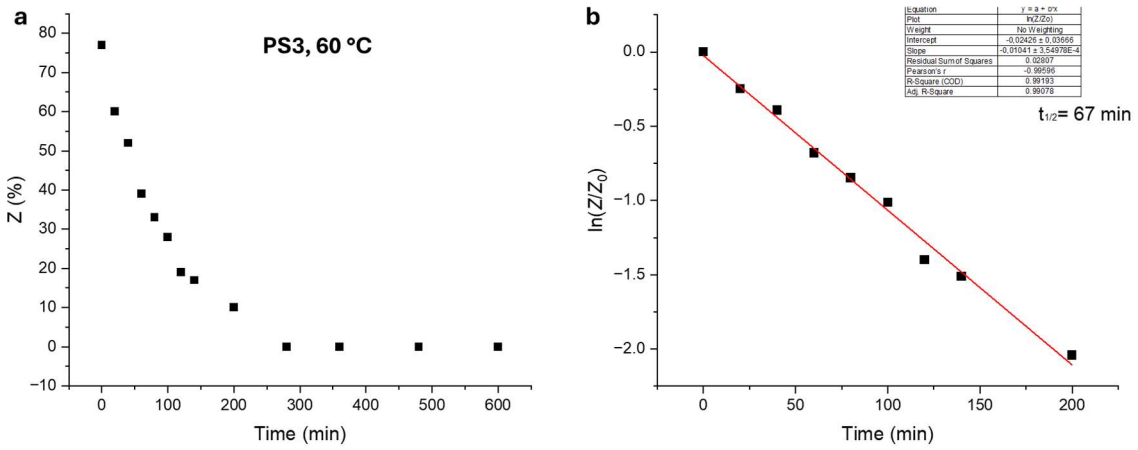

*Figure S38. Thermal stability characterization of **PS3** after 30 min irradiation with 525 nm, measured with ^{19}F NMR, THF-d8, 1 mg/mL, filtered, 60 °C.*

10 References

[1] "New Horizons in chemical space" *Nat. Rev. Drug Discov.* **2004**, *3*, 375–375.

[2] F. Käfer, C. Wang, Y. Huang, F. Bard, R. Segalman, C. K. Ober, "Polypeptoids: Exploring the Power of Sequence Control in a Photoresist for Extreme-Ultraviolet Lithography" *Adv. Mater. Technol.* **2023**, *8*, 2301104.

[3] G. E. Moore, "Cramming more components onto integrated circuits, Reprinted from Electronics, volume 38, number 8, April 19, 1965, pp.114 ff." *IEEE Solid-State Circuits Soc. Newsl.* **2006**, *11*, 33–35.

[4] K. Hakobyan, B. B. Noble, J. Xu, "The current science of sequence-defined macromolecules" *Prog. Polym. Sci.* **2023**, *147*, 101754.

[5] M. A. R. Meier, C. Barner-Kowollik, "A New Class of Materials: Sequence-Defined Macromolecules and Their Emerging Applications" *Adv. Mater.* **2019**, *31*, 1806027.

[6] S. C. Solleder, R. V. Schneider, K. S. Wetzel, A. C. Boukis, M. A. R. Meier, "Recent Progress in the Design of Monodisperse, Sequence-Defined Macromolecules" *Macromol. Rapid Commun.* **2017**, *38*, 1600711.

[7] R. V. Schneider, K. A. Waibel, A. P. Arndt, M. Lang, R. Seim, D. Busko, S. Bräse, U. Lemmer, M. A. R. Meier, "Sequence-definition in stiff conjugated oligomers" *Sci. Rep.* **2018**, *8*, 17483.

[8] O. Franco, M. Jakoby, R. V. Schneider, F. Hundemer, D. Hahn, B. S. Richards, S. Bräse, M. A. R. Meier, U. Lemmer, I. A. Howard, "Sensitizing TADF Absorption Using Variable Length Oligo(phenylene ethynylene) Antennae" *Front. Chem.* **2020**, *8*, DOI 10.3389/fchem.2020.00126.

[9] D. Hahn, R. V. Schneider, E. Foitzik, M. A. R. Meier, "A Practical and Efficient Synthesis of Uniform Conjugated Rod-Like Oligomers" *Macromol. Rapid Commun.* **2021**, *42*, 2000735.

[10] P. Bohn, M. Frölich, D. Hahn, R. V. Schneider, M. A. R. Meier, "Uniform Macromolecules: Performance of Common Analytic Instruments in Detecting Impurities" *Macromol. Chem. Phys.* **2025**, *226*, 2400396.

[11] B. Matarranz, G. Ghosh, R. Kandanelli, A. Sampedro, K. K. Kartha, G. Fernández, "Understanding the role of conjugation length on the self-assembly behaviour of oligophenyleneethynylenes" *Chem. Commun.* **2021**, *57*, 4890–4893.

[12] P. Klán, J. Wirz in *Mol. Photoswitches*, John Wiley & Sons, Ltd, **2022**, pp. 1–18.

[13] S. C. Rasmussen, "The Early History of Polyaniline: Discovery and Origins" *Substantia* **2017**, *1*, DOI 10.13128/Substantia-30.

[14] R. McNeill, R. Siudak, J. H. Wardlaw, D. E. Weiss, "Electronic Conduction in Polymers. I. The Chemical Structure of Polypyrrole" *Aust. J. Chem.* **1963**, *16*, 1056–1075.

[15] H. Shirakawa, E. J. Louis, A. G. MacDiarmid, C. K. Chiang, A. J. Heeger, "Synthesis of electrically conducting organic polymers: halogen derivatives of polyacetylene, (CH)x" *J. Chem. Soc. Chem. Commun.* **1977**, 578–580.

[16] C. K. Chiang, C. R. Fincher, Y. W. Park, A. J. Heeger, H. Shirakawa, E. J. Louis, S. C. Gau, A. G. MacDiarmid, "Electrical Conductivity in Doped Polyacetylene" *Phys. Rev. Lett.* **1977**, *39*, 1098–1101.

[17] C. K. Chiang, M. A. Druy, S. C. Gau, A. J. Heeger, E. J. Louis, A. G. MacDiarmid, Y. W. Park, H. Shirakawa, "Synthesis of highly conducting films of derivatives of polyacetylene, (CH)x" *J. Am. Chem. Soc.* **1978**, *100*, 1013–1015.

[18] C. K. Chiang, Y. W. Park, A. J. Heeger, H. Shirakawa, E. J. Louis, A. G. MacDiarmid, "Conducting polymers: Halogen doped polyacetylene" *J. Chem. Phys.* **1978**, *69*, 5098–5104.

[19] J. A. Pople, S. H. Walmsley, "Bond alternation defects in long polyene molecules" *Mol. Phys.* **1962**, *5*, 15–20.

[20] W. P. Su, J. R. Schrieffer, A. J. Heeger, "Solitons in Polyacetylene" *Phys. Rev. Lett.* **1979**, *42*, 1698–1701.

[21] J. H. Burroughes, D. D. C. Bradley, A. R. Brown, R. N. Marks, K. Mackay, R. H. Friend, P. L. Burns, A. B. Holmes, "Light-emitting diodes based on conjugated polymers" *Nature* **1990**, *347*, 539–541.

[22] E. Hückel, "Zur Quantentheorie der Doppelbindung" *Z. Für Phys.* **1930**, *60*, 423–456.

[23] G. Natta, G. Mazzanti, P. Corradini, "Polimerizzazione stereospecifica dell'acetilene" *Rendiconti Della Accad. Naz. Dei Lincei* **1958**, *25*.

[24] A. F. Diaz, K. K. Kanazawa, G. P. Gardini, "Electrochemical polymerization of pyrrole" *J. Chem. Soc. Chem. Commun.* **1979**, 635–636.

[25] T. Yamamoto, K. Sanechika, A. Yamamoto, "Preparation of thermostable and electric-conducting poly(2,5-thienylene)" *J. Polym. Sci. Polym. Lett. Ed.* **1980**, *18*, 9–12.

[26] A. G. Macdiarmid, J. C. Chiang, A. F. Richter, A. J. Epstein, "Polyaniline: a new concept in conducting polymers" *Synth. Met.* **1987**, *18*, 285–290.

[27] T. A. Chen, R. D. Rieke, "The first regioregular head-to-tail poly(3-hexylthiophene-2,5-diyl) and a regiorandom isopolymer: nickel versus palladium catalysis of 2(5)-bromo-5(2)-(bromozincio)-3-hexylthiophene polymerization" *J. Am. Chem. Soc.* **1992**, *114*, 10087–10088.

[28] V. N. Bliznyuk, S. A. Carter, J. C. Scott, G. Klärner, R. D. Miller, D. C. Miller, "Electrical and Photoinduced Degradation of Polyfluorene Based Films and Light-Emitting Devices" *Macromolecules* **1999**, *32*, 361–369.

[29] Q. Zhao, S.-J. Liu, W. Huang, "Polyfluorene-Based Blue-Emitting Materials" *Macromol. Chem. Phys.* **2009**, *210*, 1580–1590.

[30] J. Cornil, J.-L. Brédas, "Nature of the optical transitions in charged oligothiophenes" *Adv. Mater.* **1995**, *7*, 295–297.

[31] D. Beljonne, J. Cornil, H. Sirringhaus, P. J. Brown, M. Shkunov, R. H. Friend, J.-L. Brédas, "Optical Signature of Delocalized Polarons in Conjugated Polymers" *Adv. Funct. Mater.* **2001**, *11*, 229–234.

[32] S. Gambino, A. K. Bansal, I. D. W. Samuel, "Photophysical and charge-transporting properties of the copolymer SuperYellow" *Org. Electron.* **2013**, *14*, 1980–1987.

[33] T. Mori, Y. Inoue, "Charge-transfer excitation: unconventional yet practical means for controlling stereoselectivity in asymmetric photoreactions" *Chem. Soc. Rev.* **2013**, *42*, 8122–8133.

[34] Z. Li, S. A. Tolba, Y. Wang, A. Alesadi, W. Xia, "Modeling-driven materials by design for conjugated polymers: insights into optoelectronic, conformational, and thermomechanical properties" *Chem. Commun.* **2024**, *60*, 11625–11641.

[35] C. M. Wolf, L. Guio, S. Scheiwiller, V. Pakhnyuk, C. Luscombe, L. D. Pozzo, "Strategies for the Development of Conjugated Polymer Molecular Dynamics Force Fields Validated with Neutron and X-ray Scattering" *ACS Polym. Au* **2021**, *1*, 134–152.

[36] A. Alesadi, Z. Cao, Z. Li, S. Zhang, H. Zhao, X. Gu, W. Xia, "Machine learning prediction of glass transition temperature of conjugated polymers from chemical structure" *Cell Rep. Phys. Sci.* **2022**, *3*, 100911.

[37] H. Makki, C. Burke, C. B. Nielsen, A. Troisi, “Mapping the structure-function landscape of semiconducting polymers” *Mater. Horiz.* **2025**, 10.1039.D5MH00485C.

[38] S. Lu, A. Jayaraman, “Machine learning for analyses and automation of structural characterization of polymer materials” *Prog. Polym. Sci.* **2024**, *153*, 101828.

[39] R. Szweda, “Sequence- and stereo-defined macromolecules: Properties and emerging functionalities” *Prog. Polym. Sci.* **2023**, *145*, 101737.

[40] K. Ziegler, E. Holzkamp, H. Breil, H. Martin, “Das Mülheimer Normaldruck-Polyäthylen-Verfahren” *Angew. Chem.* **1955**, *67*, 541–547.

[41] P. J. Nigrey, A. G. MacDiarmid, A. J. Heeger, “Electrochemistry of polyacetylene, (CH)x: electrochemical doping of (CH)x films to the metallic state” *J. Chem. Soc. Chem. Commun.* **1979**, 594–595.

[42] X. Qian, J. Qiu, B. Hu, J. Yao, M. Zuo, Z. Wu, G. Shan, Y. Song, Q. Zheng, B. Peng, H. Li, M. Du, “Metal-Like Conductivity in Acid-Treated PEDOT:PSS Films: Surpassing 15,000 S/Cm” *ACS Appl. Mater. Interfaces* **2025**, *17*, 17164–17178.

[43] D. M. Ivory, G. G. Miller, J. M. Sowa, L. W. Shacklette, R. R. Chance, R. H. Baughman, “Highly conducting charge-transfer complexes of poly(p-phenylene)” *J. Chem. Phys.* **1979**, *71*, 1506–1507.

[44] M. Fukuda, K. Sawada, K. Yoshino, “Synthesis of fusible and soluble conducting polyfluorene derivatives and their characteristics” *J. Polym. Sci. Part Polym. Chem.* **1993**, *31*, 2465–2471.

[45] R. D. McCullough, “The Chemistry of Conducting Polythiophenes” *Adv. Mater.* **1998**, *10*, 93–116.

[46] K. Müllen, U. Scherf, “Conjugated Polymers: Where We Come From, Where We Stand, and Where We Might Go” *Macromol. Chem. Phys.* **2023**, *224*, 2200337.

[47] Z. Qiu, B. A. G. Hammer, K. Müllen, “Conjugated polymers – Problems and promises” *Prog. Polym. Sci.* **2020**, *100*, 101179.

[48] Z.-D. Yu, Y. Lu, J.-Y. Wang, J. Pei, “Conformation Control of Conjugated Polymers” *Chem. – Eur. J.* **2020**, *26*, 16194–16205.

[49] C. Xu, C. He, N. Li, S. Yang, Y. Du, K. Matyjaszewski, X. Pan, “Regio- and sequence-controlled conjugated topological oligomers and polymers via boronate-tag assisted solution-phase strategy” *Nat. Commun.* **2021**, *12*, 5853.

[50] C. Zhao, X. Lai, D. Liu, X. Guo, J. Tian, Z. Dong, S. Luo, D. Zhou, L. Jiang, R. Huang, M. He, “Molecular-dipole oriented universal growth of conjugated polymers into semiconducting single-crystal thin films” *Nat. Commun.* **2025**, *16*, 1509.

[51] N. Sharma, A. Singh, N. Kumar, A. Tiwari, M. Lal, S. Arya, “A review on polyaniline and its composites: from synthesis to properties and progressive applications” *J. Mater. Sci.* **2024**, *59*, 6206–6244.

[52] J. Jiang, A. Alsam, S. Wang, S. M. Aly, Z. Pan, O. F. Mohammed, K. S. Schanze, “Effect of Conjugation Length on Photoinduced Charge Transfer in π-Conjugated Oligomer-Acceptor Dyads” *J. Phys. Chem. A* **2017**, *121*, 4891–4901.

[53] Z. Zhuo, M. Ni, N. Yu, Y. Zheng, Y. Lin, J. Yang, L. Sun, L. Wang, L. Bai, W. Chen, M. Xu, F. Huo, J. Lin, Q. Feng, W. Huang, “Intrinsically stretchable fully π-conjugated polymer film via fluid conjugated molecular external-plasticizing for flexible light-emitting diodes” *Nat. Commun.* **2024**, *15*, 7990.

[54] J. Yang, Z. Zhao, S. Wang, Y. Guo, Y. Liu, “Insight into High-Performance Conjugated Polymers for Organic Field-Effect Transistors” *Chem* **2018**, *4*, 2748–2785.

[55] E. K. Solak, E. Irmak, “Advances in organic photovoltaic cells: a comprehensive review of materials, technologies, and performance” *RSC Adv.* **2023**, *13*, 12244–12269.

[56] X. Guo, A. Facchetti, “The journey of conducting polymers from discovery to application” *Nat. Mater.* **2020**, *19*, 922–928.

[57] D. M. De Leeuw, P. A. Kraakman, P. F. G. Bongaerts, C. M. J. Mutsaers, D. B. M. Klaassen, “Electroplating of conductive polymers for the metallization of insulators” *Synth. Met.* **1994**, *66*, 263–273.

[58] N. Calabia Gascón, H. Terryn, A. Hubin, “The role of PEDOT:PSS in (super)capacitors: A review” *Nanotechnol.* **2023**, *2*, 100015.

[59] S. Nie, Z. Li, Y. Yao, Y. Jin, “Progress in Synthesis of Conductive Polymer Poly(3,4-Ethylenedioxythiophene)” *Front. Chem.* **2021**, *9*, DOI 10.3389/fchem.2021.803509.

[60] M. Grell, D. D. C. Bradley, M. Inbasekaran, E. P. Woo, “A glass-forming conjugated main-chain liquid crystal polymer for polarized electroluminescence applications” *Adv. Mater.* **1997**, *9*, 798–802.

[61] M. Grell, W. Knoll, D. Lupo, A. Meisel, T. Miteva, D. Neher, H.-G. Nothofer, U. Scherf, A. Yasuda, “Blue Polarized Electroluminescence from a Liquid Crystalline Polyfluorene” *Adv. Mater.* **1999**, *11*, 671–675.

[62] H. Ding, A. M. Hussein, I. Ahmad, R. Latef, J. K. Abbas, A. T. A. Ali, S. M. Saeed, A. S. Abdulwahid, M. F. Ramadan, H. A. Rasool, A. Elawady, “Conducting polymers in industry: A comprehensive review on the characterization, synthesis and application” *Alex. Eng. J.* **2024**, *88*, 253–267.

[63] Q. Pei, Yang, “Efficient Photoluminescence and Electroluminescence from a Soluble Polyfluorene” *J. Am. Chem. Soc.* **1996**, *118*, 7416–7417.

[64] E. Bundgaard, F. C. Krebs, “Low band gap polymers for organic photovoltaics” *Sol. Energy Mater. Sol. Cells* **2007**, *91*, 954–985.

[65] H. Sirringhaus, R. J. Wilson, R. H. Friend, M. Inbasekaran, W. Wu, E. P. Woo, M. Grell, D. D. C. Bradley, "Mobility enhancement in conjugated polymer field-effect transistors through chain alignment in a liquid-crystalline phase" *Appl. Phys. Lett.* **2000**, *77*, 406–408.

[66] K. Lee, K. Maisel, J.-M. Rouillard, E. Gulari, J. Kim, "Sensitive and Selective Label-Free DNA Detection by Conjugated Polymer-Based Microarrays and Intercalating Dye" *Chem. Mater.* **2008**, *20*, 2848–2850.

[67] R. D. McCullough, R. D. Lowe, "Enhanced electrical conductivity in regioselectively synthesized poly(3-alkylthiophenes)" *J. Chem. Soc. Chem. Commun.* **1992**, 70–72.

[68] E. E. Sheina, J. Liu, M. C. Iovu, D. W. Laird, R. D. McCullough, "Chain Growth Mechanism for Regioregular Nickel-Initiated Cross-Coupling Polymerizations" *Macromolecules* **2004**, *37*, 3526–3528.

[69] M. Brinkmann, "Structure and morphology control in thin films of regioregular poly(3-hexylthiophene)" *J. Polym. Sci. Part B Polym. Phys.* **2011**, *49*, 1218–1233.

[70] C. Greco, A. Melnyk, K. Kremer, D. Andrienko, K. Ch. Daoulas, "Generic Model for Lamellar Self-Assembly in Conjugated Polymers: Linking Mesoscopic Morphology and Charge Transport in P3HT" *Macromolecules* **2019**, *52*, 968–981.

[71] A. T. Kleinschmidt, S. E. Root, D. J. Lipomi, "Poly(3-hexylthiophene) (P3HT): fruit fly or outlier in organic solar cell research?" *J. Mater. Chem. A* **2017**, *5*, 11396–11400.

[72] S. Burns, J. MacLeod, T. Trang Do, P. Sonar, S. D. Yambem, "Effect of thermal annealing Super Yellow emissive layer on efficiency of OLEDs" *Sci. Rep.* **2017**, *7*, 40805.

[73] H. G. Gilch, W. L. Wheelwright, "Polymerization of α-halogenated p-xylenes with base" *J. Polym. Sci. [A1]* **1966**, *4*, 1337–1349.

[74] R. O'shea, W. W. H. Wong, "Simple improvements to Gilch synthesis and molecular weight modulation of MEH-PPV" *Polym. Chem.* **2020**, *11*, 2831–2837.

[75] C. Liu, C. Xiao, J. Wang, B. Liu, Y. Hao, J. Guo, J. Song, Z. Tang, Y. Sun, W. Li, "Revisiting Conjugated Polymers with Long-Branched Alkyl Chains: High Molecular Weight, Excellent Mechanical Properties, and Low Voltage Losses" *Macromolecules* **2022**, *55*, 5964–5974.

[76] A. C, M. Z. Szymański, B. Łuszczyńska, J. Ulański, "Inkjet Printing of Super Yellow: Ink Formulation, Film Optimization, OLEDs Fabrication, and Transient Electroluminescence" *Sci. Rep.* **2019**, *9*, 8493.

[77], "Super yellow light-emitting PPV copolymer 26009-24-5," can be found under https://www.sigmaaldrich.com/DE/en/product/aldrich/900438(accessed 10 September 2025), **n.d.**

[78] R. Hu, Y. Kang, B. Z. Tang, "Recent advances in AIE polymers" *Polym. J.* **2016**, *48*, 359–370.

[79] S. Baysec, E. Preis, S. Allard, U. Scherf, "Very High Solid State Photoluminescence Quantum Yields of Poly(tetraphenylethylene) Derivatives" *Macromol. Rapid Commun.* **2016**, *37*, 1802–1806.

[80] P. Conen, F. J. O. Niedermaier, S. A. E. Mirate, M. A. R. Meier, "A Novel Synthesis Strategy for Poly(Arylene-Vinylene) Derivatives by Elemental Sulfur-Mediated Polyolefination" **n.d.**, DOI 10.1002/marc.202500166.

[81] P. Conen, R. Nickisch, M. A. R. Meier, "Synthesis of highly substituted alkenes by sulfur-mediated olefination of N-tosylhydrazones" *Commun. Chem.* **2023**, *6*, 255.

[82] Z. Li, R. Acharya, S. Wang, K. S. Schanze, "Photophysics and phosphate fluorescence sensing by poly(phenylene ethynylene) conjugated polyelectrolytes with branched ammonium side groups" *J. Mater. Chem. C* **2018**, *6*, 3722–3730.

[83] B. Erdogan, L. Song, J. N. Wilson, J. O. Park, M. Srinivasarao, U. H. F. Bunz, "Permanent Bubble Arrays from a Cross-Linked Poly(*p ara*- phenyleneethynylene): Picoliter Holes without Microfabrication" *J. Am. Chem. Soc.* **2004**, *126*, 3678–3679.

[84] M. Elter, M. Brosz, D. Sucerquia, A. Kuzhelev, D. C. Kiesewetter, M. Kurth, A. Dreuw, T. F. Prisner, J. Freudenberg, U. H. F. Bunz, F. Gräter, "Breaking Strong Alkynyl-Phenyl Bonds: Poly(para-phenylene ethynylene)s under Mechanical Stress" *J. Am. Chem. Soc.* **2024**, *146*, 27594–27599.

[85] P. Jagadesan, K. S. Schanze, "Poly(phenylene ethynylene) Conjugated Polyelectrolytes Synthesized via Chain-Growth Polymerization" *Macromolecules* **2019**, *52*, 3845–3851.

[86] Y. Braeken, P. Verstappen, L. Lutsen, D. Vanderzande, W. Maes, "Synthesis of a multifunctional poly(p-phenylene ethynylene) scaffold with clickable azide-containing side chains for (bio)sensor applications" *Polym. Chem.* **2015**, *6*, 6720–6731.

[87] A. Khan, S. Hecht, "Microwave-accelerated synthesis of lengthy and defect-free poly(m-phenyleneethynylene)s via AB′ and A2 + BB′ polycondensation routes" *Chem. Commun.* **2004**, 300–301.

[88] M. Trunk, A. Herrmann, H. Bildirir, A. Yassin, J. Schmidt, A. Thomas, "Copper-Free Sonogashira Coupling for High-Surface-Area Conjugated Microporous Poly(aryleneethynylene) Networks" *Chem. – Eur. J.* **2016**, *22*, 7179–7183.

[89] W. Milis, J. Peeters, R. Erkens, J. De Winter, P. Gerbaux, G. Koeckelberghs, "Versatile Strategy to Develop Sequence-Defined Conjugated Macromolecules: A Powerful Tool toward Tunable Optoelectronic Properties" *ACS Macro Lett.* **2024**, *13*, 1293–1303.

[90] H. A. Mills, S. Rahman, R. Zigelstein, H. Xu, B. R. Varju, T. P. Bender, M. W. B. Wilson, D. S. Seferos, "Sequence-Defined Conjugated Oligomers in Donor–Acceptor Dyads" *J. Am. Chem. Soc.* **2023**, *145*, 23519–23526.

[91] K. H. Kim, S. E. Seo, C. S. Park, S. Kim, S. Lee, C.-M. Ryu, D. Yong, Y. M. Park, O. S. Kwon, "Open-Bandgap Graphene-Based Field-Effect Transistor Using Oligo(phenylene-ethynylene) Interfacial Chemistry" *Angew. Chem.* **2022**, *134*, e202209726.

[92] L. J. O'Driscoll, M. R. Bryce, "A review of oligo(arylene ethynylene) derivatives in molecular junctions" *Nanoscale* **2021**, *13*, 10668–10711.

[93] A. Aviram, M. A. Ratner, "Molecular rectifiers" *Chem. Phys. Lett.* **1974**, *29*, 277–283.

[94] P. J. Low, S. Marqués-González in *Single-Mol. Electron. Introd. Synth. Meas. Theory* (Ed.: M. Kiguchi), Springer, Singapore, **2016**, pp. 87–116.

[95] Y. Fan, S. Pitie, C. Liu, C. Zhao, C. Zhao, M. Seydou, Y. J. Dappe, R. J. Nichols, L. Yang, "Asymmetric Effect on the Length Dependence of Oligo(Phenylene ethynylene)-Based Molecular Junctions" *J. Phys. Chem. C* **2022**, *126*, 3635–3645.

[96] Y. Zhang, S. Yang, Y. Yang, J.-C. Ren, C. J. Butch, L. Wang, W. Liu, "Rapid Prediction of Energy Level Alignment and Conductance of Single-Molecule Junctions Through Intramolecular Dipole Moment" *Adv. Funct. Mater.* **2024**, *34*, 2403836.

[97] L. Ornago, J. Kamer, M. El Abbassi, F. C. Grozema, H. S. J. van der Zant, "Switching in Nanoscale Molecular Junctions due to Contact Reconfiguration" *J. Phys. Chem. C* **2022**, *126*, 19843–19848.

[98] Z.-Z. Chen, S.-D. Wu, J.-L. Lin, L.-C. Chen, J.-J. Cao, X. Shao, C. J. Lambert, H.-L. Zhang, "Modulating Quantum Interference Between Destructive and Constructive

States in Double N-Substituted Single Molecule Junctions" *Adv. Electron. Mater.* **2023**, *9*, 2201024.

[99] O. A. Al-Owaedi, "Theoretical and modelling investigation of pendant groups effect on quantum interference for single-molecule junctions" *RSC Adv.* **2024**, *14*, 14704–14715.

[100] S. C. Yelishala, Y. Zhu, P. M. Martinez, H. Chen, M. Habibi, G. Prampolini, J. C. Cuevas, W. Zhang, J. G. Vilhena, L. Cui, "Phonon interference in single-molecule junctions" *Nat. Mater.* **2025**, 1–7.

[101] X. Sun, Y. Wang, Y. Lei, "Fluorescence based explosive detection: from mechanisms to sensory materials" *Chem. Soc. Rev.* **2015**, *44*, 8019–8061.

[102] U. H. F. Bunz, K. Seehafer, M. Bender, M. Porz, "Poly(aryleneethynylene)s (PAE) as paradigmatic sensor cores" *Chem. Soc. Rev.* **2015**, *44*, 4322–4336.

[103] A. Krywko-Cendrowska, D. Szweda, R. Szweda, "Well-Defined Conjugated Macromolecules Based on Oligo(Arylene Ethynylene)s in Sensing" *Processes* **2020**, *8*, 539.

[104] I.-B. Kim, U. H. F. Bunz, "Modulating the Sensory Response of a Conjugated Polymer by Proteins: An Agglutination Assay for Mercury Ions in Water" *J. Am. Chem. Soc.* **2006**, *128*, 2818–2819.

[105] H. Kim, B. Koo, "Iron(III) Sensors Based on the Fluorescence Quenching of Poly(phenylene ethynylene)s and Iron-Detecting PDMS Pads" *Macromol. Res.* **2021**, *29*, 360–364.

[106] H. Sharifi, M. Elter, K. Seehafer, E. Smarsly, B. Hemmateenejad, U. H. F. Bunz, "Paper and nylon based optical tongues with poly(*p*-phenyleneethynylene)-fluorophores efficiently discriminate nitroarene-based explosives and pollutants" *Talanta* **2024**, *276*, 126222.

[107] A. I. Costa, J. V. Prata, “Substituted *p*-phenylene ethynylene trimers as fluorescent sensors for nitroaromatic explosives” *Sens. Actuators B Chem.* **2012**, *161*, 251–260.

[108] E. H. Hill, Y. Zhang, D. G. Evans, D. G. Whitten, “Enzyme-Specific Sensors via Aggregation of Charged p-Phenylene Ethynylenes” *ACS Appl. Mater. Interfaces* **2015**, *7*, 5550–5560.

[109] Y. Kuang, W. Ni, H. Liu, J. Han, “Poly(p-Phenyleneethynylene)s-Based Sensor Array for Diagnosis of Clinical Diseases” *ChemMedChem* **2025**, *20*, e202400686.

[110] J.-S. Yang, T. M. Swager, “Fluorescent Porous Polymer Films as TNT Chemosensors: Electronic and Structural Effects” *J. Am. Chem. Soc.* **1998**, *120*, 11864–11873.

[111] Y. Yu, W. Ni, Q. Hu, H. Li, Y. Zhang, X. Gao, L. Zhou, S. Zhang, S. Ma, Y. Zhang, H. Huang, F. Li, J. Han, “A Dual Fluorescence Turn-On Sensor Array Formed by Poly(para-aryleneethynylene) and Aggregation-Induced Emission Fluorophores for Sensitive Multiplexed Bacterial Recognition” *Angew. Chem. Int. Ed.* **2024**, *63*, e202318483.

[112] Z. Fernández, L. Sánchez, S. Santhosh Babu, G. Fernández, “Oligo(phenyleneethynylene)s: Shape-Tunable Building Blocks for Supramolecular Self-Assembly” *Angew. Chem. Int. Ed.* **2024**, *63*, e202402259.

[113] S. Wegelin, M. A. R. Meier, “Solution Self-Assembly of Branched Macromolecules Obtained via Iterative OPE Synthesis and the Passerini Three-Component Reaction” *Macromol. Chem. Phys.* **2024**, *225*, 2300337.

[114] D. S. Philips, K. K. Kartha, A. T. Politi, T. Krüger, R. Q. Albuquerque, G. Fernández, “Interplay between H-Bonding and Preorganization in the Evolution of Self-Assembled Systems” *Angew. Chem. Int. Ed.* **2019**, *58*, 4732–4736.

[115] Y. Zhong, Y. Yang, Y. Shen, W. Xu, Q. Wang, A. L. Connor, X. Zhou, L. He, X. C. Zeng, Z. Shao, Z. Lu, B. Gong, "Enforced Tubular Assembly of Electronically Different Hexakis(m-Phenylene Ethynylene) Macrocycles: Persistent Columnar Stacking Driven by Multiple Hydrogen-Bonding Interactions" *J. Am. Chem. Soc.* **2017**, *139*, 15950–15957.

[116] A. Langenstroer, K. K. Kartha, Y. Dorca, J. Droste, V. Stepanenko, R. Q. Albuquerque, M. R. Hansen, L. Sánchez, G. Fernández, "Unraveling Concomitant Packing Polymorphism in Metallosupramolecular Polymers" *J. Am. Chem. Soc.* **2019**, *141*, 5192–5200.

[117] T. Miteva, L. Palmer, L. Kloppenburg, D. Neher, U. H. F. Bunz, "Interplay of Thermochromicity and Liquid Crystalline Behavior in Poly(p-phenyleneethynylene)s: π−π Interactions or Planarization of the Conjugated Backbone?" *Macromolecules* **2000**, *33*, 652–654.

[118] C. Anders, M. Wagner, M. Alaasar, V.-M. Fischer, R. Waldecker, Y. Zhao, T. Tan, Y. Cao, F. Liu, C. Tschierske, "Highly branched bolapolyphilic liquid crystals with a cubic A15 network at the triangle-square transition" *Chem. Commun.* **2024**, *60*, 1023–1026.

[119] J. Daniel, A. P. Satheesh, K. Kartha Kalathil, "Self-Assembly of Discrete Multi-Chromophoric Systems" *Chem. – Eur. J.* **2024**, *30*, e202401278.

[120] L. Rubert, C. Marre, P. Ximenis, R. M. Gomila, A. Frontera, B. Soberats, "Luminescent Liquid-Crystalline J-Aggregate Based on a Columnar Axial Coassembly" *J. Am. Chem. Soc.* **2025**, DOI 10.1021/jacs.5c03166.

[121] E. Smarsly, D. Daume, F. Braig, S. Koser, E. Dörsam, U. H. F. Bunz, "Poly(para-phenyleneethynylene)s as emitters in polymer LEDs" *J. Mater. Chem. C* **2018**, *6*, 11002–11006.

[122] H. Usta, D. Alimli, R. Ozdemir, E. Tekin, F. Alkan, R. Kacar, A. G. Altas, S. Dabak, A. G. Gürek, E. Mutlugun, A. F. Yazici, A. Can, "A hybridized local and charge transfer

excited state for solution-processed non-doped green electroluminescence based on oligo(p-phenyleneethynylene)" *J. Mater. Chem. C* **2020**, *8*, 8047–8060.

[123] H. Usta, D. Alimli, R. Ozdemir, S. Dabak, Y. Zorlu, F. Alkan, E. Tekin, A. Can, "Highly Efficient Deep-Blue Electroluminescence Based on a Solution-Processable A−π–D−π–A Oligo(p-phenyleneethynylene) Small Molecule" *ACS Appl. Mater. Interfaces* **2019**, *11*, 44474–44486.

[124] M. Hodecker, A. M. Driscoll, U. H. F. Bunz, A. Dreuw, "Twisting and bending photo-excited phenylethynylbenzenes – a theoretical analysis" *Phys. Chem. Chem. Phys.* **2020**, *22*, 9974–9981.

[125] M. Hodecker, Y. Kozhemyakin, S. Weigold, F. Rominger, J. Freudenberg, A. Dreuw, U. H. F. Bunz, "A Doubly Bridged Bis(phenylethynyl)benzene: Different from a Twisted Tolan" *Chem. – Eur. J.* **2020**, *26*, 16990–16993.

[126] R. Chinchilla, C. Nájera, "Recent advances in Sonogashira reactions" *Chem. Soc. Rev.* **2011**, *40*, 5084–5121.

[127] C. Liu, M. Szostak, "Decarbonylative Sonogashira cross-coupling: a fruitful marriage of alkynes with carboxylic acid electrophiles" *Org. Chem. Front.* **2022**, *9*, 216–222.

[128] W. Li, H. Ma, S. Li, J. Ma, "Computational and data driven molecular material design assisted by low scaling quantum mechanics calculations and machine learning" *Chem. Sci.* **2021**, *12*, 14987–15006.

[129] A. Jablonski, "Efficiency of Anti-Stokes Fluorescence in Dyes" *Nature* **1933**, *131*, 839–840.

[130] A. Jabłoński, "Über den Mechanismus der Photolumineszenz von Farbstoffphosphoren" *Z. Für Phys.* **1935**, *94*, 38–46.

[131] J. Franck, E. G. Dymond, “Elementary processes of photochemical reactions” *Trans. Faraday Soc.* **1926**, *21*, 536–542.

[132] E. Condon, “A Theory of Intensity Distribution in Band Systems” *Phys. Rev.* **1926**, *28*, 1182–1201.

[133] M. Kasha, “Characterization of electronic transitions in complex molecules” *Discuss. Faraday Soc.* **1950**, *9*, 14–19.

[134] G. G. Stokes, “Ueber die Veränderung der Brechbarkeit des Lichts” *Ann. Phys.* **1852**, *163*, 480–490.

[135] J. R. Lakowicz, B. R. Masters, *Principles of Fluorescence Spectroscopy, Third Edition*, Springer, **2008**.

[136] A. Endo, K. Sato, K. Yoshimura, T. Kai, A. Kawada, H. Miyazaki, C. Adachi, “Efficient up-conversion of triplet excitons into a singlet state and its application for organic light emitting diodes” *Appl. Phys. Lett.* **2011**, *98*, 083302.

[137] A. Endo, M. Ogasawara, A. Takahashi, D. Yokoyama, Y. Kato, C. Adachi, “Thermally Activated Delayed Fluorescence from Sn4+–Porphyrin Complexes and Their Application to Organic Light Emitting Diodes — A Novel Mechanism for Electroluminescence” *Adv. Mater.* **2009**, *21*, 4802–4806.

[138] J. M. Dos Santos, D. Hall, B. Basumatary, M. Bryden, D. Chen, P. Choudhary, T. Comerford, E. Crovini, A. Danos, J. De, S. Diesing, M. Fatahi, M. Griffin, A. K. Gupta, H. Hafeez, L. Hämmerling, E. Hanover, J. Haug, T. Heil, D. Karthik, S. Kumar, O. Lee, H. Li, F. Lucas, C. F. R. Mackenzie, A. Mariko, T. Matulaitis, F. Millward, Y. Olivier, Q. Qi, I. D. W. Samuel, N. Sharma, C. Si, L. Spierling, P. Sudhakar, D. Sun, E. Tankelevičiūtė, M. Duarte Tonet, J. Wang, T. Wang, S. Wu, Y. Xu, L. Zhang, E. Zysman-Colman, “The Golden Age of Thermally Activated Delayed Fluorescence Materials: Design and Exploitation” *Chem. Rev.* **2024**, *124*, 13736–14110.

[139] D. Barman, Y. Tsuchiya, C. Adachi, “Horizontally oriented MRCT-type TADF emitter achieving EQE over 40% for Sky-Blue OLED” *Nat. Commun.* **2025**, *16*, 5023.

[140] A. Köhler, H. Bässler, “Triplet states in organic semiconductors” *Mater. Sci. Eng. R Rep.* **2009**, *66*, 71–109.

[141] P. W. Atkins, R. Friedman, *Molecular quantum mechanics*, Oxford University Press, New York, **2005**.

[142] Y. Pan, W. Li, S. Zhang, L. Yao, C. Gu, H. Xu, B. Yang, Y. Ma, “High Yields of Singlet Excitons in Organic Electroluminescence through Two Paths of Cold and Hot Excitons” *Adv. Opt. Mater.* **2014**, *2*, 510–515.

[143] Y. Pan, J. Huang, W. Li, Y. Gao, Z. Wang, D. Yu, B. Yang, Y. Ma, “Theoretical investigation of high-efficiency organic electroluminescent material: HLCT state and hot exciton process” *RSC Adv.* **2017**, *7*, 19576–19583.

[144] B. Li, J. Lou, H. Zhang, G. Li, X. He, Y. Huang, N. Zheng, Z. Wang, D. Ma, B. Z. Tang, “‘Exciton Recovery’ Strategy in Hot Exciton Emitter toward High-Performance Non-Doped Deep-Blue and Host-Sensitized Organic Light-Emitting Diodes” *Adv. Funct. Mater.* **2023**, *33*, 2212876.

[145] F. Majer, L. Roß, A. L. Respondek, C. Bannwarth, A. J. C. Kuehne, “Hot Exciton versus Hot Exciplex TADF Mechanism – Effect of the Donor-Acceptor Functionalization Pattern on Anthracene-based Emitters” *ChemPhotoChem* **2024**, *8*, e202400141.

[146] Y. Xu, P. Xu, D. Hu, Y. Ma, “Recent progress in hot exciton materials for organic light-emitting diodes” *Chem. Soc. Rev.* **2021**, *50*, 1030–1069.

[147] Z. R. Grabowski, K. Rotkiewicz, W. Rettig, “Structural Changes Accompanying Intramolecular Electron Transfer: Focus on Twisted Intramolecular Charge-Transfer States and Structures” *Chem. Rev.* **2003**, *103*, 3899–4032.

[148] N. Mataga, Y. Kaifu, M. Koizumi, “Solvent Effects upon Fluorescence Spectra and the Dipolemoments of Excited Molecules” *Bull. Chem. Soc. Jpn.* **1956**, *29*, 465–470.

[149] E. Lippert, “Spektroskopische Bestimmung des Dipolmomentes aromatischer Verbindungen im ersten angeregten Singulettzustand” *Z. Für Elektrochem. Berichte Bunsenges. Für Phys. Chem.* **1957**, *61*, 962–975.

[150] M. A. Baldo, D. F. O’Brien, Y. You, A. Shoustikov, S. Sibley, M. E. Thompson, S. R. Forrest, “Highly efficient phosphorescent emission from organic electroluminescent devices” *Nature* **1998**, *395*, 151–154.

[151] T. Wang, Y. Cheng, C. Yang, “Thermally activated delayed fluorescence polymers and their application in organic light-emitting diodes” *Prog. Polym. Sci.* **2024**, *158*, 101892.

[152] Y. Wang, A. Ying, S. Gong, “Recent progress in thermally activated delayed fluorescence dendrimers for solution-processed organic light-emitting diodes” *J. Polym. Sci.* **2024**, *62*, 241–265.

[153] S. Shao, L. Wang, “Through-space charge transfer polymers for solution-processed organic light-emitting diodes” *Aggregate* **2020**, *1*, 45–56.

[154] K. M. Shaulis, B. L. Hoskin, J. R. Townsend, F. E. Goodson, C. D. Incarvito, A. L. Rheingold, “Tandem Suzuki Coupling−Norbornadiene Insertion Reactions. A Convenient Route to 5,6-Diarylnorbornene Compounds” *J. Org. Chem.* **2002**, *67*, 5860–5863.

[155] Q. Li, J. Hu, J. Lv, X. Wang, S. Shao, L. Wang, X. Jing, F. Wang, “Through-Space Charge-Transfer Polynorbornenes with Fixed and Controllable Spatial Alignment of Donor and Acceptor for High-Efficiency Blue Thermally Activated Delayed Fluorescence” *Angew. Chem. Int. Ed.* **2020**, *59*, 20174–20182.

[156] K. Albrecht, K. Matsuoka, K. Fujita, K. Yamamoto, “Carbazole Dendrimers as Solution-Processable Thermally Activated Delayed-Fluorescence Materials” *Angew. Chem. Int. Ed.* **2015**, *54*, 5677–5682.

[157] K. M. Rao, R. Ramaraghavulu, D. Kolli, S. H. Babu, S. V. P. Vattikuti, M. Godumala, “Recent breakthroughs in through-space charge transfer in π-stacked molecules as thermally activated delayed fluorescent emitters for OLED applications” *J. Mater. Chem. C* **2025**, *13*, 3091–3122.

[158] S. Wu, D. Chen, X.-H. Zhang, D. Sun, E. Zysman-Colman, “A Multiresonant Thermally Activated Delayed Fluorescent Dendrimer with Intramolecular Energy Transfer: Application for Efficient Host-Free Green Solution-Processed Organic Light-emitting Diodes” *Adv. Mater.* **2025**, *37*, 2415289.

[159] J. Jung, H. Park, H. Y. Jung, S. E. Jung, S. G. Kim, T. H. Kim, Y. J. Lim, B.-C. Ku, M. Kim, S. H. Lee, “Recent progress in liquid crystal devices and materials of TFT-LCDs” *J. Inf. Disp.* **2024**, *25*, 121–142.

[160] L. A. Wilson, “2025 Display Industry Awards: SID Recognizes Top Products and Applications” *Inf. Disp.* **2025**, *41*, 6–10.

[161] M. Flämmich, M. C. Gather, N. Danz, D. Michaelis, A. H. Bräuer, K. Meerholz, A. Tünnermann, “Orientation of emissive dipoles in OLEDs: Quantitative *in situ* analysis” *Org. Electron.* **2010**, *11*, 1039–1046.

[162] A. Graf, P. Liehm, C. Murawski, S. Hofmann, K. Leo, M. C. Gather, “Correlating the transition dipole moment orientation of phosphorescent emitter molecules in OLEDs with basic material properties” *J. Mater. Chem. C* **2014**, *2*, 10298–10304.

[163] F. Tenopala-Carmona, O. S. Lee, E. Crovini, A. M. Neferu, C. Murawski, Y. Olivier, E. Zysman-Colman, M. C. Gather, “Identification of the Key Parameters for Horizontal Transition Dipole Orientation in Fluorescent and TADF Organic Light-Emitting Diodes” *Adv. Mater.* **2021**, *33*, 2100677.

[164] A. Senes, S. C. J. Meskers, W. M. Dijkstra, J. J. van Franeker, S. Altazin, J. S. Wilson, R. A. J. Janssen, "Transition dipole moment orientation in films of solution processed fluorescent oligomers: investigating the influence of molecular anisotropy" *J. Mater. Chem. C* **2016**, *4*, 6302–6308.

[165] A. Senes, S. C. J. Meskers, H. Greiner, K. Suzuki, H. Kaji, C. Adachi, J. S. Wilson, R. A. J. Janssen, "Increasing the horizontal orientation of transition dipole moments in solution processed small molecular emitters" *J. Mater. Chem. C* **2017**, *5*, 6555–6562.

[166] R. K. Roy, A. Meszynska, C. Laure, L. Charles, C. Verchin, J.-F. Lutz, "Design and synthesis of digitally encoded polymers that can be decoded and erased" *Nat. Commun.* **2015**, *6*, 7237.

[167] G. Cavallo, S. Poyer, J.-A. Amalian, F. Dufour, A. Burel, C. Carapito, L. Charles, J.-F. Lutz, "Cleavable Binary Dyads: Simplifying Data Extraction and Increasing Storage Density in Digital Polymers" *Angew. Chem. Int. Ed.* **2018**, *57*, 6266–6269.

[168] A. C. Boukis, M. A. R. Meier, "Data storage in sequence-defined macromolecules via multicomponent reactions" *Eur. Polym. J.* **2018**, *104*, 32–38.

[169] S. Martens, A. Landuyt, P. Espeel, B. Devreese, P. Dawyndt, F. Du Prez, "Multifunctional sequence-defined macromolecules for chemical data storage" *Nat. Commun.* **2018**, *9*, 4451.

[170] M. Frölich, D. Hofheinz, M. A. R. Meier, "Reading mixtures of uniform sequence-defined macromolecules to increase data storage capacity" *Commun. Chem.* **2020**, *3*, 184.

[171] K. S. Wetzel, M. Frölich, S. C. Solleder, R. Nickisch, P. Treu, M. A. R. Meier, "Dual sequence definition increases the data storage capacity of sequence-defined macromolecules" *Commun. Chem.* **2020**, *3*, 63.

[172] J.-A. Amalian, T. T. Trinh, J.-F. Lutz, L. Charles, "MS/MS Digital Readout: Analysis of Binary Information Encoded in the Monomer Sequences of Poly(triazole amide)s" *Anal. Chem.* **2016**, *88*, 3715–3722.

[173] A. Al Ouahabi, J.-A. Amalian, L. Charles, J.-F. Lutz, "Mass spectrometry sequencing of long digital polymers facilitated by programmed inter-byte fragmentation" *Nat. Commun.* **2017**, *8*, 967.

[174] Z. C. Girvin, M. K. Andrews, X. Liu, S. H. Gellman, "Foldamer-templated catalysis of macrocycle formation" *Science* **2019**, *366*, 1528–1531.

[175] P. Chandra, A. M. Jonas, A. E. Fernandes, "Sequence and Surface Confinement Direct Cooperativity in Catalytic Precision Oligomers" *J. Am. Chem. Soc.* **2018**, *140*, 5179–5184.

[176] J. Li, Q. Qin, S. Kardas, M. Fosségré, M. Surin, A. E. Fernandes, K. Glinel, A. M. Jonas, "Sequence Rules the Functional Connections and Efficiency of Catalytic Precision Oligomers" *ACS Catal.* **2022**, *12*, 2126–2131.

[177] R. B. Merrifield, "Solid Phase Peptide Synthesis. I. The Synthesis of a Tetrapeptide" *J. Am. Chem. Soc.* **1963**, *85*, 2149–2154.

[178] R. B. Merrifield, J. Morrow. Stewart, Nils. Jernberg, "Instrument for automated synthesis of peptides" *Anal. Chem.* **1966**, *38*, 1905–1914.

[179] A. J. Mijalis, D. A. Thomas, M. D. Simon, A. Adamo, R. Beaumont, K. F. Jensen, B. L. Pentelute, "A fully automated flow-based approach for accelerated peptide synthesis" *Nat. Chem. Biol.* **2017**, *13*, 464–466.

[180] J. Su, J.-N. Mo, G. Zhang, Z. Jiang, J. Zhao, "A practical approach for oligopeptide synthesis via synergistic photoredox, cobaloxime and organophosphorus triple catalysis" *Org. Chem. Front.* **2023**, *10*, 4895–4904.

[181] C. Overby, B. Abraham, E. Adjei-Sowah, A. March, K. Ling, S. Basu, D. S. W. Benoit, "A Rapid Manual Solid Phase Peptide Synthesis Method for High-Throughput Peptide Production" *J. Biomed. Mater. Res. A* **2025**, *113*, e37922.

[182] P. F. Conlon, O. Eguaogie, J. J. Wilson, J. S. T. Sweet, J. Steinhoegl, K. Englert, O. G. A. Hancox, C. J. Law, S. A. Allman, J. H. R. Tucker, J. P. Hall, J. S. Vyle, "Solid-phase synthesis and structural characterisation of phosphoroselenolate-modified DNA: a backbone analogue which does not impose conformational bias and facilitates SAD X-ray crystallography" *Chem. Sci.* **2019**, *10*, 10948–10957.

[183] K. Kakuta, R. Kasahara, K. Sato, T. Wada, "Solid-phase synthesis of oligodeoxynucleotides using nucleobase N -unprotected oxazaphospholidine derivatives bearing a long alkyl chain" **2023**, DOI 10.1039/D3OB01255G.

[184] R. N. Zuckermann, J. M. Kerr, S. B. H. Kent, W. H. Moos, "Efficient method for the preparation of peptoids [oligo(N-substituted glycines)] by submonomer solid-phase synthesis" *J. Am. Chem. Soc.* **1992**, *114*, 10646–10647.

[185] N. Jäck, S. Nagel, L. Hartmann, "Sequence-defined polymers for biomedical applications" *Prog. Polym. Sci.* **2025**, 101993.

[186] S. C. Solleder, D. Zengel, K. S. Wetzel, M. A. R. Meier, "A Scalable and High-Yield Strategy for the Synthesis of Sequence-Defined Macromolecules" *Angew. Chem. Int. Ed.* **2016**, *55*, 1204–1207.

[187] S. C. Solleder, S. Martens, P. Espeel, F. Du Prez, M. A. R. Meier, "Combining Two Methods of Sequence Definition in a Convergent Approach: Scalable Synthesis of Highly Defined and Multifunctionalized Macromolecules" *Chem. – Eur. J.* **2017**, *23*, 13906–13909.

[188] Y.-H. Wu, J. Zhang, F.-S. Du, Z.-C. Li, “Dual Sequence Control of Uniform Macromolecules through Consecutive Single Addition by Selective Passerini Reaction” *ACS Macro Lett.* **2017**, *6*, 1398–1403.

[189] K. S. Wetzel, M. A. R. Meier, “Monodisperse, sequence-defined macromolecules as a tool to evaluate the limits of ring-closing metathesis” *Polym. Chem.* **2019**, *10*, 2716–2722.

[190] S. C. Solleder, K. S. Wetzel, M. A. R. Meier, “Dual side chain control in the synthesis of novel sequence-defined oligomers through the Ugi four-component reaction” *Polym. Chem.* **2015**, *6*, 3201–3204.

[191] S. Wang, Y. Tao, J. Wang, Y. Tao, X. Wang, “A versatile strategy for the synthesis of sequence-defined peptoids with side-chain and backbone diversity via amino acid building blocks” *Chem. Sci.* **2019**, *10*, 1531–1538.

[192] X. Ren, C. Guo, X. Li, Y. Wu, Y. Zhang, S. Li, K. Zhang, “Protecting-Group-Free Iterative Divergent/Convergent Method for Preparing Sequence-Defined Polymers” *Macromolecules* **2023**, *56*, 1045–1052.

[193] W. Konrad, C. Fengler, S. Putwa, C. Barner-Kowollik, “Protection-Group-Free Synthesis of Sequence-Defined Macromolecules via Precision λ-Orthogonal Photochemistry” *Angew. Chem. Int. Ed.* **2019**, *58*, 7133–7137.

[194] M. M. Martínez, M. Peña-López, J. P. Sestelo, L. A. Sarandeses, “Synthesis of functionalized thiophenes and oligothiophenes by selective and iterative cross-coupling reactions using indium organometallics” *Org. Biomol. Chem.* **2012**, *10*, 3892–3898.

[195] F. P. V. Koch, M. Heeney, P. Smith, “Thermal and Structural Characteristics of Oligo(3-hexylthiophene)s (3HT)n, n = 4–36” *J. Am. Chem. Soc.* **2013**, *135*, 13699–13709.

[196] R. Remy, E. D. Weiss, N. A. Nguyen, S. Wei, L. M. Campos, T. Kowalewski, M. E. Mackay, “Enthalpy of fusion of poly(3-hexylthiophene) by differential scanning calorimetry” *J. Polym. Sci. Part B Polym. Phys.* **2014**, *52*, 1469–1475.

[197] G. R. McKeown, S. Ye, S. Cheng, D. S. Seferos, “Homogenous Synthesis of Monodisperse High Oligomers of 3-Hexylthiophene by Temperature Cycling” *J. Am. Chem. Soc.* **2019**, *141*, 17053–17056.

[198] H. Xu, S. Ye, R. Zhao, D. S. Seferos, “Homogeneous Synthesis of Monodisperse Sequence-Defined Conjugated Oligomers by Temperature Cycling” *Angew. Chem. Int. Ed.* **2022**, *61*, e202210340.

[199] J. S. Schumm, D. L. Pearson, J. M. Tour, “Iterative Divergent/Convergent Approach to Linear Conjugated Oligomers by Successive Doubling of the Molecular Length: A Rapid Route to a 128Å-Long Potential Molecular Wire” *Angew. Chem. Int. Ed. Engl.* **1994**, *33*, 1360–1363.

[200] S. Huang, J. M. Tour, “Rapid bi-directional synthesis of oligo(1, 4-phenylene ethynylene)s” *Tetrahedron Lett.* **1999**, *40*, 3447–3450.

[201] J.-J. Hwang, J. M. Tour, “Combinatorial synthesis of oligo(phenylene ethynylene)s” *Tetrahedron* **2002**, *58*, 10387–10405.

[202] R. Szweda, C. Chendo, L. Charles, P. N. W. Baxter, J.-F. Lutz, “Synthesis of oligoarylacetylenes with defined conjugated sequences using tailor-made soluble polymer supports” *Chem. Commun.* **2017**, *53*, 8312–8315.

[203] M. A. Idris, S. Lee, “Recent Advances in Decarboxylative Reactions of Alkynoic Acids” *Synthesis* **2020**, *52*, 2277–2298.

[204] Y. Li, J.-Y. Liu, Y.-D. Zhao, Y.-C. Cao, “Recent advancements of high efficient donor–acceptor type blue small molecule applied for OLEDs” *Mater. Today* **2017**, *20*, 258–266.

[205] C. Mathur, R. Gupta, R. K. Bansal, “Organic Donor-Acceptor Complexes As Potential Semiconducting Materials” *Chem. – Eur. J.* **2024**, *30*, e202304139.

[206] L. Wang, W. Zhu, “Organic Donor-Acceptor Systems for Photocatalysis” *Adv. Sci.* **2024**, *11*, 2307227.

[207] F. Xie, X. Yang, P. Jin, X.-T. Wang, H. Ran, H. Zhang, H. Sun, S.-J. Su, J.-Y. Hu, “Achieving Simultaneously Ultrahigh Brightness, Extremely Low Efficiency Roll-Off and Ultralong Lifetime of Blue Fluorescent OLEDs by Using Donor–Acceptor-Type 5,9-Diarylamine Functionalized Pyrenes” *Adv. Opt. Mater.* **2023**, *11*, 2202490.

[208] H. T. Yang, Y. J. Hyeon, T. N. Le, J. E. Lee, Y.-H. Kim, M. C. Suh, “Impact of Donor and Acceptor Modification on TADF and Roll-Off Behaviors in Solution Processed OLED” *Adv. Opt. Mater.* **2024**, *12*, 2401881.

[209] Y. Takeda, “Modulating the Photophysical Properties of Twisted Donor–Acceptor–Donor π-Conjugated Molecules: Effect of Heteroatoms, Molecular Conformation, and Molecular Topology” *Acc. Chem. Res.* **2024**, *57*, 2219–2232.

[210] S. Wang, R. Zhang, R. Ding, H. Huang, H. Qi, Y. Liu, S. Ying, D. Ma, S. Yan, “Intramolecular-locking modification enables efficient asymmetric donor–acceptor–donor′ type ultraviolet emitters for high-performance OLEDs with reduced efficiency roll-off and high color purity” *Chem. Sci.* **2025**, *16*, 5518–5527.

[211] Y.-C. Cheng, X. Tang, R. Walia, T.-Y. Zhang, X.-C. Fan, J. Yu, K. Wang, C. Adachi, X.-K. Chen, X.-H. Zhang, “High-Efficiency and High Color Purity Solution-Processable Deep-Blue OLEDs Enabled by Linearly Fully Fused Acceptor-Donor-Acceptor Molecular Design” *Adv. Mater.* **n.d.**, *n/a*, 2500010.

[212] K. P. C. P, K. Rayappa Naveen, J. Hur, “Acceptor–donor–acceptor based thermally activated delayed fluorescent materials: structure–property insights and electroluminescence performances” *Mater. Chem. Front.* **2024**, *8*, 769–784.

[213] M. Song, Y.-J. Yu, Z.-Q. Feng, Z.-H. Qu, P. Zuo, H.-Y. Yan, Z.-Q. Jiang, D.-Y. Zhou, L.-S. Liao, "A red thermally activated delayed fluorescence emitter with mitigated efficiency roll-off via a π-stacked multiple donor–acceptor structure" *J. Mater. Chem. C* **2024**, *12*, 6858–6864.

[214] R. Braveenth, K. Raagulan, Y.-J. Kim, B.-M. Kim, "Recent advances in green thermally activated delayed fluorescence emitters towards high colour purity and good electroluminescence performance" *Mater. Adv.* **2023**, *4*, 374–388.

[215] Gaussian 16, Revision C.01, M. J. Frisch, G. W. Trucks, H. B. Schlegel, G. E. Scuseria, M. A. Robb, J. R. Cheeseman, G. Scalmani, V. Barone, G. A. Petersson, H. Nakatsuji, X. Li, M. Caricato, A. V. Marenich, J. Bloino, B. G. Janesko, R. Gomperts, B. Mennucci, H. P. Hratchian, J. V. Ortiz, A. F. Izmaylov, J. L. Sonnenberg, D. Williams-Young, F. Ding, F. Lipparini, F. Egidi, J. Goings, B. Peng, A. Petrone, T. Henderson, D. Ranasinghe, V. G. Zakrzewski, J. Gao, N. Rega, G. Zheng, W. Liang, M. Hada, M. Ehara, K. Toyota, R. Fukuda, J. Hasegawa, M. Ishida, T. Nakajima, Y. Honda, O. Kitao, H. Nakai, T. Vreven, K. Throssell, J. A. Montgomery, Jr., J. E. Peralta, F. Ogliaro, M. J. Bearpark, J. J. Heyd, E. N. Brothers, K. N. Kudin, V. N. Staroverov, T. A. Keith, R. Kobayashi, J. Normand, K. Raghavachari, A. P. Rendell, J. C. Burant, S. S. Iyengar, J. Tomasi, M. Cossi, J. M. Millam, M. Klene, C. Adamo, R. Cammi, J. W. Ochterski, R. L. Martin, K. Morokuma, O. Farkas, J. B. Foresman, and D. J. Fox, Gaussian, Inc., Wallingford CT, **2016**.

[216] O. S. Lee, M. C. Gather, E. Zysman-Colman, "Digichem: computational chemistry for everyone" *Digit. Discov.* **2024**, *3*, 1695–1713.

[217] T. Lu, F. Chen, "Multiwfn: A multifunctional wavefunction analyzer" *J. Comput. Chem.* **2012**, *33*, 580–592.

[218] Z. Liu, T. Lu, Q. Chen, "An sp-hybridized all-carboatomic ring, cyclo[18]carbon: Electronic structure, electronic spectrum, and optical nonlinearity" *Carbon* **2020**, *165*, 461–467.

[219] K. Zhang, Y. Zhang, Y. Ma, J. Fan, C.-K. Wang, L. Lin, "Solid-State Effect Induced Thermally Activated Delayed Fluorescence with Tunable Emission: A Multiscale Study" *J. Phys. Chem. A* **2020**, *124*, 8540–8550.

[220] Z. Wei, S. Lin, T. Zuo, Q. Li, S. Jiang, F. Qi, M. Yang, J. Gu, L. Meng, C.-Z. Lu, "Thermally activated delayed fluorescence materials with aggregation-induced emission properties: a QM/MM study" *Phys. Chem. Chem. Phys.* **2021**, *23*, 25789–25796.

[221] S. Jiang, F. Qi, D. Zhang, X. Lv, J. Song, J. Gu, J. Chen, L. Meng, "Carbonyl (CO)/N-based thermally activated delayed fluorescent materials with high efficiency and fast reverse intersystem crossing rate: a theoretical design and study" *New J. Chem.* **2023**, *47*, 7686–7693.

[222] S. Hirata, Y. Sakai, K. Masui, H. Tanaka, S. Y. Lee, H. Nomura, N. Nakamura, M. Yasumatsu, H. Nakanotani, Q. Zhang, K. Shizu, H. Miyazaki, C. Adachi, "Highly efficient blue electroluminescence based on thermally activated delayed fluorescence" *Nat. Mater.* **2015**, *14*, 330–336.

[223] J. M. Ha, S. H. Hur, A. Pathak, J.-E. Jeong, H. Y. Woo, "Recent advances in organic luminescent materials with narrowband emission" *NPG Asia Mater.* **2021**, *13*, 1–36.

[224] P. L. dos Santos, P. Stachelek, Y. Takeda, P. Pander, "Recent advances in highly-efficient near infrared OLED emitters" *Mater. Chem. Front.* **2024**, *8*, 1731–1766.

[225] X. Wu, S. Ni, C.-H. Wang, W. Zhu, P.-T. Chou, "Comprehensive Review on the Structural Diversity and Versatility of Multi-Resonance Fluorescence Emitters: Advance, Challenges, and Prospects toward OLEDs" *Chem. Rev.* **2025**, *125*, 6685–6752.

[226] K. Li, G. S. M. Tong, Q. Wan, G. Cheng, W.-Y. Tong, W.-H. Ang, W.-L. Kwong, C.-M. Che, "Highly phosphorescent platinum(II) emitters: photophysics, materials and biological applications" *Chem. Sci.* **2016**, *7*, 1653–1673.

[227] "A Standard Default Color Space for the Internet - sRGB," can be found under https://www.w3.org/Graphics/Color/sRGB.html(accessed 7 August 2025), **1996**.

[228] X. Fan, X. Hao, F. Huang, J. Yu, K. Wang, X. Zhang, "RGB Thermally Activated Delayed Fluorescence Emitters for Organic Light-Emitting Diodes toward Realizing the BT.2020 Standard" *Adv. Sci.* **2023**, *10*, 2303504.

[229] M. Wang, Y. Gong, F. Alzina, C. M. Sotomayor Torres, H. Li, Z. Zhang, J. He, "Angle-Dependent Photoluminescence Spectroscopy of Solution-Processed Organic Semiconducting Nanobelts" *J. Phys. Chem. C* **2017**, *121*, 12441–12446.

[230] N. Yoshida, H. Sasabe, H. Arai, Y. Sagae, Y. Yagi, K. Hoshi, D. Yokoyama, J. Kido, "Elucidating The Horizontal Orientation Mechanism of Emissive Transition Dipole Moment in A Series of Stick-Like Delayed Fluorescent Emitters for Ultra-High-Efficiency OLEDs" *Adv. Opt. Mater.* **2024**, *12*, 2302382.

[231] H. Imahori, Y. Kobori, H. Kaji, "Manipulation of Charge-Transfer States by Molecular Design: Perspective from 'Dynamic Exciton'" *Acc. Mater. Res.* **2021**, *2*, 501–514.

[232] Z. Lin, R. Kabe, K. Wang, C. Adachi, "Influence of energy gap between charge-transfer and locally excited states on organic long persistence luminescence" *Nat. Commun.* **2020**, *11*, 191.

[233] X. Chen, X. Zhang, X. Xiao, Z. Wang, J. Zhao, "Recent Developments on Understanding Charge Transfer in Molecular Electron Donor-Acceptor Systems" *Angew. Chem. Int. Ed.* **2023**, *62*, e202216010.

[234] R. Kaur, F. Possanza, F. Limosani, S. Bauroth, R. Zanoni, T. Clark, G. Arrigoni, P. Tagliatesta, D. M. Guldi, "Understanding and Controlling Short- and Long-Range Electron/Charge-Transfer Processes in Electron Donor–Acceptor Conjugates" *J. Am. Chem. Soc.* **2020**, *142*, 7898–7911.

[235] C. Lu, E. Cho, K. Wan, C. Wu, Y. Gao, V. Coropceanu, J.-L. Brédas, F. Li, "Achieving Nearly 100% Photoluminescence Quantum Efficiency in Organic Radical Emitters by Fine-Tuning the Effective Donor-Acceptor Distance" *Adv. Funct. Mater.* **2024**, *34*, 2314811.

[236] B.-R. Gao, H.-Y. Wang, Y.-W. Hao, L.-M. Fu, H.-H. Fang, Y. Jiang, L. Wang, Q.-D. Chen, H. Xia, L.-Y. Pan, Y.-G. Ma, H.-B. Sun, "Time-Resolved Fluorescence Study of Aggregation-Induced Emission Enhancement by Restriction of Intramolecular Charge Transfer State" *J. Phys. Chem. B* **2010**, *114*, 128–134.

[237] H. Song, K. Wang, Z. Kuang, Y. S. Zhao, Q. Guo, A. Xia, "Solvent modulated excited state processes of push–pull molecule with hybridized local excitation and intramolecular charge transfer character" *Phys. Chem. Chem. Phys.* **2019**, *21*, 3894–3902.

[238] T. Lu, "A comprehensive electron wavefunction analysis toolbox for chemists, Multiwfn" *J. Chem. Phys.* **2024**, *161*, 082503.

[239] H. Li, D. R. Powell, R. K. Hayashi, R. West, "Poly((2,5-dialkoxy-p-phenylene)ethynylene-p-phenyleneethynylene)s and Their Model Compounds" *Macromolecules* **1998**, *31*, 52–58.

[240] G. V. Loukova, A. A. Milov, V. P. Vasiliev, V. I. Minkin, "Dipole moments and solvatochromism of metal complexes: principle photophysical and theoretical approach" *Phys. Chem. Chem. Phys.* **2016**, *18*, 17822–17826.

[241] K. B. Akshaya, A. Varghese, Y. N. Sudhakar, P. L. Lobo, L. George, "Study on Photophysical Properties of N-Arylphthalamic Acid Derivative Containing 1, 2, 4-Triazole Scaffold" *J. Fluoresc.* **2017**, *27*, 1909–1922.

[242] Y. Yang, S. R. Valandro, Z. Li, S. Kim, K. S. Schanze, "Photoinduced Intramolecular Electron Transfer in Phenylene Ethynylene Naphthalimide Oligomers" *J. Phys. Chem. A* **2021**, *125*, 3863–3873.

[243] M. I. Sluch, A. Godt, U. H. F. Bunz, M. A. Berg, "Excited-State Dynamics of Oligo(p-phenyleneethynylene): Quadratic Coupling and Torsional Motions" *J. Am. Chem. Soc.* **2001**, *123*, 6447–6448.

[244] G. Duvanel, J. Grilj, A. Schuwey, A. Gossauer, E. Vauthey, "Ultrafast excited-state dynamics of phenyleneethynylene oligomers in solution" *Photochem. Photobiol. Sci.* **2007**, *6*, 956–963.

[245] Q. Lu, K. Liu, H. Zhang, Z. Du, X. Wang, F. Wang, "From Tunneling to Hopping: A Comprehensive Investigation of Charge Transport Mechanism in Molecular Junctions Based on Oligo(p-phenylene ethynylene)s" *ACS Nano* **2009**, *3*, 3861–3868.

[246] X. Zhao, C. Huang, M. Gulcur, A. S. Batsanov, M. Baghernejad, W. Hong, M. R. Bryce, T. Wandlowski, "Oligo(aryleneethynylene)s with Terminal Pyridyl Groups: Synthesis and Length Dependence of the Tunneling-to-Hopping Transition of Single-Molecule Conductances" *Chem. Mater.* **2013**, *25*, 4340–4347.

[247] I. Barboza-Ramos, H. B. Gobeze, D. Wherritt, K. S. Schanze, "Water-Soluble Poly(phenylene ethynylene)s That Contain Phosphonium Pendant Groups" *Macromolecules* **2024**, *57*, 7575–7585.

[248] P. L. Donabedian, T. K. Pham, D. G. Whitten, E. Y. Chi, "Oligo(p-phenylene ethynylene) Electrolytes: A Novel Molecular Scaffold for Optical Tracking of Amyloids" *ACS Chem. Neurosci.* **2015**, *6*, 1526–1535.

[249] S. Li, K. Bamberg, Y. Lu, F. D. Sönnichsen, A. Staubitz, "Facile Synthesis of Light-Switchable Polymers with Diazocine Units in the Main Chain" *Polymers* **2023**, *15*, 1306.

[250] K. Imato, A. Ishii, N. Kaneda, T. Hidaka, A. Sasaki, I. Imae, Y. Ooyama, "Thermally Stable Photomechanical Molecular Hinge: Sterically Hindered Stiff-Stilbene Photoswitch Mechanically Isomerizes" *JACS Au* **2023**, *3*, 2458–2466.

[251] L. D. Thai, J. Fanelli, R. Munaweera, M. L. O'Mara, C. Barner-Kowollik, H. Mutlu, "Main-chain Macromolecular Hydrazone Photoswitches" *Angew. Chem. Int. Ed.* **2024**, *63*, e202315887.

[252] M. Gao, D. Kwaria, Y. Norikane, Y. Yue, "Visible-light-switchable azobenzenes: Molecular design, supramolecular systems, and applications" *Nat. Sci.* **2023**, *3*, e220020.

[253] D. Bléger, J. Schwarz, A. M. Brouwer, S. Hecht, "o-Fluoroazobenzenes as Readily Synthesized Photoswitches Offering Nearly Quantitative Two-Way Isomerization with Visible Light" *J. Am. Chem. Soc.* **2012**, *134*, 20597–20600.

[254] W. J. Brittain, S. K. Rastogi, R. A. Rogers, P. Rinaldi, "Phenyl rotation barrier in Z-azobenzene: A physical organic problem in honor of J.D.R." *J. Phys. Org. Chem.* **2018**, *31*, e3847.

[255] Y. Shirai, T. Sasaki, J. M. Guerrero, B.-C. Yu, P. Hodge, J. M. Tour, "Synthesis and Photoisomerization of Fullerene− and Oligo(phenylene ethynylene)−Azobenzene Derivatives" *ACS Nano* **2008**, *2*, 97–106.

[256] P. W. Atkins, J. de Paula, J. J. Keeler, *Physikalische Chemie*, Wiley-WCH, **2022**.

[257] A. Antoine John, Q. Lin, "Synthesis of Azobenzenes Using N-Chlorosuccinimide and 1,8-Diazabicyclo[5.4.0]undec-7-ene (DBU)" *J. Org. Chem.* **2017**, *82*, 9873–9876.

[258] S. R. Pulley, B. Czakó, "Formal total synthesis of shikonin via Dötz benzannulation" *Tetrahedron Lett.* **2004**, *45*, 5511–5514.

[259] H. Huang, C. Karlsson, M. Strømme, M. Sjödin, A. Gogoll, "Hydroquinone–pyrrole dyads with varied linkers" *Beilstein J. Org. Chem.* **2016**, *12*, 89–96.

[260] Z. Chen, H. Wang, L. Hu, S. Zhu, R. Liu, H. Zhu, "Pt(II) diimine complexes bearing varied alkyl chains: Synthesis, tunable photophysical properties and aggregation-induced optical power limiting enhancement" *Inorganica Chim. Acta* **2022**, *531*, 120714.